UNIVERSITÀ DEGLI STUDI DI TRENTO

Queen Mary University of London

Erasmus Mundus Joint Doctorate School in Science for MAnagement of Rivers and their Tidal System

---

Federico Monegaglia

Meandering rivers morphodynamics – integrating nonlinear modeling and remote sensing

Erasmus Mundus

October 2017

Doctoral thesis in Science for MAnagement of Rivers and their Tidal System

CYCLE IV

PRIMARY INSTITUTION Department of Civil, Environmental and Mechanical Engineering, University of Trento, Trento, Italy

SECONDARY INSTITUTION School of Geography, Queen Mary University, London, UK

SUPERVISORS

Prof. Marco Tubino, University of Trento

Dr. Alex Henshaw, Queen Mary University of London

Prof. Guido Zolezzi, University of Trento Front Cover: MacKenzie River, Canada (Photo credits: Stpaulairlines.com)

Academic year 2017/2018

(This page is intentionally left blank)

THE SMART JOINT DOCTORATE PROGRAMME

Research for this thesis was conducted with the support of the Erasmus Mundus Programme[1], within the framework of the Erasmus Mundus Joint Doctorate (EMJD) SMART (Science for MAnagement of Rivers and their Tidal systems). EMJDs aim to foster cooperation between higher education institutions and academic staff in Europe and third countries with a view to creating centres of excellence and providing a highly skilled 21st century workforce enabled to lead social, cultural and economic developments. All EMJDs involve mandatory mobility between the universities in the consortia and lead to the award of recognised joint, double or multiple degrees. The SMART programme represents a collaboration among the University of Trento, Queen Mary University of London, and Freie Universit´at Berlin. Each doctoral candidate within the SMART programme has conformed to the following during their 3 years of study:

1. Supervision by a minimum of two supervisors in two institutions (their primary and secondary institutions).
2. Study for a minimum period of 6 months at their secondary institution.
3. Successful completion of a minimum of 30 ECTS of taught courses.
4. Collaboration with an associate partner to develop a particular component / application of their research that is of mutual interest.
5. Submission of a thesis within 3 years of commencing the programme.

1 This project has been (partially) funded with support from the European Commission. This publication reflects the views only of the author, and the Commission cannot be held responsible for any use which may be made of the information contained therein.

A Francesca

RINGRAZIAMENTI

Volge al termine un'esperienza durata tre anni, nel periodo finora più intenso e pregnante della mia vita, cui il percorso di dottorato ha fatto da cornice mentre una serie di vicende, di persone, e di splendide quanto inaspettate sorprese si sono alternate e sovrapposte stravolgendo quella che credevo essere la mia esistenza. Il percorso di dottorato, in maniera continuativa rispetto agli ultimi anni della laurea, mi ha fornito uno stimolo intellettuale, una visione critica ed una voglia di conoscere il mondo che prima non credevo possibili, e che mi hanno spinto verso la scoperta di nuovi ambienti intellettuali, culturali e relazionali.

La persona che più devo ringraziare per tutto questo è il Professor Marco Tubino, amico e Maestro, che non ha mai mancato di farmi avere il suo sostegno durante questi tre anni di duro lavoro, e con il quale ho passato delle bellissime serate discorrendo dei massimi sistemi davanti a qualche bicchiere di buon vino. La sua figura e la stima che ho nei suoi confronti sono costantemente di stimolo per me, sia dal punto di vista intellettuale che umano; stimolo senza il quale non sarei arrivato dove sono arrivato oggi, non sarei quello che sono oggi.

Devo poi ringraziare quella che è stata forse la più inaspettata (sicuramente la più bella) sopresa di questi tre anni, Francesca, che mi ha sempre supportato e sopportato lungo tutte le strade che ho intrapreso in questi anni e nonostante io viva perennemente con la testa fra le nuvole.

La mia famiglia, che da quasi ventinove anni mi sostiene in ogni mia scelta, e che nei periodi più bui della mia vita non ha mai smesso di riporre le sue speranze e la sua fiducia in me; se oggi sto qui a scrivere queste parole, il merito più grande va a loro; questa tesi è dedicata anche a loro.

Il secondo mio supervisore, il Professor Guido Zolezzi, che nonostante lavori venticinque ore al giorno trova sempre del tempo da dedicarmi, durante il quale imparo sempre qualcosa di nuovo. Il terzo supervisore, Alex Henshaw della Queen Mary University of London: a big thank to you Alex for your valuable advices.

Un grazie pasciuto va a tutti i colleghi che in questi anni sono orbitati attorno al mio percorso: a Marco Red per i brainstorming scientifici e per i caffè che mai gli renderò, a Simone per le avventure passate insieme in punti improbabili del globo, a Matilde per aprirmi sempre

le porte dell'ufficio e del dipartimento, a Emilio per le svariate birre nei pub londinesi di dubbia legalità, a Tarun per le conversazioni chilometriche via posta elettronica, a Luca per le dritte sulle barre che camminano, a Martino per il sale in Val Ridanna, a Jean-Philippe e Prima per l'occasione di vedere un angolo di mondo che altrimenti non avrei visto, a Sekari per averci portati in vetta, ad Alessandro per le serate londinesi, a Gregor per aver condiviso con me una bettola a Napoli, a Walter e Marco Toff per i consigli più svariati. Grazie a Marina per essere stata la miglior segretaria che poteva capitare.

Un grazie va infine a Giotto che fa le fusa in segno d'approvazione mentre scrivo queste righe.

Trento, 24 Ottobre 2017 F. M.

SOMMARIO

Durante gli scorsi decenni, lo studio e l'analisi sistematica della dinamica dei fiumi meandriformi ha interessato principalmente il filone teorico-analitico. Lo sviluppo di questi modelli ha consentito di definire le condizioni di equilibrio, di stabilità e di evoluzione dei meandri, nonchè di studiare l'interazione tra forme planimetriche o tra forme planimetriche ed altimetriche. Negli anni più recenti s'è andata altresì sviluppando una nuova branca della morfodinamica fluviale: quella dell'analisi satellitare, che da una fase embrionale si è rapidamente espansa contestualmente al rapido aumento delle risorse computazionali e satellitari. L'analisi satellitare è ormai utilizzata in numerosi campi della geofisica e questo ha fatto sì che gli ultimi anni si sviluppassero algoritmi per gli obiettivi più svariati; nel campo della morfondimamica dei fiumi meandriformi, tuttavia, l'analisi satellitare rimane per lo più circoscritta ad analisi specifiche. In particolare, la mancanza di algoritmi sofisticati per l'analisi estensiva della moltitudine di informazioni contenute nei dati satellitari oggi disponibili ha impedito di cercare nell'analisi satellitare un riscontro puntuale e sistematico dei modelli matematici che ne definisca il grado di applicabilità in contesti reali di fiumi naturali; a questa difficoltà contribuiscono anche le inevitabili ipotesi semplificative adottate nei modelli matematici.

In questo lavoro di tesi si fornisce una metodologia per l'estrazione automatica di grandi quantità di informazioni morfodinamiche da dati satellitari multitemporali e multispettrali, codificata nel software PyRIS. Parallelamente, viene sviluppato un modello analitico completo per lo studio dell'evoluzione a lungo termine di fiumi meandriformi a carattere periodico, che tiene conto di variazioni spazio-temporali di curvatura, larghezza e pendenza. Una prima componente del modello comprende l'evoluzione di larghezza e pendenza medie del canale sulla base di una nuova formulazione della conservazione del flusso di sedimenti a scala di tratto. Una seconda componente implementa invece una un modello evolutivo nonlineare per meandri periodici con larghezza variabile nello spazio e nel tempo, in cui viene tenuto conto delle interazioni nonlineari a livello del campo di moto e del trasporto solido attraverso uno schema perturbativo a due parametri.

Lo studio di una gran quantità di fiumi meandriformi liberi mediante il software PyRIS consente di ottenere una consistente quantità di osservazioni sull'evoluzione spaziale e temporale della larghezza e della curvatura del canale, con inediti livelli di dettaglio. Il modello

inoltre mostra come la larghezza e la pendenza a scala di meandro vadano invariabilmente riducendosi durante l'evoluzione planimetrica, e come l'auto-aggiustamento della geometria in condizioni *bankfull* sia controllato dal rapporto tra le scale temporali della piana e del fondo, rapporto di cui viene fornita una quantificazione per i fiumi meandriformi naturali analizzati. Il modello perturbativo nonlineare prevede invece che la coevoluzione di curvatura e larghezza si sviluppi nella forma di un ciclo d'isteresi nel tempo; inoltre, esso mostra chiaramente come la larghezza della piana si riduca drasticamente quando le condizioni di risonanza dei meandri sono superate. L'approccio modellistico prevede infine la formazione di meandri con canale più largo all'apice della curva (*wider-at-bends*) quando il meccanismo di *bank pull* domina il processo evolutivo, mentre quando è il meccanismo di *bar push* a controllare l'evoluzione i meandri sono più larghi all'inflessione (*wider-at-inflections*).

L'integrazione tra modellazione matematica e analisi satellitare multitemporale viene proposta in termini statistici; l'analisi statistica a scala di curva dell'evoluzione di parametri descrittivi della planimetria, quali la larghezza, le sue oscillazioni e la curvatura di grandi fiumi meandriformi, trovano buon riscontro nel modello matematico proposto.

Infine, l'integrazione tra modellazione analitica e indagine satellitare consente di individuare i processi chiave che regolano l'interazione tra forme altimetriche libere e forme plano-altimetriche forzate nei fiumi meandriformi: le barre migranti (libere) di sedimenti, nei fiumi a carattere meandriforme, risultano formarsi solo qualora sussistano particolari condizioni, legate principalmente all'entità dell'apporto solido del bacino, contrariamente all'idea diffusa che i fiumi meandriformi diano origine a forme altimetriche migranti solo quando il valore della loro curvatura sia mediamente basso.

ABSTRACT

During the past decades, the systematic investigation of the morphodynamics of meandering rivers mostly involved the theoretical-analytical methodology. The development of analytical models enabled the definition of equilibrium conditions, stability and evolution of river meanders and to investigate the interaction between planform and bedform processes and mechanisms. In recent years the new branch of remote sensing applied to river morphodynamics has been constantly developing simultaneously to the rapid increase of computational and satellite resources. The remote sensing analysis

is nowadays employed in a wide range fields in geophysics; for this reason, the past years have seen the prolific development of numerous algorithms for remote sensing analysis. However, remote sensing of meandering river morphodynamics has not been consistently integrated with morphodynamic modelling so far. There is a lack of sophisticated algorithms for the extraction of extensive morphodynamic information from the available remotely sensed data; this gap prevented researchers from seeking systematic validation of analytical models to define their range of applicability, and to exploit their potential for improved insight on observations in real world meandering rivers. The evolutionary dynamics of the channel width, at local and bend scale, as well as the dynamics of bars in meandering rivers represent two major unsettled issues in our present understanding of river meandering dynamics.

In this thesis I first provide a systematic methodology for the automated extraction of meandering river morphodynamic information from multitemporal, multispectral remotely sensed data, coded in the PyRIS software. Moreover, I develop an analytical model to investigate the long-term planform evolution of periodic sequences of meander bends incorporating spatio-temporal variations of channel curvature, width and slope. A first model component predicts the temporal evolution of the channel width and slope based on a novel treatment of the sediment continuity at the reach scale. A second model component is a fully analytical, evolutionary model of periodic meanders with spatially and temporally oscillating width accounting for nonlinear feedbacks in flow and sediment transport by means of a two-parameters perturbation approach.

Application of the PyRIS software to several long reaches of free-flowing meandering rivers allows me to develop a consistent set of observations on the temporal and spatial evolution of channel width and curvature with unprecedented level of detail. Furthermore, model outcomes indicate that meander-averaged width and slope invariably decrease during meander development, and that the temporal adjustment of the hydraulic geometry is controlled by the ratio between the evolutionary timescales of planform and riverbed, quantified from the analyzed meandering rivers dataset. The nonlinear perturbation model indicates that width and curvature co-evolve according to a hysteretic behavior in time and predicts that the meander belt width dramatically decreases when the meander resonance threshold is crossed. The modelling approach predicts wider-at-bend meanders when the bank pull is dominant with respect to bar push, which in turn promotes meander bends that are wider at inflections.

Analytical modeling and remote sensing analysis are mostly integrated through a statistical approach; bend-scale evolutionary analysis

of planform descriptors such as channel width, width oscillations and curvature in large pristine meandering rivers exhibit good agreement with the outcomes of the proposed analytical models.

Finally, the integration between analytical modeling and remote sensing analysis allows me to identify the key processes controlling the interaction between migrating sediment bars and planform-driven steady point bars. The conditions for the formation of migrating bars in meandering rivers are mostly related to the production of sediment supply by the basin, contrarily to the widespread idea that meandering rivers exhibiting migrating bars typically display lower values of the channel curvature.

CONTENTS

I INTRODUCTION 1

1 INTRODUCTION 3
- 1.1 Meandering rivers 3
- 1.2 Towards transitional river patterns 5
  - 1.2.1 Meandering rivers with variable width 7
  - 1.2.2 Meandering rivers with alternate migrating bars 7
- 1.3 State of the art 10
- 1.4 Research questions 17
- 1.5 Thesis roadmap 18
  - 1.5.1 Introduction 18
  - 1.5.2 Methods 19
  - 1.5.3 Results 19
  - 1.5.4 Conclusions 20

2 REMOTE SENSING OF MEANDERING RIVER MORPHODYNAMICS 21
- 2.1 Introduction 21
- 2.2 Background 22
  - 2.2.1 A brief overview on river meander morphodynamics 22
  - 2.2.2 Remote sensing of river meanders 24
  - 2.2.3 The need for automated extraction of information on river meander morphodynamics 25

3 ANALYTICAL MODELING OF MEANDERING RIVER MORPHODYNAMICS 27
- 3.1 Morphodynamics of bankfull channel geometry 27
- 3.2 Curvature-driven width oscillations 32
- 3.3 The role of bank pull and bar push 37

II METHODS 41

4 MEANDER MORPHODYNAMICS FROM REMOTELY SENSED DATA 43
- 4.1 Data 43
- 4.2 Methods 44
  - 4.2.1 River mask extraction 45
  - 4.2.2 Planform extraction: centerline coordinates, curvature and channel width 47
  - 4.2.3 Local migration vectors and individual bend separation 50
  - 4.2.4 Sediment bar dynamics 53

4.3 Example application of PyRIS 56
4.3.1 Planform extraction 57
4.3.2 Individual bend separation and migration rates 58
4.3.3 Sediment bar dynamics 62
4.4 Discussion 63
4.4.1 Planform extraction 64
4.4.2 Individual bend separation and local migration vectors 65
4.4.3 Sediment bar dynamics 65
4.5 Conclusion 66
5 THE PLANFORM DEVELOPMENT OF MEANDERING RIVERS 69
5.1 Evolution of bankfull hydraulic geometry 70
5.2 Interaction between width oscillations and curvature 76
5.2.1 Flow Field and Sediment Transport 76
5.2.2 Planform evolution 79
5.3 Mathematical solution 84
5.3.1 Perturbation approach 84
5.3.2 Perturbation solution 87

III RESULTS 93
6 EXPLORING REMOTELY SENSED MORPHODYNAMIC DATA 95
6.1 Remotely sensed morphodynamic information 95
6.2 Evolution of bankfull channel width 113
6.3 Bend-scale analysis of planform descriptors 118
6.4 Scales and dynamics of migrating bars along meandering rivers 128
6.5 Discussion and conclusions 135
7 THE HYDRAULIC GEOMETRY OF EVOLVING GRAVEL-BED MEANDERING RIVERS 139
7.1 Results 139
7.2 Discussion and conclusions 142
8 AUTOGENIC WIDTH CHANGE AND CURVATURE IN EVOLVING MEANDER BENDS 149
8.1 Results 149
8.2 Discussion and conclusions 156
8.2.1 Mutual interaction between width and curvature under sub- and super-resonant regimes 156
8.2.2 Theoretical predictions and field observations 159
9 ALLOGENIC WIDTH CHANGE: THE ROLE OF BANK PULL AND BAR PUSH 167
9.1 Results 167
9.2 Discussion and conclusions 174
10 ALTERNATE MIGRATING BARS AND MEANDERING 177

10.1 A brief theoretical background 177
10.2 Results 178
10.3 Discussion and conclusions 181

IV CONCLUSIONS 183

11 CONCLUSIONS AND FUTURE PERSPECTIVES 185
11.1 Summary of conclusions 185
11.2 Perspectives 187

BIBLIOGRAPHY 189

LIST OF FIGURES

Figure 1.1 Sediment point bar at the inner bank of a meander bend (Red River, Texas). 4

Figure 1.2 Temporal evolution of a meandering planform with convective instability (from Lanzoni and Seminara 2006). 5

Figure 1.3 Example of meandering and braiding streams. 6

Figure 1.4 Brice's modified classification for single thread streams, after Lagasse et al., 2004 (from Brice 1982). 7

Figure 1.5 Sacramento River, California, is an example of meandering river width width variations (photo credits: DigitalGlobe, Google Maps). 8

Figure 1.6 Alternate migrating bars in artificially straightened (*a*) and natural meandering (*b*) rivers. 9

Figure 1.7 The Rio Beni (Bolivian Amazon) can be considered as one of the largest and most movable *wider-at-bends* meandering rivers. Image (2003, false color) from `landsat.usgs.gov`. 14

Figure 1.8 Rio Ucayali close to Pucallpa city (Perù) in 2001 (false color). False color image from `landsat.usgs.gov`. 15

Figure 2.1 Illustrative examples of river patterns. (*a*) False color map of the meandering Rio Huallaga (Brazil) with chutes. Abandoned meanders (cutoff residuals or oxbow lakes) provide evidence of morphological activity and planform development (Landsat false color composite, 2000 bands 7,4,2). (*b*) Infrared map of the anabranching river Paranà (Paraguay, Landsat infrared composite 2011 bands 4,3,2). 23

Figure 2.2 Illustrative examples of meander migration modes generated by a periodic mathematical model. (*a*) Purely downvalley migration. (*b*) Purely cross-valley migration. 24

Figure 3.1 Sketch of the planform development of a meander bend. (*a*) View from the top of migrating bank lines. (*b*) Transverse displacement of a cross-section. 28

Figure 3.2 Examples of meander bend dynamics and the expected influence on channel slope. (*a*) Planform evolution of the Rio Beni (Bolivia) between 1988 and 2010, around a cutoff occurred in 1989. (*b*) Planform development of a sequence of meander bend of the Rio Beni between 1988 and 2010. (*c*) 1D numerical simulation of the bed profile change after a neck cutoff. (*d*) 1D numerical simulation of the bed profile change after the (sudden) elongation of an individual meander bend. The false color composites in panels (*a*) and (*b*) are taken from the Landsat archive. 30

Figure 3.3 Examples of the occurrence of channel width oscillations associated with point bars (*a*, *b*) and mid-channel bars (*c*, *d*) in natural meandering rivers. (*a*) Rio Ucayali (Perù). (*b*) Sacramento River (USA). (*c*) Rio Beni (Bolivia). (*d*) Bermejo River (Paraguay). Images: 2015 DigitalGlobe, Landsat. 35

Figure 3.4 (*a*) Brice's river pattern classification, adapted from Lagasse et al., 2004. (*b*,*c*) Examples of meandering river patterns with width variations: Rio Beni, Bolivia (*b*) and Rio Purus, Brazil (*c*). 38

Figure 4.1 Application of 3 classifiers to a reach of the River Xingu (Brazil) and thresholding. (*a*) NDVI index. (*b*) MNDWI index. (*c*) SWIR band. (*d*) Thresholding of the NDVI index. (*e*) Thresholding of the MNDWI index. (*f*) Thresholding of the SWIR band. 46

Figure 4.2 Binary mask of the River Xingu as obtained by merging the three individual masks reported in figure 4.1. (*a*) Before binary noise removal. (*b*) After binary noise removal. 47

Figure 4.3 Distance transform (white-to-blue colormap) and skeletonization (red line) on the River Xingu mask presented in Figure 4.2b; (*a*) Before pruning, with spur noise (50 iterations). (*b*) After pruning, spur noise removed (50 iterations). 48

Figure 4.4 Sketch for bend separation in PyRIS. (*a*) Synthetic planform centerline. (*b*) Curvature distribution along the centerline. The s coordinate denotes the downstream coordinate of the channel axis (equation 2a), $\mathcal{C}$ is the local intrinsic curvature of the centerline (equation 2c). The dots correspond to the inflection points (zero-crossings of the centerline curvature distribution) separating individual meander bends. The numbers represent the indexes of the corresponding meander bend (downstream with respect to the inflections). 51

Figure 4.5 Local migration rates for a short reach of the meandering Prut River (border between Romania and Moldova, Bisht et al. in prep.) between 1915 and 1960. Centerlines have been extracted by river masks digitized from historical maps with 1m resolution (Bisht et al., in prep.). (*a*) Local migration rates reprojected in the local downvalley and crossvalley direction. Vertical lines indicate inflection points. (*b*) Migration vectors plotted as arrows (gray) between the two planforms. Thick dots on the planform centerlines represent the inflection points. (*c*) Identification of a large cutoff on another reach of the Prut River. PyRIS automatically recognized that no migration rates have to be computed for the bends that have been cut off. 52

Figure 4.6 Automated bars detection, labeling and reprojection example from a reach of the Xingu River. (*a*) Landsat false color composite 1984, bands 5,4,3. (*b*) River mask and bar index over-imposed on the same false color composite. (*c*) River mask with labeled bars reprojected on the intrinsic reference system (above) and colorbar (below). 54

Figure 4.7 Correlation between river bars and their rates of downstream migration in PyRIS. (*a*) Bar migration in georeferenced spatial coordinates (x, y). (*b*) Bar migration in the reprojected intrinsic reference system (s, n). 55

Figure 4.8 Temporal evolution of a point bar on an individual meander bend of the Ucayali River (Perù). (*a*) Point bar in the bend-scale normalized intrinsic reference system $(\tilde{s}, n)$. (*b*) Point bar on the geospatial reference system (x, y) superimposed on the Landsat real color composite, 2006 bands 5,4,3. 56

Figure 4.9 Multitemporal extraction of planform centerlines for an anabranching river, plotted over Landsat false color composites. (*a*) Main channel of a reach of the anabranching Amazon River (Brazil, Landsat false color composite, 2000, bands 7,4,2). (*b*) Chute cutoff on the Ucayali River close to the city of Pucallpa (Peruvian Amazon, Landsat false color composite, 2005, bands 5,4,3). (*c*) Abrupt main channel change at a bifurcation and multiple neck cutoffs on the Rio Beni (Bolivia, Landsat false color composite, 2000, bands 5,4,3). 58

Figure 4.10 Validation of the proposed methodology for the local centerline migration rates against the morphodynamic model of Seminara et al., 2001. (*a*) Local migration vectors according to the model (above) and those computed by PyRIS (below). (*b*) Downvalley and crossvalley migration rates computed by PyRIS (continuous line) and by the morphodynamic model (dashed line); values (above) and relative errors (below). 60

Figure 4.11 Assessment of downvalley and crossvalley migration rates after a massive cutoff on the Ucayali River (Perù) between 1998 and 1999. (*a*) Planform development highlighting the massive cutoff occurred in 1997 (Landsat false color composite, 2005, bands 5,4,3). (*b*) Bend-averaged local migration rates in the local downvalley and crossvalley directions. 62

Figure 4.12 Spatially distributed local bar migration rates along a reach of the Rio Xingu (Brazil) averaged between 1984 and 2011. 63

Figure 5.1 Sketch for the evolution of bankfull hydraulic geometry of an individual meander bend 72

Figure 5.2 Sketch of a meandering reach with width variations and notation used in the mathematical model. 76

Figure 5.3 Sketch for the planform development of the channel axis and banks. 80
Figure 5.4 Sketch of decoupled bank migration model and notation. 84
Figure 5.5 Transverse structure of the fundamental components of the perturbation solutions at different orders. (*a*) $\mathcal{O}(\nu)$ solution. (*b*) $\mathcal{O}(\delta)$ solution. (*c*) $\mathcal{O}(\nu^2)$ solution. (*d*) $\mathcal{O}(\delta)$ solution. 88
Figure 6.1 River reaches analyzed within the present work. The acronyms are reported in table 6.1. The marker colors indicate the Total Suspended Sediment (TSS) per unit width. 96
Figure 6.2 Characteristic values of several hydraulic quantities of the analyzed reaches against the TSS per unit width. Upward facing triangles are associated with rivers displaying migrating bars, downward facing triangles with rivers displaying only steady bars. 103
Figure 6.3 Satellite false color images of some of the river reaches analyzed in the present chapter. 105
Figure 6.4 Wavelet analysis for some river reaches analyzed in this chapter. 110
Figure 6.5 Dominant wavenumbers and median curvature ratios for each of the analyzed planform reaches against the Total Suspended Sediment per unit width. Upward facing triangles are associated with rivers displaying migrating bars, downward facing triangles with rivers displaying only steady bars. 112
Figure 6.6 Distribution of curvatures and wavenumbers in the dataset provided by Lagasse et al., 2004. Figure reprinted from Zolezzi et al., 2012b. 113
Figure 6.7 Planform development of an individual meander bend of the Rio Beni (Bolivian Amazon). (*a*) Planform development of the channel centerline. (*b*) Evolution of bend sinuosity. 114
Figure 6.8 Evolution of an individual meander bend of the River Ucayali between 1987 and 2009. (*a*) Planform development. (*b*) Evolution of the bend sinuosity σ and of the average channel width W^*. 115
Figure 6.9 Distribution of bend sinuosity along the four reaches investigated. 116

Figure 6.10 Boxplots of the bankfull channel width for individual meander bends against bend sinuosity of four large meandering rivers of the Amazon basin. The scatter represents the widths of the individual meander bends analyzed (sinuosities have been rescaled for the sake of clarity). 117

Figure 6.11 Evolution of the bankfull channel width for the four analyzed rivers. The first plot shows the evolution of the median (line with point markers) and of the 25% and 75% percentiles (shaded area). The second plot compares the evolution of the channel widths by normalizing them with respect to the "initial" median width W_0^* at $1 \leqslant \sigma < 1.1$. 118

Figure 6.12 Bend scale evolutionary dynamics of planform perturbations for the Rio Beni (Bolivia). 119

Figure 6.13 Bend scale evolutionary dynamics of planform perturbations for the Rio Ucayali (Perù). 120

Figure 6.14 Bend scale evolutionary dynamics of planform perturbations for the Rio Mamore (Bolivia). 120

Figure 6.15 Bend scale evolutionary dynamics of planform perturbations for the Rio Huallaga (Perù). 121

Figure 6.16 Bend scale evolutionary dynamics of planform perturbations for the Rio Jurua (Brazil). 121

Figure 6.17 Bend scale evolutionary dynamics of planform perturbations for the Rio Jutai (Brazil). 122

Figure 6.18 Bend scale evolutionary dynamics of planform perturbations for the Rio Purus (Brazil). 122

Figure 6.19 Bend scale evolutionary dynamics of planform perturbations for the Rio Putumayo (Brazil). 123

Figure 6.20 Bend scale evolutionary dynamics of planform perturbations for the Rio Araguaia (Brazil). 123

Figure 6.21 Bend scale evolutionary dynamics of planform perturbations for the Rio Xingu (Brazil). 124

Figure 6.22 Bend scale evolutionary dynamics of planform perturbations for the Rio das Mortes (Brazil). 124

Figure 6.23 Bend-scale evolution of meander wavenumbers. The first plot shows the evolution of the median (line) and of the 25% and 75% percentiles (shaded area). The second plot compares the evolution of meander wavenumbers normalized by their median value λ_0 at $1 \leqslant \sigma < 1.2$. 125

Figure 6.24 Bend-scale evolution of channel curvature ratio. The first plot shows the evolution of the median (line) and of the 25% and 75% percentiles (shaded area). The second plot compares the evolution of curvature ratios normalized by their median value ν_0 at $1 \leqslant \sigma < 1.2$. 126

Figure 6.25 Bend-scale evolution of the amplitude of width oscillations. The first plot shows the evolution of the median (line) and of the 25% and 75% percentiles (shaded area). The second plot compares the evolution of width oscillation amplitudes normalized by their median value δ_0 at $1 \leqslant \sigma < 1.2$. 127

Figure 6.26 Distribution of width oscillation amplitudes and wavenumbers in the dataset provided by Lagasse et al., 2004. Figure reprinted from Zolezzi et al., 2012b. 128

Figure 6.27 Downstream shift of alternate migrating bars in the Rio Xingu (Brazil). Contours show the annual position of bare sediment. 128

Figure 6.28 Scatter plots for scales and dynamics of sediment bars in the Rio Xingu (Brazil, 1984-2012). 130

Figure 6.29 Boxplots for scales and dynamics of sediment bars in the Rio Xingu (Brazil, 1984-2012). 131

Figure 6.30 Scatter plots for scales and dynamics of sediment bars in the Rio das Mortes (Brazil, 1984-2012). 132

Figure 6.31 Boxplots for scales and dynamics of sediment bars in the Rio das Mortes (Brazil, 1984-2012). 133

Figure 6.32 Scatter plots for scales and dynamics of sediment bars in the Rio das Araguaia (Brazil, 1984-2012). 134

Figure 6.33 Boxplots for scales and dynamics of sediment bars in the Rio Araguaia (Brazil, 1984-2012). 135

Figure 7.1 Evolution of the bankfull hydraulic geometry of a sequence of sine-generated meanders as a function of the timescale ratio $\mathcal{R}_T$. Initial conditions are $\beta_0 = 10$, $\tau_{*0} = 0.1$, $d_{s0} = 0.01$, $\lambda_0 = 0.1$. All the variables are plotted against meander sinuosity, which is used as a proxy of time. The floodplain porosity p_f is equal to the riverbed porosity $p_b = 0.4$. (*a*) Evolution of the river planform at intermediate timesteps for $\mathcal{R}_T = 10^1$. (*b*) Evolution of the normalized bankfull flow depth. (*c*) Evolution of the normalized bankfull channel width. (*d*) Evolution of the normalized channel slope. 140

Figure 7.2 Evolution of the bankfull hydraulic geometry under changing floodplain porosity p_f. Initial conditions are $\beta_0 = 10$, $\tau_{*0} = 0.1$, $d_{s0} = 0.01$, $\lambda_0 = 0.1$, while $\mathcal{R}_T$ was set to 10. (*a*) Evolution of the normalized bankfull channel width. (*b*) Evolution of the normalized channel slope. 141

Figure 7.3 Values of $\mathcal{R}_T$ against the discharge ratio Q_s^*/Q^* for natural meandering rivers of the Amazon basin: Ar (Araguaia), Be (Beni), Br (Branco), Hu (Huallaga), Ju (Juruà), Jt (Jutai), Mo (Mamorèo), M1 (Mamorè1), M2 (Mamorè2), Ma (Madre dei Diòs), P1 (Purus1), P2 (Purus2), Uc (Ucayali), Pt (Putumayo), Xi (Xingu). The color of the markers represents the value of the TSS per unit width. 143

Figure 7.4 Evolution of the bankfull hydraulic geometry according to three different models: present model (blue lines), standard model detailed in Zolezzi et al., 2009 (orange line), physically-based bank erosion/deposition model proposed by Eke et al., 2014a without (green line) and with (red line) the modification to overcome dramatic width changes. (*a*) Evolution of the sediment transport capacity. (*b*) Evolution of the channel slope. (*c*) Evolution of the channel width. (*d*) Evolution of the channel depth. 145

Figure 7.5 Planform structure of four large rivers from the Amazon basin. Flow enters from the bottom in all the pictures. (*a*) Rio Purus (Brazil). (*b*) Rio Jurua (Brazil). (*c*) Rio Mamorè (Bolivia). (*d*) Rio Beni (Bolivia). 146

Figure 8.1 Evolutionary dynamics of a sub-resonant meander with autogenic width oscillations. Initial values of parameters: $\beta = 10$, $d_s = 0.01$, $\tau_* = 0.1$, $\lambda_0 = 0.1$, $|\theta_1| = 0.01$. 150

Figure 8.2 Evolutionary dynamics of a super-resonant meander with autogenic width oscillations. Initial values of parameters: $\beta = 20$, $d_s = 0.01$, $\tau_* = 0.1$, $\lambda_0 = 0.1$, $|\theta_1| = 0.01$. 151

Figure 8.3 Effect of the autogenic width variations on meander's shape parameters: comparison between variable width (solid lines) and constant width simulations (dashed lines) as a function of the width ratio β. Initial values of parameters: $d_s = 0.01$, $\tau_* = 0.1$, $\lambda_0 = 0.1$. 152

Figure 8.4 The peak amplitude δ_{max} of width variations as a function of the aspect ratio, measured with respect to its resonant value β_R, for different sets of flow conditions (τ_*, d_s) and initial meander wavenumber $\lambda_0 = 0.1$. 152

Figure 8.5 The position of the widest section ψ_{width} along half a meander wavelength between two consecutive apexes as a function of the width ratio, measured with respect to its resonant value β_R, for different sets of flow conditions (τ_*, d_s) and initial meander wavenumber $\lambda_0 = 0.1$. The values of ψ_{width} are computed when the width oscillation amplitude reaches its peak. 153

Figure 8.6 The maximum floodplain width Δy_{max}, scaled with the reference channel width, as a function of the width ratio, measured with respect to its resonant value β_R, for different sets of flow conditions (τ_*, d_s) and initial meander wavenumber $\lambda_0 = 0.1$ (full markers). Empty markers refer to the results of the equiwidth model ($\delta = 0$). 153

Figure 8.7 The phase lag of the $\mathcal{O}(\nu)$ and $\mathcal{O}(\nu^2)$ perturbations of longitudinal velocity with respect to curvature distribution in the (λ, β) plane, with $\tau_* = 0.1$ and $d_s = 0.01$. The red dashed curve represents the marginal stability curve, separating unstable (meander formation) and stable conditions (meander suppression). The green continuous curve in panel *a* represents the separation between downstream migrating (mainly subresonant) and upstream migrating (mainly superresonant) meanders. 160

Figure 8.8 Temporal hysteresis curves in the coevolution of curvature and width variations in developing meanders, for different values of the aspect ratio β. Initial conditions: $d_s = 0.01, \tau_* = 0.1, \lambda_0 = 0.1$. 161

Figure 8.9 Evolutionary dynamics of width oscillation and curvature along two individual meander bends of the Rio Beni (Bolivian Amazon). (*a*, *b*) Multitemporal positions of the channel centerline. Temporal spacing between subsequent centerlines is one-two years year. The underlying image is a 1996 Landsat (landsat.usgs.gov) false color. (*c*, *d*) Observed temporal relation between curvature ratio ν and amplitude of width oscillation δ. (*e*, *f*) Time growth of sinuosity. The colored marks represent the legend for panels (*a*-*d*). 162

Figure 8.10 Reach-averaged evolution of meander bends of two large rivers from the Amazon basin extracted from three decades of Landsat images (1985-2015) of a 400 km reach (Rio Beni) and of a 900 km reach (Rio Ucayali). Box-plots of bend-scale values of: (*a*) curvature ratio ν, Rio Beni (Bolivian Amazon). (*b*) width oscillations δ, Rio Beni. (*c*) curvature ratio ν, Rio Ucayali (Peruvian Amazon). (*d*) width oscillations δ, Rio Ucayali. The upper and lower limits of boxes correspond to the 84th and 16th percentile, respectively, with vertical lines extending to the 95th and 5th percentile of the category. The percentage of bends, within the examined reach and the whole set of images, for each class of sinuosity σ is reported on top of each box. 165

Figure 8.11 The predicted upper-bound value of peak curvature, ν_{max} is plotted as a function of the Cartesian wavenumber, Λ (red line), and is compared with observed values of curvature ratio, ν, from the whole dataset of Lagasse et al., 2004. River bends are classified according to Brice, 1975. 166

Figure 9.1 Planform evolution of a sequence of meander bends with self-evolving banks, $\mathcal{R}_T = 10$, $\mathcal{K} = -0.1$, initial conditions: $\beta = 35, \tau_* = 0.1, d_s = 0.01$ as a function of the norm alized sinuosity σ. Autogenic and allogenic width oscillations are in constructive interference. (*a*) River centerline (dashed red line) and banks (continuous black lines) during planform development (the channel width was rescaled for the sake of clarity). (*b*) Amplitudes of channel width oscillations. (*c*) Hysteresis curves of channel curvature and width variations. (*d*) Position of channel width oscillations. 169

Figure 9.2 Planform evolution of a sequence of meander bends with self-evolving banks, $\mathcal{R}_T = 1$, $\mathcal{K} = +0.2$, initial conditions: $\beta = 30, \tau_* = 0.1, d_s = 0.01$ as a function of the norm alized sinuosity σ. Autogenic and allogenic width oscillations are in destructive interference. (*a*) River centerline (dashed red line) and banks (continuous black lines) during planform development (the channel width was rescaled for the sake of clarity). (*b*) Amplitudes of channel width oscillations. (*c*) Hysteresis curves of channel curvature and width variations. (*d*) Position of channel width oscillations. 170

Figure 9.3 Evolution of the bankfull hydraulic geometry as a function of the bank shift ratio $\mathcal{K}$, with initial conditions $\beta = 10, \tau_* = 0.1, d_s = 0.01$. $\mathcal{R}_T$ was set to 10. (*a*) Aspect ratio. (*b*) Channel slope. 171

Figure 9.4 Width oscillation as a function of the aspect ratio for different values of $\mathcal{K}$, initial conditions $\tau_* = 0.1, d_s = 0.01$, timescale ratio $\mathcal{R}_T = 10$. (*a*) Autogenic width oscillation amplitude. (*b*) Allogenic width oscillation amplitude. 172

Figure 9.5 Influence of $\mathcal{K}$ on the channel width distribution. (*a*) Absolute distance between the widest section and the bend apex in radians at peak amplitude of width oscillation δ. $|\omega| = 0$ corresponds to the bend apex, $|\omega| = \pi/2$ to meander inflections. (*b*) Peak amplitude of width variations. The shape of the markers corresponds to the aspect ratio β, the color to the timescales ratio $\mathcal{R}_T$. 172

Figure 9.6 Dimensionless floodplain width as a function of the initial aspect ratio β and of the ratio between bank shift rates $\mathcal{K}$ for $\mathcal{R}_T = 100$. 173

Figure 9.7 Areas of constructive and destructive interference between autogenic and allogenic width variations on the λ, β plane, for $\tau_* = 0.1, d_s = 0.01$ and $\mathcal{K} > 0$. For $\mathcal{K} < 0$ the scenario is reversed. The green line indicates meander stability, the black line represents maximum bend amplification. 175

Figure 10.1 Nonlinear regression for the reference hydraulic and planform parameters. Upward facing triangles are associated with migrating bars, downward facing triangles with steady bars. 179
Figure 10.2 Observed vs predicted dominant bar style for the analyzed river reaches. 181

LIST OF TABLES

Table 5.1 Symmetry properties and wavenumbers of the perturbation solutions for the longitudinal velocity U_{ij}. 86
Table 6.1 River reaches analyzed in the present thesis with acronyms and Total Suspended Sediment (TSS) per unit width and the bar regime. TSS is expressed in MTon/years. 98
Table 10.1 Regression data for the reference hydraulic and planform parameters. 180

LIST OF ACRONYMS

AWEI	Automated Water Extraction Index
COI	Cone Of Influence
ETM+	Enhanced Thematic Mapper
ESA	European Space Agency
GWS	Global Wavelet Spectrum
MNDWI	Modifiend Normalized Difference Water Index
MIR	Mid Infrared
MSS	Multispectral Scanner
NDVI	Normalized Difference Vegetation Index
NDWI	Normalized Difference Water Index
NIR	Near Infrared
NRMSE	Normalized Root Mean Square Error
OLI	Operational Land Imager

PCS	Parametric Cubic Spline
PyRIS	Python – RIvers from Satellite
SRTM	Shuttle Radar Topography Mission
SWIR	Short Wave Infrared
TIRS	Thermal Infrared Sensor
TM	Thematic Mapper
USGS	United States Geological Survey
WPS	Wavelet Power Spectrum

LIST OF SYMBOLS

A	[—]	Rate of lateral bank accretion
A_{bar}	[—]	Amplitude of alternate bars
$\tilde{B}$	[L]	Channel half-width
B	[L]	Average channel half-width
b	[L]	Channel half-width oscillation
C	[—]	Chezy coefficient
$\mathcal{C}$	$[L^{-1}]$	Centerline curvature
C_f	[—]	Friction coefficient
D	[L]	Water depth
D_s^*	[L]	Grain size
E	[—]	Rate of lateral bank erosion
$\mathcal{F}_r$	[—]	Froude number
g^*	$[L\,T^{-2}]$	Acceleration due to gravity
$\mathcal{K}$	[—]	Rate of bank pull or bar push
L	[L]	Intrinsic meander length
L_{bar}	[L]	Bar length
$\mathcal{L}$	$[L^{-1}]$	Differential operator
$\mathcal{M}$	[—]	Meander migration coefficient
n	[L]	Cross-sectional transverse coordinate
$\mathbf{n}_b$	[—]	Versor normal to the channel banks
N	$[L^{-1}]$	Metric coefficient
p_f	[—]	Floodplain's bed material porosity
p_b	[—]	Riverbed porosity
q_s	$[L^2\,T^{-1}]$	Streamwise sediment discharge per unit width
q_n	$[L^2\,T^{-1}]$	Transverse sediment discharge per unit width
Q	$[L^3\,T^{-1}]$	Bankfull water discharge
Q_s	$[L^3\,T^{-1}]$	Sediment discharge

r_p	[—]	Porosity ratio
$\mathcal{R}_T$	[—]	Floodplain/riverbed timescale ratio
R	[L]	Radius of curvature
s	[L]	Downstream longitudinal coordinate
$\tilde{S}$	[—]	Longitudinal channel slope
$\bar{s}$	[L]	Streamwise distance from previous meander inflection
s_c	[L]	Downstream position of sediment bar centroid
t	[T]	Time
T	[T]	Time scaled with planform migration
u	$[L\,T^{-1}]$	Streamwise velocity
U	$[L\,T^{-1}]$	Depth-averaged streamwise velocity
U_A	$[L\,T^{-1}]$	Antisymmetrical depth-averaged streamwise velocity
U_S	$[L\,T^{-1}]$	Symmetrical depth-averaged streamwise velocity
U_R	$[L\,T^{-1}]$	Threshold velocity for bank erosion/accretion
v	$[L\,T^{-1}]$	Transverse velocity
V	$[L\,T^{-1}]$	Depth-averaged transverse velocity
$\mathbf{v}$	$[L\,T^{-1}]$	Depth averaged flow velocity vector
$\mathbf{V}_{ij}^{(k)}$	$[L\,T^{-1}]$	Perturbation solutionat order $\mathcal{O}(ij)$ with k-periodicity
v_b	$[L\,T^{-1}]$	Streamwise migration rate of sediment bar
W	[L]	Channel width
x	[L]	Longitudinal coordinate
y	[L]	Transverse coordinate
β	[—]	Half width-to-depth ratio
β_c	[—]	Critical half width-to-depth ratio
β_R	[—]	Resonant half width-to-depth ratio
d_s	[—]	Relative roughness
Δ	[—]	Submerged relative density
δ	[—]	Width oscillation amplitude
δ^{auto}	[—]	Autogenic width oscillation amplitude
δ^{allo}	[—]	Allogenic width oscillation amplitude
ϵ	[]	Scale of migrating bar amplitude
η	[L]	Bed Elevation
γ	[—]	Ratio between erosion rate and accretion rate
λ	[—]	Meander wavenumber
λ_{bar}	[—]	Bar wavenumber
Λ	[L]	Cartesian meander length
ν	[—]	Curvature ratio
ν_c	[—]	Critical curvature ratio for migrating bar suppression
ω	[—]	Width oscillation phase lag
ω^{auto}	[—]	Autogenic width oscillation phase lag
ω^{allo}	[—]	Allogenic width oscillation phase lag
ϕ	[—]	Channel bank angle from the channel centerline
Φ	[—]	Sediment transport function

ψ_{curv}	[—]	Bend apex's angle and 1-harmonic bend apex
ψ_{width}	[—]	Widest section's angle from 1-harmonic bend apex
θ	[—]	Centerline inflection angle
τ_*	[—]	Shields stress
σ	[—]	Meander sinuosity
ξ	$[L\,T^{-1}]$	Channel width change rate
ζ	$[L\,T^{-1}]$	Lateral centerline migration rate
ζ_b	$[L\,T^{-1}]$	Lateral bank migration rate

Part I

INTRODUCTION

1 GENERAL INTRODUCTION

In this chapter I introduce meandering rivers and their main characteristics. On this basis I further introduce the class of transitional river patterns, herein intended as the wide river class spanning between the morphological and morphodynamic characteristics of meandering rivers and those of braiding rivers, with particular emphasis on the coexistence of channel curvature and channel width variations. A particular class of rivers, that I herein deliberately include in the class of transitional river patterns, is presented: a class of meandering rivers where alternate migrating bars coexist with the sinuous, curvilinear structure of the channel axis. I then provide a general picture on the state of the art in the field of meandering and transitional river morphodynamics, which is the main subject of this thesis, specifically through the approaches of analytical morphodynamic modeling and remote sensing applications. The chapter ends with the identification of few research questions arising from this brief introduction.

1.1 MEANDERING RIVERS

Meandering rivers are beautiful, single-thread, alluvial riverine systems in which the centerline of the channel exhibits a curvilinear structure while flowing from upstream to downstream. River meanders carve their shape into the floodplain by alternating processes of bank erosion and deposition respectively at the inner and at the outer banks.

The curvilinear character of the channel axis drives the water flow towards the outer bank, resulting in a higher flow velocity close to the bank toe, capable to remove bank material under flood conditions and eventually leading to bank collapse, which results in an outward lateral shift of the meander bend (Hooke, 1979; Nanson and Hickin, 1983; Howard, 1992; Mosselman, 1992, 1998; Hooke and Yorke, 2010; Eke et al., 2014b). In addition, the channel curvature forces secondary helical flow circulations on the cross-sectional plane (orthogonal to the main flow direction) which are structured in such a way that the

bed material sediments are dragged towards the inner bank where the so-called *point bars* (figure 1.1) are formed, whereas towards the outer bank the maximum of erosion occurs (figure 1.1, see Einstein 1926; Rozowski 1957; de Vriend 1977; Kalkwijk and de Vriend 1980; Lane 1998; Zolezzi and Seminara 2001a).

The interest of the scientific community in meandering river morphodynamics has been constantly increasing in the twentieth century also due to its growing range of applicability, from oil discovery (Henriquez et al., 1990; Swanson, 1993; Sun et al., 1996), to stream restoration (Kondolf, 2006), agricultural management (Graf, 2008) just to name a few. Meanders are found in extraterrestrial environments such as on the "red planet" (Moore et al., 2003; Matsubara et al., 2015).

Figure 1.1: Sediment point bar at the inner bank of a meander bend (Red River, Texas).

Furthermore, the constantly increasing focus in river restoration highlights important implications such as the re-qualification of ecosystem services connected to natural rivers, the floods-related civil protection and management of sediment budgets and poses the need for better understanding of this often occurring river class.. Moreover, being many large rivers defining borders between countries and being some of them very active, understanding their dynamics has also geopolitical consequences. The management of riverine environments, especially those heavily impacted by anthropic pressure and hydropower plants, requires an in-depth comprehension of the theoretical basis and reliable predictive monitoring, together with management instruments and modern methodologies for extracting and analysing field and remotely sensed data.

The second half of the past century has seen the development of a fortunate and prolific tradition in analytical meander morphodynamics: a number of scientists implemented the linear and nonlinear (Stuart, 1971) stability analysis in the field of meandering river morphodynamics and the concept of meander instability took place: meanders are a consequence of an instability process, in which an initially straight channel whose straightness is slightly perturbed may become unstable, under certain conditions, and the perturbation grows up to an indefinite sequence of meander bends, including compound loops and complex shapes. Blondeaux and Seminara, 1985 developed a unified morphodynamic theory for river meander formation: their work

showed that the formation of meandering rivers is subject to a wavelength (or wavenumber) selection process; only perturbations having long enough wavelengths would become *unstable* and give rise to a meandering planform. Instability was shown to possess a mostly convective nature by Lanzoni and Seminara, 2006, leading to the fact that the instability only travels in one direction: if the stability occurs, it will mainly affect the channel in the downstream direction (see figure 1.2). Zolezzi and Seminara, 2001a provided a general mathematical formulation of the morphodynamic problem in meandering rivers with arbitrary curvature distributions and proved the existence of two distinct regimes of morphodynamic influence: in this case the influence is referred to the in-channel propagation of morphodynamic information, mainly carried through river bars. The morphodynamic influence, however, has implications also on the planform shape of meandering rivers, according to the planform development model proposed by Seminara et al., 2001.

Figure 1.2: Temporal evolution of a meandering planform with convective instability (from Lanzoni and Seminara 2006).

On the other hand, the increasing availability of remotely sensed data and related analytical techniques pushed another branch of researchers in river morphodynamics to promote the study of meandering rivers from a remote sensing perspective. Applications of remote sensing to meandering river morphodynamics have spanned from the study of the effects of cutoffs Schwenk and Foufoula-Georgiou, 2015, to the analysis of floodplain heterogeneity (Schwendel et al., 2015), to the development of software and algorithms that, one step after another, contributed to an increasing level of automation of the elaboration of remotely sensed data, in order to increase the capability of scientists to access morphodynamic data.

1.2 TOWARDS TRANSITIONAL RIVER PATTERNS

Natural rivers exhibit a continuum of patterns roughly spanning between the classes meandering rivers and braiding rivers (figure 1.3). The regularity of meandering rivers, despite the range of shapes and loops they exhibit, is probably reason why they are among the most

widely studied natural systems on earth. The complexity of the remaining part of the morphological spectrum of natural river patterns complicates the systematic study of those rivers and in some cases makes it nearly impossible. However, transitional rivers are very common in nature.

(a) Meanders of the river Jurua, Brazilian Amazon (photo credits: Crear Amazonìa, http://moralesa-crearedspa-2015.blogspot.it/2015/08/).

(b) The River Waimakariri, New Zealand, is an example of braided river (photo credits: Chris Below, Geography 401, Professor Harry Jolt, https://people.uwec.edu/jolhm/NZ/Below/Home.html).

Figure 1.3: Example of meandering and braiding streams.

Several classifications were proposed over the years in order to organize rivers in classes (Leopold and Wolman 1957; Brice 1982; Gurnell et al. 2009, see also figure 3.4). Even though this subdivision significantly contributed to the overall knowledge of natural river systems, a large gap still persists in the quantitative knowledge related to the class of transitional river patterns, i.e. meandering rivers in which some characteristic features occur, typical of braiding or anabranching rivers, including mid-channel bars, islands, anabranching structures, secondary channels (see figure 1.5) or migrating bars. They can be found either as standalone river reaches or in the transition between high energy braided rivers flowing down steep glacial valleys and their downstream meandering counterpart wandering through the alluvial floodplain.

In this thesis I will focus the attention on two specific types of transitional river patterns: (i) meandering rivers displaying spatial oscillations of the channel width and (ii) meandering rivers exhibiting migrating sediment bars.

1.2.1 Meandering rivers with variable width

Meandering rivers with width oscillations exhibit interesting characteristics, and they are sometimes more active and movable from a morphological point of view than their regular meandering counterparts, either in terms of planform dynamics (Brice, 1975, 1982; Hooke, 2007; Hooke and Yorke, 2010) or in terms of bedform dynamics (Hooke, 1986; Luchi et al., 2010a; Hooke and Yorke, 2011). Some large examples of these active transitional reaches are the Rio Beni (Bolivian Amazon, see e.g. Gautier et al. 2007, 2010; Schwendel et al. 2015; Constantine et al. 2014, figure 1.7) and the Rio Ucayali (Peruvian Amazon, see Lamotte 1990; Constantine et al. 2014; Puhakka et al. 1992, figure 1.8). The latter is a particularly interesting example of highly dynamics transitional river: its bends have been interacting with the city of Pucallpa (Abizaid, 2010) due to massive cutoffs that occurred upstream, forcing a significant movement of the downstream bends towards the city and causing significant erosional issues to the city itself (Ettmer and Alvarado-Ancieta 2010; Schwenk and Foufoula-Georgiou 2015; Schwenk et al. 2016).

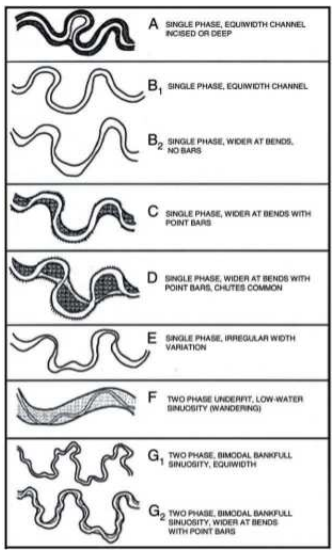

Figure 1.4: Brice's modified classification for single thread streams, after Lagasse et al., 2004 (from Brice 1982).

The gap in understanding the physical processes taking place in meandering rivers with width oscillations is both theoretical and practical. As a consequence of the strongly nonlinear dynamics involved, such as the occurrence of emerging topography, chute cutoffs and local channel widening/narrowing, the mathematical modeling of such river patterns is much more complex than that of regular meanders.

1.2.2 Meandering rivers with alternate migrating bars

In this thesis I deliberately choose to include into the transitional river class a particular class of meandering rivers which exhibits alternate migrating bars (figure 1.6b). This particular type of meandering rivers exhibit some features that make it slightly different with respect to the classical meandering rivers; these rivers typically display low

sinuosities and low to no planform activity, although their bedform configuration has a high rate of change due to the downstream migration of bedforms. In this particular class of transitional meandering rivers the alternate migrating bars are in morphodynamic competition with the steady point bars related to meandering patterns (Tubino and Seminara, 1990). Laboratory experiments (Kinoshita and Miwa, 1974) and nonlinear stability analysis (Seminara and Tubino, 1989; Tubino and Seminara, 1990) suggest that there is a threshold (depending on flow field and sediment transport parameters) of channel curvature above which alternate migrating bars no longer form.

Figure 1.5: Sacramento River, California, is an example of meandering river width width variations (photo credits: DigitalGlobe, Google Maps).

In fact, river bedforms are morphological expressions of the interaction between flow of water and transported sediments in rivers. They play a key role for different river uses, including flood protection, navigation, as well as support a variety of fluvial and riparian habitats and mediate bio-geochemical processes that control water quality through surface-subsurface water exchanges (Harvey et al., 1996; Malard et al., 2002), overall representing a fundamental component of the instream fluvial dynamics. River bedforms having size that scale with the width of the channel are known as bars, and have been studied extensively since more than five decades (Hansen, 1967; Callander, 1969; Engelund and Skovoaard, 1973; Parker, 1976; Fredsøe, 1978; Colombini et al., 1987; Tubino and Seminara, 1990; Schielen et al., 1993; Crosato and Mosselman, 2009; Siviglia et al., 2013; Adami et al., 2016) through complementary approaches–field and experimental observations, morphodynamic theories and numerical models. However, our present knowledge of the morphological dynamics of bars mainly comes from experimental (Kinoshita and Miwa, 1974; Jaeggi, 1984; Whiting and Dietrich, 1993; Crosato et al., 2012) and theoretical approaches with related field observations still limited to few channelised, regulated streams, and a huge knowledge gap for self-formed, near-natural meandering rivers under semi-pristine conditions.

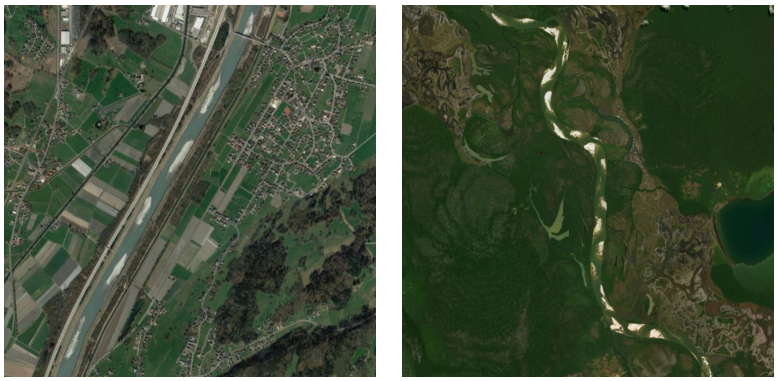

(a) Rhine River, Switzerland (photo credits: DigitalGlobe, Google Maps).

(b) Xingu River, Brazil (photo credits: DigitalGlobe, Google Maps).

Figure 1.6: Alternate migrating bars in artificially straightened (*a*) and natural meandering (*b*) rivers.

Single-thread rivers host two different types of fluvial bars, controlled by different physical mechanisms. Point bars occur in river bends in the form of sedimentary deposits attached to the convex banks (inner banks) associated with scour pools on the opposite concave bank. Formation of point bars originates from curved streamlines forced by channel curvature, causing helical flows that shift sediments from the outer to the inner side of a bend. Such process is reinforced by asymmetric shoaling of high-momentum fluid towards the outer bank, which further increases the shear stress in scoured regions, thus selectively enhancing fluvial erosion by removal of sediments fallen from scoured banks at the bank toe. Point bars are therefore highly associated with meander planform development, which they closely follow and force by keeping attached at the evolving convex banks through time. Alternate bars have apparently similar shapes, but result from a different physical origin. Their regular sequence of streamwise alternating scours and deposits alternating at opposite banks has been theoretically interpreted in the form of bed topography waves, which develop because of an intrinsic physical instability of the interaction between the water flow and the movable sediment of the river bed (Colombini et al., 1987; Schielen et al., 1993). Differently from point bars, alternate bars can move downstream, shifting their position relative to the planform.

Migrating alternate bars have been mostly observed in artificially embanked, nearly straightened reaches of regulated gravel-bed rivers, especially after major morphological regulation of large rivers, mostly turned into single-threads in industrialised countries (Engels 1914;

Werth 2014; Adami et al. 2016, figure 1.6a). Morphodynamic theories indicate that migrating alternate bars can also occur in curved river channels, co-existing or even suppressing the topographic expressions of point bars, though critical maximum curvatures exist that eventually inhibit the instability process responsible for their occurrence.

The appearance of alternate bars in newly embanked river channels at the crossing between the XIX and XX centuries was somehow unexpected and unfavourable to several societal purposes, like river navigation or protection of built structures. Promoting river channel bends to suppress alternate bars development and migration became part of common technical knowledge at the basis of river engineering (e.g. Jansen et al. 1994, p.340), to promote morphologically stable river conditions. At a scientific level, a debate arose whether alternate bars could explain the origin of meandering, further discarded in the mid 1980s.

However, still a clear gap remains because observations on the actual long-term dynamics of alternate and point bars in real river systems are still rare, which strongly limits our basic understanding of fundamental fluvial processes. The predicted occurrence of alternate bars in meandering or sinuous channels, also observed in laboratory experiments (Kinoshita and Miwa, 1974; Whiting and Dietrich, 1993), lacks supporting analysis from the real world.

So it is still poorly known whether self-formed single thread rivers may actually develop migrating bars and, most of all, which are the controls on such dynamics.

In this thesis I also document on the systematic occurrence of migrating alternate bars in mid-size to large freely meandering rivers and analyse them comparatively to other freely meandering rivers in the same physiographic region where bar migration does not occur at all.

1.3 STATE OF THE ART

In the past years, a wide network of researchers focused the attention on the quantitative investigation of meandering rivers.

The pioneering work of Leopold and Wolman 1957, 1960; Langbein and Leopold 1966 set the basis for meandering river morphodynamics as systematic discipline, making use of quantitative field observation in order to infer general properties and characteristics of such kind of river systems. These works helped understanding why some rivers tend to become meandering, explaining such tendency in terms of the principle of minimum work: Leopold and Wolman 1960 introduced

the concept of sine-generated curve as a description of the channel axis of meanders, showing that such a curve is the curve that minimises the total work in bending. Analogously, such a curve minimizes the changes in direction (*Theory of Minimum Variance*, Langbein and Leopold 1966).

Though stability theories of river meanders were introduced by the early works of Hansen, 1967; Callander, 1969; Fredsøe, 1978 when meandering rivers were erroneously thought to be driven by alternate migrating bars (*bar theory*), the systematic approach to meandering river morphodynamics had a fundamental turning point since the *bend theory* was introduced by Partheniades and Paaswell, 1970. The definition of a flow field-based threshold for bank erosion/deposition associated to the excess velocity (or Shields stress, or depth) between the two banks allowed to define the planimetric configurations that were actually able to develop meanders rather than to suppress them.

Johannesson and Parker, 1989 and Blondeaux and Seminara, 1985 applied perturbation methods to the flow and sediment transport in periodic meander bends and identified the instability of meandering rivers where the excess stress locates at the outer bank of the channel, showing that a wavenumber selection controls the phenomenon: only long meander bends are able to remove floodplain material from the outer bank, and therefore force the outwards migration of the bend itself. Under the hypothesis underlying this model, the inner bank advances at the exact same rate as the outer one retreats due to sediment deposition. Furthermore, Blondeaux and Seminara, 1985 showed that bend amplification is related to a resonance mechanism acting on steady bars associated with the river planform.

The theoretical understanding on the evolutionary dynamics of meandering rivers has strongly increased after Zolezzi and Seminara, 2001a and Seminara et al., 2001, who introduced an integro-differential equation for the evolution of the channel curvature along meandering rivers. In this model, although the solution for flow and sediment transport is linear, geometrical nonlinearities are accounted for. Indeed Seminara et al., 2001 demonstrated that in order to model the planform development of river meanders, high order solutions of the hydro-morphodynamics were not required, whereas geometrical nonlinearities were a key ingredient for morphodynamic models. Through its application, two distinct behaviours arose depending on the width-to-depth ratio of the channel. The so-called resonant width-to-depth ratio (Blondeaux and Seminara, 1985), corresponding to the frequency of resonance of the linear system, was showed to be a threshold, above which the morphodynamic influence is able to propagate upstream, while in the sub-resonant case solely downstream influence occurs (Zolezzi and Seminara, 2001a). Resonance has effects

on the shape of river meanders, as sub-resonant meanders are generally upstream-skewed, whereas super-resonant ones are downstream-skewed.

The planform development model has received field validation over the years; e.g. Pizzuto and Meckelnburg, 1989 verified in the field the proportionality between bank retreat and advance to the excess near-bank velocity, as it first hypothesized by Ikeda et al., 1981. Furthermore, Luchi et al., 2007 have applied the bend theory to observed changes in a weakly meandering reach connected to a braided network in the Alps and showed that the theory is reliable for predicting the characteristic spatial scales of meander bends.

The challenge of width oscillations along meandering rivers is introduced for the first time in a review paper by Seminara, 2006. This breakthrough came from empirical observations showing that the width of meandering rivers usually exhibits an oscillation which is correlated with channel curvature (Solari and Seminara, 2005; Seminara, 2006; Luchi et al., 2010b; Zolezzi et al., 2012b). Nonlinearity of sediment transport implies that the sediment transport capacity per unit width oscillates along river meanders as a function of the bed topography. Hence, in order for sediment transport to be conserved, the width must (passively) vary according to the bed topography (Solari and Seminara, 2005; Luchi et al., 2012); this is, however, just one of the mechanisms associated with width oscillations in meandering rivers.

From the empirical point of view, many meandering rivers show a consistent longitudinal oscillation of their width (Brice, 1982; Luchi et al., 2010a; Eke et al., 2014a). Width maxima may be located either at the bend apex, or at meander inflection, or between the two. The first case is that of meandering rivers so-called "wider-at-bends",which have been shown to be among the most morphologically active types of meanders (Brice, 1982). The fact that meandering rivers whose width undergoes relevant oscillations are the most dynamic is enforced by a more recent paper by Constantine et al., 2014, who investigated several rivers within the Amazon basin in South America. Their work highlights that rivers flowing down the Andine region, and thus carrying huge amounts of sediments, are generally the ones displaying the highest migration rates, while supply-limited rivers are generally less dynamical. A closer look to those rivers shows that rivers with high sediment loads are those showing significant oscillations of their width and exhibit large point bars and mid-channel bars. Conversely, the ones with the lowest sediment supply are those more prone to form alternate migrating bars, as illustrated later within this thesis.

Meandering rivers whose width undergoes significant oscillations usually exhibit some characteristics of braided rivers, such as the for-

mation of emerging mid-channel bars and islands, which in turn affect strongly nonlinear mechanisms such as those of chute cut-offs. The stability of these transitional meanders, in which the width oscillates according to the curvature distribution, has been shown to be slightly different from that of the classical ones, depending on the phase lag between width maximum (Luchi et al., 2011) and bend apex. Luchi et al., 2010b observed that mid-channel bars are formed both by the oscillation of the curvature, which has a nonlinear forcing function on the bed topography able to form mid-channel bars, and by a pre-existing oscillation of the channel width. Still remains open the following question: what drives channel width oscillations? The linear stability of width oscillations in straight reaches was investigated by means of a perturbation approach by Repetto et al., 2002. They showed that width oscillations are always stable if no external drivers come into play, which means that the perturbation solution for the flow field associated with a width oscillation will always suppress that oscillation, for the length scales typical of meandering rivers. Therefore, the curvature appears to be one of the forcing functions of width variations, and thus of mid-channel bars; in theis case the width oscillation is called "autogenic". On the other hand, width oscillations could be forced by different rates of bank shift: the retreating bank might move faster than the advancing one ot *vice versa*; in this case the width oscillations are called "allogenic".

Only in very recent years have width variations and curvature been coupled and applied to evolutionary models, in the context of a renewed interest by the scientific community in developing new and physically based models for river bank erosion (e.g., Lauer and Parker 2008; Eke et al. 2014b). Parker et al., 2011 proposed a new framework for bank erosion modelling, Eke et al., 2014a analyzed the context in which an initially straight river reach, with constant width, evolves as a sequence of periodic meander bends in which the banks are free to evolve on their own. Although the treatment of bank deposition processes is simplified, their analysis shows that during the planform evolution of the river reach the width undergoes periodic oscillations correlated with the curvature. Even though they employ a simplified numerical model, hence not separating the individual physical processes (autogenic and allogenic), their work shows that spatial width variations in natural meandering rivers occur as a consequence of different lateral migration rates of the eroding and accreting bank and also as a consequence of the flow field and sediment transport modification induced by the curvature. It appears that the two different processes occur simultaneously, interacting with one another. The first one depends upon a parameter that accounts for a different rate of lateral shift of the two banks depending on whether they are eroding or

accreting, which seems to force overwidening (overnarrowing) close to the bend apex when the erosion/deposition ratio is positive (negative). The second one seems to occur also when erosion and deposition rates are equal, as overwidening tends to be produced farther away from the bend apex.

However, it is not clear whether these two individual physical processes occur simultaneously and to what extent they interact with one another. For these reasons, a nonlinear analytical model would be of interest, and specifically a model able to account for interactions between width and sinuosity by separating individual physical processes, applied to the planform development model of Seminara et al., 2001.

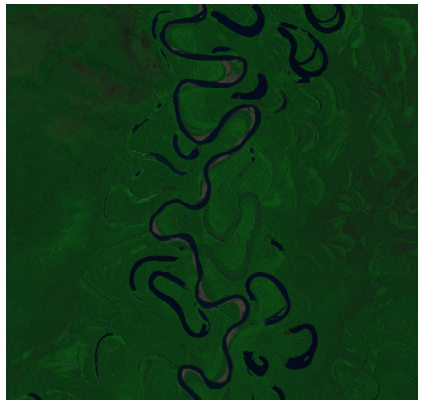

Figure 1.7: The Rio Beni (Bolivian Amazon) can be considered as one of the largest and most movable *wider-at-bends* meandering rivers. Image (2003, false color) from `landsat.usgs.gov`.

The proposed approach would be limited to the analysis of the interaction between processes in a simplified scenario. Analytical modeling is typically based on simplifying assumptions that require conceptualizations of the problem that do not foresee highly complex geometries such as channel with the presence of islands (Latrubesse et al., 2005; Gurnell et al., 2009), secondary channels (e.g. Abad et al., 2013) and chute cutoffs (Constantine et al., 2009; Grenfell et al., 2012, 2014). Hence, the analysis of nonlinear interactions in river morphodynamics over complex domains requires the use of numerical models.

Numerical models are an important tool in modeling complex river systems. Accurate algorithms have been developed in the past years in order to account for important features of meandering rivers, such as channel curvature (Begnudelli et al., 2010) and secondary flows (Lane, 1998; Abad et al., 2008; Nicholas et al., 2013). Moreover, as a consequence of the general improvement of computing resources, very efficient algorithms have been developed in order to run long term simulations on supercomputers (de la Asunción et al., 2012). Numerical modeling has allowed in recent years to model meandering rivers with variable width (Asahi et al., 2013), braiding and transitional rivers (Nicholas et al., 2013; Nicholas, 2013b,a). In particular, Nicholas et al., 2013; Nicholas, 2013a proposed a thorough modelling

framework able to reproduce both braiding and meandering characteristics, and hence put a milestone for the simulation of transitional river patterns. However, although numerical modeling allows for the treatment of very complex scenarios, it does not allow to study the key processes and mechanisms individually. On the other hand, the systematic application of numerical models require accurate and detailed bed topography and channel structure data. The understanding of river processes and the validation of analytical and numerical models necessarily runs through the accurate and systematic analysis of such data, which has led to the development of methods and algorithms for the detection of high resolution data from satellite images and LiDAR data (Kinzel et al., 2013; Legleiter and Roberts, 2009).

Figure 1.8: Rio Ucayali close to Pucallpa city (Perù) in 2001 (false color). False color image from landsat.usgs.gov.

Another important branch of morphodynamic research is making its own way into the analysis of satellite multispectral images; from the development of a number of indexes able to identify vegetation (e.g. Carlson and Riziley, 1997) and water (Gao, 1996; Xu, 2006; Feyisa et al., 2014), to bathimetry mapping and water depth retrieval (e.g.Legleiter et al., 2004; Legleiter and Roberts, 2009). In particular, bathimetric mapping could be regarded as a very powerful monitoring tool, but it has many limitations as it is not very reliable for water depths up to some meters (Legleiter and Roberts, 2009). This last consideration leads to an heisembergian uncertainty in monitoring rivers from satellite images: I want to study the movement of meandering and transitional rivers, and on one hand I need large rivers, for which I also have the field data for calibration (e.g. Gautier et al. 2010; Trigg et al. 2012), because the spatial resolution of freely available satellite images is currently quite low. On the other hand such rivers are not shallow and, according to Constantine et al., 2014, they typically carry huge suspended sediment loads, which makes almost impossible for light radiation to penetrate the water and hence their depth is not predictable.

Even though we are not able to reliably map the bathimetry of such large meandering rivers, yet we are able to investigate their planimetric development. Systematic improvements in satellite geosciences are

preparing the ground for the analysis of larger and larger datasets, that will require some kind of automated procedure; in particular, an automatic procedure able to detect the main river planform in terms of its channel centerline and local channel width is the first step for a systematic analysis of channel dynamics in meandering and transitional rivers. Such a procedure shall involve thresholding and segmentation algorithms (e.g. Otsu, 1979) based on NDVI (Normalized Difference Vegetation Index, Kriegler et al., 1969), NDWI (Normalized Difference Water Index, Gao, 1996), MNDWI (Modified Normalized Difference Water Index, Xu, 2006) or AWEI (Automated Water Extraction Index, Feyisa et al., 2014), on which a methodology for automatically reading the channel centerline from upstream to downstream (pixel by pixel) shall be built, and for detecting the main channel branch in correspondence of anabranching structures, bifurcations, chute channel and emerging islands. One more need in the context of remote sensing meander morphodynamics is a meander migration algorithm able to automatically detect inflection points, to compute local migration rates between subsequent planforms and to capture bend cutoffs. Although few methodologies were proposed in this context over the years (e.g. Lauer, 2006), they do not seem to suffice with the typical planimetric and altimetric complexities of transitional rivers. Moreover, no literature is available so far on the meander migration algorithms including cutoff capturing, which is a fundamental feature of transitional rivers.

Finally, even though retrieving bathimetry from remotely sensed images is not an options for large transitional rivers, in many cases their bars are emerging, especially at low flow stages, which still allow us for a partial analysis of the dynamics of bedforms, especially in that particular class of meandering rivers with migrating bars that we decided to include into the transitional meandering river classification for the purposes of this thesis.

The present work aims at providing an in-depth understanding of some of the characteristics and properties of meandering and transitional rivers, by means of a comprehensive theory coupling the dynamics of width and curvature along evolving meander bends, including internally- and externally-driven width oscillation, and an integrated framework for the automated temporal analysis of satellite images of meandering, transitional and anabranching rivers. The latter will be presented as a modular software called PyRIS, that is applied to a number of large natural meandering and transitional rivers.

1.4 RESEARCH QUESTIONS

In this section I will summarize the research questions that, implicitly or explicitly, emerged in the previous sections, when research gaps were highlighted.

The first research question constitutes the main plot of the entire thesis and is embodied in the title as well. Can we integrate meander morphodynamic theories and analytical modeling with remote sensing applications? These two research fields have always proceeded side by side, but barely looking at each other. Meander morphodynamicists often look at remote sensing data and images and try to find some evidence of what their theories predict, but with rather static views due to the large amount of work usually required to extract multitemporal information, and often solely in a qualitative manner. One of the main purposes of this work is to provide an easy-to-use instrument to the morphodynamics community that can provide useful, quantitative and especially multitemporal data that can be used to look for feedbacks for the theoretical predictions. I called this instrument P_yRIS (Python–RIvers from Satellite) and I will illustrate some applications of this methodology to provide support to my other theoretical research questions.

The general research question posed above is addressed through multiple smaller questions regarding the dynamics of meandering and transitional river patterns. Firstly, how does the bankfull hydraulic geometry of an evolving meandering river change? This question is not as simple as it appears: it is widely accepted that the riverbed change of an evolving meander bed has the sole purpose of connecting two fixed riverbed elevations (upstream downstream ends). However, this assumptions is not supported by any real world evidence and, especially, does not take in any account the change in sediment transport capacity related with slope reduction and its relation with a fixed, externally imposed sediment supply. Also, the reach-averaged, bankfull channel width is usually assumed to be constant in time. So the question could be posed in the following, simpler terms: how do the reach-averaged bankfull channel width and channel slope vary along an evolving meander bend?

However, the width of a meandering river does not solely vary in time: it also varies in space. The oscillations of channel width along meander bends have been investigated in the past years in terms of equilibrium (static solutions) or through numerical models, that can answer some general questions, but do not let insights in the individual physical processes governing the evolutionary phenomena. Therefore, the following question regards the channel width oscillations: how does the channel width vary in space and time? How do channel

width oscillations form and develop? If a contributions to the oscillation of channel width is given by curvature nonlinearity, how does this interact with the width oscillations due to the difference between rates of erosion and accretion (i.e., those due to bar push and bank pull mechanisms)?

Finally, one question tackles with the class of meandering rivers with migrating bars that herein I include in the transitional classification: why, how and under which conditions does it happen? Which is the key driver to alternate migrating bars in meandering rivers? The theory alone doesn't seem to help: by investigate a large number of meandering and transitional rivers, I observed similar statistics in terms of channel curvature; this fact seems to discredit that meandering rivers with migrating bars have lower curvatures. To this aim I will quantitatively integrate the theoretical framework proposed by Seminara and Tubino, 1989; Tubino and Seminara, 1990 with remote sensing data and show that, rather than the channel curvature, it is a group of parameters that control the style of bars in meandering rivers; on top of these parameters I identify the sediment supply.

1.5 THESIS ROADMAP

This thesis is divided into 4 parts:

I. introduction;

II. methods;

III. results;

IV. conclusions.

Each part is divided into chapters, and each chapter in further divided into sections. Some sections are divided into subsections.

1.5.1 Introduction

The introductory part contains a general introduction (chapter 1) on meandering (section 1.1) and transitional (section 1.2) rivers, where meandering river patterns displaying either width variations and migrating bars are illustrated, and a state of the art (section 1.3) specifically targeting mathematical modeling and remote sensing. The chapter follows with the research questions (section 1.4) arising from the general introductory part and ends with the present section (roadmap of the thesis).

Two more chapters are included in the introductory part. Chapter 2 describes extensively the state of the art and aims of this research in terms of remote sensing of meandering and transitional river patterns (and more). Chapter 3 illustrates the state of the art and aims in terms of nonlinear modeling of meandering and transitional rivers. Three main contexts are investigated: (i) the evolution of the bankfull hydraulic geometry in evolving meander bends in section 3.1, (ii) the evolution of curvature-driven width oscillations in meandering rivers in section 3.2, and (iii) the role of bank pull and bar push in the evolution of meandering rivers in section 3.3.

1.5.2 Methods

The methods part is divided into two chapters. The first chapter (4) illustrates the software PyRIS to extract morphodynamic data from satellite images (section 4.2), which is one scientific output of the present thesis, gives an overview its applications (section 4.3) and discuss them (section 4.4). In the second chapter (5) I develop the analytical nonlinear evolutionary model for the coevolution of bankfull hydraulic geometry (section 5.1), curvature and width oscillations (section 5.2).

1.5.3 Results

The results part is divided into 5 chapters, each one specifically showing a particular class of results.

Chapter 6 illustrates some evolutionary data for large natural meandering/transitional rivers over a 30+ years period: in section 6.1 the reference bankfull hydraulic geometry and planform descriptors are quantified for 20 rivers; for 4 of those rivers I analyze the bend-scale evolutionary dynamics of bankfull channel width in section 6.2; the evolution of bend-scale planform descriptors of 11 rivers is computed in section 6.3; finally, the dynamics of migrating bars in 3 transitional rivers of the dataset is reported in section 6.4.

Chapter 7 reports the results of the bankfull hydraulic geometry model (section 7.1) and compares them with the results of remote sensing (section 7.2). Chapter 8 investigate the role of curvature nonlinearity (*autogenic mechanism*) in generating width oscillations and their feedback on planform development (section 8.1); the results are compared with the remotely sensed ones and a mechanistic explanation of the autogenic process is attempted. Chapter 9 extends the results of the previous chapter by including the effects of bar push and bank pull (section 9.1). Results are discussed in section9.2. Finally, chap-

ter 10 provides a systematic, in-depth integration between remotely sensed data and a nonlinear model in order to provide an explanation to the existence of the class of meandering rivers with migrating bars. A brief overview of the model employed is provided in section 10.1, the application in reported in section 10.2 and the results and implications are discussed in section 10.3.

1.5.4 Conclusions

The conclusion part is composed by only one chapter (chapter 11) containing a summary of the conclusions, that are already extensively treated in various chapters, in section 11.1 and a brief outline of possible future perspectives (section 11.2).

2 REMOTE SENSING OF MEANDERING RIVER MORPHODYNAMICS

In this chapter I set the scene in the context of remote sensing of meandering river morphodynamics. A brief overview of the morphodynamic processes that are of interest for this part is reported in subsection 2.2.1, while a review of the methodologies and algorithms developed so far during the years in the field of remote sensing applied to meander morphodynamics is provided by subsection 2.2.2. Finally, I recall the motivation for a higher level automation in extracting morphodynamic automation from remotely sensed data in the context of meandering river dynamics. The core and development of the PyRIS software for the automated extraction of meandering river morphodynamics from multitemporal multispectral satellite data together with tests and example applications is reported in chapter 4 in the methods part.

2.1 INTRODUCTION

Traditionally, the planform evolution of river meanders has been studied through analytical models (Ikeda et al., 1981; Johannesson and Parker, 1989; Seminara et al., 2001), field data (Hooke, 2007; Hooke and Yorke, 2011; Leopold and Wolman, 1960; Lewin, 1972) and numerical models (Asahi et al., 2013; Eke et al., 2014a; Howard, 1992; Sun et al., 1996). Only recently has the power of modern computers and the availability of geospatial imagery made it possible for researchers to investigate meander morphodynamics from remotely sensed data. In this chapter I present a process-based software, PyRIS (Python–RIvers from Satellite), which allows for automated extraction of information on meander morphodynamics from multispectral remotely sensed data, by isolating individual physical processes occurring in evolving meander bends. PyRIS was specifically designed for river meander morphodynamic analysis, but it includes properties that can be applied to a broader range of channel patterns, such as anabranching rivers. Specifically, PyRIS performs fully automated computations for (i) river planform centerline extraction in meandering and anabranch-

ing river patterns, (ii) local centerline migration rates from multitemporal sequences of river centerlines, and (iii) analysis of large-scale sediment bedform dynamics. In the present work, PyRIS is developed and tests for each of the aforementioned computations are presented, by application to large real-world rivers, mainly from the Amazon basin, in order to prove the ability of PyRIS to deal with different morphological river patterns, properties and dynamics.

2.2 BACKGROUND

In this section I present some background on meandering river morphodynamics and I discuss the state of the art of remote sensing applications in this research field.

2.2.1 A brief overview on river meander morphodynamics

Meandering is one of the most intriguing and highly dynamical processes occurring in alluvial riverine environments. The process of meandering occurs as freely evolving rivers with curvilinear planforms wander through their floodplains, carving the landscape and reworking its sediments through the mechanisms of river bank erosion and accretion (Edwards and D. H. Smith, 2002; Hooke et al., 2011; Hooke, 2003; Leopold and Wolman, 1960; Seminara, 2006). Large-scale sediment bedforms called bars usually develop at the inner banks of meander bends (point bars), gently connecting the floodplain with the river bed (Kasvi et al., 2013; Legleiter et al., 2011; Nanson and Hickin, 1983). A steeper slope connects the channel bed to the outer bank, where the flow depth is generally higher (Eke, 2013; Mosselman, 1998). Point bars eventually coexist with alternate migrating bars as shown by experimental, analytical and numerical modeling (Kinoshita and Miwa, 1974; Schuurman et al., 2016; Tubino and Seminara, 1990). Alternate bars are shorter in length and migrate downstream the channel whereas point bars do not (Blondeaux and Seminara, 1985; Colombini et al., 1987; Tubino, 1991).

The analysis of sediment bar dynamics in real meandering rivers has received little attention in the past decades in contrast with the availability of a large body of theoretical and modelling work (e.g., Zolezzi et al. 2012a). However, recent works started addressing the importance of sediment bars in a wide range of morphodynamic studies focused on real rivers, including effects of massive deforestation on sediment dynamics in the Amazon (Latrubesse et al., 2009), influence of point bar development on the mechanisms of meander migra-

tion (Eke et al., 2014b; Hooke and Yorke, 2011; van de Lageweg et al., 2014), effects of mid-channel bar development on planform stability and structure of meandering rivers (Luchi et al., 2010a,b), alternate bar dynamics in channelised reaches (Adami et al., 2016).

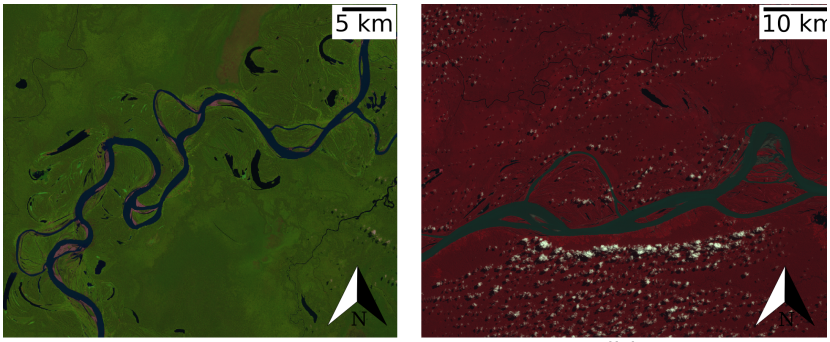

Figure 2.1: Illustrative examples of river patterns. (*a*) False color map of the meandering Rio Huallaga (Brazil) with chutes. Abandoned meanders (cutoff residuals or oxbow lakes) provide evidence of morphological activity and planform development (Landsat false color composite, 2000 bands 7,4,2). (*b*) Infrared map of the anabranching river Paranà (Paraguay, Landsat infrared composite 2011 bands 4,3,2).

Meander bends undergo temporal amplification and translation (Eke et al., 2014a; Güneralp and Rhoads, 2009; Motta et al., 2012; Seminara et al., 2001), deformation (Kinoshita, 1961; Schwenk et al., 2015; Seminara et al., 2001) and eventually cutoff processes (Hooke, 2004) when they grow enough to cut themselves out (neck cutoff, e.g Camporeale et al., 2008, see also figure 2.1a) or when they are overridden by secondary channels (chute cutoff, e.g. Constantine et al. 2009; Kasvi et al. 2013; Kleinhans and van den Berg 2011). A spatially-distributed indicator of meander planform dynamics is the local migration rate, which represents the local rate of movement of the river centerline and corresponds to the average between the local rate of erosion of the retreating bank and the local rate of accretion of the advancing one (Eke et al., 2014a,b).

Meandering rivers are commonly viewed as single-thread fluvial patterns, though several transitional styles of meandering actually exist characterised by the presence of secondary and multiple channels (Figure 2.1b). These transitional meanders may present some similarities with anabranching river systems typical of the largest rivers on Earth like the Amazon river (Latrubesse, 2008), where the main channel splits into multiple sinuous branches which merge together repeat-

edly in space. In contrast to many meandering rivers, anabranching channels are relatively stable in time (Nanson and Knighton, 1996).

2.2.2 Remote sensing of river meanders

Most image processing and geospatial analysis tools make it possible nowadays to classify and analyse the earth surface through pixel-distributed indices that map vegetation (Carlson and Riziley, 1997), water (Feyisa et al., 2014; Gao, 1996; Xu, 2006) and lithology (Ninomiya, 2004). The combination of such indices allows for identifying river and water boundaries in a semi-automated fashion (Güneralp et al., 2013, 2014). A number of approaches for the extraction of channel centerlines (Fisher et al., 2013; Schwendel et al., 2015; Schwenk et al., 2016; Schwenk and Foufoula-Georgiou, 2015) and banks (Güneralp et al., 2014, 2013; Merwade, 2007; Pavelsky and L. C. Smith, 2008; Rowland et al., 2016; Schwenk et al., 2016) from river masks has been developed so far. Centerline extraction is generally performed by skeletonising the channel mask (Fisher et al., 2013; Pavelsky and L. C. Smith, 2008) and then subsequently vectorising the medial axis pixels from the upstream end to the downstream end, provided no multiple channel patterns such as anabranching occur in the channel mask, or, in a recently developed approach, by computing the shortest path between the planform endpoints (Schwenk et al., 2016).

Figure 2.2: Illustrative examples of meander migration modes generated by a periodic mathematical model. (*a*) Purely downvalley migration. (*b*) Purely crossvalley migration.

The most common approach in studying the planform evolution of river meanders is to determine the migration rates and direction of their channel centerline. The average channel migration at the reach scale can be computed by the area between two channel centerlines obtained from temporally subsequent images divided by their average length (e.g. Constantine et al. 2014; Constantine 2006). Conversely, local river bank erosion and accretion rates can be quantified by computing the minimum distance transform of two temporally subsequent river banks (Peixoto et al., 2009; Rowland et al., 2016; Schwenk et

al., 2016). Lauer, 2006 implemented a more physically-based method for calculating the rates of centerline migration in a GIS environment (ArcGIS Channel Planform Statistics toolbox). This tool interpolates a sequence of Bèzier curves between subsequent channel centerlines and cumulates their orthogonal distances. However, such a method fails close to the apexes of meander bends when the migration is dominantly downvalley (Figure 2.2a, see Aalto et al. 2008; Lauer and Parker 2008), while generally succeeding where the migration is predominantly crossvalley (Figure 2.2b).

2.2.3 The need for automated extraction of information on river meander morphodynamics

There are four main reasons for better automation in the extraction of meander morphodynamics information from multispectral remotely sensed data. First, to date there is no software, to my knowledge, that can perform a robust river centerline extraction from multispectral data and that is able to automatically detect the centerline of the main channel (when the channel bifurcates into a main and a secondary channel). Robust extraction is further complicated by the presence of tributaries and abandoned channels which are involuntarily incorporated in river masks. On the other hand, difficulty in capturing the main flow is enforced by the presence of secondary channels and anabranching structures. Second, the river planform migration rates computed with existing methods necessitate manual correction as these methods are not able to determine the migration rates close to the bend apexes with an acceptable accuracy. Thirdly, to my knowledge, the multitemporal analysis of instream sediment bar dynamics is still performed through tedious manual procedures by means of GIS tools. Finally, a systematic feedback between models and observation is still limited by the scarcity of comparable data: although a large quantity of remotely sensed data is available nowadays, such data needs to be processed in a simple and efficient way to be suitable for systematic analysis and comparison with increasingly used river morphodynamic models.

The aim of this part of research is to develop and test a fully automated, process-based software (PyRIS) for the extraction of extensive meander morphodynamic information from multispectral remotely sensed images through three main steps: (i) river planform centerline extraction, (ii) computation of local centerline migration rates and (iii) multitemporal analysis of sediment bar dynamics.

Thus, pyRIS provides a significant improvement on the state of the art by implementing such computations in a fully automated and process-based manner.

3 ANALYTICAL MODELING OF MEANDERING RIVER MORPHODYNAMICS

This chapter introduces the problem of evolution of meandering rivers in terms of bankfull hydraulic geometry, channel curvature and channel width oscillations. The question about the adaptation of bankfull channel geometry, which in morphodynamic models is represented by the so-called reference flow conditions, is posed in section 3.1. This is a fundamental problem because, as I will highlight later on, it represents the basic state above which morphodynamic models are built. However, its treatment has always been strongly simplified and taken for grant. Section 3.2 focuses on the particular set of spatial channel width variations, i.e. the autogenic width variations forced by curvature nonlinearity. In section 3.3 I will focus on autogenic width oscillations, which are determined by different rates between riverbank advance and retreat. The processes arising by these differences give rise to the bar push and bank pull mechanisms, that force meander migration either through a faster advance of the inner bank (bar push) or through faster retreat of the outer one (bank pull).

3.1 MORPHODYNAMICS OF BANKFULL CHANNEL GEOMETRY

The planform development of meandering rivers is driven by the alternation of floods and low flows occurring in natural riverine environments, which leads, in turn, to the interaction between the erosion of the outer riverbank (mostly during floods) and the accretion of the inner one (mostly during low flows, Hooke 1979; Eke et al. 2014b; Zen et al. 2016). Bank erosion and deposition are led by the mutual feedbacks between a network of complex, intermittent, small scale processes such as vegetation encroachment (Parker et al., 2011; Eke et al., 2014b; Zen et al., 2016), root formation (Konsoer et al., 2016), flow separation (Leeder and Bridges, 1975; Hodskinson and Ferguson, 1998) and slump blocks armoring and failure (Parker et al., 2011). Key factors on which this network depends include, among others, sediment production (Constantine et al., 2014), water supply variability (Hooke,

1979) and vegetation growth and dynamics (B. Eaton et al., 2010; Perucca et al., 2007). A sketch of the planform evolution of a meander bend is drawn in Figure 5.2.

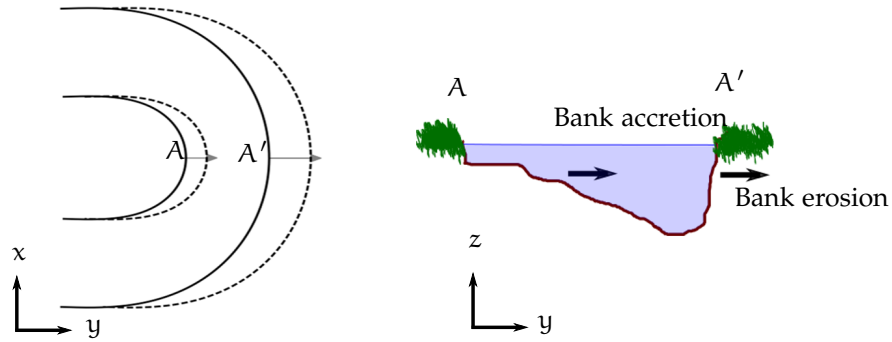

Figure 3.1: Sketch of the planform development of a meander bend. (*a*) View from the top of migrating bank lines. (*b*) Transverse displacement of a cross-section.

However, when studying the long-term evolution of meandering rivers, the processes of riverbank erosion and accretion are typically averaged over the very long timescale of planform development (Ikeda et al., 1981; Mosselman, 1998; Lanzoni and Seminara, 2006), hence they can be treated as continuous processes driven by bankfull hydraulic geometry (Seminara et al., 2001; Lanzoni and Seminara, 2006; Zolezzi et al., 2009; Eke et al., 2014a). Some empirical observations appear to support this hypothesis (Pizzuto and Meckelnburg, 1989; Luchi et al., 2007). Bankfull hydraulic geometry (longitudinal channel slope, channel width and flow depth) is related in the first place to the formative water discharge, which is conventionally defined as the value of water discharge causing the water depth to exceed the bank levels whereby the water flow starts spilling onto the floodplain (Leopold and Maddock, 1953; Parker et al., 2007; Wilkerson and Parker, 2010). Such a discharge is usually referenced to some 1.5–2 years return period flood (Leopold et al., 1964; Williams, 1978). Moreover, bankfull hydraulic geometry depends on a number of factors including the planform geometry, the grain size distribution, the sediment supply, the presence of vegetation at the banks and the cohesion of bank material. A characteristic riverbed grain size distribution rules bed roughness and the rate of sediment transport. However, formative discharge and grain size can generally be considered as given, external independent variables as they depend on hydrological regime and sediment production, respectively, of the river basin. On the contrary, bankfull hydraulic geometry changes as a consequence of the plan-

form elongation of the meandering river induced by bank erosion and bank accretion.

In single-thread rivers at equilibrium, the regime formulas proposed by (Parker et al., 2007; Wilkerson and Parker, 2010) suggest that bankfull hydraulic geometry is mostly related to the bankfull discharge and to a representative sediment grain size.

This empirically suggests that once a specific river is identified through formative discharge and grain size, its equilibrium bankfull hydraulic geometry is univocally defined, no matter how sinuous the river has carved its path into the floodplain. However, there is a degree of scatter in the data (particularly in the channel slope) suggesting that some other factor such as the sinuosity may play a role. On the other hand, bankfull channel geometry should change during the planform evolution of a meandering river for at least two reasons: (i) the elongation of a channel connecting two floodplain points implies a proportional reduction of the channel slope (Zolezzi et al., 2009; Eke et al., 2014a), and (ii) any variation of the local slope implies a counteracting mechanism forced by the disequilibrium between the sediment supply and the sediment transport capacity.

These two counteracting mechanisms appear to be linked to different timescales. While the former is related to the planform development timescale, and hence proceeds at the temporal scale of the lateral channel shift associated to bank erosion and deposition, the latter is strongly related to the one-dimensional riverbed timescale (the so-called "Exner scale"). The above statement opens a wide range of scenarios, since the rates of planform change in natural meandering rivers can vary over several orders of magnitudes, even when related to the scales of the rivers themselves (Constantine et al., 2014), and so do the rates of sediment transport.

Figure 3.2 illustrates a possible mechanism of reshaping of the channel slope based on an example of the planform dynamics of the Rio Beni, a highly dynamic meandering river from the Bolivian Amazon (Constantine et al., 2014; Schwendel et al., 2015). Panel 3.2a shows the planform development following a neck cutoff. A high rate of planform change is observed in the reach immediately downstream the cutoff, while before and after that short reach the planform appears to be more stable. This suggests that the slope change associated with the neck cutoff can trigger a higher morphodynamic activity, as a number of authors observed in the past years (e.g., Hooke 2004; Camporeale et al. 2008; Schwenk and Foufoula-Georgiou 2015). Panel 3.2c shows the temporal evolution of the longitudinal bed profile of a river reach undergoing a meander cutoff, whereas the rest of the river planform is assumed to keep steady. The longitudinal bed profile is initially in equilibrium with the sediment supply under formative conditions,

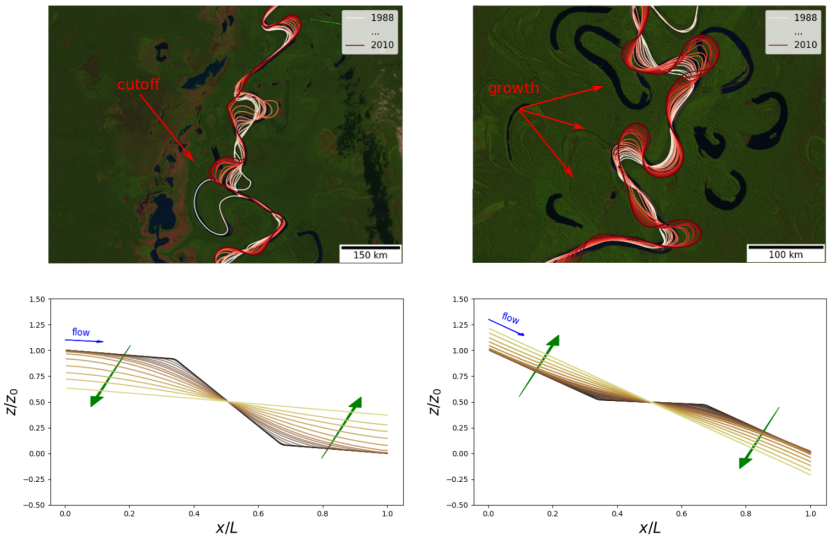

Figure 3.2: Examples of meander bend dynamics and the expected influence on channel slope. (*a*) Planform evolution of the Rio Beni (Bolivia) between 1988 and 2010, around a cutoff occurred in 1989. (*b*) Planform development of a sequence of meander bend of the Rio Beni between 1988 and 2010. (*c*) 1D numerical simulation of the bed profile change after a neck cutoff. (*d*) 1D numerical simulation of the bed profile change after the (sudden) elongation of an individual meander bend. The false color composites in panels (*a*) and (*b*) are taken from the Landsat archive.

and after the cutoff the riverbed undergoes reshaping until the slope is once again in equilibrium with the sediment supply.

Panel 3.2b reports the planform evolution of a sequence of meander bends along the Rio Beni. Conceptually, the planform evolution of an individual meander bend may be regarded as the inverse mechanism with respect to the meander cutoff; although the process is not instantaneous as the neck cutoff, it involves a slope change due to the increase of sinuosity which is expected to be contrasted by the slope reshaping mechanism due to the difference between sediment supply and sediment transport capacity. Panel 3.2d shows the one-dimensional evolution of the longitudinal bed profile following the (sudden) elongation of an individual meander bend. Figure 3.2 suggests, from both an empirical and a numerical point of view, that the capability of evolving meander bends to rework the river bed to a new slope depends upon the planform development rate, meaning that a river meander whose planform development rate is low may have the time to adapt its bed slope, while a river meander evolving quickly

may not give enough time to its slope to adapt to the new planform configuration.

Although the challenge of the bankfull hydraulic geometry has been undertaken since the 50s (Leopold and Maddock, 1953; Parker, 1979; Parker et al., 2007; Wilkerson and Parker, 2010), bankfull hydraulic geometry was usually related to the framework of channel equilibrium. The problem of the variability of bankfull hydraulic geometry due to meander evolution from incipient formation to cutoff was only addressed in very recent years (Parker et al., 2011; Eke et al., 2014a).

Most of the analytical and numerical meander morphodynamic models developed so far, although allowing for an increasing degree of sophistication in the solution of the flow field and sediment transport equations (Camporeale et al., 2007), employ drastically simplified formulations for the bankfull hydraulic geometry. In these models, summarized in Zolezzi et al., 2009 either the channel slope is assumed to decrease proportionally to meander elongation (Seminara et al., 2001; Chen and Duan, 2006; Frascati and Lanzoni, 2009; Zolezzi et al., 2009; Eke et al., 2014a,b), or, conversely, a constant reference bankfull hydraulic geometry is employed (Seminara, 2006). Unfortunately, the former approach lacks of a fundamental ingredient of one-dimensional morphodynamics as it does not account for the conservation of sediment transport: the slope keeps becoming gentler, the channel width keeps constant and the sediment transport capacity drops consequently. Conversely, the latter does not account for the process of meander elongation; this model provides some equilibrium value to the bankfull hydraulic geometry. Bolla Pittaluga et al., 2014 and Lanzoni et al., 2015 successfully employed the hypothesis of equilibrium bankfull geometry to compute the riverbed profile of quasi-steady channel planforms, where the sediment transport capacity is assumed to match exactly the sediment supply; Bolla Pittaluga et al., 2014 applied an equilibrium model to predict the bed profile of the Magra River (Italy) and Lanzoni et al., 2015 applied the same formulation to an intermediate reach of the Po River (Italy) and found good agreement between the computed equilibrium profile and the measured one. However, whether a regime of natural rivers exists is still a matter of debate. B. C. Eaton et al., 2004 argue that the timescales required by a river reach to reach an equilibrium condition are such that geomorphic and land use changes cannot be disregarded. However, Parker et al., 2007 and Wilkerson and Parker, 2010 provide evidence of good adaptation of empirical regime formulas to a wide range of alluvial rivers.

Finally, Eke et al., 2014a proposed a physically-based model for the hydraulic geometry of evolving meander bends that accounts for the variation of bankfull channel width; however, they maintain the hy-

pothesis of slope decreasing proportionally to meander elongation, which leads in the end to a nonphysical drop of the bankfull channel width. They overcame this issue by assuming a slope-dependent bankfull Shields stress according to Li et al., 2014, which allows them to reduce the bankfull channel width drop. However, this correction forces their model to compute the threshold discriminating between bank erosion or bank accretion as a function of the channel slope, and hence changing during the planform development. Furthermore, their model, similarly to the constant width one, does not take the conservation of sediment transport capacity into account.

The choice of the evolutionary model for the bankfull hydraulic geometry has also implications on the morphodynamic regime and the morphodynamic influence (Zolezzi and Seminara, 2001a; Seminara et al., 2001; Lanzoni et al., 2006; Zolezzi and Seminara, 2001b). Zolezzi and Seminara, 2001a; Seminara et al., 2001 showed that there exist a threshold β_R of the width-to-depth ratio β of the channel, called "resonant aspect ratio": when $\beta < \beta_R$, the morphodynamic influence is strictly directed downstream, whereas when $\beta > \beta_R$ the morphodynamic information can travel upstream. Zolezzi et al., 2009 analyzed the evolution of β and β_R through a mathematical model in developing meander bends and observed that a transition from subresonant ($\beta < \beta_R$) and superresonant ($\beta > \beta_R$) occurs quite frequently as meanders develop. The subresonant (superresonant) character of meanders is mainly observed through their shape: subresonant (superresonant) meanders are downstream (upstream) skewed (Seminara et al., 2001; Zolezzi et al., 2009). However, both the aspect ratio β and the resonance threshold β_R depend strongly on the bankfull hydraulic geometry, therefore the definition of a consistent evolutionary model is a problem that needs to be addressed.

3.2 CURVATURE–DRIVEN WIDTH OSCILLATIONS IN EVOLVING MEANDER BENDS

The dynamics of meandering rivers has been studied for decades taking the curvature of the channel axis as the relevant planform descriptor, while only in recent years the complementary role of the spatial and temporal dynamics of channel width has been also considered. Several studies have recognized the relevance of width oscillation on meander dynamics, for their implications on both stability (Luchi et al., 2011) and dynamics (Luchi et al., 2010a, 2012; Eke et al., 2014a) of meander bends and on different styles of meandering (Zolezzi et

al., 2012b), despite the relative paucity of comprehensive field data on width oscillations in meandering rivers.

Constantine et al., 2014 pointed out a strong correlation between the degree of sediment supply, the rate of morphological activity and the variability in channel width in meandering rivers of the Amazon River basin. Specifically, rivers draining the highly sediment-productive Andine area showed the higher planform migration rates and variability in channel width. These observations suggest that higher dynamicity positively correlates with width fluctuations, consistently with the meandering river classification proposed by Brice, 1975, which in addition suggests that highly dynamic meandering rivers have the widest sections close to the bend apexes. Conversely, width maxima located closer to meander inflections may correspond to lesser morphological activity (Brice, 1975; Luchi et al., 2011), although this does not seem to be valid in general.

After an earlier attempt by Chen and Duan, 2006, modeling of width variations in meandering rivers has been mainly developed in two stages. In a first stage, Luchi et al., 2010a,b, 2011 proposed a second order perturbation expansion of the flow field and sediment transport equations in which both curvature and width oscillations are taken into account. Their analytical solution clearly shows that width variability has a primary effect on meander stability, depending upon the amplitude of width variations and their location (phase lag) with respect to the curvature. The theory builds upon well-known linear solutions developed for both regular meanders (Blondeaux and Seminara, 1985; Zolezzi and Seminara, 2001a) and variable width channels (Repetto et al., 2002). In particular, the former solution highlighted the resonant behavior of river meanders, which allows for a discrimination between sub- and super-resonant meanders, based on the value of the width-to-depth ratio. Such a distinction enforces the different evolutionary patterns observed for the two categories (sub- and super-resonant), which is due to the change of phase that occurs when the linear solution crosses the resonant state: sub-resonant meanders are typically upstream skewed, while super-resonant meanders are typically downstream skewed (Seminara et al., 2001). An extension to the case of arbitrary distributions of channel width and curvature was proposed by Frascati and Lanzoni, 2013, who successfully reproduced the associated bed morphology along the Po River (Italy). Feedbacks of width variations on meander dynamics (Luchi et al., 2011) and of curvature on width variations (Luchi et al., 2010b) due to nonlinear interactions were conceptualized by Zolezzi et al., 2012b. Furthermore, Luchi et al., 2012 showed that, due to nonlinearity of sediment transport, an oscillation of the channel width is required along meander bends for sediment discharge to be conserved.

The second modeling stage has mainly focused on physically-based approaches to the processes of bank erosion and accretion (Lauer and Parker, 2008; Eke et al., 2014a,b), for which a simplified treatment is generally adopted in perturbation theories. In the numerical model of Eke et al., 2014a,b the novel bank migration relation proposed by Parker et al., 2011 is applied to each bank depending on whether erosion or deposition takes place.

The work of Eke et al., 2014a highlights that the behavior of the amplitude of width oscillations over time is similar to that of the curvature of the bend apex, but with a slightly time-phased peak. Starting from a straight reach with a periodic perturbation of the curvature, channel width is found to oscillate at a double frequency compared to curvature, consistently with the hypothesis of Luchi et al., 2011. Peak values of both curvature and width oscillation agree with the ranges observed by Lagasse et al., 2004 and Zolezzi et al., 2012b, the behavior of width oscillations depending on the ratio γ between bank erosion and bank accretion rates. According to Eke et al., 2014a, when $\gamma > 1$ (erosion faster than accretion) width maxima tend to develop near the bend apexes, while they shift towards the inflection point when erosion and accretion proceed at nearly the same rate ($\gamma \simeq 1$).

In general, the mechanics of erosion and accretion are driven by different processes (e.g. Darby et al. 2002; Mosselman 1992; Zen et al. 2017) and therefore the rates of advance and retreat of the banks are different when observed at the timescale of one or few flood events competent to drive morphological change. However, such a difference seems to be no longer relevant for several meandering rivers when the cumulative effect of accretion and erosion is analyzed on longer timescales (Mosselman, 1998; Zen et al., 2016). In this case spatial width oscillations may arise as a consequence of an instream "autogenic" mechanism that is related to the interactions between the flow and the evolving bed topography, rather than being associated to different bank processes acting at unbalanced rates. Luchi et al., 2010a observed the inception of a mid-channel bar in the River Bollin (UK), with both opposite banks subject to erosion at the same site. This supports the existence of such an "autogenic" mechanism able to trigger width variations in meandering rivers by means of instream processes, as opposite to an "allogenic", bank-driven mechanism, whereby channel width would oscillate because of differences in the processes controlling the migration of opposite banks.

The existence of both instream autogenic and allogenic triggering mechanisms for spatial width oscillations in meanders was already envisaged by Luchi et al., 2010b and Zolezzi et al., 2012b. Observations suggest that where width variations are mainly caused by an autogenic mechanism, a mid-channel bar is found in the widest sec-

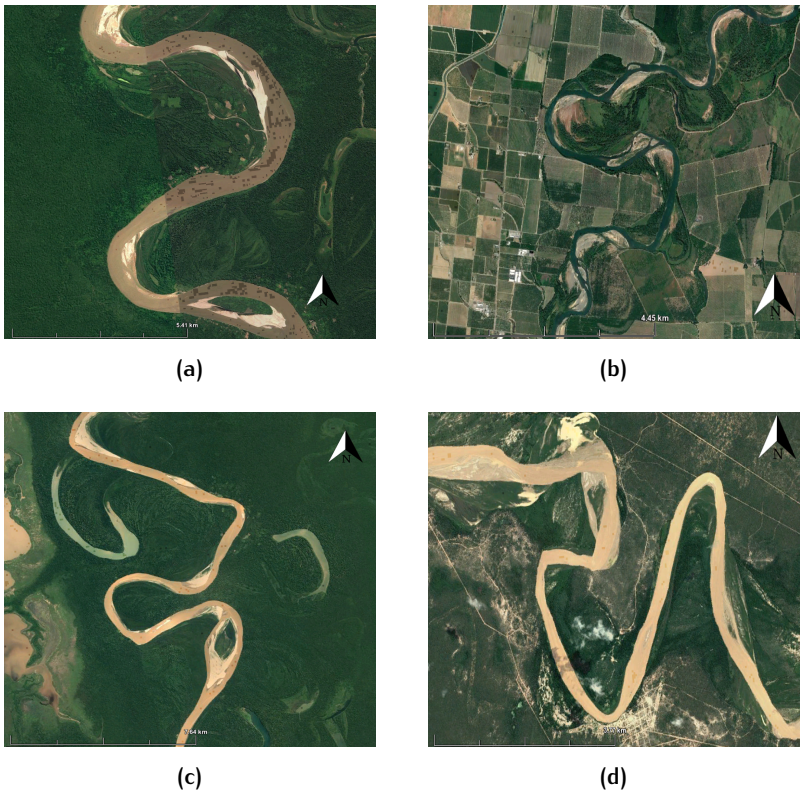

Figure 3.3: Examples of the occurrence of channel width oscillations associated with point bars (*a*, *b*) and mid-channel bars (*c*, *d*) in natural meandering rivers. (*a*) Rio Ucayali (Perù). (*b*) Sacramento River (USA). (*c*) Rio Beni (Bolivia). (*d*) Bermejo River (Paraguay). Images: 2015 DigitalGlobe, Landsat.

tion, while a point bar dominates the widest section of a meandering river where the bank-driven mechanism is mainly responsible for spatial width oscillations. Figure 3.3 illustrates this concept by showing four examples of meandering river reaches with the widest sections located in correspondence of a point bar (a,b) and of a mid-channel bar (c,d). In figure 3.3 (a,b) the two opposite banks seem to reveal different processes, due to the presence of a point bar at one bank (suggesting accretion) and a sharp transition from the wet channel to the vegetated floodplain at the other bank (suggesting erosion). Conversely, the opposite banks in the widest sections of panels (c,d) associated with a mid-channel bar are both characterized by the absence of a point bar, suggesting they both may undergo erosion while widening the river locally.

The above observations set the question of understanding how the autogenic and allogenic mechanisms interact during meander growth and how they might affect meander planform evolution itself, leading to different evolutionary trajectories. Such understanding is constrained by the lack of a fully analytical modeling framework for the planform evolution of meandering rivers with oscillating width, because the models proposed so far rely on numerical solutions and therefore it is not easy to single out the role of different physical effects and fully explore the range of variability of flow parameters.

I firstly aim to investigate the planform evolution of a meandering channel with spatially oscillating width by extending the analytical framework of the classical bend theory, which was based on a linear model for flow and bed topography in equiwidth meandering channels. I incorporate its linear and nonlinear "relatives" accounting for the flow-bed topography linearly forced by spatial width oscillations in a straight channel (Repetto et al., 2002) and nonlinearly forced by curvature in an equiwidth channel (Luchi et al., 2010b), along with the nonlinear effect of width oscillations on curvature. I then develop a planform evolutionary framework which goes back to the approach originally proposed by Seminara et al., 2001, but also accounts for the temporal and spatial dynamics of the channel width, including both "autogenic" and "allogenic" contributions, herein analyzed both separately and together. Under such unified theoretical approach, the solutions for the flow-bed topography forced at different orders of approximations by curvature, width oscillations as well as by their nonlinear interactions are used to feed a bank migration law that reduces to the classical centerline migration relation used in meander morphodynamic models under the assumptions of constant channel width. The present approach has the key advantage of allowing a clear isolation of different physical mechanisms controlling width evolution in space and time in evolving meanders.

3.3 THE ROLE OF BANK PULL AND BAR PUSH

Mathematical models typically employ the two-dimensional structure of the flow field and sediment transport as the main driver of the planform evolution of river meanders (Partheniades and Paaswell, 1970; Parker et al., 1983; Howard, 1992; Seminara et al., 2001; Seminara, 2006; Camporeale et al., 2007), though the floodplain composition and heterogeneity are also recognized to affect the planimetric structure of meanders (Howard, 1996; Peakall et al., 2007; Güneralp and Rhoads, 2011).

For decades the planform evolution of meandering rivers in space and time has been modeled solely through the temporal change of the curvature of the channel centerline (Parker et al., 1983; Seminara et al., 2001; Seminara, 2006; Camporeale et al., 2007), whereby the rate of centerline's lateral shift ζ^* is made proportional to the excess streamwise velocity between the two banks (Hasegawa, 1977; Ikeda et al., 1981; Seminara et al., 2001), immediately outside the bank boundary layers, as

$$\zeta^* = \mathcal{M}\left(u^*_{\text{outer bank}} - u^*_{\text{inner bank}}\right), \tag{1}$$

where M is a dimensionless migration coefficient and u^* is the depth-averaged streamwise velocity. Hereafter, an asterisk $(*)$ will denote dimensional quantities. The above model is often expressed in terms of excess Shields stress τ_* (Parker et al., 2011) or excess water depth d^* (Mosselman, 1998) or by combinations of these parameters. More mechanistic descriptions of the physics of bank erosion (Darby et al., 2002; Darby and Thorne, 1996; Darby et al., 2007; Langendoen and Simon, 2008; Duan and Y., 2010; Parker et al., 2011; Motta et al., 2012; Asahi et al., 2013; Eke et al., 2014b) and accretion (Coulthard and Van De Wiel, 2006; Parker et al., 2011; Eke et al., 2014b; Zen et al., 2016) have been developed over the past years. Parker et al., 2011; Eke et al., 2014a provide a detailed picture involving armoring and failure of slump blocks of the channel banks. A mechanistic model for the bank accretion process was proposed by Zen et al., 2016, who developed a bio-morphodynamic model in which the growth of the bank is related to a vegetation growth model. However, despite the lack of a mechanistic description of the processes of bank erosion and bank accretion, the model reported in equation (1) has received some field validation (Pizzuto and Meckelnburg, 1989) and it has been successfully employed in several meander morphodynamic models (Johannesson and Parker, 1989; Howard, 1992; Odgaard, 1986; Parker and Andrews, 1986; Sun et al., 1996; Seminara et al., 2001; Camporeale et al., 2005). Mosselman and Crosato, 1991 argue that the cohesiveness of the banks

provides a mechanistic justification itself of Partheniades-like relations such as (1).

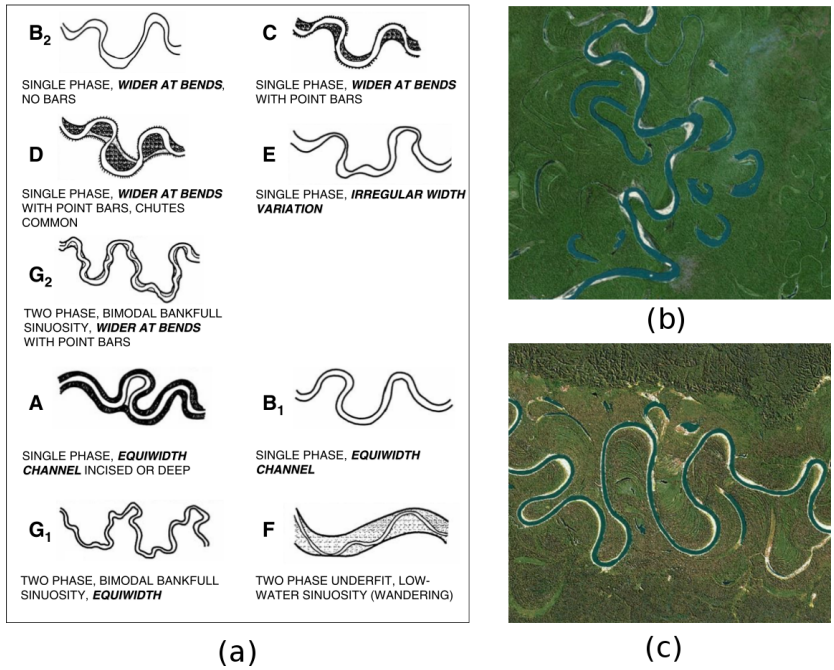

Figure 3.4: (*a*) Brice's river pattern classification, adapted from Lagasse et al., 2004. (*b,c*) Examples of meandering river patterns with width variations: Rio Beni, Bolivia (*b*) and Rio Purus, Brazil (*c*).

In recent years the role of channel width oscillations began to be considered as a key factor in modeling the stability and dynamics of meandering rivers. The bankfull channel width of meandering rivers displays longitudinal oscillations that shift in space and vary in time; the classification proposed by Brice, 1975 and lately refined by Lagasse et al., 2004 discriminates the dynamicity of meandering river patterns through the distribution of width oscillations along their bends. According to Brice, 1975's classification, the so-called *wider-at-bends* meandering rivers are the most dynamic in terms of planform development whereas an irregular distribution of width oscillation appears to have a stabilizing effect on the planform development. Luchi et al., 2011 developed a nonlinear perturbation model that allowed to investigate the role of width oscillations on planform stability. Their analysis showed that *wider-at-bends* meanders are more prone to planform development due to the nonlinear interaction between curvature and width oscillation, increasing the velocity excess between the two banks.

The presence of width oscillations can be related, in the first place, to the formation of mid-channel bars arising as a consequence of flow nonlinearity (Luchi et al., 2010b); such a process is called "autogenic" since it is solely due to nonlinearity of the flow field. Such width oscillations are nonlinearly forced by the channel curvature (Luchi et al., 2010b) and experience a growth and decay similar to that of the curvature during the planform development, as will be shown in this thesis, which limits the significance of such autogenic width variations to low-sinuosity meanders. The decay is also related to the linear self-suppression mechanism of the channel width oscillation that was first described by Repetto et al., 2002.

On the other hand, "allogenic" width oscillations occur according to the processes of bank pull (i.e. when the rate of bank retreat is higher than rate of bank advance) and bar push (vice versa) in evolving meander bends (Eke et al., 2014b; van de Lageweg et al., 2014). The interaction between channel curvature and channel width oscillation was also investigated by Eke et al., 2014a through a numerical framework where bank erosion and accretion were modeled through a the mechanistic approach proposed by Parker et al., 2011. The detailed description of the bank processes coupled with the nonlinear numerical model allowed Eke et al., 2014a to model the interaction between the nonlinear autogenic width oscillation process and the allogenic processes of bank pull/bar push. The difference between the rates of bank advance and retreat was identified through a parameter whose effect was primarily the change in position of the widest cross-section along meander loops. When the retreating bank proceeds at a faster rate than the advancing one (bank pull) the widest section tends to be located closer to the bend apex (*wider-at-bends*), while smaller ratios between erosion and accretion (bar push) led towards *wider-at-inflections* patterns. However, the complexity of the descriptors of bank mechanics employed by Eke et al., 2014a does not allow to isolate individual physical processes (autogenic and allogenic) and to understand to what extent one dominates over the other.

Width oscillations represent only a portion of the changes that channel width may undergo during meander development. The channel width develops width oscillations around a reference bankfull channel width which, in turn, is as well subjected to change during planform development. More generally, the bankfull hydraulic geometry (width and slope) of the meandering channel changes as a consequence of the process of meander elongation, which leads to changes in riverbed slope and channel width. The problem of bankfull channel geometry of meandering rivers was intensively investigated during the past sixty years (Leopold and Maddock, 1953; Parker, 1979; Parker et al., 2007; Wilkerson and Parker, 2010). However, as already mentioned

in section 3.1, the evolution of bankfull channel geometry during the planform development of river meanders has received little to no attention until the past few years and, in particular, the hypothesis underlying most of meandering planform evolution models relates the longitudinal channel slope univocally to the sinuosity of the channel, without accounting for the conservation of the sediment discharge, whilst the bankfull channel width is typically assumed to be constant. Parker et al., 2011; Eke et al., 2014a relaxed the latter hypothesis through a freely variable channel width; however, the evolution of the bankfull channel width provides nonphysical results compatibly with a channel slope varying proportionally to meander elongation.

Part II

METHODS

4 MEANDER MORPHODYNAMICS FROM REMOTELY SENSED DATA

In this chapter I introduce PyRIS (Python–RIvers from Satellite), a fully automated, process-based software for extracting extensive information on meandering and anabranching river morphodynamics from multitemporal satellite imagery. PyRIS provides a sequence of three main automated computations: (i) detection of planform centerline of the main river channel including complex river patterns, (ii) computation of local migration vectors between subsequent centerlines, and (iii) analysis of sediment bars dynamics. The software was validated against several test cases, particularly on large meandering and anabranching rivers from the Amazon basin. Tests prove the capability of PyRIS to automatically detect the main channel path in anabranching structures and to capture main channel changes such as chute cutoffs. A unique novel feature of PyRIS is its ability to investigate the dynamics of river bars. The work suggests the potential of PyRIS to extract extensive, multitemporal meandering river morphodynamic information from remotely sensed data with unprecedented automation levels.

4.1 DATA

PyRIS is specifically designed for the Landsat Level1 Product (http://landsat.usgs.gov/), from which it can extract river masks by combining the spectral bands. However, PyRIS can also perform computations on river masks computed externally, hence skipping the mask extraction procedure. An example is provided in section 4.2.3, where the channel planform is extracted from digitized historical maps (see Figure 4.4).

Landsat Level1 Data Products consist of a wealth of multispectral data, with band designations including Visible (RGB), Thermal Infrared (TIR), Near and Middle InfraRed (NIR, MIR), Short Wave InfraRed (SWIR) and more. Analysis of Landsat archive has been successfully applied in the fluvial context by many authors, e.g. Constantine et al., 2014; Henshaw et al., 2013; Schwendel et al., 2015; Schwenk

et al., 2016. Multitemporal analysis of Landsat data usually requires the application of an atmospheric correction to the image frames in order to account for differences in cloud cover and exposition between image frames, when shared training data are applied for river detection. PyRIS however, does not require any atmospheric correction since there is no training data computed for a particular time frame and applied on other time frames (Song et al., 2001): the river planform is detected in each image frame individually and independently on the other time frames.

There are basically four Landsat types of data, namely

- Landsat1–5 MultiSpectral Scanner (MSS): four bands, 60m resolution;
- Landsat4–5 Thematic Mapper (TM): 7 bands, 30m resolution;
- Landsat7 Enhanced TM (ETM+): 8 bands, 30m resolution;
- Landsat8 Operational Land Imager (OLI) and Thermal Infrared Sensor (TIRS): 11 bands, 30m resolution.

PyRIS requires Landsat Data belonging to the set of Landsat4–5 TM Landsat7 ETM+ and Landsat8 OLI and Landsat8 TIRS for the computation of the river masks. PyRIS exploits the fact that some spectral bands have peaks in the absorption or reflection for particular types of landcover, such as vegetation (NIR), water (MIR) and minerals (SWIR).

The choice of Landsat as the standard input data poses an intrinsic limit to the spatial scale of rivers that can be processed through PyRIS: since the resolution of Landsat bands on which PyRIS operates is 30m, the range applicability consists of "large" rivers, namely channels with at least 300m width (for which the error on channel width is lower than 20%).

4.2 METHODS

I illustrate the core methods and algorithms implemented in the software PyRIS. PyRIS is written in the Python language and makes convenient use of the object-oriented properties of such language. Several freely-available, non-standard Python libraries are required, namely NumPy (T. E. Oliphant, 2006), SciPy (Jones et al., 2001–), Scikits-Image (Van der Walt et al., 2014) and GDAL (Butler, 2004).

The sequence of computations provided by PyRIS can be summarized as follows: (i) river mask extraction from raw multispectral data;

(ii) planform extraction from the river mask; (iii) separation of individual meander bends and computation of the local centerline migration vectors; (iv) analysis of the sediment bedform dynamics.

4.2.1 River mask extraction

PyRIS extracts of the channel network by a pixel-based thresholding which combines the following image derived data layers/bands:

1. NDVI (Normalized Difference Vegetation Index);
2. MNDWI (Modified Normalized Difference Water Index);
3. SWIR (Short Wave InfraRed Band).

By combining indexes 1–3 PyRIS automatically delineates the river body by considering water and sediment, and it enforces river boundaries delineation by excluding vegetated pixels. Specifically, the exclusion of vegetated pixels from the river body is performed through an approach similar to that proposed by Subramaniam et al., 2011, relying on the NDVI (Carlson and Riziley, 1997), which assigns a brightness value to each pixel proportionally to its vegetation percentage. Water pixels are included by computing pixel values of the MNDWI index (Xu, 2006), which computes a brightness value depending on the percentage of water in the pixel (Xu, 2005; Subramaniam et al., 2011; Lu et al., 2011; Feyisa et al., 2014). On the other hand, natural rivers usually display a component of emerging sediments that belong to the morphologically active channel, and as such are submerged under bankfull conditions. For sediment bars to be included in the river body I employ the SWIRband (band 7 in OLI, TIRS and TM Landsat missions), as recommended by the USGS (https://www2.usgs.gov/faq/node/3859) in order to detect mineral deposits.

Each of the data layer undergoes a thresholding procedure in order to obtain three different masks. The thresholding is performed through the Otsu thresholding method (Otsu, 1979), which computes the brightness histogram of the classifier and defines a threshold value by assuming that two classes only exist and by maximizing their interclass variance. The thresholding procedure is applied to the NDVI and MNDWI classifiers, while the SWIR band is normalized (floating point values between -1 and +1) and then thresholded to the value 0. Such a procedure on the SWIR band was necessary as the area covered by the emerging sediment is typically small, hence the histogram frequencies would eventually be too low for class recognition in the Otsu thresholding method. Once each of the classifiers as been thresholded, I obtain three binary masks, which consist of binary images denoting

whether the classifier value is above or below the given threshold, hereafter identified by white and black respectively. Figure 4.1 illustrates the three classifiers associated with their specific masks.

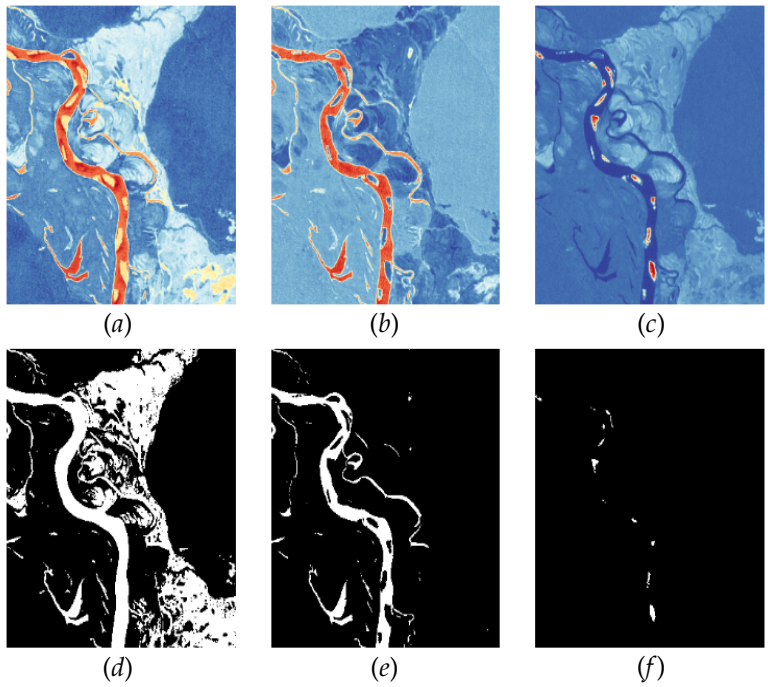

Figure 4.1: Application of 3 classifiers to a reach of the River Xingu (Brazil) and thresholding. (*a*) NDVI index. (*b*) MNDWI index. (*c*) SWIR band. (*d*) Thresholding of the NDVI index. (*e*) Thresholding of the MNDWI index. (*f*) Thresholding of the SWIR band.

PyRIS computes the river mask by means of well establish binary morphological operations involving the three masks, such as dilation, erosion, opening, closing (Haralick et al., 1987; Serra, 1986, 1982). First, the MNDWI mask is dilated through a structuring element scaled by a fraction of the river width. An intermediate mask is then created by applying a `binary_and` operator to the NDVI and the dilated MNDWI masks (i.e., the intermediate mask corresponds to the product of the two masks). A `binary_or` operation between such intermediate mask and the segmented SWIR mask allows us to account for emerging sediment bars in the final mask (i.e., the sediment mask complements the intermediate one). Binary noise due to either tributaries, clouds, small water bodies such as oxbow lakes and humidity is removed through a binary filter combining `binary_opening` operations and it-

erative removal of small objects (Figure 4.2). The binary filter that I implemented in PyRIS allows for maintaining an acceptable level of noise (Figure 4.2). In other words, the noise is eventually not entirely removed, but the residual noise is low enough to be automatically removed with a fair level of computational effort by the pruning and axis extraction algorithms.

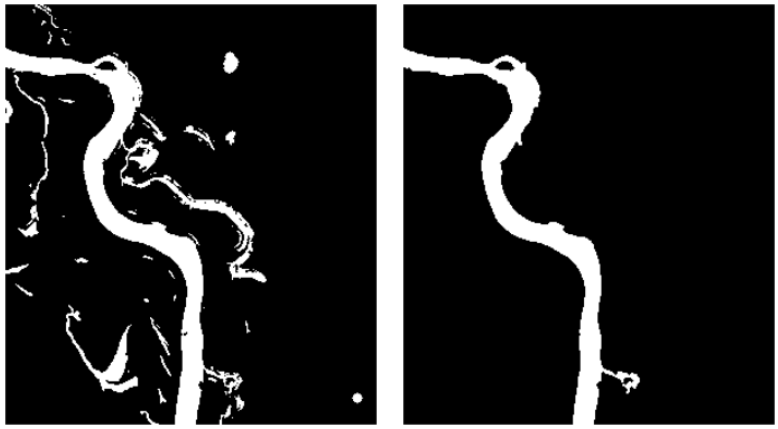

Figure 4.2: Binary mask of the River Xingu as obtained by merging the three individual masks reported in figure 4.1. (*a*) Before binary noise removal. (*b*) After binary noise removal.

4.2.2 Planform extraction: centerline coordinates, curvature and channel width

Common algorithms for the extraction of the channel centerline from a binary mask are specifically designed for a very trivial scenario, i.e. when the mask holds, from a mathematical point of view, a simply connected set of pixels (Fisher et al., 2013; Pavelsky and L. C. Smith, 2008; Rowland et al., 2016). A recently developed approach (Schwenk et al., 2016) enables one to extract the centerline in the multibranching scenario by computing the shortest flow path. However, the shortest path does not generally represent the main flow path, since the latter may avulse occur longer branches. As an example, chute channels are shorter than the main channel, but they usually carry a much smaller amount of discharge; they can eventually grow in size after significant floods and become the main channel leading to chute cutoffs, but such a complex process cannot be captured by a planform extractor that selects the shortest path. The centerline extraction typically proceeds through a skeletonisation algorithm (e.g. Zhang and

Suen 1984) followed by a pruning of the skeleton (e.g. Bai et al. 2007; Choi et al. 2003) which allows to remove spur noise.Hence, when a mask contains holes denoting either a bifurcation, a chute channel or an anabranching structure, one would be interested in extracting the path of the main channel, i.e. the path with the larger average channel width. With an novel algorithm specifically designed for this latter scenario one would also automatically be able to filter out residual branches whereby binary noise due to tributaries and oxbows occurs.

In PyRIS I applied a skeletonization procedure followed by a pruning algorithm. Such a pruning algorithm allows for removing the remaining spur noise connected to the channel skeleton (Figure 4.3). Some of the noise may eventually remain and it will definitely be cleaned lately by the centerline vectorisation. Therefore, the only aim of the pruning algorithm here is to reduce the computational effort of the centerline vectorisation.

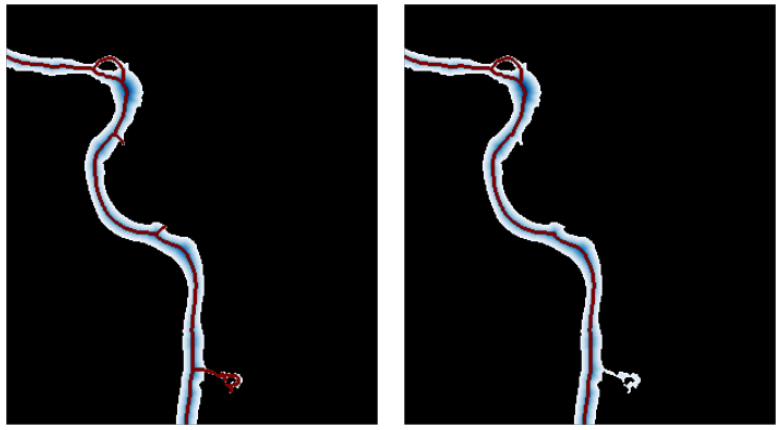

Figure 4.3: Distance transform (white-to-blue colormap) and skeletonization (red line) on the River Xingu mask presented in Figure 4.2b; (*a*) Before pruning, with spur noise (50 iterations). (*b*) After pruning, spur noise removed (50 iterations).

In order to extract the centerline, the skeleton of the river mask must be vectorized. In other words, its points must be read as coordinate pairs (x, y) in *upstream-to-downstream* order. Vectorizing the centerline is a trivial operation when the skeleton consists of a unique branch, i.e. it does not bifurcate and spurs are removed, (e.g. Dey and Bhattacharya 2013; Fisher et al. 2013; Pavelsky and L. C. Smith 2008; Rowland et al. 2016). Such operation requires to read the centerline points *neighbor-after-neighbor* starting from the inlet point straight down to the outlet.

A much more sophisticated procedure must be adopted in the case in which bifurcations, chute and secondary channels or residual spurs are present. The latter is the case of many natural river systems, and especially of the world's largest rivers, which tend to develop anabranching patterns in their lowland courses, for which a correct and robust identification of main channel is required. In PyRIS I implemented a centerline vectorisation algorithm which is automatically able to distinguish the main channel from secondary ones by means of a recursive procedure which analyses all the possible paths the flow could take. It is important to note that this procedure also allows for removing automatically from the planform all the spur noise left from the pruning algorithms. In fact, in most software applications the pruning algorithm must be iteratively run from the user until convergence is reached because the number of iterations required is not known *a priori*.

The work-flow of the centerline vectorisation algorithm of PyRIS can be summarized as follows:

1. automatically locate initial point of the planform (which could be anywhere inside the mask);
2. save current point into a coordinate list;
3. move to neighboring point and remove current point from skeleton;
4. iterate steps (2)-(3) until either one of the following conditions is matched:
   a) no neighbors are found;
   b) more than one neighbor are found;
5. if (4a) is matched, then the end of the branch is found and returned;
6. if (4b), then start from each of the neighboring points and run recursively through steps (2-7)
7. append to the coordinate list the main channel branch through a selection procedure.

Every time a bifurcation is encountered, the main channel path is selected by analyzing the downstream branches: of such branches, the average widest path in terms of channel width is selected, except in some specific cases (when a branch is way too short compared to the other, it is discarded, because it would represent either a cutoff residual or a spur branch). PyRIS implements other possibilities for the

definition of the main channel, namely the selection of the widest/-narrowest branch and of the longest/shortest one.

Once the centerline coordinates are vectorized, i.e. two arrays containing x and y values in terms of pixel positions are computed, they are georeferenced through the geographical transform metadata included in the remotely sensed data when available. The geographical reference allows for representation of the centerline properties in proper geographical coordinates and superposition of multiple planform shapes from different time periods. Once the centerline points are computed, a Parametric Cubic Spline (PCS) interpolation is performed (Güneralp and Rhoads, 2007), where a smoothing factor is eventually applied in order to avoid singularities and the resulting high frequency noise when computing the channel curvature.

Centerline arc-length s_i, inflection angle $\theta_i(s_i)$ and curvature $\mathcal{C}_i(s_i)$ for each coordinate pair (x_i, y_i) are readily computed, respectively, as

$$s_i = \sqrt{(x_i - x_{i-1})^2 + (y_i - y_{i-1})^2}, \tag{2a}$$

$$\theta_i = \arctan\left(\frac{y_i - y_{i-1}}{x_i - x_{i-1}}\right), \tag{2b}$$

$$\mathcal{C}_i = \frac{\theta_{i+1} - \theta_{i-1}}{s_{i+1} - s_{i-1}} \tag{2c}$$

together with local values of channel width. The latter is approximated by the values of the distance transform of the river mask computed at the centerline points.

4.2.3 Local migration vectors and individual bend separation

I implemented a centerline migration algorithm that is able to compute the local vectors (magnitudes and directions) of the migration of the river planform centerline. The zero crossings of the centerline curvature spatial distribution are denoted as *inflection points* separating individual meander bends, which are in turn labeled and linked throughout the temporal evolution of the river centerline (see Figure 4.4).

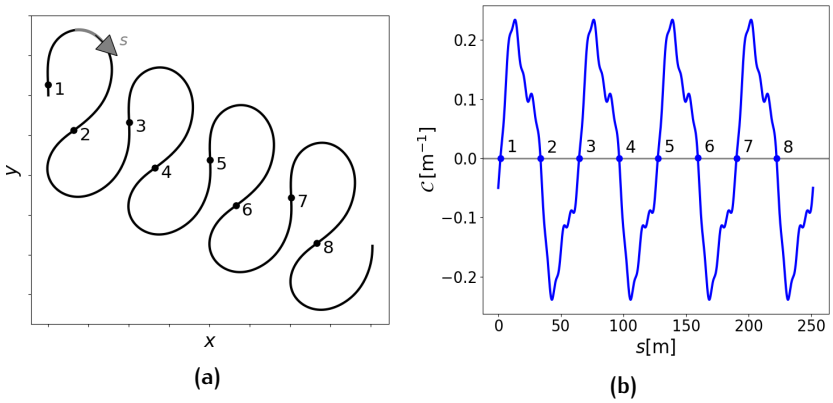

Figure 4.4: Sketch for bend separation in PyRIS. (*a*) Synthetic planform centerline. (*b*) Curvature distribution along the centerline. The s coordinate denotes the downstream coordinate of the channel axis (equation 2a), $\mathcal{C}$ is the local intrinsic curvature of the centerline (equation 2c). The dots correspond to the inflection points (zero-crossings of the centerline curvature distribution) separating individual meander bends. The numbers represent the indexes of the corresponding meander bend (downstream with respect to the inflections).

If the user does not require the application of the smoothing procedure to the channel centerline during the planform extraction (see previous section), PyRIS enables for the filtering of the high frequency noise of the intrinsic curvature distribution of the planform centerline by computing a smoothed PCS. This is particularly relevant for bend separation because high-frequency noise creates a large number of nonphysical inflection points on the channel axis. The inverse transform allows to exclude the high frequency noise from the channel curvature by comparing its scales of oscillations with those of the dominant frequencies in the curvature signal, which are orders of magnitude longer.

Once the curvature is filtered, the remaining inflection points can be isolated and correlated through time when performing multi-temporal analysis.

I computed the local migration vectors following a *bend scale* approach. For each individual meander bend of the planform at some time frame, a PCS interpolation is made for the configuration of the same bend in the next time frame, in order to have a biunivocal point-to-point correlation. Then, I determined the migration vectors by the spatial segments connecting each pair of correlated points. Finally, I set thresholds on the temporal variation of individual bend metrics (sinuosity and length) in order to capture bend cutoffs, for which the

migration vectors are not computed. Bend length is defined as the portion of centerline arc-length between two inflections; bend sinuosity is the bend length divided by the Cartesian length between the two inflections; when a bend undergoes cutoff, i.e. it cuts itself out, its sinuosity and length drop significantly and it does not make sense to compute the migration vectors.

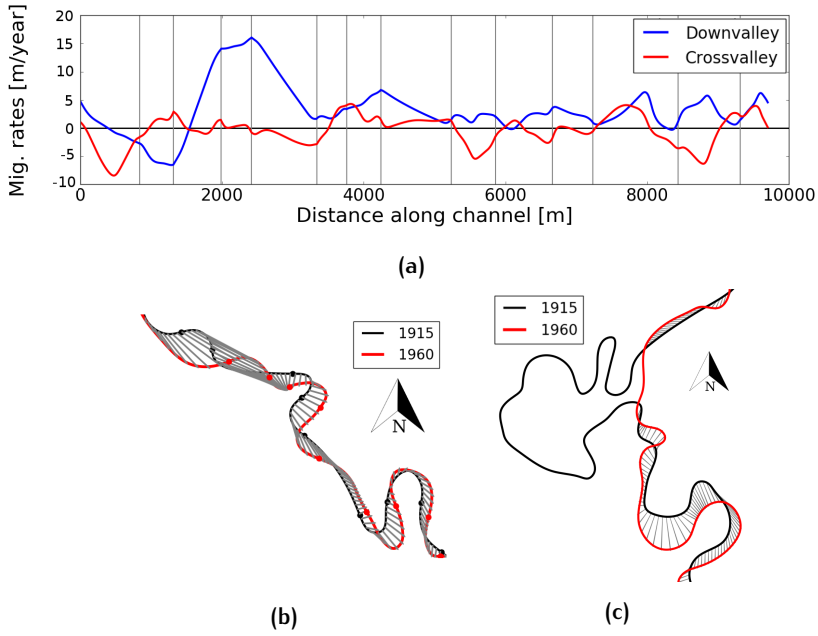

Figure 4.5: Local migration rates for a short reach of the meandering Prut River (border between Romania and Moldova, Bisht et al. in prep.) between 1915 and 1960. Centerlines have been extracted by river masks digitized from historical maps with 1m resolution (Bisht et al., in prep.). (*a*) Local migration rates reprojected in the local downvalley and crossvalley direction. Vertical lines indicate inflection points. (*b*) Migration vectors plotted as arrows (gray) between the two planforms. Thick dots on the planform centerlines represent the inflection points. (*c*) Identification of a large cutoff on another reach of the Prut River. PyRIS automatically recognized that no migration rates have to be computed for the bends that have been cut off.

The x and y components of the local centerline migration vectors can be reprojected on different directions, such as downvalley and crossvalley (Figure 4.5). Note that the massive downward shift in the first few bends of the Prut River (Figure 4.5b) is correctly represented by the downvalley migration blue curve in Figure 4.5a, whereas nearly

no crossvalley migration is observed (red line). Local downvalley and crossvalley directions are defined for each individual bend. The local downvalley direction is defined as the direction corresponding of the straight line joining the inflection points of the bend, while the local crossvalley direction is the one orthogonal to the downvalley one and points towards the bend apex.

4.2.4 Sediment bar dynamics

An important novel feature of PyRIS compared to existing software is an automated procedure that allows for systematic and quantitative analysis of the dynamics of sediment bars in meandering, single-thread rivers by using multispectral remotely sensed data. In the present analysis, I distinguish between the sediment bars that migrate along the channel and the point bars, which tend to keep fix with respect to the channel planform.

The analysis of longitudinal and lateral movement of steady and migrating channel bars in evolving meander bends is conveniently performed with reference to a dimensionless, intrinsic coordinate reference system (s,n). The (s,n) system of coordinates (Merwade et al., 2005; Legleiter and Kyriakidis, 2006; Luchi et al., 2011; J. D. Smith and Mclean, 1984) is locally aligned with the curvilinear arc-length of the channel centerline, normalized by the averaged channel half-width (s) and the direction orthogonal to the channel axis,x normalized by the local channel half-width (n), respectively. The coordinate s ranges from 0 (first point of the planform) to the length of the examined reach, divided by the average channel half-width. Coordinate n ranges between -1 for the right bank and $+1$ for the left bank; $n = 0$ represents the transverse position of the channel centerline.

The coordinate transformation from a Cartesian (x, y) system to the orthogonal curvilinear (s, n) system results into a straightened equi-width representation of a meandering channel, on which I reproject the SWIR band values. PyRIS then identifies the sediment bars at each time frame through a thresholding procedure on the reprojected SWIR data of the image. This procedure automatically identifies the regions occupied by individual bare sediment bars in each image frame. Each bar is uniquely labeled by assigning it a Bar Index, which is a unique integer number ranging from 1 (upstream) to the total number of bars (downstream), whereas the value 0 is assigned to channel regions in which no bare sediment appear. PyRIS computes the bar areas and bar centroids for each time frame.

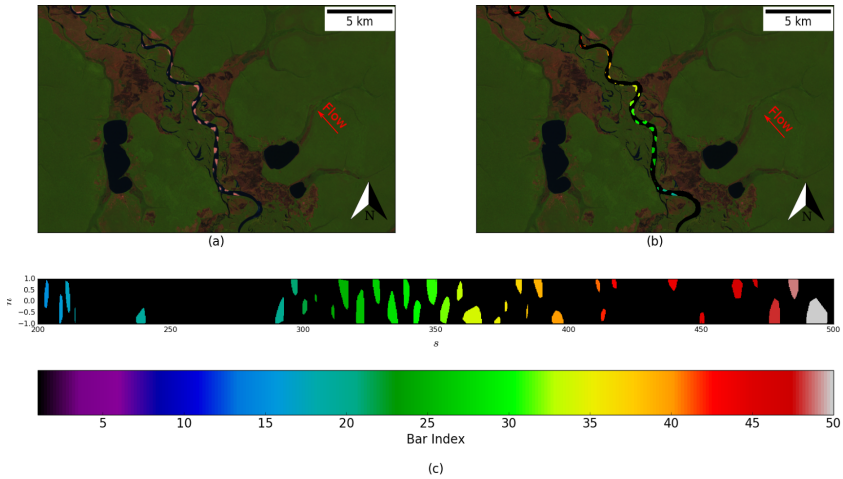

Figure 4.6: Automated bars detection, labeling and reprojection example from a reach of the Xingu River. (*a*) Landsat false color composite 1984, bands 5,4,3. (*b*) River mask and bar index over-imposed on the same false color composite. (*c*) River mask with labeled bars reprojected on the intrinsic reference system (above) and colorbar (below).

To analyze the temporal evolution of individual bars, each bar has to be tracked through different time frames. Such tracking is computed by a bend-scale selection based on thresholds on intrinsic and Cartesian distances. In other words, I identify sediment bars for each individual meander bend in a given time frame and find its representation in the following time frame. The position of each bar is normalized by its position relatively to the bend apex of an equivalent sine-generated curve, i.e. to the midpoint of the arc-length of the bend, and by the length of the entire bend, in order to filter out the effect of temporal bend elongation on the movement of the bar centroids. The bar migration rate of an individual bar is computed as the distance between the normalized positions of the centroids in subsequent time frames divided by the time window.

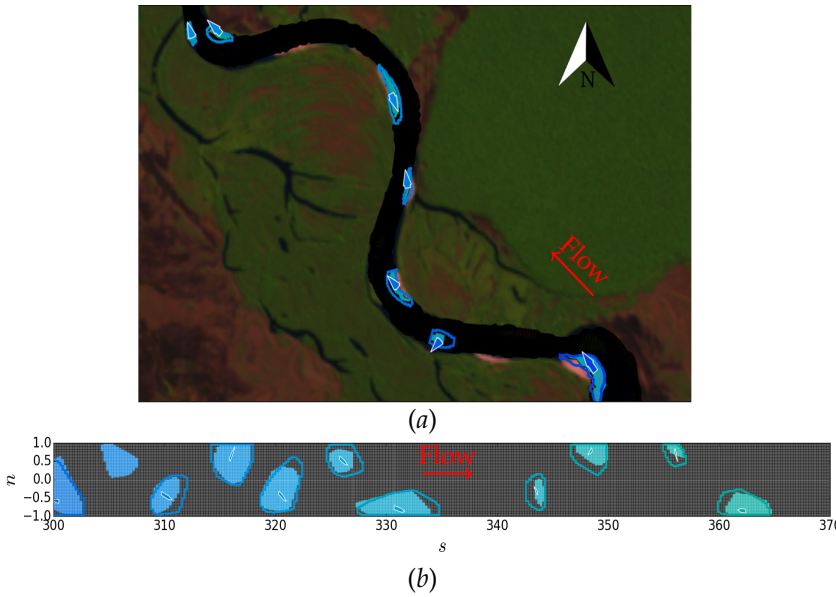

Figure 4.7: Correlation between river bars and their rates of downstream migration in PyRIS. (*a*) Bar migration in georeferenced spatial coordinates (x, y). (*b*) Bar migration in the reprojected intrinsic reference system (*s*, n).

Each bar centroid is associated with an (x,y) coordinate pair and a corresponding (s,n) coordinate pair. PyRIS tracks each sediment bar within a river channel through time and computes the rates of its downstream migration v_{bar} by differentiating in time the s coordinate of their centroids, with respect to the time interval dt between subsequent images

$$v_{bar} = \frac{ds_c}{dt}. \tag{3}$$

In addition, the wavelength L of each bar is computed by computing the spatial difference between the s coordinates of two subsequent bar centroids along the same bank from the same time frame

$$L = s_{ci+1} - s_{ci}. \tag{4}$$

PyRIS represents the temporal development of point bars on an individual evolving meander bend by reprojecting the bar at different time frames on a bend-scaled reference system in which the bend streamwise coordinate $\tilde{s}$ spans between $\tilde{s} = -1$ (upstream inflection point) and $\tilde{s} = 1$ (downstream inflection point). In such a case, the point $\tilde{s} = 0$ represents the bend apex of an equivalent sine-generated bend. Figure 4.8 represents the position of a point bar in an evolving mean-

der bend in the two reference systems, during few years of planform development of the river.

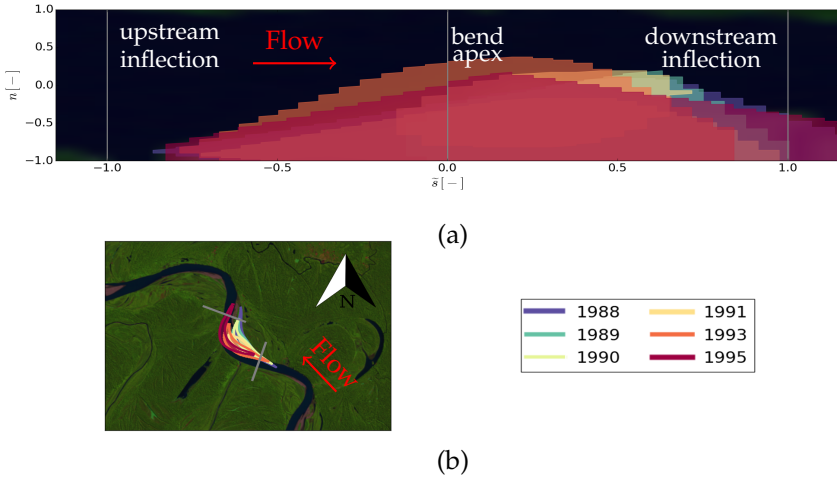

Figure 4.8: Temporal evolution of a point bar on an individual meander bend of the Ucayali River (Perù). (*a*) Point bar in the bend-scale normalized intrinsic reference system $(\tilde{s}, n)$. (*b*) Point bar on the geospatial reference system (x, y) superimposed on the Landsat real color composite, 2006 bands 5,4,3.

Panel 4.8b illustrates the position of the point bar in the geospatial reference system, showing the intrinsic complexity of analysis of bar evolution when a meander bend is rapidly changing. On the contrary, in the intrinsic normalized reference system of panel 4.8a, the bar position with respect to the bend apex of an equivalent sine-generated bend highlights the evolutionary dynamics of the point bar independently from the temporal deformation of the meander bend.

4.3 EXAMPLE APPLICATION OF PyRIS

I illustrate several possible applications of PyRIS to show its potential in the investigation of the shapes and dynamics of the planform and large-scale bedforms (bars) of large meandering rivers in the Amazon basin. The focus of these applications is on the potential of the centerline extraction algorithm, on the sediment bar tracking method, and on the channel migration algorithm, which is tested against migration rates predicted by an analytical model of meander migration. I finally applied the migration algorithm to quantify the modes of

migration of individual meander bends in a large meandering river undergoing a massive cutoff.

4.3.1 Planform extraction

One of the novelties provided by PyRIS is its ability to automatically detect the main flow path in multi-thread reaches, like in the case of meandering rivers with chute channels and of anabranching systems. Figure 4.9 illustrates the results obtained by applying the sequence of algorithms presented in section 4.2.2 to morphological configurations in which abrupt diffluences from the main flow direction occur (the default main channel selection method is employed). Figure 4.9a shows the extraction of the main channel (red line) from large anabranching structures in the Amazon River. Figure 4.9b and 4.9c highlight the ability of PyRIS to capture chute cutoffs and abrupt main channel changes at bifurcations: in Figure 4.9b a bifurcation is evolving over time and at some point the main channel switches from one branch to the other. Conversely, neck cutoffs (4.9c) are trivial to capture because only one channel is commonly active at each time provided the flow stage is not too high.

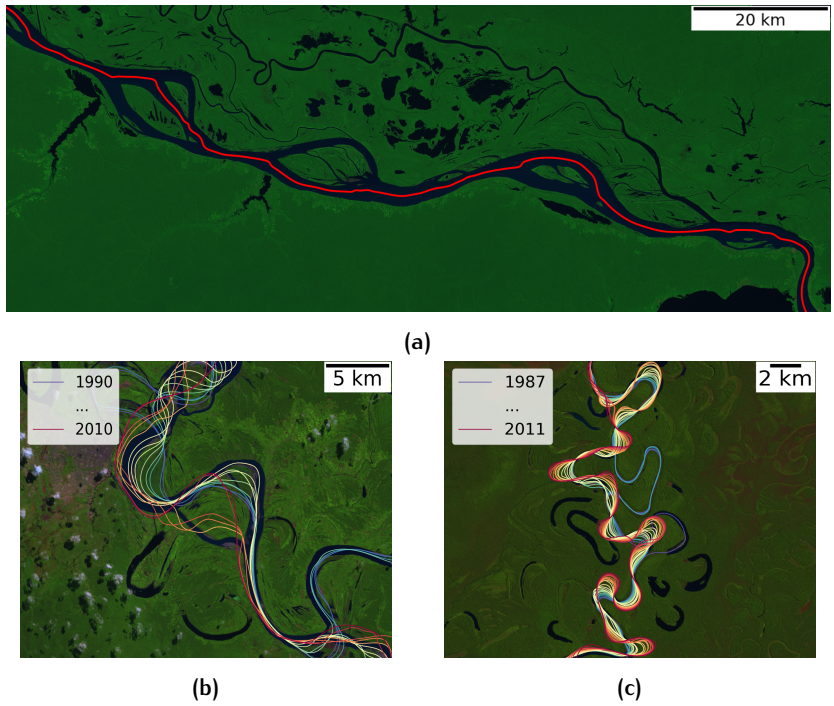

Figure 4.9: Multitemporal extraction of planform centerlines for an anabranching river, plotted over Landsat false color composites. (*a*) Main channel of a reach of the anabranching Amazon River (Brazil, Landsat false color composite, 2000, bands 7,4,2). (*b*) Chute cutoff on the Ucayali River close to the city of Pucallpa (Peruvian Amazon, Landsat false color composite, 2005, bands 5,4,3). (*c*) Abrupt main channel change at a bifurcation and multiple neck cutoffs on the Rio Beni (Bolivia, Landsat false color composite, 2000, bands 5,4,3).

4.3.2 Individual bend separation and migration rates

I tested the methodology that I utilized in PyRIS for computing centerline migration rates against the migration rates obtained from an analytical model for meander evolution (Zolezzi and Seminara, 2001a; Seminara et al., 2001). For the testing, I used a synthetic periodic planform, which is commonly used in theoretical morphodynamic models for meandering rivers, because of its capacity of isolation and quantification of individual physical processes occurring during planform evolution of meander bends. The morphodynamic model I used assumes that every centerline point migrates outwards orthogonally to the local tangent of the centerline. Since the migration magnitude de-

pends on the curvature distribution, each point has a different net migration rate, leading to a net non-orthogonal migration between large timesteps. Therefore, I calculate the migration of individual points of the centerline between the initial and the final configurations and compare them with the ones extracted through the PyRIS centerline migration algorithm (Figure 4.10a).

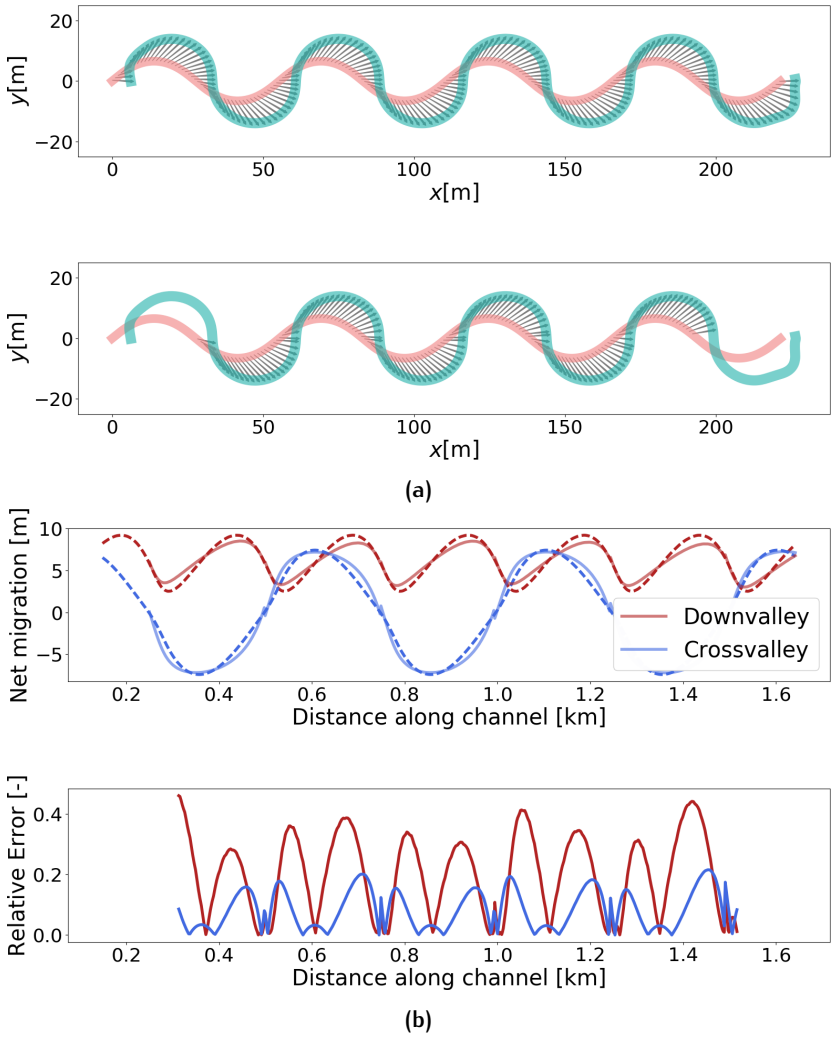

Figure 4.10: Validation of the proposed methodology for the local centerline migration rates against the morphodynamic model of Seminara et al., 2001. (*a*) Local migration vectors according to the model (above) and those computed by PyRIS (below). (*b*) Downvalley and crossvalley migration rates computed by PyRIS (continuous line) and by the morphodynamic model (dashed line); values (above) and relative errors (below).

Figure 4.10b illustrates that PyRIS tends to underestimate the crossvalley migration rates (blue line), which, in this case, coincide with the migration rates in the y direction of Figure 4.10a. The local relative error in the lower panel of Figure 4.10b is computed as the difference between the local migration rate computed by PyRIS and that

predicted by the morphodynamic model, divided by half the range of values. The error tends to be reduced when moving close to the inflection points and the bend apex. Conversely, the downvalley migration rates (here coinciding with the migration rates in the x direction) tend to be partly overestimated. The normalized root mean square errors (NRMSE) between the model-predicted migration rates and those computed by PyRIS are 0.167 and 0.115 for the downvalley and the crossvalley migration rates, respectively.

Figure 4.11 illustrates the application of PyRIS to calculate the migration rates of the Ucayali River after a massive cutoff (Abizaid, 2010). In Figure 4.11a the channel centerlines close to the cutoff location are reported for several years, while panel 4.11b shows the values of local crossvalley and downvalley migration rates averaged over every individual bend of the planform between 1998 and 1999. The implications of such a large cutoff on channel migration were discussed by Schwenk and Foufoula-Georgiou, 2015 and by Schwenk et al., 2016, who used the ratio between migration areas and centerline lengths to quantify migration rates. This allowed to observe whereby the effect of the cutoff affecting the reach-scale planform dynamics through waves of increasing migration rates propagating both upstream and downstream. By computing the local migration magnitudes and directions through PyRIS it is possible to enforce and further expand such findings by separately quantifying the modes of migration (downvalley, crossvalley) of individual meander bends in the proximity of the cutoff. Figure 4.11 shows that the cutoff largely promotes downvalley migration, both upstream and downstream, over crossvalley migration: the magnitudes of downvalley migration upstream (smaller bend indexes) and downstream (larger bend indexes) of the cutoff are considerably larger compared to those of crossvalley migration for the same bends.

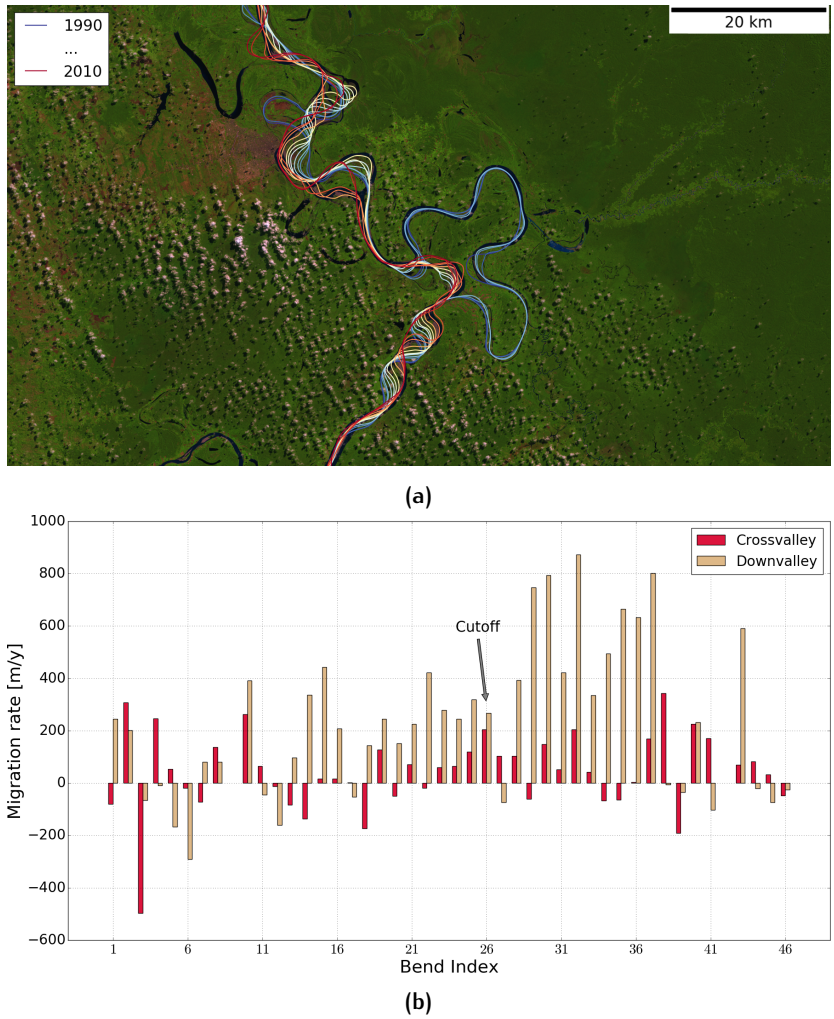

Figure 4.11: Assessment of downvalley and crossvalley migration rates after a massive cutoff on the Ucayali River (Perù) between 1998 and 1999. (*a*) Planform development highlighting the massive cutoff occurred in 1997 (Landsat false color composite, 2005, bands 5,4,3). (*b*) Bend-averaged local migration rates in the local downvalley and crossvalley directions.

4.3.3 Sediment bar dynamics

A specific novel feature of PyRIS compared to existing tools with similar aims is its ability to perform multitemporal analysis of sediment bar dynamics in single-thread rivers. An example of such feature is reported in Figure 4.12, which shows the spatial distribution of the

local river bar migration rates in a reach of the Rio Xingu (Brazil) computed over roughly 20 Landsat image frames between 1984 and 2011. The migration rates were initially computed as centroid-based discrete values, then they were spatialized over all the river pixels through a spatial interpolation. The map shows the spatial distribution of local migration rates over more than twenty years, quantify areas where the migration dynamics of bars within the channel are accelerated (red areas) or inhibited (yellow areas).

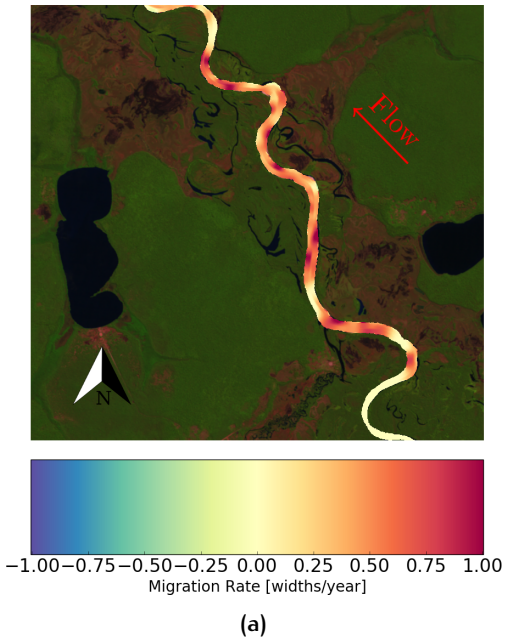

Figure 4.12: Spatially distributed local bar migration rates along a reach of the Rio Xingu (Brazil) averaged between 1984 and 2011.

4.4 DISCUSSION

This work introduces PyRIS, a fully automated, process-based extractor of river morphodynamics from remotely sensed multispectral images. PyRIS was initially specifically designed for multitemporal analysis of river meander morphodynamics, but it includes many properties that may come handy for broader applications in the analysis of other river channel patterns, such as anabranching channels. In this section I discuss the main strengths, limitations and novel features of PyRIS in relation to its three main components (planform extraction,

bend-scale analysis and local migration, sediment bar dynamics) described in section 4.2.

4.4.1 Planform extraction

The mask extraction procedure has been applied to several meandering and anabranching river planforms, and each of them allowed extensive subsequent analysis of centerline development, migration rates and bar dynamics. The PyRIS mask extraction algorithm is nevertheless the first step in trying to automate such a process, which nowadays is still performed through time-consuming procedures, either manual or computer-aided (e.g. Güneralp et al. 2013). Moreover, this approach enables for multitemporal analysis without requiring for atmospheric correction of Landsat data (Song et al., 2001). The applicability of such a procedure is unfortunately restricted to natural meandering rivers, due to the assumption of the presence of the vegetation cover around the river, and so far to the Landsat data only. However, PyRIS allows to compute the river masks externally and to extract the river planforms starting from river masks. Furthermore, by accepting river masks as input, PyRIS can potentially be applied to any kind of multitemporal spatial data, including aerial and drones-captured data. Implication of the latter feature may include monitoring and management purposes, such as monitoring river discharge, sediment budgets and planform changes.

One of the main novelties of PyRIS is the recursive centerline extraction method. Such a procedure is able to build the correct main channel path even in the case of complex morphological patterns; conversely, related existing software (e.g. Fisher et al. 2013; Merwade 2007; Pavelsky and L. C. Smith 2008; Rowland et al. 2016; Schwenk and Foufoula-Georgiou 2015) requires main channel branches to be a-priori defined by the user. A similar approach, able to deal with multiple branches, was recently developed by Schwenk et al., 2016, but it can only account for the length of the branches and for their width, leading to the extraction of the shortest path, which does not necessarily coincide with the main channel path. Moreover, another key novelty of PyRIS is its way to extract multitemporal river planforms, which enables for capturing in an automated fashion discontinuous deviations from a main channel, i.e. when bifurcations, chute channels and cutoffs or anabranches occur.

4.4.2 Individual bend separation and local migration vectors

A novel approach for computing the local channel migration vectors (magnitude and direction) allows one to investigate meander morphodynamics with unprecedented level of detail. The migration algorithm involves the separation and correlation of individual meander bends during time, allowing a straightforward comparison with the outcomes of river morphodynamic theories and models in terms of the temporal development of individual meander bends. The core advantage is the ability to correctly process migration rates in meander bends with dominantly downvalley mode of migration, overcoming previous limitations found in existing algorithms, which cannot correctly compute migration rates close to the bend apexes (e.g. Aalto et al. 2008; Lauer and Parker 2008). Moreover, whereas other existing software applications with similar goals can compute either an average value for a river reach (e.g. Constantine et al. 2014; Constantine 2006) or a local magnitude (Peixoto et al., 2009; Rowland et al., 2016; Schwenk et al., 2016). By reprojecting the migration vectors over the downvalley and crossvalley directions, PyRIS allows to define the modes of migration of individual meander bends and of entire river reaches. I illustrated one application of such reprojection together with the individual bend separation by defining the bend-scale modes of migration in the large meandering Ucayali River following a well-known massive cutoff (Abizaid, 2010; Schwenk et al., 2016; Schwenk and Foufoula-Georgiou, 2015). The robustness of the algorithm is supported by the quantification of deviations between the expected local centerline migration rates and those predicted by an analytical periodic model for meander planform evolution. Such deviations show an oscillating relative error which has a maximum NRMSE of $\mathcal{O}(10\%)$ for both downvalley and crossvalley migration rates of bend apexes and tends to vanish near meander inflections.

4.4.3 Sediment bar dynamics

A completely novel feature of PyRIS is the methodology able to automatically investigate the dynamics of sediment bars along evolving meandering rivers, which potentially can be extended to a wider range of river channel patterns. Up to now, studies on the multitemporal dynamics of river bars have been limited because of the constraints associated with thee manual digitization of channel bars (e.g. Adami et al. 2016; Latrubesse et al. 2009). PyRIS allows to overcome such limitation and to automatically compute the spatial and temporal distributions of sediment bar migration rate, spatial occurrence and size. I applied

the bar dynamics analysis for quantifying the distribution of large scale mobility of the channel bed along a river reach.

The requirements for the applicability of PyRIS to the computation of bar dynamics are represented by the availability of multi-spectral images within a range of flow stages allowing sediment bars to emerge from the water surface by a sufficient amount (i.e. area larger than the pixel resolution). Such conditions depend on both the flow conditions under which the data is remotely sensed and the resolution of the sensor. Moreover, whereas central bars may be vegetated and therefore treated as islands by PyRIS, bank-attached bars that are completely covered by vegetation are not included in the river mask.

4.5 CONCLUSION

Meandering rivers are one of the most widely studied systems on Earth, although knowledge on their actual dynamics is still limited in that the scientific community is still lacking automated software able to extensively extract morphodynamic features from multitemporal remotely sensed data. To overcome such gap, the present work aims to introduce the process-based software PyRIS (Python–RIvers from Satellite) and to illustrate its ability of extracting extensive information on meandering river morphodynamics with unprecedented automation levels.

PyRIS provides three main computations: (i) channel centerline extraction from either multispectral remotely sensed data or binary masks through a novel recursive algorithm able to capture the main channel at the occurrence of channel bifurcations, secondary channel and anabranching, (ii) the computation of local channel centerline migration rates and directions through a novel bend-scale approach, which provides a significant improvement to the state of the art through the ability of computing such rates in an proper manner even when the migration rates is dominantly downvalley, and (iii) analysis of sediment bars dynamics by quantifying the local rates of change of the channel bed in evolving meander bends.

Our methodology for the local migration rates of the channel centerline compares well with analytical model outcomes, and distribution of errors between PyRIS and model are quantified. To my knowledge, the PyRIS software provides the first successful attempt to quantify local sediment bar dynamics in evolving meandering rivers. I reckon that PyRIS can provide a significant improvement to the state of the art understanding of meander river morphodynamics, which can benefit researchers in river morphodynamics by allowing them to extract

extensive information from multispectral remotely sensed data in a simple and fully-automated manner. Finally, though PyRIS has been specifically designed for the analysis of meandering or anabranching river patterns and morphodynamics, some of its algorithms (such as the one for the main channel detection) have the potential for broader applications, possibly including hemodynamics and remote navigation.

5 THE PLANFORM DEVELOPMENT OF MEANDERING RIVERS

In this chapter an analytical model for the coevolution of channel curvature, width and longitudinal bed slope in evolving periodic meander bends is developed. I firstly address the problem of the bankfull hydraulic geometry (section 5.1) i.e. I will consider an equivalent straight rectangular channel under bankfull conditions subjected to elongation. The elongation leads to a decreasing trend for the average channel bed slope, and this mechanism is contrasted by excess sediment supply with respect to sediment transport capacity. The change in bankfull flow conditions has an effect on the channel width as well, which asymptotically tends to adapt to the equilibrium conditions. In section 5.2 I undertake the challenge of planform development of gravel bed meandering rivers with freely evolving banks. To this aim I formulate and apply a novel planform evolution model based on the framework of the classical bend theory of river meanders (e.g., Ikeda et al. 1981), and able to account for local width change over space and time, tied to the local hydro-morphodynamics by means of a three-way feedback process. The flow field and sediment transport are modeled through the two dimensional Shallow Water-Exner model in intrinsic curvilinear form, while the equation for the evolution of the channel banks is developed accounting for different rates of bank advance and bank retreat associated with the processes of bar push and bank pull. In section 5.3 I perform a nonlinear perturbation expansion of the basic state (bankfull hydraulic geometry) with small periodic oscillations of channel curvature and channel width; under the assumption of regular, sinusoidal width and curvature oscillations, the system reduces to a set of ordinary differential equations, formally identical to those presented by Seminara et al., 2001 but with two additional equations for the longitudinal autogenic and allogenic oscillations of the channel width, that integrate the bankfull hydraulic geometry models developed in section 5.1.

5.1 AN ANALYTICAL MODEL FOR THE BANKFULL HYDRAULIC GEOMETRY OF EVOLVING MEANDER BENDS

Let us consider an evolving sequence of periodic meander bends, each identical to both the previous and to the next one. In the context of bankfull hydraulic geometry I will generally refer to a one-dimensional, cross section-averaged formulation of the flow field and sediment transport.

The river centerline undergoes a lateral migration rate ζ^* due to the cumulative effects of erosion of the outer bank and accretion of the inner one. The migration rate ζ^* is usually defined as proportional to the difference between the depth-averaged streamwise velocity u^* between the two banks (Hasegawa, 1977; Ikeda et al., 1981; Seminara et al., 2001; Seminara, 2006; Camporeale et al., 2007; Eke et al., 2014a), as follows

$$\zeta^* = M\left(u^*_{\text{left bank}} - u^*_{\text{right bank}}\right) \tag{5}$$

where M is a migration coefficient, representing the timescale of the planform development process, typically around $10^{-6} - 10^{-8}$, (see e.g. Camporeale et al. 2005, 2007).

This sequence of meander bends is initially represented by a quasi-straight channel, whereas the temporal planform development leads to a sinuous configuration. I identify the bankfull hydraulic geometry at a specific time level through the variables $\tilde{S}$, W^* and D^*, respectively the longitudinal bed slope, the bankfull channel width and the cross section-averaged bankfull flow depth. Restricting the attention to the so-called reference flow conditions, I consider any spatial variability due to the presence of a channel curvature as a small perturbation that does not affect the reach-averaged bankfull conditions. This hypothesis is well supported in the literature provided the channel curvature ratio is a small parameter (see e.g. Ikeda et al. 1981; Johannesson and Parker 1989; Blondeaux and Seminara 1985; Tubino and Seminara 1990; Zolezzi and Seminara 2001a; Seminara 2006; Zolezzi et al. 2012b; Eke et al. 2014a). Hence, I assume a spatially-invariant bankfull hydraulic geometry within our configuration of indefinite periodic meander bends. I will indicate with the pedix 0 the values of the variables at the incipient formation of meanders, in the quasi-straight configuration where meander sinuosity σ is close to one (intrinsic meander length close to Cartesian meander length).

Equation 5 can be split into two equations describing the lateral shift ζ_b^* of the two channel banks as

$$\zeta_b^*\Big|_{\pm B^*} = \pm 2\mathcal{M}\left(u_{\pm B^*}^* - U_R^*\right), \tag{6}$$

where U_R^* represents some threshold on the cross section-averaged streamwise velocity above which only bank erosion occurs and below which only bank accretion occurs, and B^* is half the bankfull channel width ($W^* = 2B^*$); $\pm B^*$ represents either the left (+) or right (−) bank.

It is straightforward to combine the bank shift rates (6) to obtain the migration rate of the channel centerline ζ^* and the bankfull width change rate ξ^* as

$$\zeta^* = \frac{1}{2}\left(\zeta_b^*\Big|_{\text{left bank}} - \zeta_b^*\Big|_{\text{right bank}}\right), \tag{7a}$$

$$\xi^* = \frac{1}{2}\left(\zeta_b^*\Big|_{\text{left bank}} + \zeta_b^*\Big|_{\text{right bank}}\right), \tag{7b}$$

$$\tag{7c}$$

where ξ^* is the rate of change of the channel width that can be written explicitly as follows:

$$\frac{dW^*}{dt^*} = M\left(u_{\text{left bank}}^* + u_{\text{right bank}}^* - 2U_R^*\right). \tag{8}$$

Note that (8) provides a Partheniades and Paaswell, 1970-like model for the evolution of the channel width, where the bank erosion/accretion are only related to the longitudinal bankfull velocity. A detailed description of the local bank processes is beyond the scope of this work: the combination of individual processes such as bar push and bank pull (van de Lageweg et al., 2014; Eke et al., 2014b), slump blocks mechanics (Parker et al., 2011), effects of vegetation on flow resistance (Darby, 1999) is assumed to converge to a simple law such as (8) on the large timescale of planform development. Note also that (8) implicitly assumes that the channel banks shift with a certain rate scaled by the coefficient $\mathcal{M}$, regardless the bank is retreating or advancing. An extension of the model to different rates of bank migration is presented in the next chapter.

The choice of a threshold for the bankfull flow velocity U_R^* opens a range of possibilities:

A. the instantaneous bankfull flow velocity U^* can be used; in this case, the bankfull channel width keeps constant during the planform elongation;

B. the bankfull flow velocity U_0^* at incipient meander formation, assuming that the bankfull flow is initially in equilibrium with the external conditions;

c. a time-dependent model, such as the one proposed by Li et al., 2014; Eke et al., 2014a that, however, does not have a mechanistic justification.

However, according to the regime formulas of Parker et al., 2007 and Wilkerson and Parker, 2010, once a representative discharge and a representative grain size are assigned, suitable equilibrium values of the bankfull hydraulic geometry parameters are identified. Hence, it is reasonable to assume that the threshold value U_R^* is equal to some regime bankfull flow velocity univocally determined once the hydrology and sediment grain size are given; therefore U_R^* is constant in the geological timescale (provided, of course, that the hydrological regime is statistically invariant over that timescale). Hence, I set U_R^* constant and equal to the streamwise flow velocity at incipiente meander formation, which means that I consider a river whose evolutionary stages vary in the neighborhood of quasi-equilibrium conditions. Any macroscopic deviation from the equilibrium conditions would in general drive the channel width to asymptotically shift towards the equilibrium conditions.

I now seek an evolutionary equation for the evolution of the channel slope. I consider an evolving portion of channel of length, say one meander wavelength L^*, and cross section-averaged riverbed elevation $\widetilde{\eta}^*$ between its endpoints. At incipient formation the length is L_0^* and the bed elevation drop is $\widetilde{\eta}_0^*$. The channel slope is given by

$$\tilde{S} = \frac{\widetilde{\eta}^*}{L^*}. \tag{9}$$

Figure 5.1 depicts the situation. By computing the ratio $S = \tilde{S}/\tilde{S}_0$

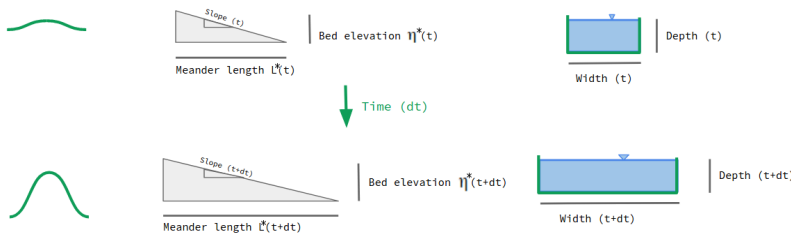

Figure 5.1: Sketch for the evolution of bankfull hydraulic geometry of an individual meander bend

and differentiating with respect to time t^* I obtain

$$\frac{d\widetilde{S}}{dt^*} = \widetilde{S}\left[-\frac{1}{L^*}\frac{dL^*}{dt^*} + \frac{1}{\widetilde{\eta}^*}\frac{d\widetilde{\eta}^*}{dt^*}\right]. \tag{10}$$

In order to define the time evolution of the riverbed drop $\widetilde{\eta}^*$ I integrate the Exner equation over the volume of sediments subtended by the meander bend (taking the mean elevation of its endpoint as the zero-level), in the form

$$(1-p_b)\frac{d}{dt^*}\left(L^* W^* \widetilde{\eta}^*\right) = Q^*_{s0} - Q^*_s + (1-p_f)\frac{d}{dt^*}\left(L^* W^* D^*\right), \quad (11)$$

where p_b and p_f are representative porosities of the riverbed and floodplain, respectively. Q^*_s represents the total sediment transport, under the hypothesis that the latter coincides with the sediment transport capacity, which is given by $Q^*_s = W^*\sqrt{g^* \Delta {D^*_s}^3}\Phi(\tau_*)$, where $\Phi(\tau_*)$ is a sediment transport formula (herein I adopt the formula proposed by Meyer-Peter and Müller (1948) under the assumption of dominant bedload transport).

Equation (11) requires some explanation. I refer to the conservation of sediment mass integrated over a meander wavelength L^*: the total volume of sediment is given by $L^* W^* \widetilde{\eta}^*$, and any variation of the volume is primarily due to the disequilibrium between the constant input sediment supply Q^*_{s0} and the sediment transport capacity Q^*_s. As a meander bend evolves, the portion of floodplain occupied by the channel changes, resulting in a net input sediment load entering the channel (see also Lauer and Parker 2008) which can be approximated as the change in floodplain volume $L^* W^* D^*$ occupied by the river at bankfull conditions at a certain time (the third term on the right hand side of equation 11). The floodplain porosity $p_f \in [0, 1]$ accounts for the percentage of the floodplain matrix that does not contributes to the bed material load within the channel. Hence, $1 - p_f$ is the net portion of eroded floodplain that contributes to the sediment transport. Note that the model neglects the eventual aggradation/degradation of the entire reach.

Finally, I define the normalized slope and dimensionless channel width, bed elevation, water depth, flow velocity and time respectively as follows

$$\begin{aligned} S &= \frac{\tilde{S}}{\tilde{S}_0}, \quad W = \frac{W^*}{W^*_0}, \quad \widetilde{\eta} = \frac{\widetilde{\eta}^*}{D^*_0}, \\ D &= \frac{D^*}{D^*_0}, \quad U = \frac{U^*}{U^*_0}, \quad T = 4M\frac{U^*_0}{W^*_0}t^* \end{aligned} \quad (12)$$

and I introduce the meander wavenumber

$$\lambda = \frac{\pi W^*}{L^*}. \quad (13)$$

where U^* is the cross section-averaged streamwise flow velocity and L^* the meander wavelength.

Bankfull hydraulic geometry is typically characterized by three dimensionless parameters: the aspect ratio, the Shields stress and the relative roughness, which are defined as follows

$$\beta = \frac{W^*}{2D^*}, \quad \tau_* = \frac{C_f U^{*2}}{g^* \Delta D_s^*}, \quad d_s = \frac{D_s^*}{D^*}, \tag{14}$$

where C_f is the friction coefficient, U^* the streamwise, cross section-averaged flow velocity, g^* the acceleration due to gravity, Δ the submerged specific density and D_s^* some characteristic grain size of the riverbed.

In the context of bankfull hydraulic geometry, I can write equation (8) in dimensionless form, provided I employ the cross section-averaged value U^* in place of the local values of streamwise velocity u^* as follows

$$\frac{dW}{dT} = \frac{1}{2}(U - U_R) \tag{15}$$

where $U_R = U_R^*/U_0^*$.

By expanding the derivatives and substituting into (9) I obtain the following evolutionary equation for the normalized reference channel slope

$$\begin{aligned} \frac{dS}{dT} = \left(1 + \frac{3}{10} r_p \frac{W}{\widetilde{\eta}}\right)^{-1} \Bigg[& \left(2 - r_p \frac{D}{\widetilde{\eta}}\right) \frac{S}{\lambda} \frac{d\lambda}{dT} \\ & - \left(3 - \frac{2}{5} r_p \frac{D}{\widetilde{\eta}}\right) \frac{S}{W} \frac{dW}{dT} \\ & + \mathcal{R}_T \frac{\lambda S}{2\pi W^2 \widetilde{\eta}} \left(1 - W \frac{\Phi(\tau_*)}{\Phi_0(\tau_{*0})}\right) \Bigg], \end{aligned} \tag{16}$$

where $r_p = (1 - p_f)/(1 - p_b)$ and the parameter

$$\mathcal{R}_T = \frac{\sqrt{g^* \Delta D_s^{*3}} \Phi(\tau_{*0})}{2M(1 - p_b) D_0^* U_0^*} \tag{17}$$

represents the ratio between the celerity of riverbed evolution and the celerity of planform migration or, equivalently, the ratio between the timescales of planform evolution and riverbed evolution, respectively. Few words will help explain the structure of equation (16). Firstly, the evolution of the channel slope is related to meander elongation through the derivative of meander wavenumber. This term recalls the well-known model in which the slope drops proportionally to meander elongation. Secondly, the evolution of the slope depends on the change in channel width. This result accounts both for the change in the scale of the meander wavenumber (see equation (13)) and for

the variation of riverbed sediment volume contained in the meander wavelength due to widenings/narrowings. All these terms depend upon the ratio r_p which accounts for the bed material income due to sediment exchange with the planform. Finally, the last term of the right hand side of the equation introduces the ratio between the timescales of the planform and the bed. If the value of $\mathcal{R}_T$ is small (ideally equal to 0), then the planform development occurs so rapidly that the riverbed has no time to adapt to the new planform configuration; in this case the last term becomes negligible and the bed slope tends to be proportional to meander elongation (however, in the context of meandering rivers the lower bound of $\mathcal{R}_T$ is 1). On the contrary, when the value of the ratio $\mathcal{R}_T$ is large (in the limit for $\mathcal{R}_T \to \infty$), then the last equation reduces to $W\Phi(\tau_*) = \Phi(\tau_{*0})$: the processes of local sedimentation balance the slope change due to meander elongation: the sediment transport capacity balances the sediment supply and the bankfull hydraulic geometry converges to the equilibrium conditions.

Finally, the model (which is summarized by equations 15 and 16) requires an additional equation defining the planform elongation, i.e. $\frac{d\lambda}{dT}$, which is one of the subjects of the following section. The equation that I am going to develop follows strictly the model proposed by Seminara et al., 2001. This model basically provides two evolutionary equations, one for the meander wavenumber and one for the channel curvature. They depend on one another but, under the assumptions made for the specific problem of the bankfull hydraulic geometry, the effect of the channel curvature is negligible. Therefore only the equation for the evolution of meander wavenumber is of interest in this context. Note that the evolution of meander wavenumber implicitly describes the evolution of meander sinuosity, which is an increasing function of the time (from incipient formation to cutoff). Hence, any growing function of time as an evolutionary equation for planform sinuosity (e.g. a linear growth) would fit the present aim.

5.2 INTERACTION BETWEEN WIDTH OSCILLATIONS AND CURVATURE IN EVOLVING MEANDER BENDS

5.2.1 Flow Field and Sediment Transport

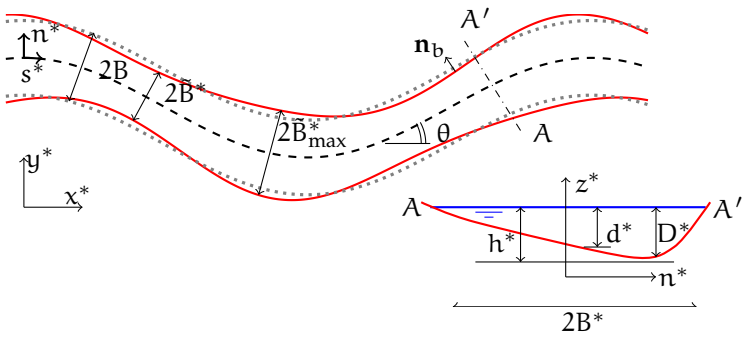

Figure 5.2: Sketch of a meandering reach with width variations and notation used in the mathematical model.

I consider a periodic, sine-generated meandering river with variable width, a constant slope and uniform grain size d_s^*. Figure 5.2 depicts the situation. Hydrodynamics and sediment transport are described by the two-dimensional depth-averaged model derived from the quasi-steady three-dimensional Reynolds averaged Navier-Stokes equations coupled with the Exner equation. I adapt the above model to an intrinsic curvilinear coordinate reference system (s^*, n^*), where s^* represents the longitudinal coordinate measured along the channel axis and n^* is the transverse coordinate orthogonal to s^*.

Let us define

$$\mathcal{C}^*(s^*) = -\frac{\partial \theta}{\partial s^*}, \tag{18}$$

the intrinsic curvature of the river reach measured along the channel axis, where θ is the inflection angle of channel centerline with respect to a Cartesian axis x^*; $\widetilde{B}^*(s^*)$ the half width of the channel, measured as orthogonal to the channel axis, and ϕ the local angle of the bank profile with respect to the channel axis, such that

$$\tan(\phi) = \frac{\partial \widetilde{B}^*}{\partial s^*}. \tag{19}$$

I also conveniently define the following dimensionless quantities

$$(s, n) = (B^{*^{-1}} s^*, \widetilde{B}^{*^{-1}} n^*), \tag{20a}$$

$$(u, v) = U^{*^{-1}}(u^*, v^*), \tag{20b}$$

$$(H, D) = D^{*^{-1}}(\mathcal{F}_0^{-2} h^*, d^*), \tag{20c}$$

$$(q_s, q_n) = (g^* \Delta d_s^{*3})^{-1/2}(q_s^*, q_n^*), \tag{20d}$$

where (u^*, v^*) are the components of the depth-averaged velocity vector, h^* denotes the water surface elevation with respect to a reference horizontal plane, d^* is the water depth, $\mathbf{q}^* = (q_s^*, q_n^*)$ is the bedload discharge vector per unit width. The transverse coordinate n has been stretched to match the local channel width, therefore lateral boundary conditions are to be imposed at $n = \pm 1$. Furthermore, U^*, D^* and $\mathcal{F}_0$ denote the mean velocity, depth and Froude number of the uniform flow that would occur, for the given discharge, grain size and slope, in an infinitely long rectangular channel of spatially constant width $W^* = 2B^*$ (corresponding to the reference bankfull conditions defined in the previous section). Such reference conditions can be univocally described by fixing the values of the dimensionless parameters β, τ_* and d_s defined by equation (14).

I then split the half channel width in the form

$$\widetilde{B}^*(s^*) = B^* + b^*(s^*), \tag{21}$$

and conveniently define the longitudinal distributions of centerline curvature and half width in the following dimensionless form:

$$\mathcal{C}(s) = \mathcal{C}^* R^*, \quad \widetilde{B}(s) = \frac{\widetilde{B}^*}{B^*}, \quad b(s) = \frac{4b^*}{\widetilde{B}^*_{max} - \widetilde{B}^*_{min}}, \tag{22}$$

where R^* is a representative value of the channel radius of curvature (in the following twice the radius of curvature at the bend apex of a sine-generated channel centerline) and B^*_{max} is the maximum value of the half width within a meander wavelength. Substituting (21) and (22) into (18) and (19) I obtain

$$\frac{\partial \theta}{\partial s} = -\nu\, \mathcal{C}, \tag{23a}$$

$$\tan(\phi) = \delta\, \frac{\partial b}{\partial s}, \tag{23b}$$

where two dimensionless parameters arise, namely the curvature ratio ν and the amplitude of channel width oscillations δ:

$$\nu = \frac{B^*}{R^*}, \qquad \delta = \frac{\widetilde{B}^*_{max} - \widetilde{B}^*_{min}}{4B^*}. \tag{24}$$

Hereafter, the formulation for the flow field and sediment transport follows closely the one reported in Zolezzi et al., 2012b, which the interested reader is referred to. Here I briefly outline the main assumptions and closures adopted.

1. Secondary flows are accounted for through a procedure originally introduced by Zolezzi and Seminara, 2001a, in which both dispersive terms and bed shear stresses associated to spiral flows due to streamline curvature are parameterized by coefficients k_i, $i = 0,\dots,5$ (see Zolezzi and Seminara 2001a, pagg.189–191). The total streamline curvature $\mathcal{C}_s$ is computed as the sum of the curvature of the channel centerline and the curvature associated with local streamline deviation from channel centerline in the form:
$$\mathcal{C}_s = v\mathcal{C} - \frac{uv_{,s} - vu_{,s}}{u^2 + v^2}. \tag{25}$$

2. The mean bed shear stress vector $\boldsymbol{\tau} = (\tau_s, \tau_n)$ is defined as
$$(\tau_s, \tau_n) = \widetilde{C}_f \sqrt{u^2 + v^2}\,(u, v + \tau_k), \tag{26}$$
where
$$\tau_k = \left[\frac{u\mathcal{C}_s d}{\beta\sqrt{\widetilde{C}_f}} \left(k_3 + \frac{k_5 d_{,s}}{\beta\sqrt{\widetilde{C}_f}} \right) + \frac{k_4 d^2 (u\mathcal{C}_s)_{,s}}{\beta^2 \widetilde{C}_f} \right], \tag{27}$$
represents the secondary flow contribution.

3. The components of the local sediment discharge are expressed by means of the following relations which account for both shear stress and the downslope pull of gravity:
$$q_s = \Phi \left\{ \cos\delta_q \left[1 - \frac{1}{2} \left(\frac{\eta_{,s}}{\beta\,(1 + v\hat{n}\mathcal{C})} \right)^2 \right] - \sin\delta_q \left(\frac{\eta_{,s}\eta_{,\hat{n}}}{\beta^2\,(1 + v\hat{n}\mathcal{C})} \right) \right\}, \tag{28a}$$
$$q_n = \Phi \sin\delta_q \left[1 - \frac{1}{2} \left(\frac{\eta_{,n}}{\beta} \right)^2 \right], \tag{28b}$$
where
$$\sin\delta_q = \left(\frac{\tau_n}{|\boldsymbol{\tau}|} - \frac{r}{\beta\sqrt{\tau_*}} \eta_{,\hat{n}} \right), \tag{29}$$
$\Phi = \Phi(\tau_*)$ is the bed load function, $\eta = \mathcal{F}_0^2 h - d$ is the bed elevation, $\hat{n} = n\widetilde{B}$ and r is an empirical coefficient approximately equal to 0.5 (Talmon et al., 1995). The formula of Parker, 1990 is employed to compute sediment transport.

The resulting two dimensional model for the flow field and sediment transport reads:

$$N\mathcal{L}_b(ud) + \widetilde{B}^{-1}(vd)_{,n} + N\nu\, \mathcal{C} vd = 0, \tag{30a}$$

$$NU\mathcal{L}_b(u) + \widetilde{B}^{-1} v u_{,n} + N\nu\, \mathcal{C} uv + N\mathcal{L}_b(h) + N\beta \frac{\tau_s}{d} = 0, \tag{30b}$$

$$NU\mathcal{L}_b(v) + \widetilde{B}^{-1} v v_{,n} - N\nu\, \mathcal{C} u^2 + \widetilde{B}^{-1} h_{,n} + \beta \frac{\tau_n}{d} = 0, \tag{30c}$$

$$N\mathcal{L}_b(q_s) + \widetilde{B}^{-1}(q_n)_{,n} + N\nu\, \mathcal{C}\, q_n = 0, \tag{30d}$$

where

$$N = \frac{1}{1 + \nu n \widetilde{B} \mathcal{C}}, \quad \mathcal{L}_b = \frac{\partial}{\partial s} - \delta \frac{n}{\widetilde{B}} \frac{\partial b}{\partial s} \frac{\partial}{\partial n}, \tag{31}$$

arise as a consequence of the metric coefficients of the adopted curvilinear system and of the stretching of the transverse variable needed to accommodate to width variations.

System (30) is associated with four boundary conditions, imposing lateral impermeability to both flow and sediment discharge:

$$(u, v) \cdot \mathbf{n}_b = 0, \quad (q_s, q_n) \cdot \mathbf{n}_b = 0, \qquad (n = \pm 1), \tag{32}$$

where $\mathbf{n}_b$ denotes the unit vector locally orthogonal to the banklines. In the longitudinal direction I impose periodic boundary conditions.

5.2.2 Planform evolution

In order to model the planform development of meandering rivers with spatially and temporally variable width, I integrate the approach of Seminara et al., 2001 through an additional equation describing the temporal evolution of the spatial width oscillations.

The analysis is based on three key simplifying hypothesis. First, I assume the time scale of planform development to be sufficiently long to allow for the instantaneous adaptation of the flow field and bed topography to planform changes (curvature, width and length). This implies that as ν and δ coevolve in time, the flow and bed topography can be obtained from the steady solution of (30) and therefore they change in time only parametrically. Furthermore, on such a long timescale the bank migration process can be viewed as a continuous, rather than intermittent, process. Last, I focus the attention on width changes due to perturbations of flow field and bed topography with respect to the reference state. Therefore I assume that such state, which changes slowly in time, does not produce any variation of the average channel width $2B^*$.

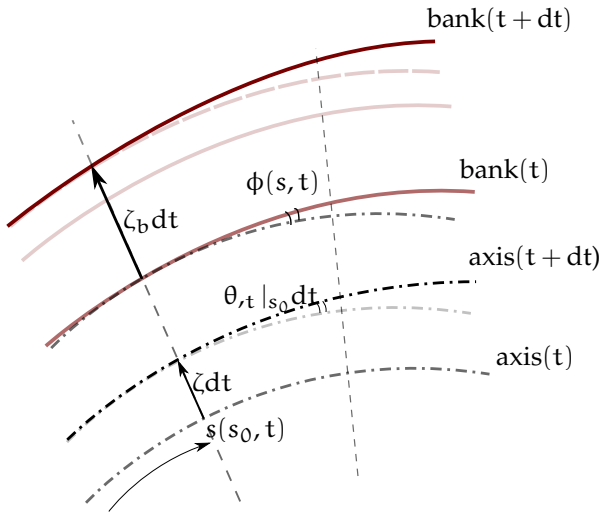

(a) Sketch of the model for planform development of channel axis and banks.

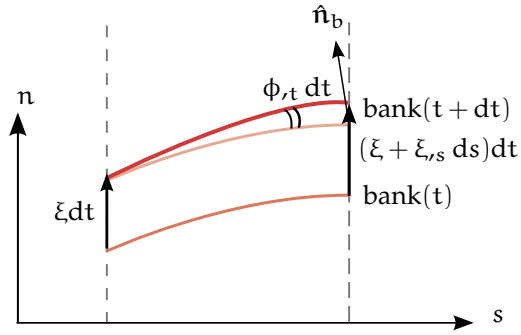

(b) The model for bank development projected onto the curvilinear reference frame (the versor $\hat{\mathbf{n}}_b$ is locally orthogonal to the channel bank).

Figure 5.3: Sketch for the planform development of the channel axis and banks.

I refer to the geometrical construction reported in figure 5.3 to develop an evolutionary equation for the bank profile. Let us consider a local rate of migration of the channel bank ζ_b, orthogonal to the channel axis, scaled with the reference velocity U^*. The migration rate ζ_b

can be decomposed into a transversally anti-symmetrical contribution ζ and a transversally symmetrical contribution ξ, such that

$$\zeta_b|_{n=\pm 1} = \zeta \pm \xi, \tag{33}$$

where $n = \pm 1$ denotes the outer and inner bank, respectively. Therefore, ζ represents the lateral migration rate of the channel axis, while ξ represents the local migration rate of the bank with respect to the channel axis. From purely geometrical constraints the following relations are readily found:

$$\left.\frac{d\theta}{dt}\right|_{s_0} dt\, ds = \zeta_{,s}\; ds\, dt, \tag{34a}$$

$$\phi_{,t} \cos(\phi)^{-1}\, dt\, ds = \xi_{,s}\; ds \cos(\phi)\, dt, \tag{34b}$$

where t is the dimensionless time, scaled with the flow time-scale B^*/U^*, and s_0 denotes the cross-section whose location is s at time t. The Lagrangian derivative can be expanded as follows

$$\left.\frac{d}{dt}\right|_{s_0} = \frac{\partial}{\partial t} + \frac{ds}{dt}\frac{\partial}{\partial s}, \tag{35}$$

where the material derivative of the arc-length can be computed (see Seminara et al. 2001) as

$$\frac{ds}{dt} = -\int_0^s \zeta \frac{\partial \theta}{\partial s}\, ds. \tag{36}$$

Hence, equations (34) become:

$$\theta_{,t} - \theta_{,s} \int_0^s \zeta\, \theta_{,s}\, ds = \zeta_{,s}\,, \tag{37a}$$

$$\left(1 + \tan^2 \phi\right) \phi_{,t} = \xi_{,s}\,. \tag{37b}$$

Equations (37) describe the planimetric evolution of a meandering river with freely variable width in intrinsic form. The integro-differential term in (37a) accounts for the history of the deformation process of the channel centerline which affects the evolution of the channel axis. Equation (37a), which was first proposed by Seminara et al., 2001, implies a cubic geometric nonlinearity in the evolution of the channel centerline. The cosine term in (37b) is due to the different elongation of the bank with respect to the centerline and to the adopted definition of the bank migration rate ξ as orthogonal to the channel axis. Being ζ the odd part of ζ_b, I expect θ to be an odd function. This fact is enforced by the structure of (37a), implying the cubic nonlinearity. On the other hand, I expect ϕ to be an even function, being ξ the even

part of ζ_b. The latter is enforced by the presence of the cosine term in the bank inflection equation (37b).

When periodic, sine-generated meanders are of interest, the structure of equations (37) suggests a Fourier expansion of the variables θ and ϕ of the form:

$$\theta(s,t) = \sum_{k=1}^{\infty} \theta_m(t)\, e_m(s,t) + \text{c.c.}, \quad m = 2k-1, \tag{38a}$$

$$\phi(s,t) = \sum_{k=1}^{\infty} \phi_m(t)\, e_m(s,t) + \text{c.c.}, \quad m = 2k, \tag{38b}$$

where the complex notation is conveniently employed, c.c. represents the conjugate of a complex number, $e_m(s,t) = \exp[im\lambda(t)s]$, and λ is the dimensionless meander wavenumber, scaled with the reference channel half-width B^*. I note that λ is time dependent because meander sinuosity changes as curvature develops in time. I also note that only odd harmonics ($m = 1, 3, \dots$) need to be considered in (38a) as a consequence of the cubic nonlinearity of the equation (37a).

Recalling equation (23b), one can readily see that expansion (38b) implies that the fundamental wavenumber of width oscillations is chosen as twice the wavenumber of curvature variations. This hypothesis relies on the assumption that to each meander bend corresponds an oscillation of channel width, which therefore displays two maxima over one meander wavelength. This is consistent with the few existing observations on real meanders (e.g. Seminara 2006; Luchi et al. 2011; Eke et al. 2014a) and is also implicit in Brice, 1975's classification scheme for meandering rivers. Furthermore, the spatial structure set by (38b) arises as a natural consequence of the autogenic nonlinear mechanism that produces width oscillations, as discussed in the next section 5.3.1.

If I keep only the first term of the expansion (38a) I recover the classical sine-generated distribution. Using (23a) I then obtain:

$$\nu = \lambda\,|\theta_1|. \tag{39}$$

Including also the second term of (38a) I recover the Kinoshita, 1961 distribution of curvature, in dimensionless form:

$$\mathcal{C} = 2\left[\cos(\lambda s) - C_F \cos(3\lambda s) - C_S \sin(3\lambda s)\right], \tag{40}$$

where

$$C_F = -3\frac{\mathfrak{I}(\theta_3)}{|\theta_1|}, \qquad C_S = -3\frac{\mathfrak{R}(\theta_3)}{|\theta_1|}, \tag{41}$$

are the fattening and skewing coefficient, respectively.

Finally, a closure relation for the bank migration rate ζ_b is required in order to solve equations (37). During the past years a number

of models able to reproduce bank erosion and accretion mechanics leading to variations in channel width were developed. Mechanistic approaches for bank erosion processes were proposed by Duan and Julien, 2005 and Chen and Duan, 2006, who accounted for the sediment transport close to the banklines, and by Parker et al., 2011 and Motta et al., 2012, who provided a physical description of the mechanics of bank processes such as the failure of slump blocks. Simplified models for bank erosion were proposed by Mosselman, 1992; Darby et al., 2002; Jang and Shimizu, 2005; Rüther and Olsen, 2007; Darby et al., 2007, while a rational, process-based description of bank accretion processes was provided by Zen et al., 2016. However, including complex bank sub-models into a perturbation scheme as the one adopted in this paper is not straightforward. Simplified models that are able to approximately describe the key processes on longer timescale were widely used in the literature (Partheniades and Paaswell, 1970; Ikeda et al., 1981; Seminara et al., 2001; Zolezzi et al., 2012b). Besides the complexity of including a bank erosion/accretion model with a high level of detail into an analytical framework, I consider that on the long timescale of planform evolution of meandering rivers the effects of most of the processes that locally rule the advance and retreat of channel banks tend to be mitigated.

In Seminara et al., 2001 the centerline's migration rate is assumed to be proportional to the difference between the velocity at the outer bank and that at the inner bank. A novel element in the present approach, which is needed to allow width to locally evolve, is the possibility for each bank to migrate independently. The concept underpinning such novel formulation is graphically illustrated in figure 5.4. Namely, the migration rate of each bank is set as proportional to the difference between the velocity at the bank and a threshold value, here assumed to coincide with the reference flow velocity U^*. In dimensionless form, such bank migration model reads:

$$\zeta_b|_{n=\pm1} = \begin{cases} \pm 2E\left(u|_{n=\pm1} - U_R\right), & \text{if } u|_{n=\pm1} > U_R, \\ \pm 2A\left(u|_{n=\pm1} - U_R\right), & \text{if } u|_{n=\pm1} < U_R, \end{cases} \tag{42}$$

where E is a bank erosion coefficient, A is a bank accretion coefficient, and U_R is a threshold streamwise velocity discriminating between bank erosion and accretion. The factor 2 has been added for consistency with the traditional method. Note that equation (42) resembles the traditional constant-width model if the choice $U_R = U$ is employed and $E = A$. Equilibrium analysis provides linear relations between dimensionless bankfull flow variables and hydraulic discharge (Leopold and Maddock, 1953; Parker et al., 2007; Wilkerson and Parker, 2010) once a representative grain size is selected. Being the bankfull hydraulic discharge and the grain size distribution,

to some extent, externally imposed parameters, it is reasonable to set the equilibrium conditions as threshold conditions towards which the river planform asymptotically transitions.

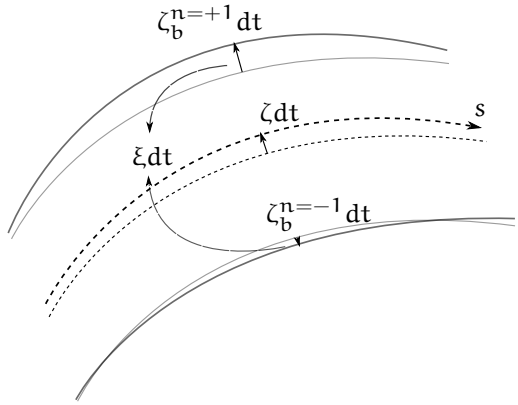

Figure 5.4: Sketch of decoupled bank migration model and notation.

Equations (42) are then combined is such a way that half their difference and their average give rise to the centerline migration rate ζ and to the local width change rate ξ, respectively:

$$\zeta = \frac{1}{2}\left(\zeta_b^{n=+1} - \zeta_b^{n=-1}\right), \tag{43a}$$

$$\xi = \frac{1}{2}\left(\zeta_b^{n=+1} + \zeta_b^{n=-1} - 2\right). \tag{43b}$$

Equation (43a) recovers the classical lateral migration law for the channel centerline originally proposed by Ikeda et al., 1981, while equation (43b) describes the temporal evolution of the spatial channel width oscillations. I note that setting the threshold velocity at the fixed value U^* implies that I neglect the adaptation of the average channel width to the slow time change of the reference flow due to meander elongation. Though the latter process could be easily incorporated into the model (see for instance Eke et al., 2014a), I adopt here such approximation in order to single out the role of flow and bed perturbations.

5.3 MATHEMATICAL SOLUTION

5.3.1 Perturbation approach

The two dimensional hydrodynamics and sediment transport problem (30) is solved analytically by means of a second-order two param-

eters (ν, δ) expansion. The analysis is based on the recognition that the values of ν and δ are typically much smaller than unity in real meandering rivers; for instance, Zolezzi et al., 2012b examined the spatial series of curvature and width for the class-C bends reported in the large dataset of Lagasse et al., 2004 showing that average δ values are typically slightly less than 0.1, with values up to $\delta \simeq 0.2$ for very few bends, while ν falls in the range $(0.05 \div 0.2)$ and rarely exceeds 0.25.

Hence, I employ the following expansion of the unknown variables:

$$\begin{aligned} \boldsymbol{v} = \boldsymbol{V} &+ \nu \left(\boldsymbol{V}_{10}^{(1)} C_1 e_1 + \boldsymbol{V}_{10}^{(3)} C_3 e_3 + \text{c.c.} \right) \\ &+ \delta \left(\boldsymbol{V}_{01}^{(2)} b_2 e_2 + \text{c.c.} \right) \\ &+ \nu^2 \left(\boldsymbol{V}_{20}^{(0)} + \boldsymbol{V}_{20}^{(2)} C_1^2 e_2 + \text{c.c.} \right) \\ &+ \nu\delta \left(\boldsymbol{V}_{11}^{(1)} \overline{C}_1 b_2 e_1 + \boldsymbol{V}_{11}^{(3)} C_1 b_2 e_3 + \text{c.c.} \right), \end{aligned} \tag{44}$$

where $\boldsymbol{V}_{ij}^{(k)} = (U_{ij}^{(k)}, V_{ij}^{(k)}, H_{ij}^{(k)}, D_{ij}^{(k)})^T$, $\boldsymbol{V} = (1, 0, H(s), 1)^T$ and the overbar $(\bar{\cdot})$ denotes the conjugate of a complex number. In order to keep the analysis as simple as possible, yet retaining the fundamental interactions between curvature and width variations, I have only included the first two terms of the curvature distribution arising from (38a) and the fundamental component of width oscillations:

$$\mathcal{C}(s) = C_1 e_1 + C_3 e_3 + \text{c.c.}, \quad b(s) = b_2 e_2 + \text{c.c.}. \tag{45}$$

Furthermore, in (44) I have only considered the non-linear terms ($\nu\delta$, ν^2) that arise from the interaction between the fundamental components (e_1, e_2) of curvature and width distributions.

The solution (44) is used to feed the planform evolution model (37) through the bank and centerline migration relations (43).

The $\mathcal{O}(\nu)$ linear solution represents the classical flow field solution forced by the presence of linearly forced bars in a regular sequence of sine-generated meander bends; its analytical solution has been for long time employed in the analysis of meander stability (Blondeaux and Seminara, 1985) and evolution (Seminara et al., 2001). Its transverse structure is anti-symmetrical and oscillates longitudinally with the same frequency of the curvature.

The $\mathcal{O}(\delta)$ linear solution was first derived by Repetto et al., 2002 and represents the flow-bed topography response to a periodically varying width along a straight reach. Its transverse structure is symmetrical, giving rise to a spatial sequence of mid-channel bars.

The $\mathcal{O}(\nu^2)$ nonlinear self interaction consists of two terms. Firstly, the longitudinally oscillating $U_{20}^{(2)}$ term has a transverse symmetrical

structure and it may be the cause of the presence of mid-channel bars in meandering rivers, as shown by Luchi et al., 2010a. Being transversally symmetrical, it is the leading curvature perturbation that can interact with width variation in the processes of local widening and narrowing because of the same transverse structure. Moreover, its wavenumber intrinsically emerges as twice that of curvature, consistently with the assumption made on channel width in 38b. Secondly, the longitudinally constant term $U_{20}^{(0)}$ has a transverse symmetrical structure and its integral on the cross section modifies the reference hydraulic conditions; hence, longitudinally constant terms play an effect in the evolution of the bankfull hydraulic geometry.

The $\mathcal{O}(\nu\delta)$ nonlinear mixed interaction is instead anti-symmetrical and embodies the effect of width variations on bend dynamics (Luchi et al., 2011), because its spatial structure exactly corresponds to that of the $\mathcal{O}(\nu)$ first order solution. Expansion (44) suggests that width oscillations also affect the development of the third longitudinal harmonic e_3 of curvature distribution, which is responsible for fattening and skewing of meander shape, through the term $\mathbf{V}_{11}^{(3)}$. The role of such contribution, which was not previously investigated, may turn out to be relevant in the final stage of meander evolution as the role of e_3 component becomes significant at relatively high sinuosity.

Solution $(\nu^i\delta^j)$	**Order**	**Wavenumber**	**Transverse structure**
$U_{10}^{(1)}$	$\mathcal{O}(\nu)$	λ	anti-symmetric
$U_{10}^{(3)}$	$\mathcal{O}(\nu)$	3λ	anti-symmetric
$U_{01}^{(2)}$	$\mathcal{O}(\delta)$	2λ	symmetric
$U_{20}^{(0)}$	$\mathcal{O}(\nu^2)$	0	symmetric
$U_{20}^{(2)}$	$\mathcal{O}(\nu^2)$	2λ	symmetric
$U_{11}^{(1)}$	$\mathcal{O}(\nu\delta)$	λ	anti-symmetric
$U_{11}^{(3)}$	$\mathcal{O}(\nu\delta)$	3λ	anti-symmetric

Table 5.1: Symmetry properties and wavenumbers of the perturbation solutions for the longitudinal velocity U_{ij}.

Symmetry properties of the perturbation solution at different orders are summarized in table 5.1. I note that, from the mathematical point of view, the channel width of meandering rivers is continuously forced towards spatial oscillations ($\mathcal{O}(\nu^2)$ effect). In summary, mutual feedbacks between width and curvature are primarily accounted for in the $\mathcal{O}(\nu^2)$ solution and in $\mathcal{O}(\nu\delta)$ solution (Luchi et al., 2011). More

details on the relation between the solution at different perturbation orders can be found in Zolezzi et al., 2012b.

5.3.2 Perturbation solution

Substituting the expansion (44) into the system (30) I derive an ordinary differential system in the transverse direction for each unknown at every order of the perturbation expansion, which can be conveniently written in matrix form:

$$\begin{pmatrix} a_{11}^{ij} & a_{12}^{ij}\frac{d}{dn} & a_{13}^{ij} & a_{14}^{ij} \\ a_{21}^{ij} & a_{22}^{ij} & a_{23}^{ij}\frac{d}{dn} & a_{24}^{ij} \\ a_{31}^{ij} & a_{32}^{ij}\frac{d}{dn} & a_{33}^{ij} & a_{34}^{ij} \\ a_{41}^{ij} & a_{42}^{ij}\frac{d}{dn} & a_{43}^{ij}\frac{d^2}{dn^2} & a_{44}^{ij} + a_{45}^{ij}\frac{d^2}{dn^2} \end{pmatrix} \begin{pmatrix} U_{ij} \\ V_{ij} \\ H_{ij} \\ D_{ij} \end{pmatrix} = \begin{pmatrix} b_1^{ij}(n) \\ b_2^{ij}(n) \\ b_3^{ij}(n) \\ b_4^{ij}(n) \end{pmatrix}. \quad (46)$$

Each system of equations can be easily solved once lateral boundary conditions are imposed (equation 32); they take the form:

$$\left(V_{ij}, \frac{d\left(\mathcal{F}_0^2 H - D\right)}{dn} \right) = \pm \left(b_{ij}^5, b_{ij}^6 \right) \quad (n = \pm 1). \quad (47)$$

The solution of (46) yields the transverse structure of the perturbations of flow field and bed topography at the different orders of approximation. Here I focus on the longitudinal velocity perturbations, which in the present approach (42) are responsible for bank migration. In particular, solutions U_{10} and U_{11} are anti symmetric and therefore involved in bend amplification, while U_{20} and U_{01}, being both symmetric, regulate autogenic width adjustments along meander bends. The solutions are reported in figure 5.5.

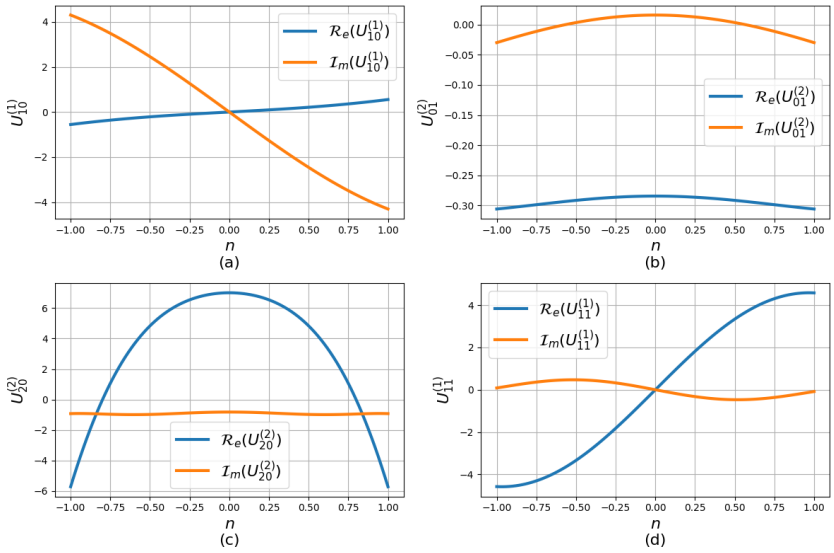

Figure 5.5: Transverse structure of the fundamental components of the perturbation solutions at different orders. (*a*) $\mathcal{O}(\nu)$ solution. (*b*) $\mathcal{O}(\delta)$ solution. (*c*) $\mathcal{O}(\nu^2)$ solution. (*d*) $\mathcal{O}(\delta)$ solution.

Figure 5.5 shows the transverse solutions of the main components (e_1- and e_2-terms) of the perturbation solution for the streamwise velocity U (44). Odd longitudinal harmonics (1 and 3) have transversally anti-symmetrical velocity components, whereas the even longitudinal harmonic (2) is transversally symmetrical.

By inserting the perturbation expansion (44) into the bank migration model (42) and equating symmetrical contributions

$$U_S = (\delta U_{01}^{(2)} b_2 e_2 + \nu^2 U_{20}^{(0)} + \nu^2 U_{20}^{(2)} C_1^2 e_2 + \text{c.c.})_{n=1} \tag{48}$$

and anti-symmetrical contributions

$$\begin{aligned} U_A = (&\nu U_{10}^{(1)} C_1 e_1 + \nu\delta U_{11}^{(1)} \overline{C_1} b_2 e_1 \\ &+ \nu U_{10}^{(3)} C_3 e_3 + \nu\delta U_{11}^{(3)} C_1 b_2 e_3 + \text{c.c.})_{n=1}, \end{aligned} \tag{49}$$

I approximate the bank migration law as follows in order to solve it analytically

$$\begin{aligned} \zeta_b|_{n=\pm1} = \pm 2 \sum_{U_K} &\begin{cases} E U_K, & \text{if } U_K > 0, \\ A U_K, & \text{if } U_K < 0, \end{cases}, \\ &(U_K = U_A, U_S, 1 - U_R), \end{aligned} \tag{50}$$

which gives rise, when inserted into (43), to

$$\zeta = 2\mathcal{M}U_A, \tag{51a}$$

$$\xi = 2\mathcal{M}\frac{1}{2}\left[(1-U_R)+U_S+\mathcal{K}\left(|1-U_R|+|U_A|+|U_S|\right)\right], \tag{51b}$$

where

$$\mathcal{M} = \frac{E+A}{2} \quad \text{and} \quad \mathcal{K} = \frac{E-A}{E+A} \tag{52}$$

are the centerline migration rate and the normalized difference between bank erosion rate and bank accretion rate.

Note that the concept of $\mathcal{K}$ is similar to the γ parameter employed by Eke et al., 2014a. The absolute values in (50) can be represented through Fourier series: the modulus of the generic $F_L = f_k e_k + \text{c.c.}$ gives

$$|f_k e_k + \text{c.c.}| = \frac{4|f_k|}{\pi} + \sum_{m=1}^{\infty} \frac{2}{(4m^2-1)\pi} f_k^{(2m)} e_{2m} + \text{c.c.}. \tag{53}$$

Consistently with (38b) I truncate the series to $m = 1$ and I obtain the following planform change rates, where each harmonic contribution has been isolated,

$$\zeta_1 = \left(\nu C_1 U_{10}^{(1)} + \nu\delta\overline{C}_1 b_2 U_{11}^{(1)}\right)_{n=1}, \tag{54a}$$

$$\zeta_3 = \left(\nu C_3 U_{10}^{(3)} + \nu\delta C_1 b_2 U_{11}^{(3)}\right)_{n=1}, \tag{54b}$$

$$\begin{aligned}\xi_0 = \Big(&1+\nu^2 U_{20}^{(0)} - U_R + \mathcal{K}\left|1+\nu^2 U_{20}^{(0)} - U_R\right| \\ &+ \frac{4\mathcal{K}}{\pi}\left|\nu C_1 U_{10}^{(1)} + \nu\delta\overline{C}_1 b_2 U_{11}^{(1)}\right| \\ &+ \frac{4\mathcal{K}}{\pi}\left|\delta b_2 U_{01}^{(2)} + \nu^2 C_1^2 U_{20}^{(2)}\right|\Big)_{n=1},\end{aligned} \tag{54c}$$

$$\begin{aligned}\xi_2 = \Big(&\delta b_2 U_{01}^{(2)} + \nu^2 C_1^2 U_{20}^{(2)} \\ &+ \frac{2\mathcal{K}}{3\pi}\left(\nu C_1 U_{10}^{(2)} + \nu\delta\overline{C}_1 b_2 U_{11}^{(2)}\right)\Big)_{n=1},\end{aligned} \tag{54d}$$

being

$$\zeta = 2\mathcal{M}(\zeta_1 e_1 + \zeta_3 e_3) + \text{c.c.} \tag{55a}$$

$$\xi = 2\mathcal{M}(\xi_0 + \xi_2 e_2) + \text{c.c.}. \tag{55b}$$

It is important to note that the anti-symmetrical perturbations of the flow field act on the centerline migration rate ζ, while symmetrical

perturbations either force or damp the local widening rate ξ. Therefore, from a linear point of view, curvature forced ν-perturbation produces effects on meander amplification, while δ-perturbation, forced by width variation, affects the width changes. From the two-dimensional analysis of Repetto et al., 2002, the $\mathcal{O}(\delta)$ linear solution for the longitudinal velocity at the bank (the first term in the right hand side of equation (54d)) turns out to invariably produce a self-suppressing effect, at least for the values of the wavenumber relevant for the present analysis. Therefore, the mechanisms able to produce width variation are the autogenic effect related to the second order solution for curvature perturbation, $\mathcal{O}(\nu^2)$ and the $\mathcal{K}$-related allogenic effect.

The $\mathcal{K}$-terms in equations (54) account for the allogenic mechanisms of bank pull (prevailing when $\mathcal{K} > 0$) and bar push (prevailing when $\mathcal{K} < 0$), while the ξ_0 term accounts for the variation of the reach-averaged bankfull channel width.

Finally, the planform development model requires an evolution equation for the reach-averaged channel slope S. I employ the evolution model developed in section 5.1 relating the evolution of the channel slope to meander elongation, evolution of bankfull channel width and change in sediment discharge with respect to the sediment supply, where nonlinear $\mathcal{O}(\nu^2)$ constant contributions are accounted for, as follows

$$\begin{aligned}\frac{dS}{dt} = \left(1+\frac{3}{5}r_p\frac{B}{\widetilde{\eta}+\nu^2\eta_{20}^{(0)}}\right)^{-1}\Bigg[&\left(2-r_p\frac{d+\nu^2D_{20}^{(0)}}{\widetilde{\eta}+\nu^2\eta_{20}^{(0)}}\right)\frac{S}{\lambda}\frac{d\lambda}{dt}+\\ &-\left(3-\frac{2}{5}r_p\frac{d+\nu^2D_{20}^{(0)}}{\widetilde{\eta}+\nu^2\eta_{20}^{(0)}}\right)\frac{S}{B}\frac{dB}{dt}\\ &+\mathcal{R}_T\frac{\lambda S}{8\pi B^2(\widetilde{\eta}+\nu^2\eta_{20}^{(0)})}\left(1-w\left(\frac{\Phi(\tau_*)}{\Phi_0(\tau_{*0})}+\nu^2q_{s_{20}}^{(0)}\right)\right)\Bigg]\end{aligned} \tag{56}$$

where represents the dimensionless bed elevation drop of meander bends, r_p account for the bed material load exchange from the floodplain through erosion and deposition (if $r_p = 0$ the sediment exchange with the floodplain is neglected), $\phi(\tau_*)$ is the dimensionless bedload transport and $\mathcal{R}_T$ accounts for the order of magnitude of the ratio between the planform development timescale and the sediment transport timescale. The latter regulates the trend of channel slope to strongly decrease proportionally to meander elongation when the riverbed has not enough time to re-adapt its slope to the sediment supply ($\mathcal{R}_T$ small) or to reshape towards the sediment supply-imposed slope due to the conservation of sediment mass.

Expansions (38) and (55) are finally incorporated into the planimetric evolution model (37). The resulting system of ordinary differential equations eventually reads:

$$\frac{d\theta_1}{dT} = i\lambda\left[\left(A+\overline{A}\right)\theta_1 - \frac{A_2}{2}\overline{\theta}_1 + \frac{3}{2}\overline{A}_2\theta_3 - \frac{3}{4}A_4\overline{\theta}_3 + \zeta_1\right], \tag{57a}$$

$$\frac{d\theta_3}{dT} = i\lambda\left[3\left(A+\overline{A}\right)\theta_3 + \frac{A_2}{2}\theta_1 - \frac{\overline{A}_4}{4}\theta_1 - \frac{A_6}{2}\overline{\theta}_3 + 3\zeta_3\right], \tag{57b}$$

$$\frac{d\lambda}{dT} = i\lambda^2\left(A_0 - \overline{A}_0\right), \tag{57c}$$

$$\frac{d\phi_2}{dT} = 2i\lambda\left[\left(1-2\left|\phi_2\right|^2\right)\xi_2 - {\phi_2}^2\,\overline{\xi}_2\right], \tag{57d}$$

$$\frac{dB}{dT} = \frac{1}{2}B\,\xi_0 \tag{57e}$$

$$\begin{aligned}\frac{dS}{dT} = {} & \left(1+\frac{3}{5}r_p\frac{B}{\eta+\nu^2\eta_{20}^{(0)}}\right)^{-1}\left[\left(2-r_p\frac{d+\nu^2D_{20}^{(0)}}{\eta+\nu^2\eta_{20}^{(0)}}\right)\frac{S}{\lambda}\frac{d\lambda}{dT}\right.\\ & -\left(3-\frac{2}{5}r_p\frac{d+\nu^2D_{20}^{(0)}}{\eta+\nu^2\eta_{20}^{(0)}}\right)\frac{S}{2}\xi_0\\ & \left.+\mathcal{R}_T\frac{\lambda S}{8\pi B^2(\eta+\nu^2\eta_{20}^{(0)})}\left(1-w\frac{\Phi(\tau_*)+\nu^2q_{s_{20}}^{(0)}}{\Phi_0(\tau_{*0})}\right)\right],\end{aligned} \tag{57f}$$

where the migration coefficient $\mathcal{M}$ has been absorbed into the dimensionless time, $T = 2\mathcal{M}t$, and

$$A_0 = \overline{\zeta_1}\theta_1 + 3\overline{\zeta_3}\theta_3, \tag{58a}$$

$$A_2 = \zeta_1\theta_1 + 3\overline{\zeta_1}\theta_3 - \zeta_3\overline{\theta_1}, \tag{58b}$$

$$A_4 = \zeta_3\theta_1 + 3\zeta_1\theta_3, \tag{58c}$$

$$A_6 = 3\zeta_3\theta_3, \tag{58d}$$

$$A = -\left(\frac{A_2}{2} + \frac{A_4}{4} + \frac{A_6}{6}\right). \tag{58e}$$

Equations (57)a–b describe the temporal evolution of the centerline curvature, while (57c) quantifies meander elongation as curvature and width coevolve. These equations are formally identical to those derived by Seminara et al., 2001 for constant width meanders. However, the terms on the right hand side include the effect of width oscillations which is felt through the dependence on δ of the components of the migration rate ζ_1, ζ_3 (equations 54a–b). Therefore, their solution is coupled with that of equation (57d) describing the temporal evolution of width oscillations, which in turn are affected by curvature through the dependence on the autogenic $\mathcal{O}(\nu^2)$ term and on the allogenic $\mathcal{O}(\mathcal{K}\nu)$ and $\mathcal{O}(\mathcal{K}\nu\delta)$ terms appearing in (54d). The ξ_0 accounts for

the variation of reach-averaged bankfull channel width related to the presence of bar push ($\mathcal{K} < 0$) or bank pull ($\mathcal{K} > 0$) mechanisms. The channel slope changes according to meander elongation and bankfull channel width change rate, but a dampening mechanism related to the decrease of sediment transport capacity with respect to the sediment supply also occurs. As a limiting case, system (57) can be reduced to the classical constant width case by setting $\delta = 0$. On the other hand, the evolutionary solution for a straight channel with periodic width can be obtained by setting $\nu = 0$.

As for the interaction between channel curvature and channel width oscillations, the purely autogenic mechanism can modeled by setting $\mathcal{K} = 0$ and is analyzed in detail in chapter 8, while the interaction between autogenic and allogenic width oscillations and curvature is presented in chapter 9.

The solution of (57) has been computed by means of a variable-coefficient ordinary differential equation system solver with fixed leading-coefficient implementation, backward differentiation method and adaptive numerical timestep in order to achieve both stability and a good level of accuracy. The initial condition has been set in terms of a small amplitude sine-generated meander, whose initial wavenumber is λ_0, with given initial values of the reference flow parameters (β, τ_* and d_s), while ϕ has been set equal to zero. At each time step the complex coefficients that describe the distribution of curvature and width oscillations in (45) are computed through equations (23) in the following form:

$$\nu C_m = -mi\lambda\theta_m, \quad (m = 1, 3), \quad \delta b_2 = -\frac{i\phi_2}{2\lambda}. \tag{59}$$

Recalling the definitions (24) and (39) of the parameters ν and δ, one can readily prove that $|C_1| = |b_2| = 1$.

Part III

RESULTS

6 EXPLORING REMOTELY SENSED MORPHODYNAMIC DATA

This chapter summarizes the multitemporal meander morphodynamic data that can be simultaneously extracted through PyRIS and their potential. Firstly, I will try to characterize a number of pristine meandering and transitional rivers from the South America and Africa in terms of bankfull hydraulic geometry and planform structure through data extracted through remote sensing, literature and gauging stations (section 6.1). Secondly, I will investigate the temporal evolution of the bankfull channel width in some morphologically active rivers (section 6.2); the analysis is conducted through a bend-scale approach, by analyzing each bend individually and looking at the evolution of the statistics of the channel width. Thirdly, I will study the bend-scale evolution of the planform descriptors, such as meander wavenumbers, channel curvature and width oscillations (section 6.3). All the bend-scale analyses use the individual bend sinuosity as a proxy of the evolutionary time of meander bends. Finally, some of the rivers in the analyzed dataset exhibit alternate migrating sediment bars; in section 6.4 I study the spatial scales and the downstream migration rates of these bars relatively to the local planform morphology.

6.1 REMOTELY SENSED MORPHODYNAMIC INFORMATION

In this section I will give an overview of the multitemporal data that can be obtained through the application of PyRIS to Landsat archive's datasets and of their integration with other real world data. Specifically, I make use of such data in order to provide a general characterization of bankfull hydraulic geometry and planform structure of a number of natural meandering and transitional rivers from the South America and Africa.

The database of fluvial gauges in South America[1] holds data for discharge, sediment concentration and sediment transport measures for most of the rivers of the Amazon Basin; the data is not always available and in some cases I perform an estimation. The open data from the SRTM satellite mission provides a single scan (in 2014) of the earth surface elevation with a 60m resolution. These data allows the reconstruction of free surface slopes for the rivers analyzed herein: the topography is interpolated and projected over the river planforms extracted through PyRIS; the minimum elevation of each cross-section is computed and the one-dimensional, downstream free surface elevation is computed. Because of the lack of bed topography data I employed the streamwise free surface slope as a proxy of the streamwise bed slope, assuming that backwater effects are negligible.

Total Suspended Sediment (TSS) estimates in Mton/year for those South American rivers are provided in Lima et al., 2001, 2004, 2005. The map reported in figure 6.1 shows all the rivers analyzed in the present thesis, including two reaches from Africa.

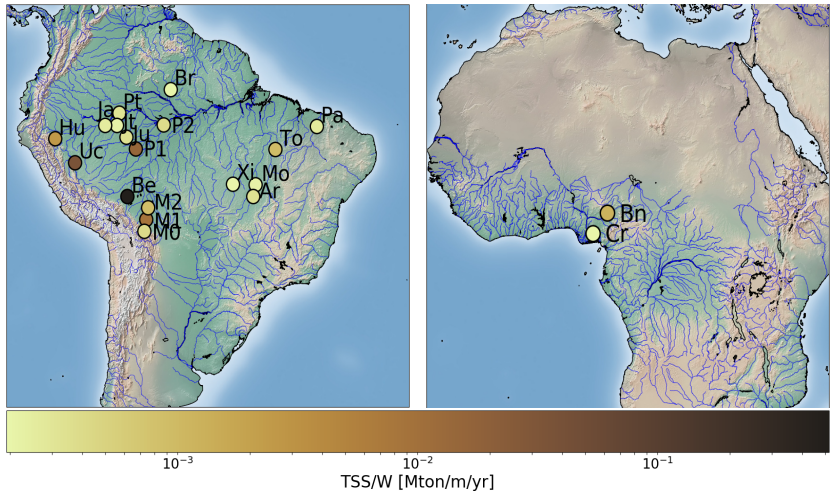

Figure 6.1: River reaches analyzed within the present work. The acronyms are reported in table 6.1. The marker colors indicate the Total Suspended Sediment (TSS) per unit width.

Table 6.1 reports the acronyms employed to denote river reaches in figure 6.1 together with their TSS and bar regime. The bar regime is called either *migrating* or *steady*: the *migrating* regime means that migrating bars are observed, though they may alternate with steady

1 Data is freely available at http://hidroweb.ana.gov.br/HidroWeb.asp?TocItem=1080&TipoReg=7&MostraCon=true&CriaArq=false&TipoArq=0&SerieHist=true and http://www.snirh.gov.br/hidroweb/

bars; on the other hand, the *steady* regime means that no migrating bars occur. Note that "steady" does not mean that bars do not change their position in time, as the the channel evolves in time and the bars adapt accordingly. Migrating bars are systematically migrating in the streamwise direction within the channel, steady bars are not.

For all the rivers I directly compute reference values of the following variables, starting from the PyRIS extraction: curvature ν, wavenumber λ, free surface slope S, channel width W^*. Data for the water discharge Q^*, the Total Suspended Sediment TSS and the characteristic grain size D_s^* were not available for all the study cases; however, I found either one or two of such variables in research papers and other sources of literature or from gauging stations.

Where some of the above variables are missing, I estimate them through the following normal flow and sediment transport formulas:

$$Q^* = CW * \sqrt{g^* S} D^{*3/2}, \tag{60a}$$

$$Q_s^* = W^* \sqrt{g^* \Delta D_s^{*3}} \Phi(\tau_*), \tag{60b}$$

where the Engelund-Hansen formula (Engelund and Hansen, 1967) for total sediment transport in normal flow conditions

$$\Phi(\tau_*) = \frac{0.05}{C} \tau_*^{5/2}, \qquad \tau_* = \frac{S}{\Delta d_s} \tag{61}$$

is used, consistently with the way the TSS is estimated in Lima et al., 2001, 2004, 2005. Furthermore, the Chezy coefficient $C = C_f^{-2}$ is computed according to the formula proposed by Wilkerson and Parker, 2010 in their equation (40). Equations (60), together with (61) and the Chezy formula provided by Wilkerson and Parker, 2010, are conveniently inverted and combined to compute the missing variables. Different combinations of these four equations provide surprisingly consistent results for most of the estimates computed through this methodology.

Acronym	Name	TSS	bars	Country
Ar	Araguaia	15[2]	migrating	South America
Be	Beni	212[3]	steady	South America
Br	Branco	2.7[4]	migrating	South America
Hu	Huallaga	71[5]	steady	South America
Ja	Javari	4.63[6]	steady	South America
Jt	Jutai	2[7]	steady	South America
Ju	Jurua	12[8]	steady	South America
Mo	Mamoreo	13[9]	steady	South America
M1	Mamore1	82[10]	steady	South America
M2	Mamore2	42[11]	steady	South America
Mo	Mortes	1.42[12]	migrating	South America
Pa	Parnaiba	10.14[13]	migrating	South America
P1	Purus1	103[14]	steady	South America
P2	Purus2	32[15]	steady	South America
Pt	Putumayo	24[16]	steady	South America
To	Tocantins	58[17]	migrating	South America
Uc	Ucayali	205[18]	steady	South America
Xi	Xingu	0.33[19]	migrating	South America
Bn	Benue	61.4[20]	migrating	Africa
Cr	Cross	2.14[21]	steady	Africa

Table 6.1: River reaches analyzed in the present thesis with acronyms and Total Suspended Sediment (TSS) per unit width and the bar regime. TSS is expressed in MTon/years.

The collected data and the computed parameters that allow me to compare hydraulic quantities with the TSS of the rivers considered in the analysis are reported in figure 6.2.

2 Based on Constantine et al., 2014; Lima et al., 2004, 2005
3 Based on Constantine et al., 2014; J. Guyot et al., 1996
4 Based on Constantine et al., 2014; Filizola and J. L. Guyot, n.d.
5 Based on Constantine et al., 2014; Armijos et al., 2013
6 Computed based on Landsat and SRTM data and Wikipedia
7 Based on Constantine et al., 2014; Dunne et al., 1998
8 Based on Constantine et al., 2014
9 Based on Constantine et al., 2014; J. Guyot et al., 1996; Wittmann et al., n.d.
10 Based on Constantine et al., 2014; J. Guyot and Bourges, 1994; J. Guyot et al., 1996; J. L. e. a. Guyot, 2007
11 Based on Constantine et al., 2014; Wittmann et al., n.d.
12 Computed based on Landsat and SRTM data and Lima et al., 2004; I assumed the sediment size to equal the ones of the surrounding analyzed rivers, which were very close
13 Computed based on Landsat and SRTM data and Dillenburg and Hesp, 2008; Spiegelberg, 2010 and Wikipedia
14 Based on Constantine et al., 2014; Filizola and J. L. Guyot, n.d.
15 Based on Constantine et al., 2014; Filizola and J. L. Guyot, n.d.; Dunne et al., 1998
16 Based on Constantine et al., 2014; Dunne et al., 1998
17 Computed based on Landsat and SRTM data and Latrubesse et al., 2005
18 Based on Constantine et al., 2014; J. L. e. a. Guyot, 2007
19 Based on Constantine et al., 2014; Lima et al., 2004, 2005
20 Computed based on Landsat and SRTM data and Chinenyeze and Ozibo, 2017; Andersen and Golitzen, 2005
21 Computed based on Landsat and SRTM data and Udo and Uko, 2014; Edet and Offiong, 2002

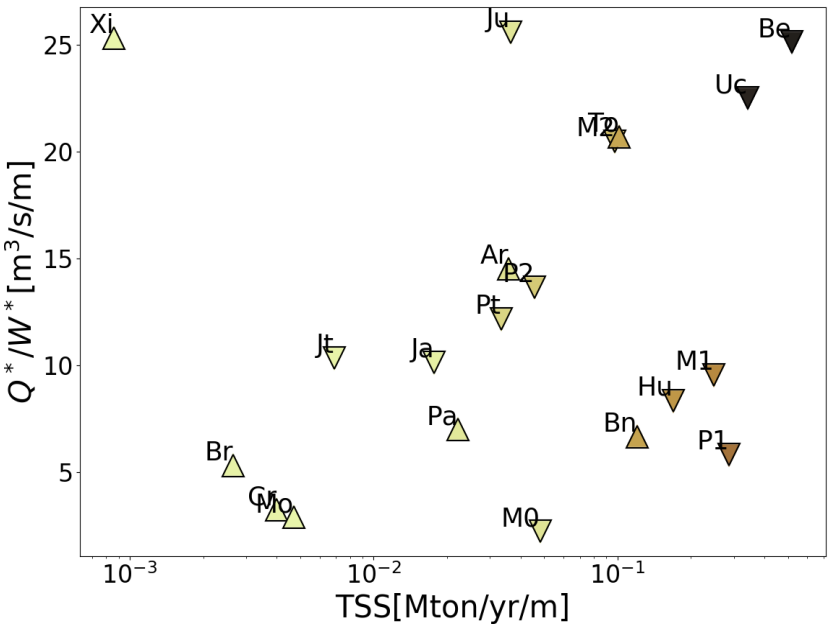

(a) Bankfull water discharge per unit width

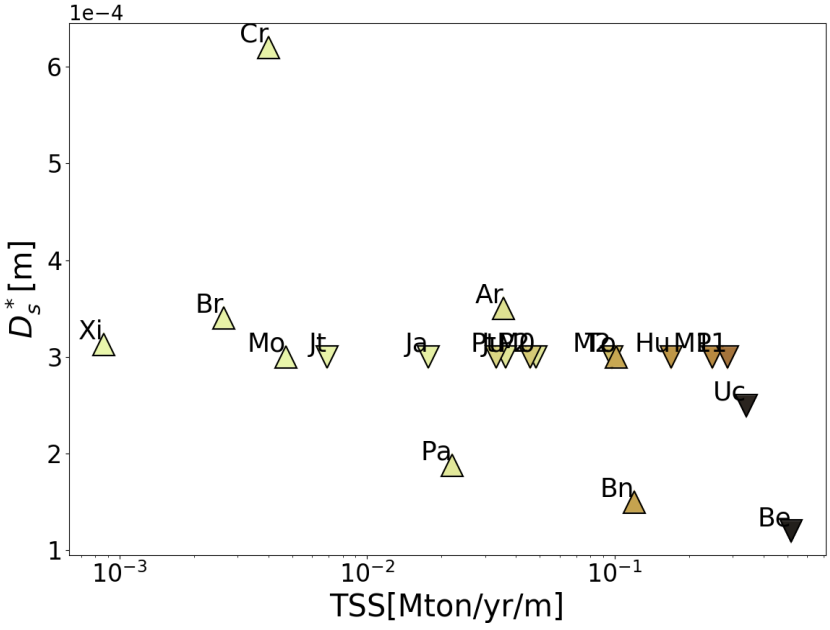

(b) Reference grain size

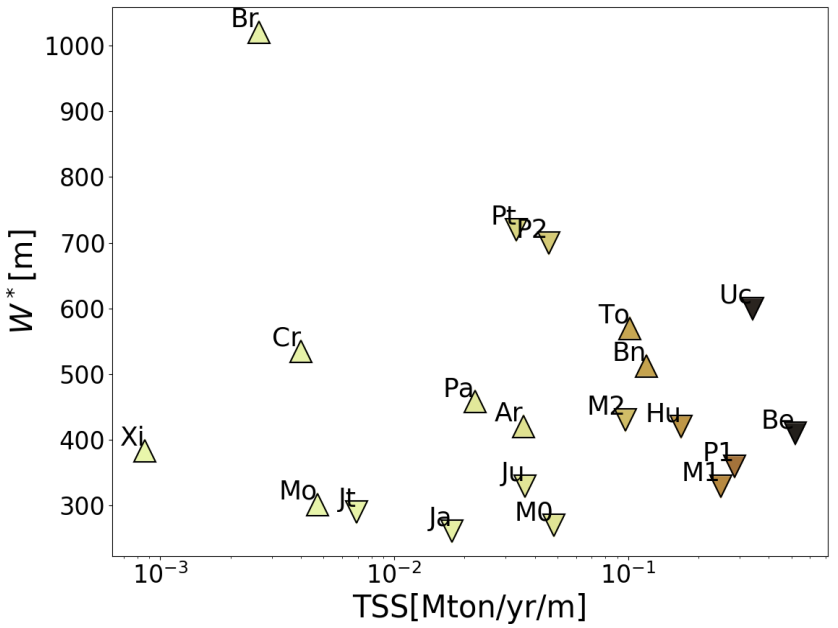

(c) Bankfull channel width

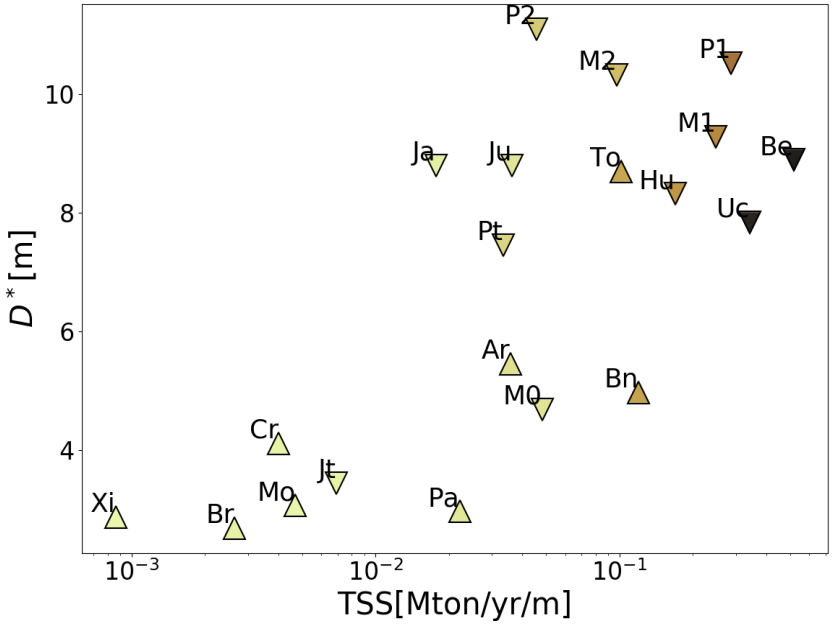

(d) Bankfull flow depth

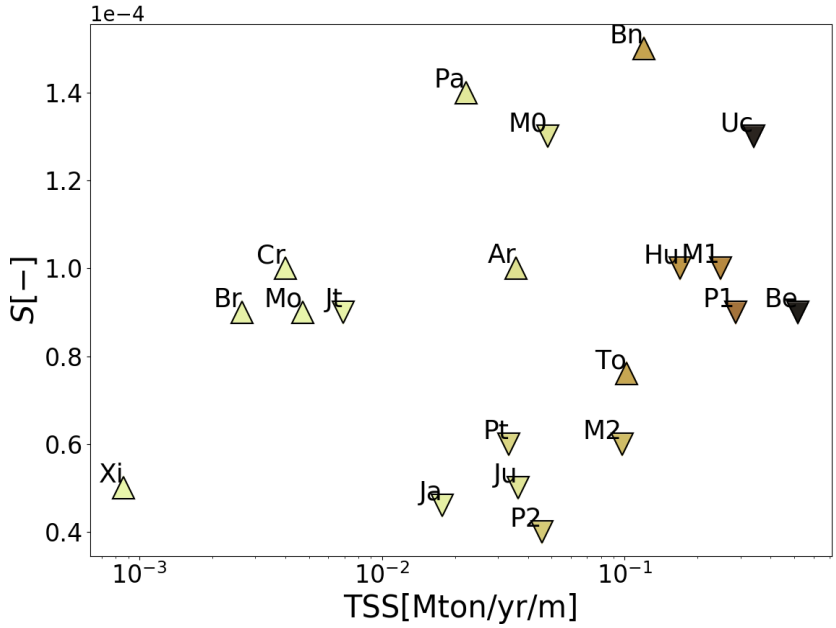

(e) Free surface slope

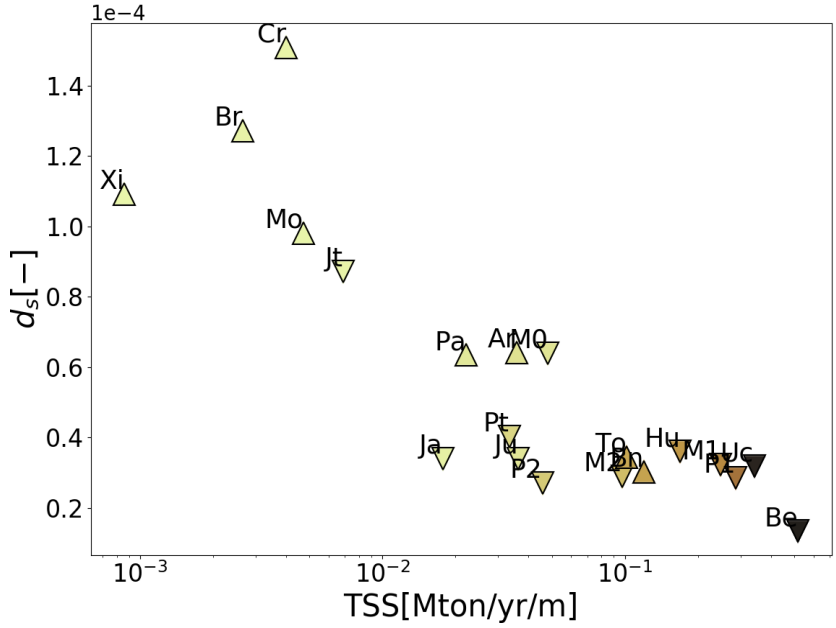

(f) Relative roughness

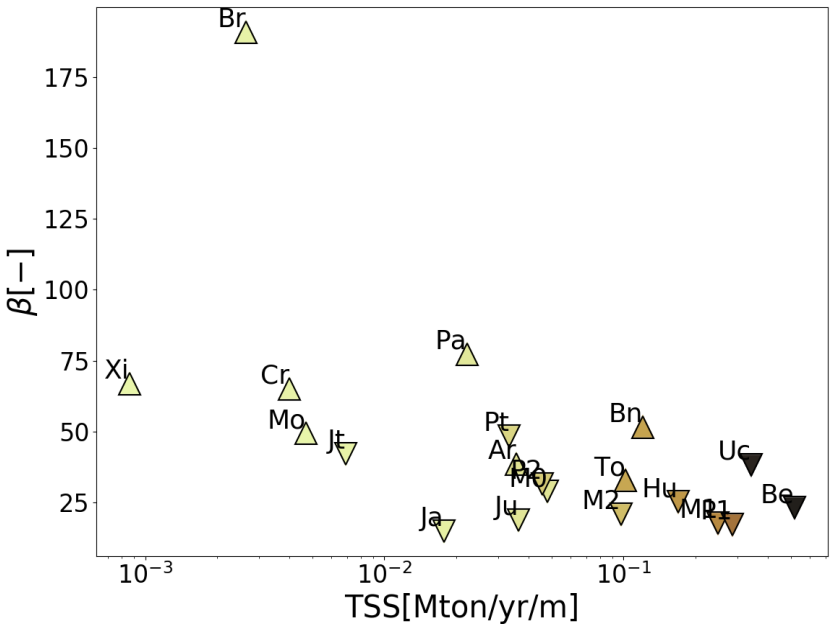

(g) Aspect ratio

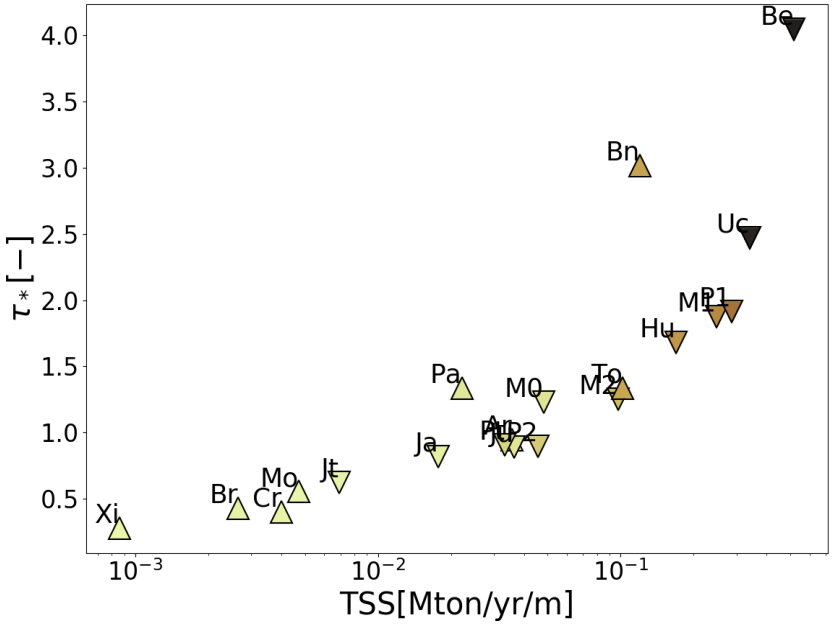

(h) Shields stress

Figure 6.2: Characteristic values of several hydraulic quantities of the analyzed reaches against the TSS per unit width. Upward facing triangles are associated with rivers displaying migrating bars, downward facing triangles with rivers displaying only steady bars.

Figure 6.2 shows the collected or estimated hydraulic quantities and parameters for the rivers analyzed in the present thesis. Some trends are clearly visible in 6.2, especially those regarding quantities that were derived through equations (60); however, some kind of trend can be seen in almost every scatter plot shown. Some scatter in inevitably present, due to a number of limitations including:

- I am dealing with very heterogeneous data;
- free surface slopes may be subjected to some backwater effect;
- sediment grain size measurements may be sensitive to the location of the gauging stations;
- gauging stations are not available on every reach analyzed, therefore some assumptions or averages are made;
- channel widths are subjected to a 30 meters pixels resolution.

However, the results are quite consistent. Grain sizes are homogeneous over the whole Amazonian region (except the Rio das Mortes for which I was not able to find any data and therefore I assumed the same bed material median size as the others), while bankfull normal depths are a growing function of TSS per unit width. Aspect ratios are quite large compared to those usually employed in analytical models and observed in small meandering rivers analyzed in most of the literature on meandering rivers. The Rio Branco (Br) has a huge half width-to-depth ratio due to its transitionality, which makes it something hardly definable as meandering, as most other reaches analyzed herein. In fact, many of the river reaches analyzed herein display migrating bars, anabranches, chutes and so on. Aerial images of some of the rivers are reported in figure 6.3

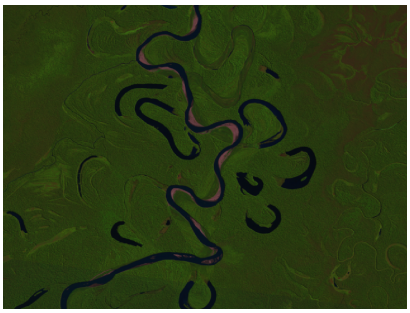

(a) Rio Beni, Bolivia (Be)

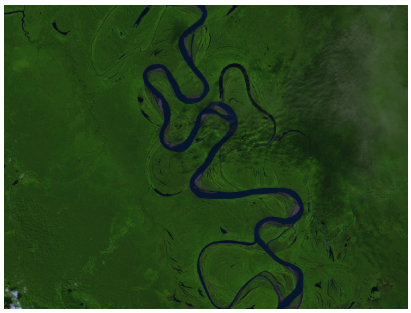

(b) Rio Ucayali, Perù (Uc)

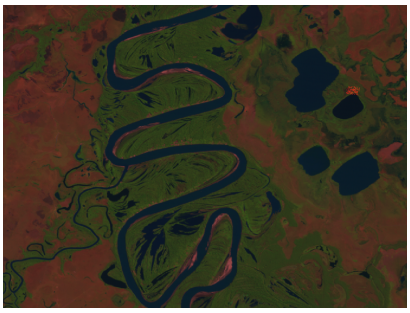

(c) Rio Mamorè, Bolivia (M1)

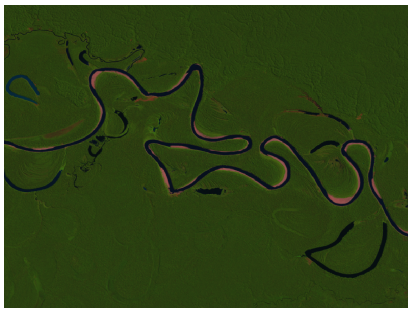

(d) Rio Purus, Brasil (P1)

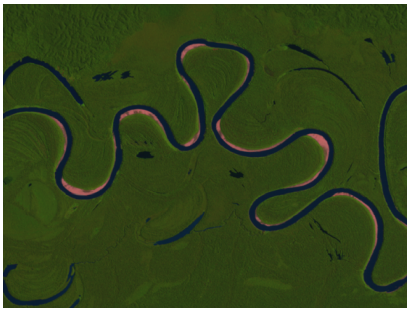

(e) Rio Jurua, Brasil (Ju)

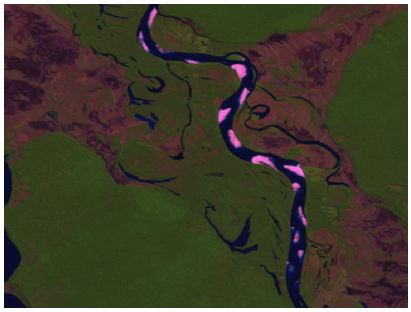

(f) Rio Xingu, Brasil (Xi)

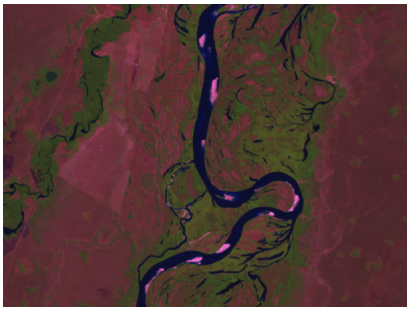

(g) Rio das Mortes, Brasil (Mo)

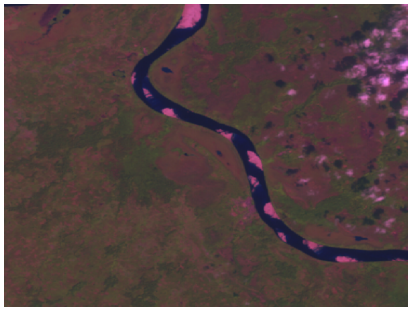

(h) Cross River, Africa (Cr)

Figure 6.3: Satellite false color images of some of the river reaches analyzed in the present chapter.

Another important quantity that is characterizes to meander morphodynamics is the meander wavenumber λ. Given a curvature signal, which is computed by PyRIS as the local derivative along the channel centerline of the centerline inflection angle, the difficulties in computing the wavenumber are mostly due to the non-periodicity of natural meandering rivers. Therefore, I employed a continuous wavelet transform (Torrence and Compo, 1995; Zolezzi, 2014) to compute the global wavelet power spectrum of the channel curvature. Such a spectrum typically peaks on some dominant value of the meander wavenumber, which can be taken as a reference one for the entire planform reach provided this is homogeneous in terms of spatial structure.

Figure 6.4 shows the wavelet analysis carried out on the planform centerlines of three river reaches analyzed within this chapter. For each subfigure (a,b and c) four panels are reported. The first panel shows the dimensionless centerline curvature computed along the centerline (i.e., in intrinsic coordinates). Panel b shows the river planform centerline, while panels c and d report the continuous wavelet transform and the global wavelet spectrum. The former is computed by means of a "DOG_2" mother wavelet (second derivative of a Gaussian), also known as the "Mexican Hat", which is a real-valued wavelet suitable for detecting peaks in the original signal (Torrence and Compo, 1995); the second derivative of its convolution over the curvature signal constitutes a scale representation of the second derivative of the curvature itself (Vermeulen et al., 2016). The subsequent application of the mother wavelet to the original signal by changing the wavelet frequency (herein the wavenumber is used to quantify the frequency) provides the Wavelet Power Spectrum (WPS), from which the Global Wavelet Spectrum (GWS) is obtained by averaging the WPS along the longitudinal coordinate s and multiplying it by the variance of the signal. The Cone Of Influence (COI), represented by the black continuous line in panel c and by the dashed orange line in panel d, isolates the significant areas (where the influence of the boundaries are negligible). The area outside the COI in panel c and the portion of the GWS smaller than the COI in panel d are not significant.

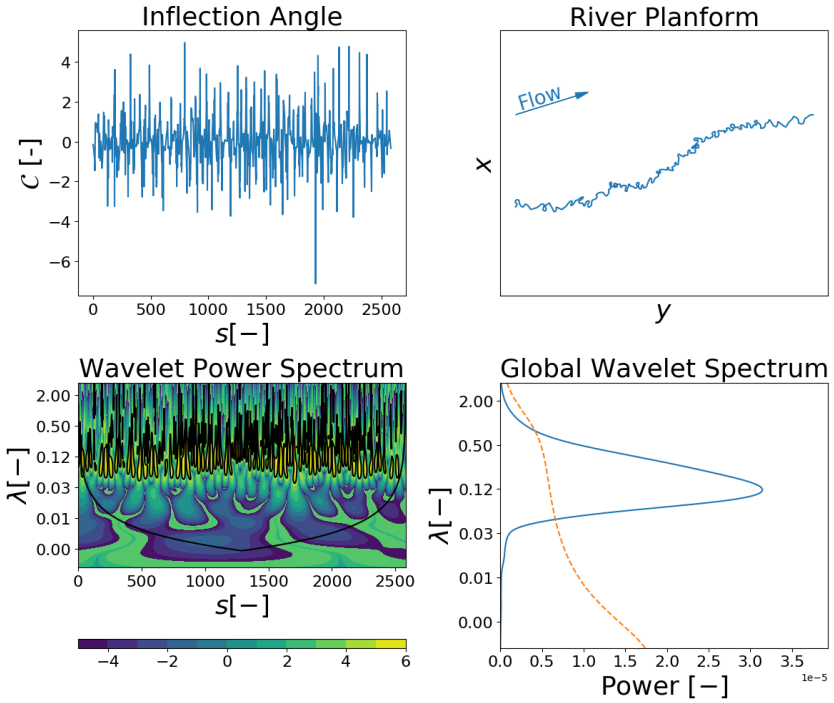

(a) Rio Beni, Bolivia (Be)

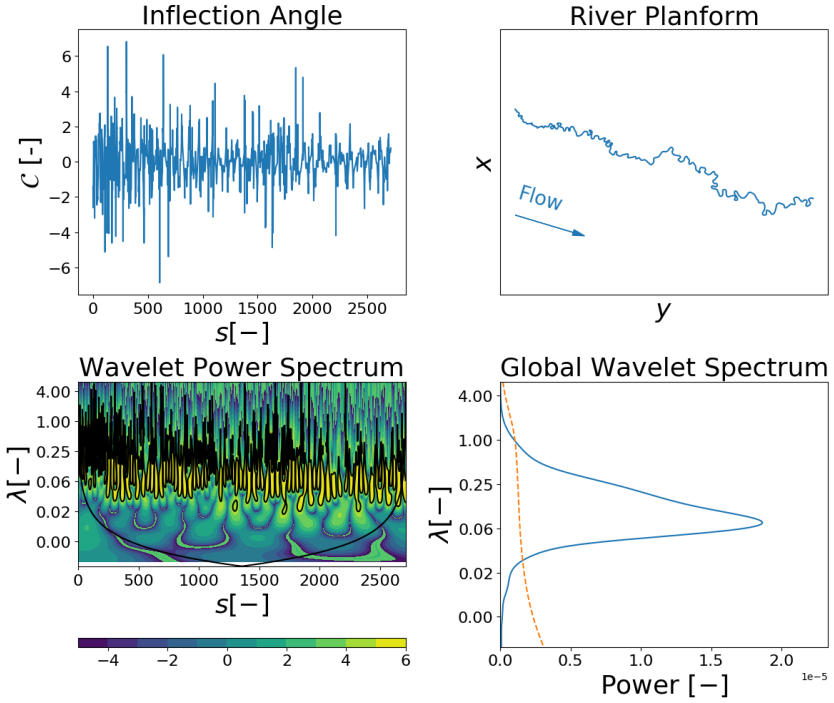

(b) Rio Ucayali, Perù (Uc)

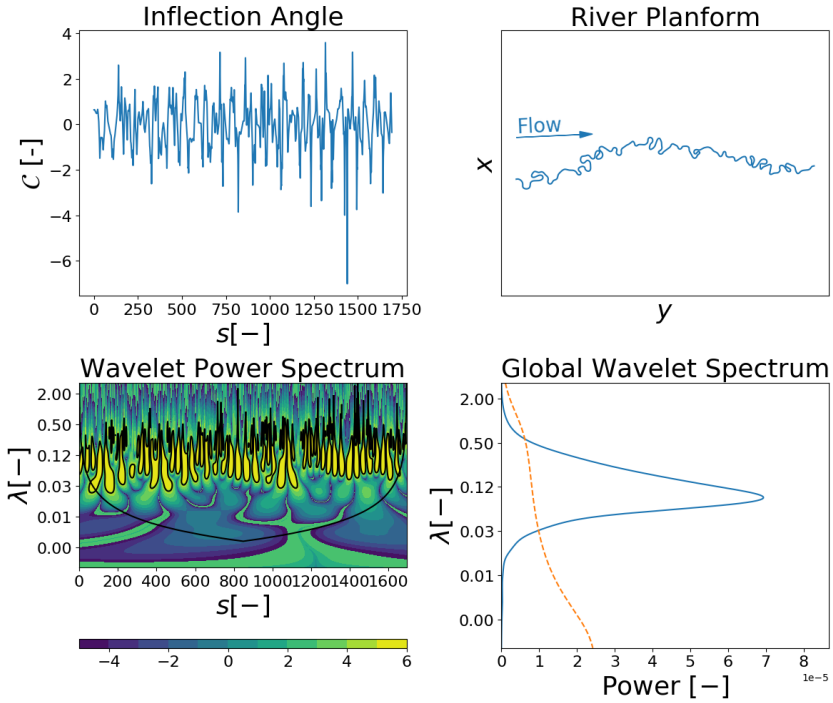

(c) Rio Mamorè, Bolivia (Mo)

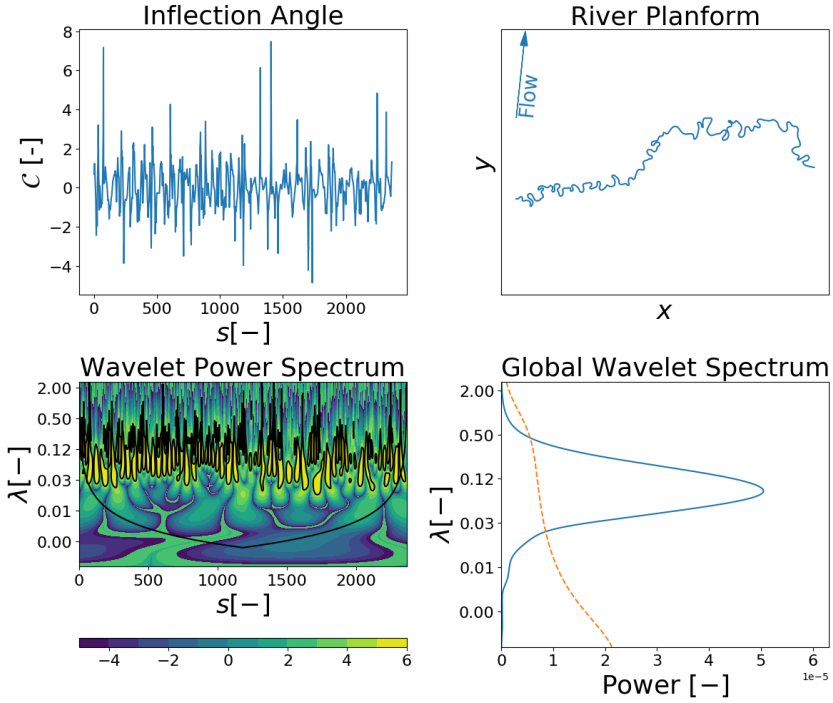

(d) Rio Javari, Brazil (Ja)

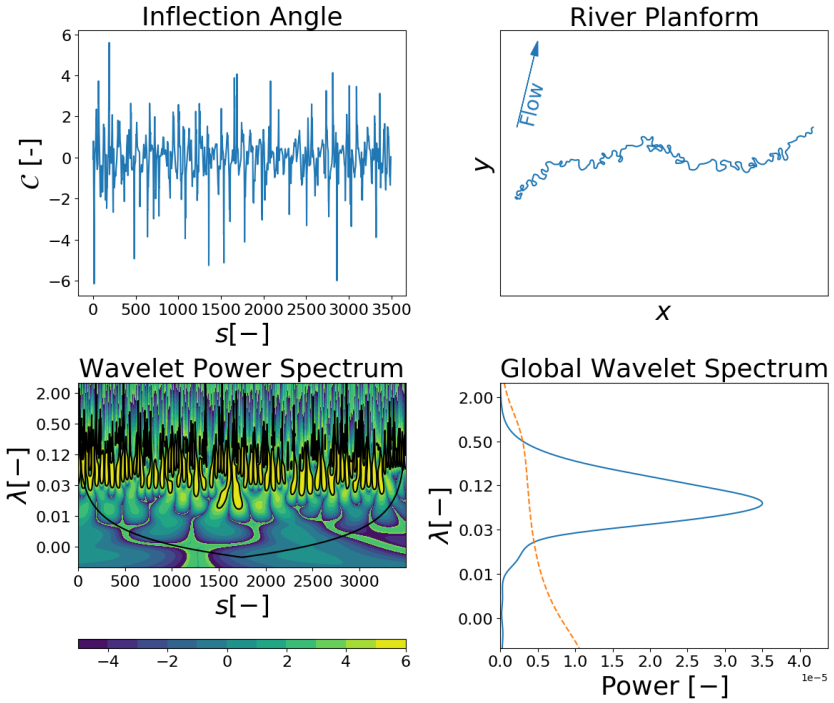

(e) Rio Purus, Brazil (P1)

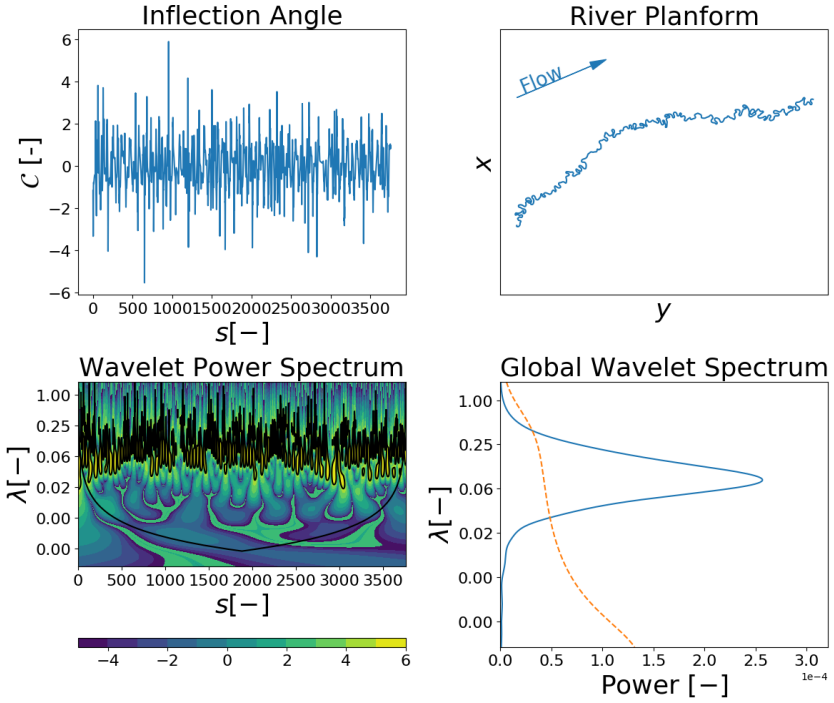

(f) Rio Jutai, Brazil (Jt)

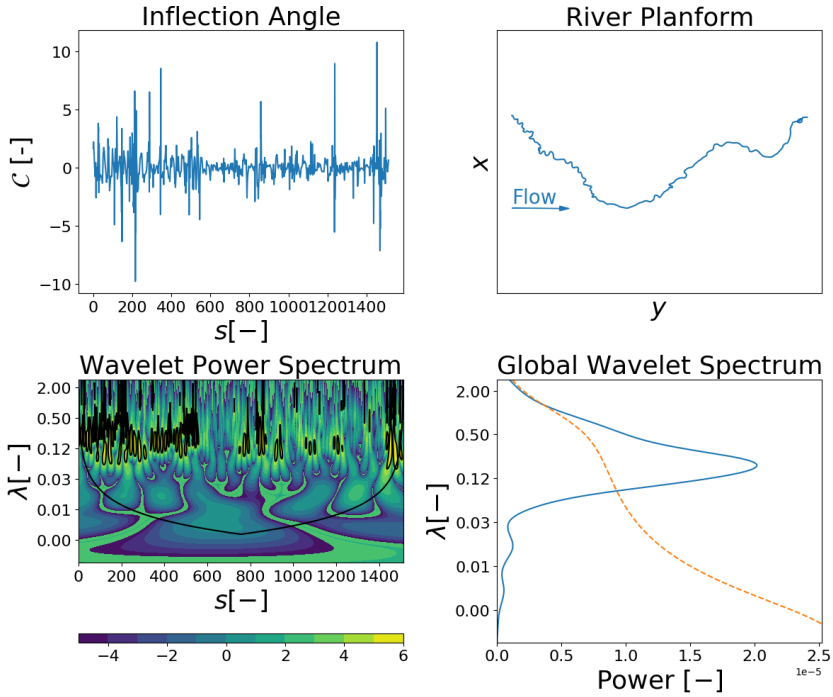

(g) Rio Xingu, Brazil (Xi)

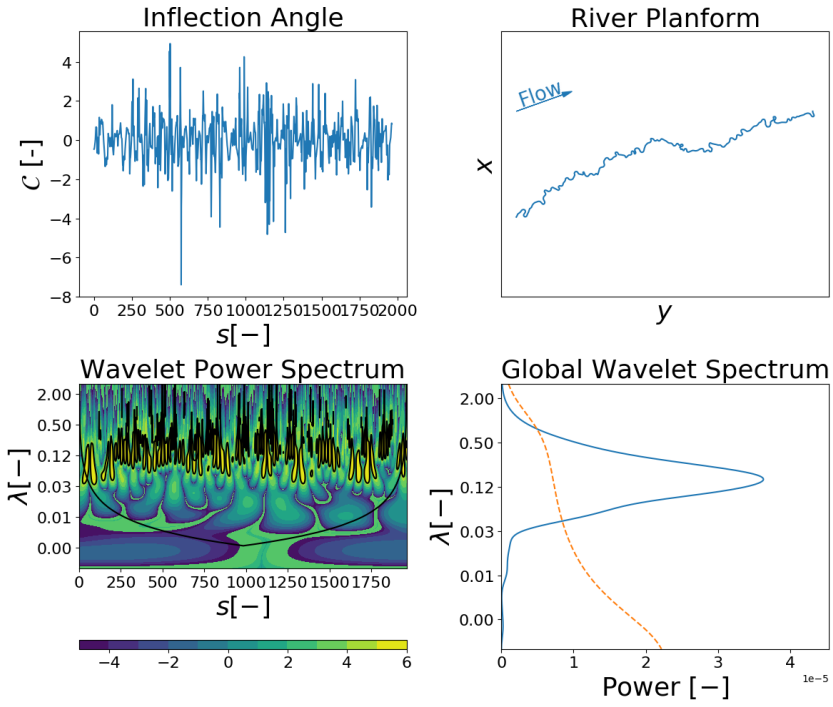

(h)

Figure 6.4: Wavelet analysis for some river reaches analyzed in this chapter.

The application of the wavelet analysis provides a dominant wavenumber for each river planform reach analyzed in the present chapter. Furthermore, reference value for the curvature ratio ν can be obtained from curvature series over multiple years observations by taking a statistical momentum of the absolute value of the channel curvature. The results are reported in figure 6.5, where the wavenumbers (panel a) and median curvature ratios (panel b) are plotted against the sediment supply per unit width TSS/W^*.

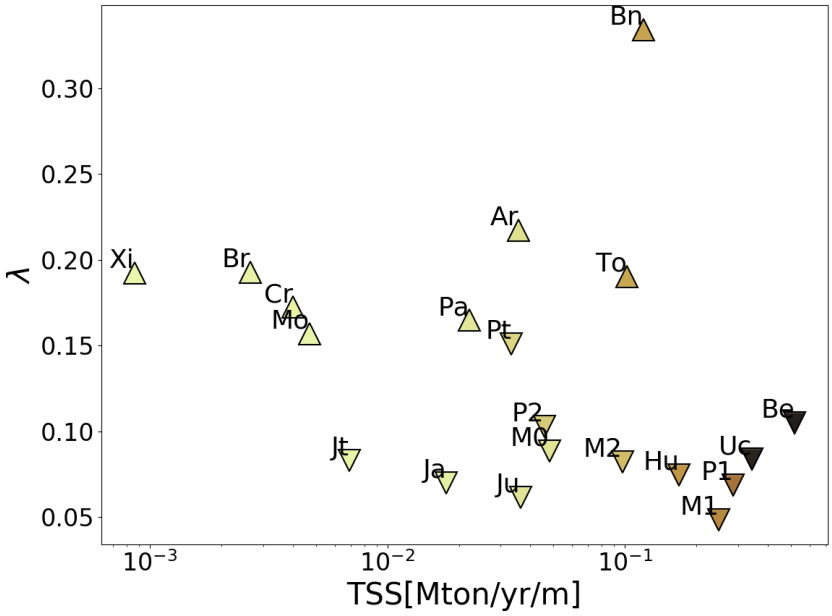

(a) Dominant wavenumber

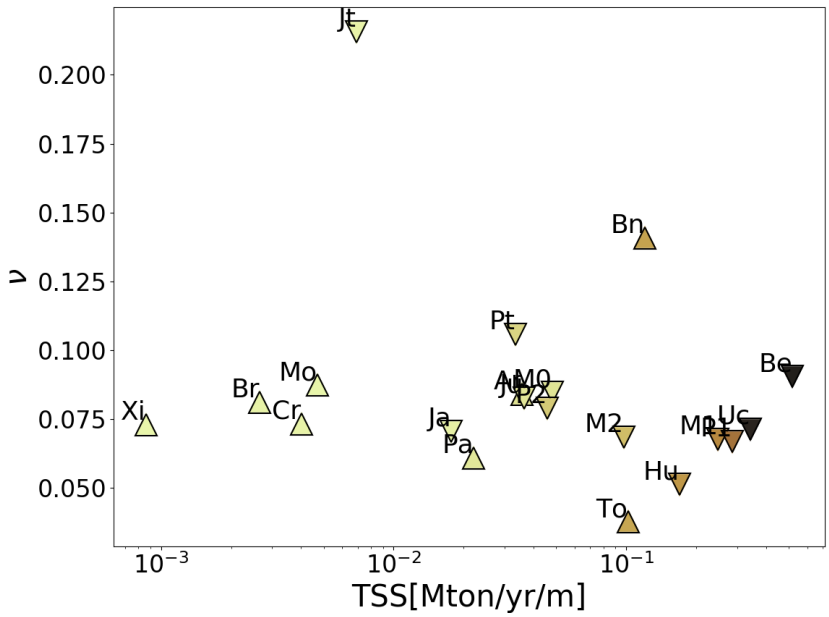

(b) Median curvature ratio

Figure 6.5: Dominant wavenumbers and median curvature ratios for each of the analyzed planform reaches against the Total Suspended Sediment per unit width. Upward facing triangles are associated with rivers displaying migrating bars, downward facing triangles with rivers displaying only steady bars.

Despite theoretical meander morphodynamic models are mostly based on the hypothesis of dominant bedload transport and they are based on simplified schemes, the characteristic wavenumbers estimated through the wavelet analysis on the planform centerlines are consistent with those predicted by the morphodynamic theories (Blondeaux and Seminara, 1985; Seminara and Tubino, 1992). According to the morphodynamic theories, meandering rivers select their wavenumbers mostly depending on the reference flow conditions; the latter are defined by the three dimensionless parameters β, τ_* and d_s. An example of selected wavenumbers (corresponding to the conditoins of maximum meander amplification) is reported in figure 9.7 in chapter 9. Figure 6.5a shows a slightly, scattering decreasing trend of meander wavenumbers with increasing TSS. Furthermore, rivers exhibiting migrating bars (upward-facing triangular markers) display higher wavenumbers, on average, with respect to rivers with steady bars (downward-facing triangular markers). This latter fact is further investigated in chapter 10, where I investigate the mechanisms controlling the migration of bars in meanders.

The curvature ratios are also consistent with those reported by Zolezzi et al., 2012b based on the dataset of Lagasse et al., 2004, that are shown in figure 6.6.

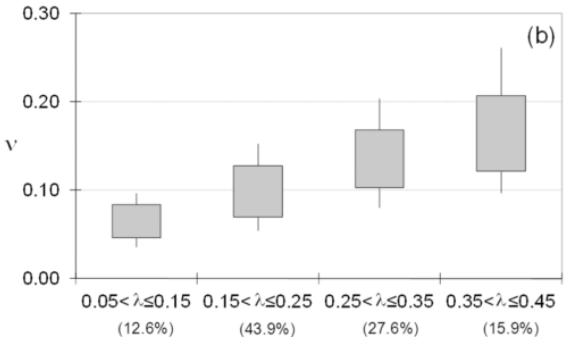

Figure 6.6: Distribution of curvatures and wavenumbers in the dataset provided by Lagasse et al., 2004. Figure reprinted from Zolezzi et al., 2012b.

It is of particular relevance that the fact that median curvature ratios do not significantly vary between the analyzed reaches (except individual cases) despite the difference in river patterns, ranging from meandering, to transitional with migrating bars, to transitional with width variations, chutes and islands. This fact is also further investigated in chapter 10; it is commonly thought that migrating bars may develop in meandering rivers if the channel curvature is low: however, figure 6.5b shows that between rivers exhibiting migrating bars and those only displaying point bars no significant difference occurs.

6.2 BEND-SCALE ANALYSIS OF REMOTELY SENSED BANKFULL CHANNEL WIDTHS

In this section I investigate the temporal evolution of bankfull channel width in meandering rivers through multitemporal remotely sensed data. The data is taken from the Landsat archive (landsat.usgs.gov) which provides multispectral information spanning roughly the last 40 years with a spatial resolution of 30m and a temporal resolution of a couple of weeks. The analysis of the Landsat imagery is performed through the software PyRIS (chapter 4), which allows for the fully automated extraction of meandering river planforms from sets of temporally subsequent Landsat images. Sequences of satellite data retrieved over variable time periods (roughly between 1984 and 2015,

depending on the availability and quality of data) were used, typically one image every one or two years when available. I analyzed four large natural meandering rivers from the Amazon basin, particularly the Rio Beni (Bolivia), the Rio Mamorè (Bolivia), the Rio Huallaga (Perù) and the Rio Ucayali (Perù). The choice of these rivers is driven mainly by their size and by the information I have about their degree of planform change. The size is of fundamental importance since the resolution of freely available satellite imagery, such as Landsat images, poses a restriction to a 30m pixel resolution. Therefore the confidence interval is acceptable, to some degree, only for rivers whose width is larger than 400m (15% confidence interval with respect to the correct segmentation of borderline pixels). Also, I restricted our attention to river reaches that are homogeneous, to some degree, in terms of their floodplain cover and water discharge.

PyRIS is able to define the local bankfull channel width by performing a binary cross-segmentation of vegetation, sediment and water indexes from the multispectral datasets: banklines are located at the interface between vegetation and water or bare sediment, being the latter included within the channel body. A bend-scale analysis has been performed, i.e. each individual meander bend has been separated and its planform evolution has been tracked through time, for every river reach of the analyzed dataset.

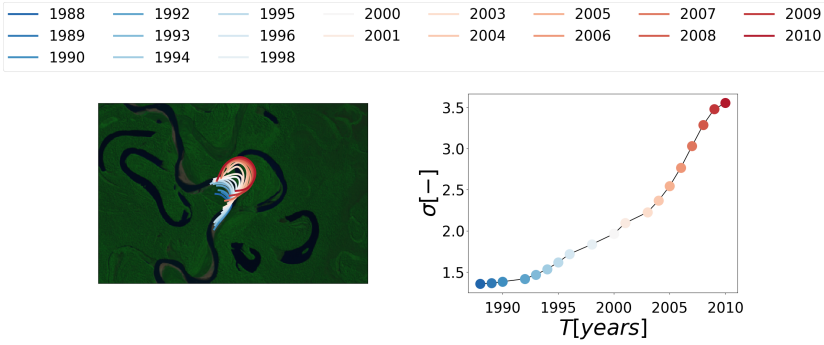

Figure 6.7: Planform development of an individual meander bend of the Rio Beni (Bolivian Amazon). (*a*) Planform development of the channel centerline. (*b*) Evolution of bend sinuosity.

The sinuosity of an individual meander bend is defined as the ratio between the intrinsic bend length, measured along the channel axis, L^* and the Cartesian distance between its endpoints Λ^* as

$$\sigma = \frac{L^*}{\Lambda^*}. \tag{62}$$

Typically an evolving meander bend increases its sinuosity during the planform development from incipient formation to cutoff. The software divides each river planform into individual meander bends, and each meander bend is associated with a sinuosity σ as defined by equation 62. Hence, I use the bend sinuosity as a proxy of time, in such a way that I can compare individual meander bends at different evolutionary stages and analyze statistically how the bend-scale bankfull channel width changes with bend sinuosity (age). Figure 6.7 illustrates an example of an evolving individual meander bend increasing its sinuosity over time. Meander bends at incipient formation have typically a low sinuosity ($\sigma \simeq 1$), while the planform development increases the bend intrinsic length L^* with a rather stable Cartesian length Λ^*, resulting in a progressive increase of the bend sinuosity σ.

Figure 6.8 provides a visual example of evolution of bankfull channel width of an individual meander bend of the River Beni between 1987 and 2000. Panel 6.8a illustrates the planform evolution of the meander bend. Panel 6.8b reports the evolution of the individual bend sinuosity and width during the planform development of the bend itself, in which the time is denoted by the colors of the markers. The sinuosity σ increases from the value of 1.5 to a value of 4 between 1987 and 2000. The individual meander bend reported in the figure shows a sharp 14% decrease of the bankfull channel width in the initial stage, followed by a slight increase and by a stabilization of the width around 89% of the initial value.

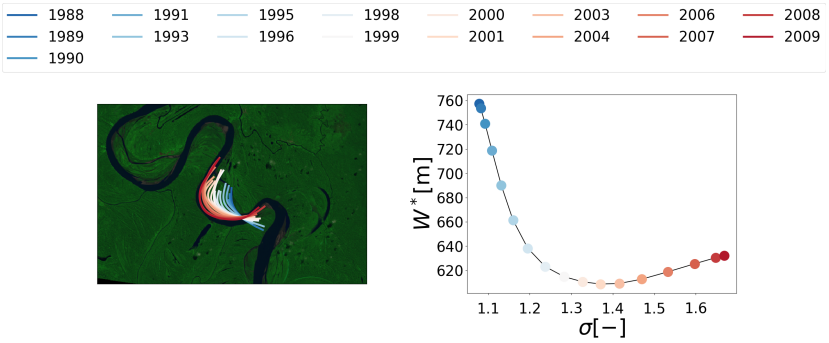

Figure 6.8: Evolution of an individual meander bend of the River Ucayali between 1987 and 2009. (*a*) Planform development. (*b*) Evolution of the bend sinuosity σ and of the average channel width W^*.

Hence, by plotting bankfull channel widths against the sinuosity for individual meander bends I provide a dynamic representation of the spatio-temporal evolution of the bend-scale bankfull channel widths. The sinuosity intervals were chosen considering that relatively low values of bend sinuosity are more frequent than large values in real-

world meandering rivers (see figure 6.9) although covering an acceptable range of sinuosity classes.

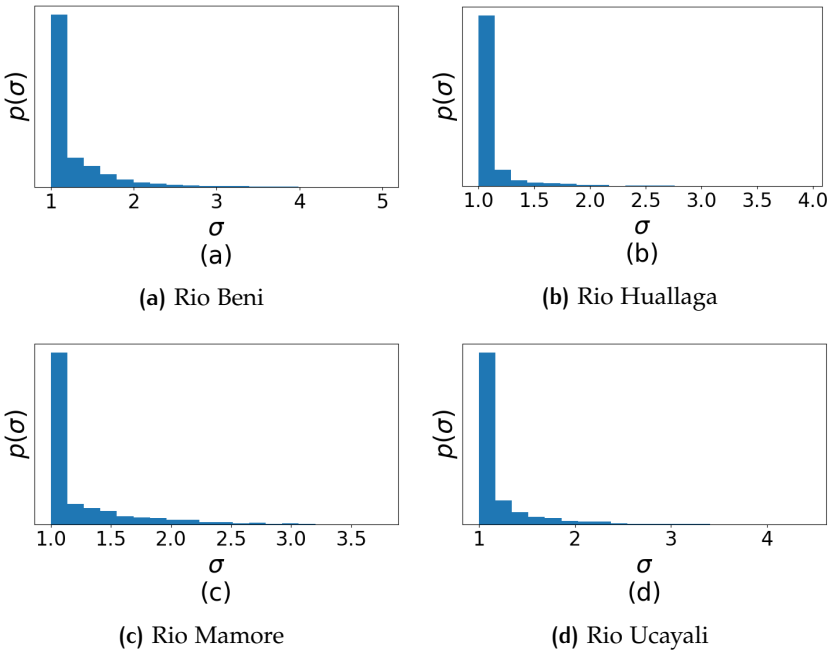

(a) Rio Beni

(b) Rio Huallaga

(c) Rio Mamore

(d) Rio Ucayali

Figure 6.9: Distribution of bend sinuosity along the four reaches investigated.

Boxplots in Figure 6.10 illustrate the bend-scale, spatio-temporal trends of bankfull channel width against bend sinuosity for several bends of each of the four analyzed reaches across two-three decades of planform development.

Although Figure 6.10 shows a certain degree of oscillation in the data, a slight decrease in bend-scale bankfull channel width for increasing sinuosity can be observed. If I restrict our attention to the range between 25% and 75% percentiles, and especially on the medians, it appears that the bankfull width of natural meander bends is subjected to some degree of oscillation during planform development (increasing bend sinuosity) and, eventually, to a decrease.

The Mamorè River (Panel 6.10b), for example, has a fairly constant width regardless of the bend sinuosity, while the Rio Huallaga (Panel 6.10c) shows a more relevant decrease of its widths. I also cross-checked that: (i) trends hold when changing the sinuosity intervals, and (ii) that no significant reduction of the reach-averaged channel width occurs in time due to embankments, deforestation or building fo dams. Figure 6.11 shows the change of channel width with sinuosity for all the four rivers.

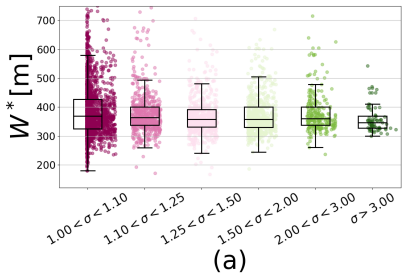

(a) Rio Beni (Bolivia), 1987–2011. Scene identifiers for the Landsat data used are: 001069, 001070.

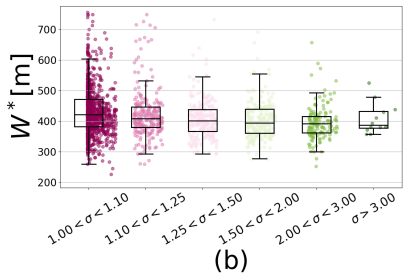

(b) Rio Mamorè (Bolivia), 1989–2011. Scene identifiers for the Landsat data used are: 233069, 233070.

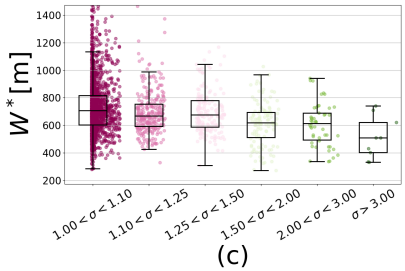

(c) Rio Huallaga (Peru), 1988–2005. Scene identifiers for the Landsat data used are: 007064, 007065.

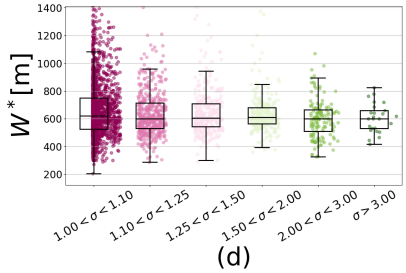

(d) Rio Ucayali (Peru), 1989–2010. Scene identifiers for the Landsat data used are: 006065, 006066, 006067.

Figure 6.10: Boxplots of the bankfull channel width for individual meander bends against bend sinuosity of four large meandering rivers of the Amazon basin. The scatter represents the widths of the individual meander bends analyzed (sinuosities have been rescaled for the sake of clarity).

All the rivers exhibit a slight decrease in channel width with increasing sinuosity with respect to their initial value; the amplitude of the 25%-75% range of percentiles is larger for larger median channel widths. The most significant drop in channel width is observed in the Rio Huallaga, which exhibits a 20% reduction. Hence, the variation of bankfull channel width seems to depend on some characteristic of the river; the planfom cover is quite uniform for all the analyzed reaches, although the Mamorè river is (partially) laterally constrained. The rate of change of the bankfull channel width in evolving meandering rivers is further investigated through the analytical approach in chapter 7.

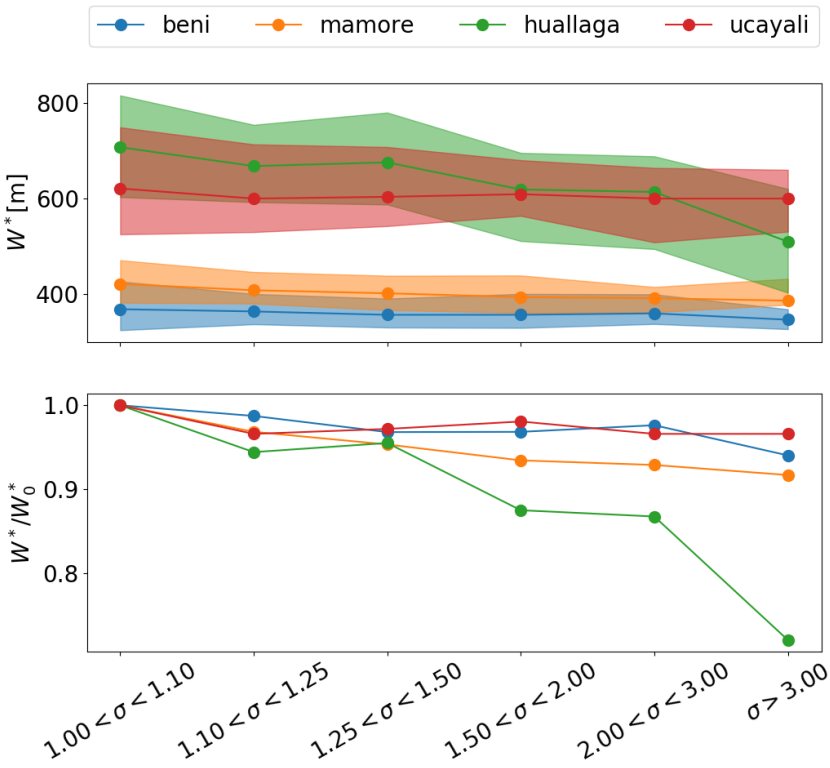

Figure 6.11: Evolution of the bankfull channel width for the four analyzed rivers. The first plot shows the evolution of the median (line with point markers) and of the 25% and 75% percentiles (shaded area). The second plot compares the evolution of the channel widths by normalizing them with respect to the "initial" median width W_0^* at $1 \leqslant \sigma < 1.1$.

6.3 BEND-SCALE ANALYSIS OF PLANFORM DESCRIPTORS

In this section I reconstruct the bend-scale evolutionary dynamics of planform descriptors of some of the Amazonian meandering river reaches presented in the previous section of this chapter. The same approach employed in the analysis of bankfull widths is employed; the river planform is divided into individual meander bends according to the PyRIS algorithm presented in section 4.2 and each bend is assigned a value for any of the variables considered: the bend wavenumber λ, the curvature ratio ν, the amplitude δ of width oscillations and the position of the largest cross-section of a meander bend, respectively. Figures 6.12, 6.13, 6.14, 6.15, 6.16, 6.17, 6.18, 6.19, 6.20, 6.21 and 6.22

illustrate such evolutionary dynamics for a number river reaches (respectively the Rio Beni, Rio Ucayali, Rio Mamore, Rio Huallaga, Rio Jurua, Rio Jutai, Rio Purus, Rio Putumayo, Rio Araguaia, Rio Xingu, Rio das Mortes). The first four rivers (Rio Beni, Rio Ucayali, Rio Mamore, Rio Huallaga) have a very high sediment load, hence their bends are significantly changing during the 30 years observation period. The following four (Rio Jurua, Rio Jutai, Rio Purus, Rio Putumayo) have lower sediment load and hence the inter-annual variability of planform structures is much lower, resulting in less significant statistics. The last three rivers (Rio Araguaia, Rio Xingu, Rio das Mortes) have a very small sediment load and therefore result in almost no planform change over the years. Hence, the statistics are the least significant since the individual bend values over multiple years are almost overlapping.

The scatter points were rescaled in terms of sinuosity σ for the sake of clarity. The polar plots report the position of the width maxima along the bends; the distance of the scatter points from the middle represents the associated bend sinuosities.

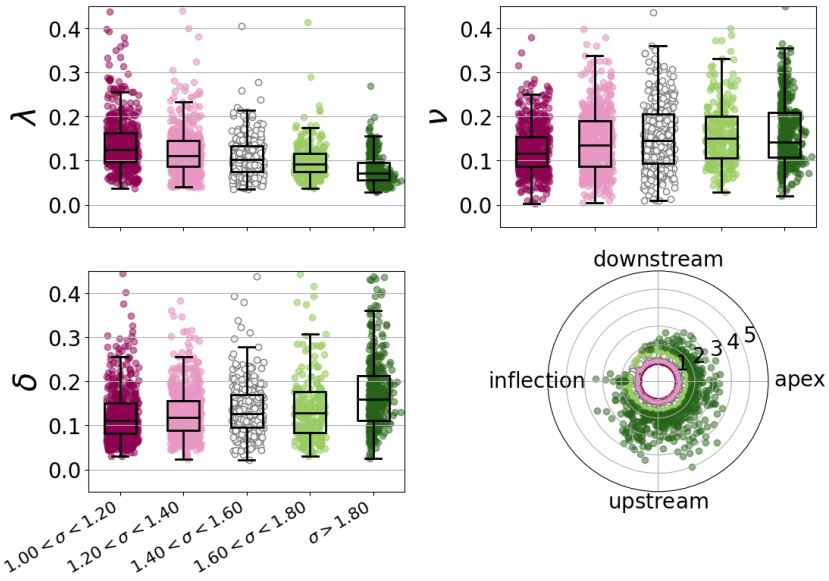

Figure 6.12: Bend scale evolutionary dynamics of planform perturbations for the Rio Beni (Bolivia).

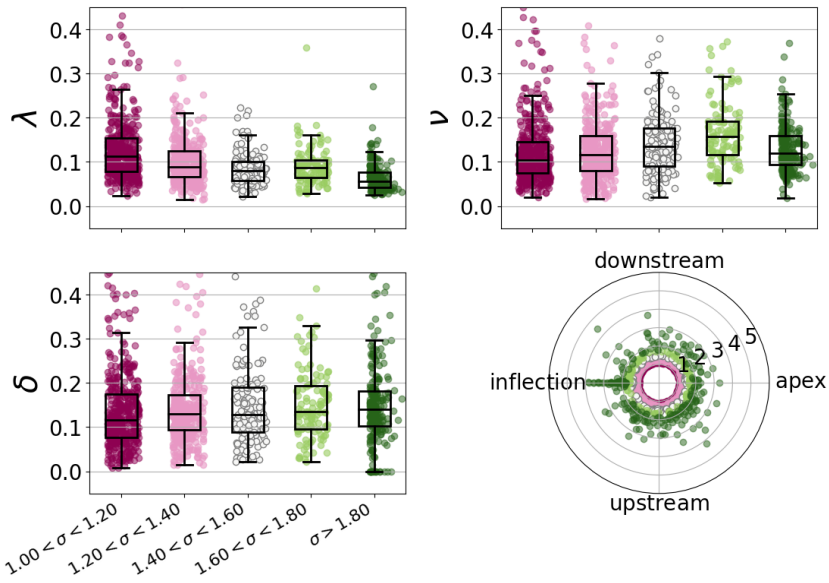

Figure 6.13: Bend scale evolutionary dynamics of planform perturbations for the Rio Ucayali (Perù).

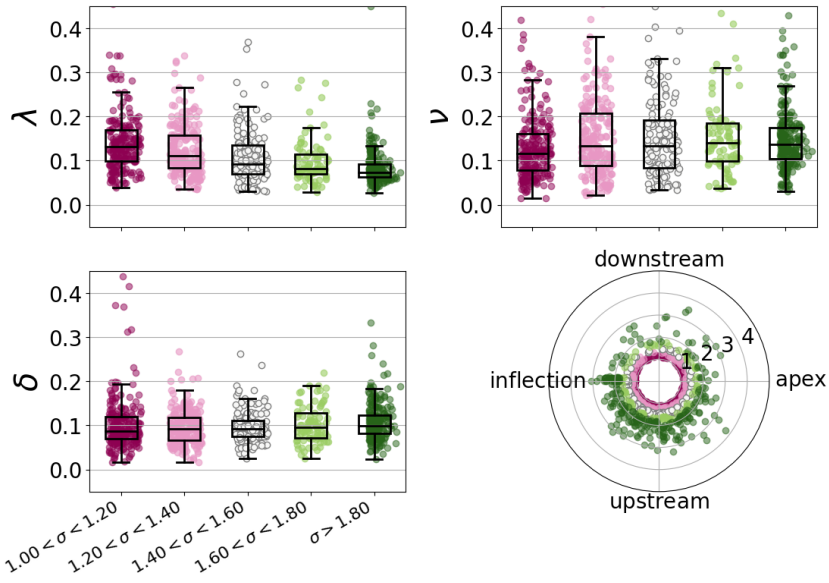

Figure 6.14: Bend scale evolutionary dynamics of planform perturbations for the Rio Mamore (Bolivia).

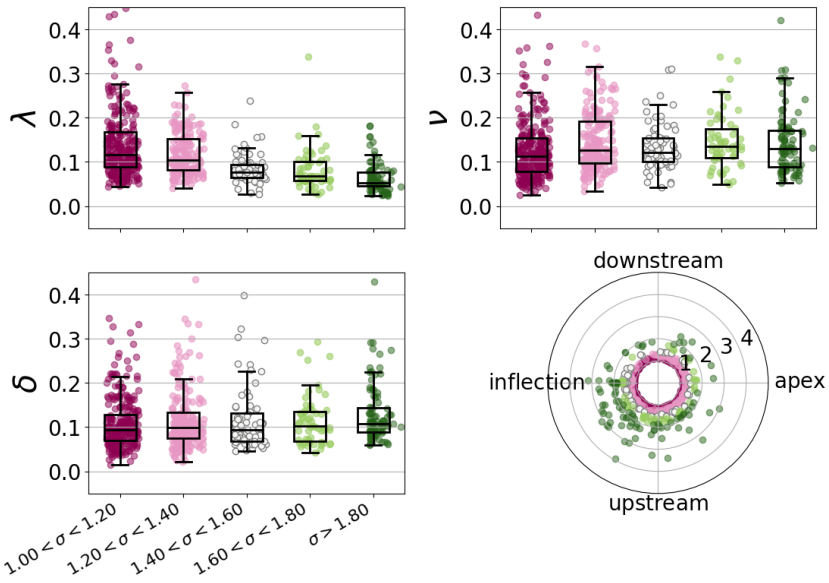

Figure 6.15: Bend scale evolutionary dynamics of planform perturbations for the Rio Huallaga (Perù).

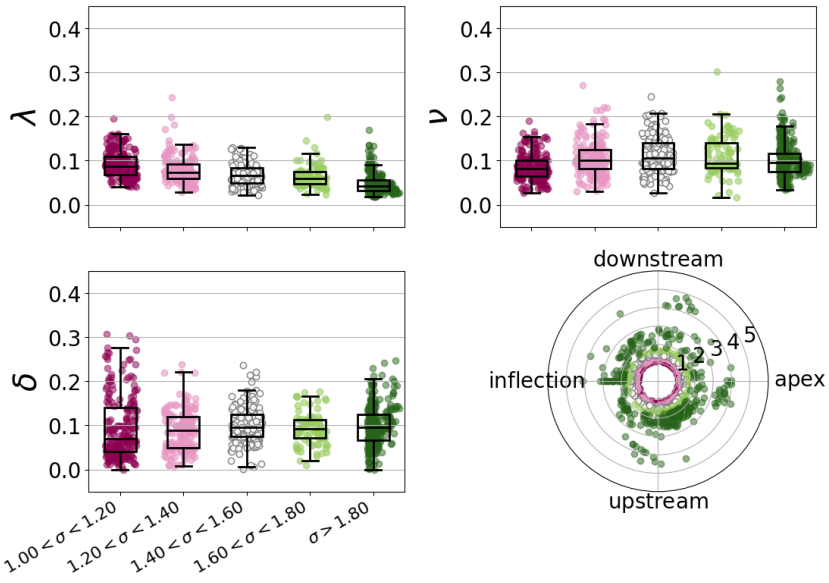

Figure 6.16: Bend scale evolutionary dynamics of planform perturbations for the Rio Jurua (Brazil).

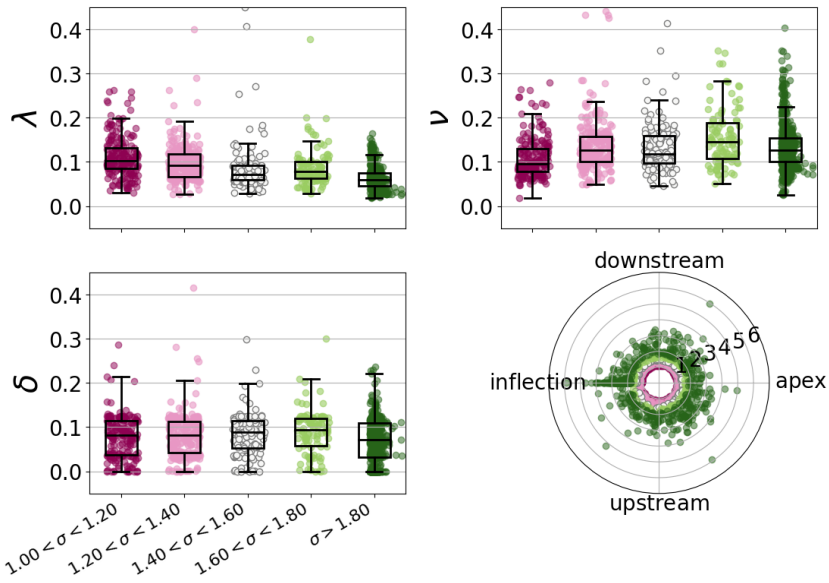

Figure 6.17: Bend scale evolutionary dynamics of planform perturbations for the Rio Jutai (Brazil).

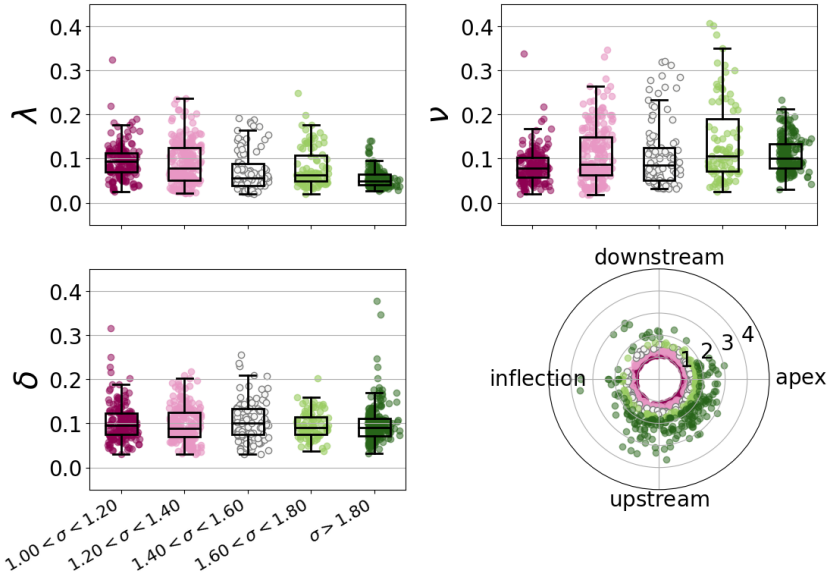

Figure 6.18: Bend scale evolutionary dynamics of planform perturbations for the Rio Purus (Brazil).

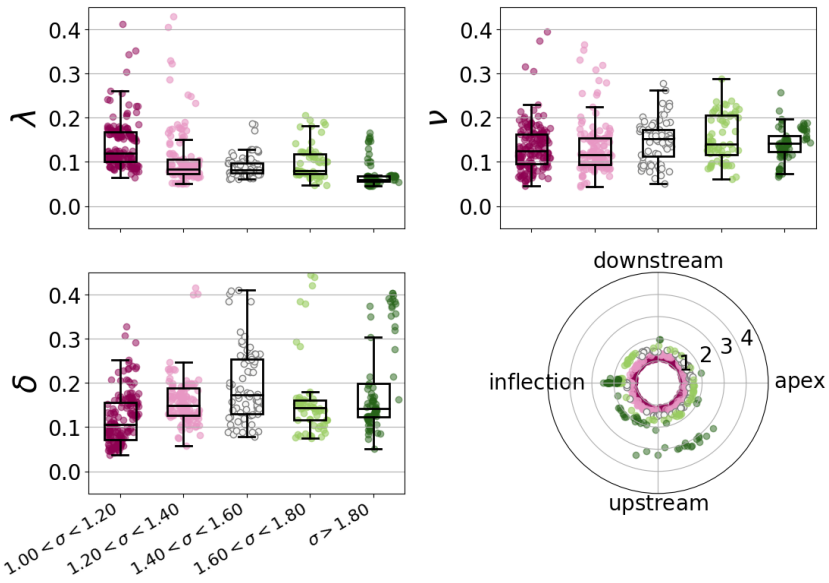

Figure 6.19: Bend scale evolutionary dynamics of planform perturbations for the Rio Putumayo (Brazil).

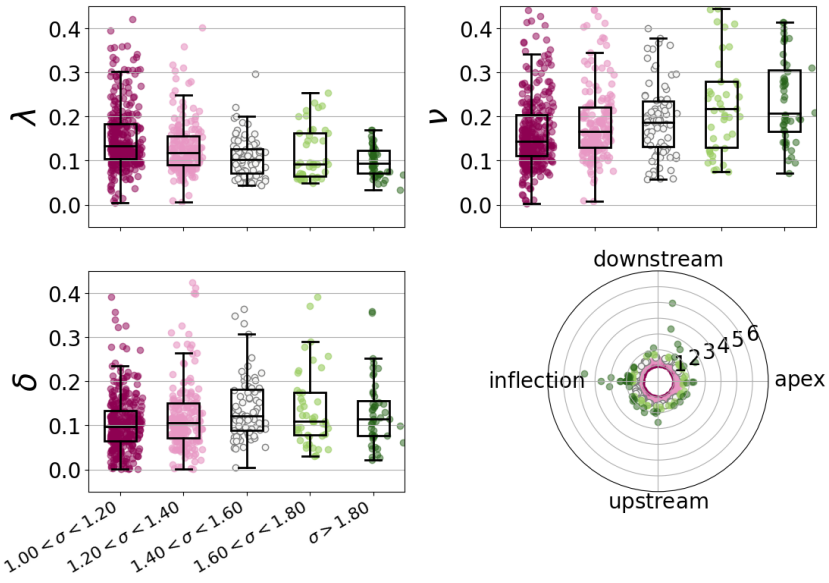

Figure 6.20: Bend scale evolutionary dynamics of planform perturbations for the Rio Araguaia (Brazil).

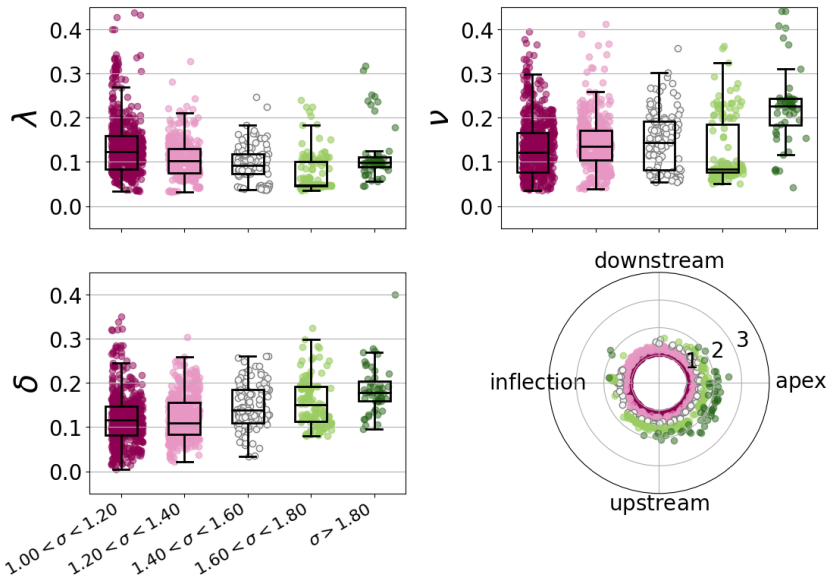

Figure 6.21: Bend scale evolutionary dynamics of planform perturbations for the Rio Xingu (Brazil).

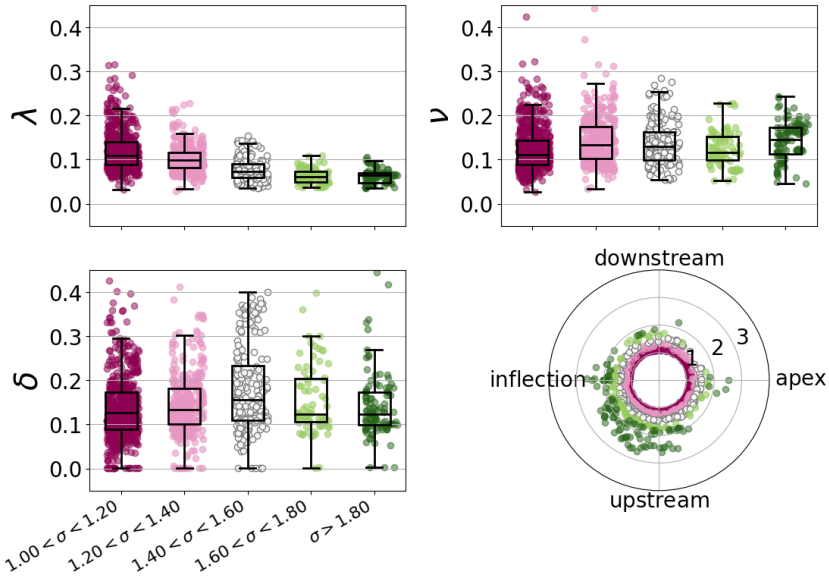

Figure 6.22: Bend scale evolutionary dynamics of planform perturbations for the Rio das Mortes (Brazil).

The planform descriptors follow some general trends. The intrinsic meander wavenumber obviously decreases in time (with increasing

sinuosity); this is quite obvious since the sinuosity is the ratio between the Cartesian wavenumber and the intrinsic wavenumber, hence a hyperbolic trend is expected (the Cartesian wavelength does not change significantly during the planform development). However, the fact that this result provides some support to the employed approach.

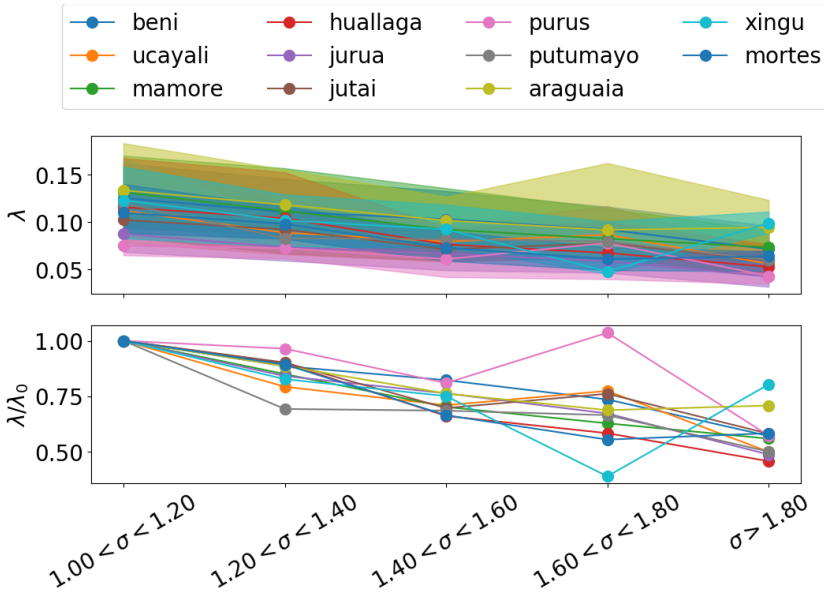

Figure 6.23: Bend-scale evolution of meander wavenumbers. The first plot shows the evolution of the median (line) and of the 25% and 75% percentiles (shaded area). The second plot compares the evolution of meander wavenumbers normalized by their median value λ_0 at $1 \leqslant \sigma < 1.2$.

The curvature ratio ν (computed as the median of the absolute value of the curvature distribution of the individual meander bend) has a peak behavior; small values of ν are observed at low sinuosity. They increase with increasing sinuosities up to a peak that is reaches typically when the sinuosity is between 1.6 and 1.8, then a decreasing trend occurs. The channel width oscillations are more complex. The amplitude sometimes display a trend similar to that of the curvature, while in other cases more complex behaviors are observed. The positions of width maxima are computed with respect to the mid-point of the bend, mid-way between two consecutive inflection points, in accordance to the theoretical models (that generally relate to an equivalent sine-generated meander bend, whose bend apex lies in the middle). At low sinuosities the positions of width maxima are well distributed over the entire range, including inflection points and bend apexes;

however, during the planform development they mostly shift towards the upstream or downstream side of the meander bend. Very few bends exhibit width maxima at the bend apex when the sinuosity becomes significant.

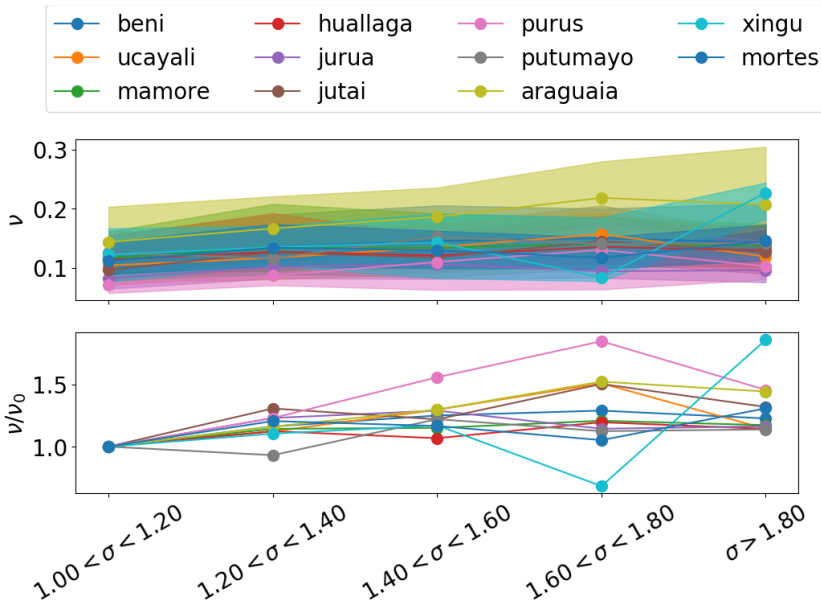

Figure 6.24: Bend-scale evolution of channel curvature ratio. The first plot shows the evolution of the median (line) and of the 25% and 75% percentiles (shaded area). The second plot compares the evolution of curvature ratios normalized by their median value ν_0 at $1 \leqslant \sigma < 1.2$.

Figures 6.23, 6.24 and 6.25 compare the trends for different river reaches. The evolution of meander wavenumbers is consistent for all the reaches investigated: a marked decrease is observed and the 25%-75% range follows the decrease accordingly. The channel curvature has a more scattering behavior and its tenporal variation is weak; however, a marked peak is observed in the range $1.6 \leqslant \sigma < 1.8$ for most of the reaches. This fact is investigated through the analytica model and discussed in section 8.2. Finally, the amplitude δ of width oscillations is probably the most scattering one; however, a clear peak occurs, for most of the investigated reaches, in the range $1.4 \leqslant \sigma < 1.6$, slightly before than the curvature peak. This fact is investigated through the analytical model in chapters 8 and 9.

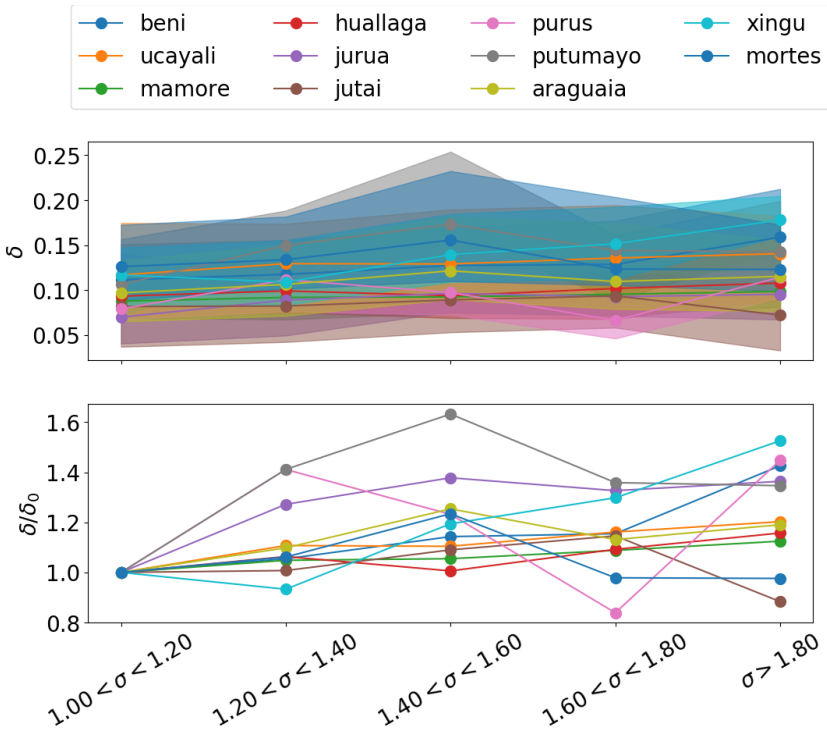

Figure 6.25: Bend-scale evolution of the amplitude of width oscillations. The first plot shows the evolution of the median (line) and of the 25% and 75% percentiles (shaded area). The second plot compares the evolution of width oscillation amplitudes normalized by their median value δ_0 at $1 \leqslant \sigma < 1.2$.

Furthermore, the values of δ are consistent with those observed by Zolezzi et al., 2012b based on the dataset of Lagasse et al., 2004 and reported in figure 6.26. Higher values are observed in some of the river reaches analyzed in the rpesent thesis with respect to those investigated by Zolezzi et al., 2012b; however, it should be taken into account that the rivers analyzed herein are mostly suspended load-dominated, while the dataset of Lagasse et al., 2004 referes to bedload-dominated river reaches. Moreover, the pixel resolution of Landsat data used herein introduces a relative error which is particularly significant when computing width oscillations.

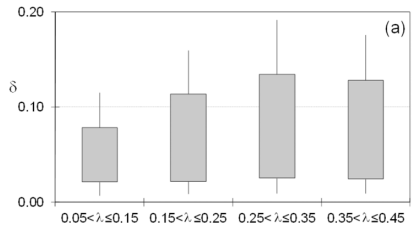

Figure 6.26: Distribution of width oscillation amplitudes and wavenumbers in the dataset provided by Lagasse et al., 2004. Figure reprinted from Zolezzi et al., 2012b.

6.4 SCALES AND DYNAMICS OF MIGRATING BARS ALONG MEANDERING RIVERS

The dynamics of alternate migrating bars along meandering rivers can be referred to the local planform configuration through remote sensing analysis. Figure 6.27 illustrates the migration of alternate migrating bars along the Rio Xingu from a remote sensing perspective.

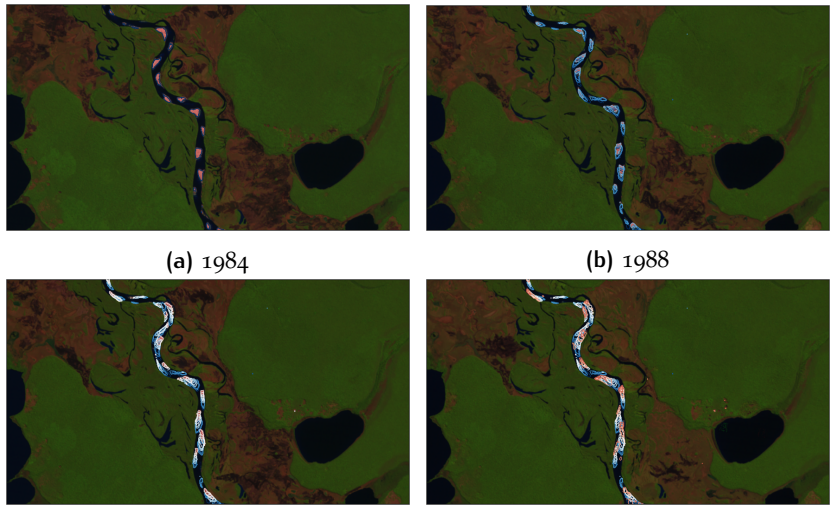

(a) 1984 **(b)** 1988

(c) 1993 **(d)** 1997

Figure 6.27: Downstream shift of alternate migrating bars in the Rio Xingu (Brazil). Contours show the annual position of bare sediment.

PyRIS allows to isolate and track through time each sediment bars, either steady or migrating: to each bare sediment bar a centroid is assigned. The latter is denoted by the position in the intrinsic s, n co-

ordinate reference system. Similarly, the distance between subsequent bars along the same bank of a meander enables to define the local bar wavenumber

$$\lambda_{bar} = \frac{\pi W^*_{bend}}{L^*_{bar}}, \tag{63}$$

where L^*_{bar} is the bar length (distance between consecutive bar centroids along the same river bank). The normalization was computed by means of the bend-averaged channel width W^*_{bend} in order to filter out significant variations in the channel width that may occur from upstream to downstream but maintaining a longitudinal scale significantly longer than that of migrating bars.

Hence, to each bare sediment bar corresponds a value of the local properties of the channel: a centerline curvature and a channel width in particular. By plotting together the yearly results for local centerline curvature and channel width against local bar migration rate v_{bar} or local bar wavenumber I can reconstruct the dependence of bar properties on the local planform properties. Figure 6.28 reports the scatter plots of local channel curvature ratio and dimensionless width against the local bar migrations rates and wavenumbers, also reported in boxplots in figure 6.29. A strong dependence of both bar wavenumber and migration rate on both local normalized centerline curvature and channel width is observed:

- bars are shorter and migrate faster where the curvature is lower, and the shortest and fastest bars occur in quasi-straight reaches; hence, despite the existence of migrating bars in meandering rivers, the curvature affects their dynamics and tend to suppress them;

- curvature slows down and elongates the migrating bars, and eventually bars tend to become steady and attain wavenumbers comparable with that of meanders for high curvature ratios; migrating bars tend to have much higher wavenumbers than steady bars and, when the curvature is relatively high, river bars tend to form as point bars rather than migrating bars;

- bar wavenumbers shorten and bar speed increases when the channel width is larger; this reflects the fact that the regime of alternate migratking bars is stringly dominated by the aspect ratio of the channel (Tubino and Seminara, 1990).

It is also of importance that bar migration rate seems to significantly slow down after a peak is reached for a normalized channel width roughly close to 1.5; this may be due to the fact that increasing the

width-to-depth ratio the amplification: in fact, when the aspect ratio increases significantly the migrating bar regime can be strongly altered (Colombini et al., 1987).

Figures 6.30 and 6.31 show analogous trends for the steady and alternate migrating bars of a similar river–the Rio das Mortes (Brazil)–while figures 6.32 and 6.33 report the results for the Rio Araguaia. The results for the Rio das Mortes and the Rio Araguaia are consistent with those of the Xingu; the trends show a significant decrease in downstream bar migration rate as well as in the bar wavenumber with the channel curvature, whereas the channel width has an opposite effect. Hence, channel planform appears to control the scales and dynamics of both points and alternate migrating bars.

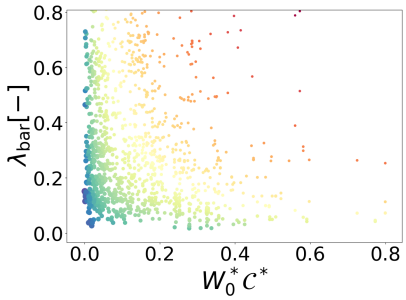

(a) Bar wavenumber against local dimensionless channel curvature.

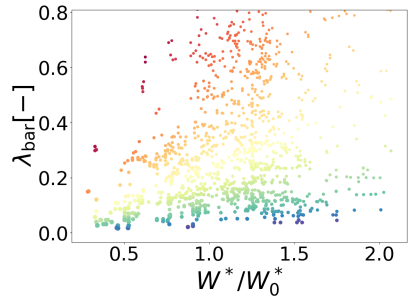

(b) Bar wavenumber against local dimensionless channel width.

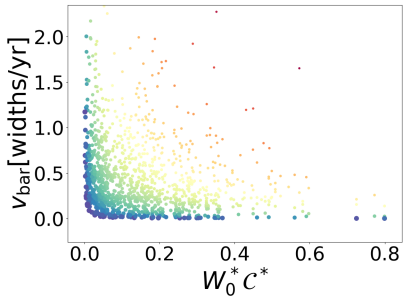

(c) Bar migration rate against local dimensionless channel curvature.

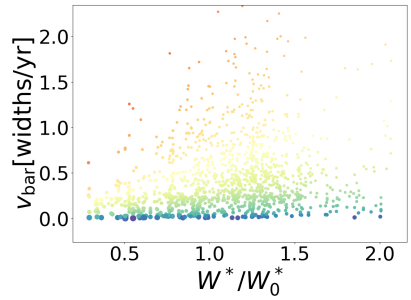

(d) Bar migration rate against local dimensionless channel width.

Figure 6.28: Scatter plots for scales and dynamics of sediment bars in the Rio Xingu (Brazil, 1984-2012).

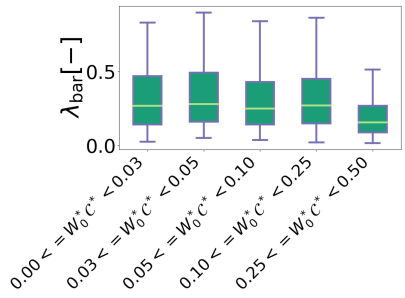

(a) Bar wavenumber against local dimensionless channel curvature.

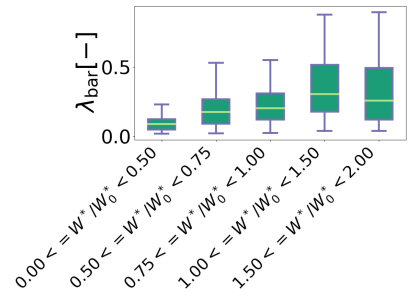

(b) Bar wavenumber against local dimensionless channel width.

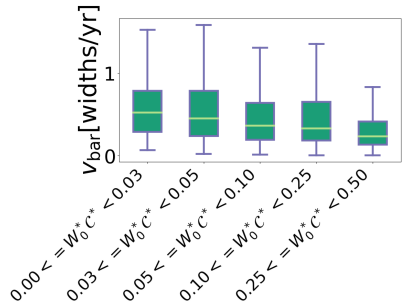

(c) Bar migration rate against local dimensionless channel curvature.

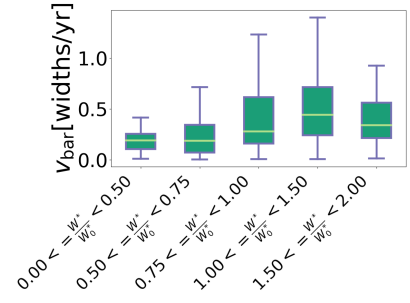

(d) Bar migration rate against local dimensionless channel width.

Figure 6.29: Boxplots for scales and dynamics of sediment bars in the Rio Xingu (Brazil, 1984-2012).

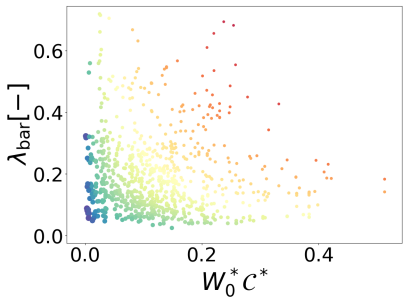

(a) Bar wavenumber against local dimensionless channel curvature.

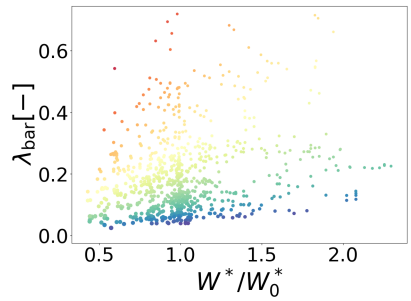

(b) Bar wavenumber against local dimensionless channel width.

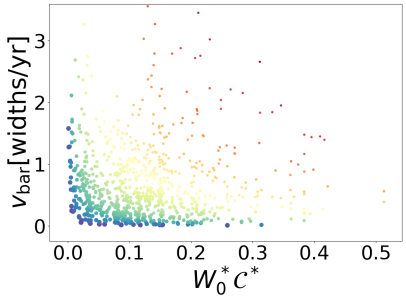

(c) Bar migration rate against local dimensionless channel curvature.

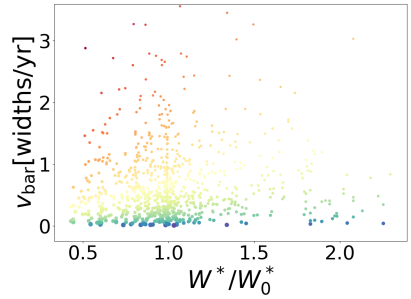

(d) Bar migration rate against local dimensionless channel width.

Figure 6.30: Scatter plots for scales and dynamics of sediment bars in the Rio das Mortes (Brazil, 1984-2012).

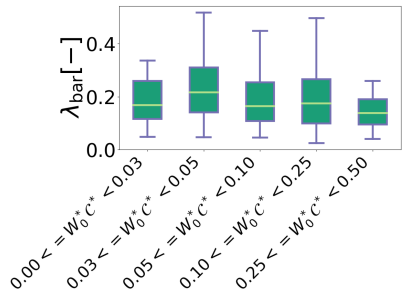

(a) Bar wavenumber against local dimensionless channel curvature.

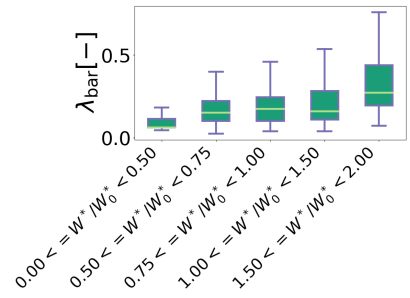

(b) Bar wavenumber against local dimensionless channel width.

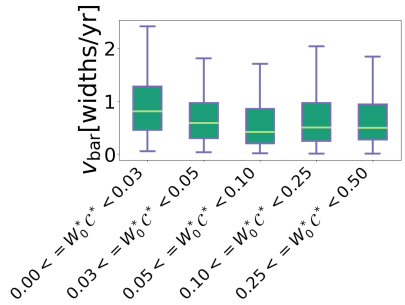

(c) Bar migration rate against local dimensionless channel curvature.

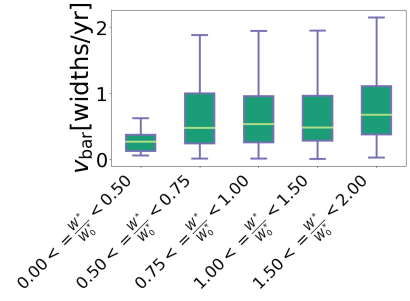

(d) Bar migration rate against local dimensionless channel width.

Figure 6.31: Boxplots for scales and dynamics of sediment bars in the Rio das Mortes (Brazil, 1984-2012).

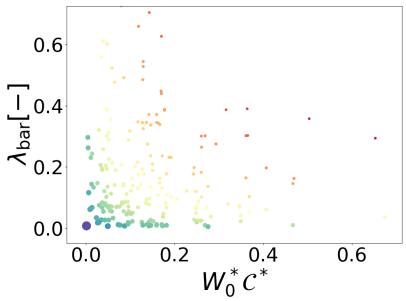

(a) Bar wavenumber against local dimensionless channel curvature.

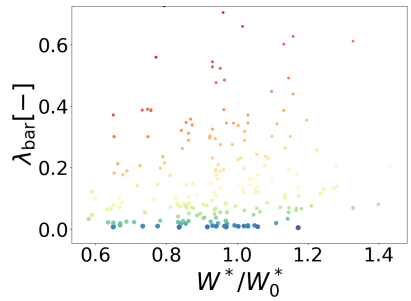

(b) Bar wavenumber against local dimensionless channel width.

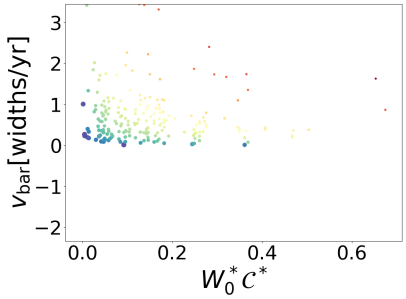

(c) Bar migration rate against local dimensionless channel curvature.

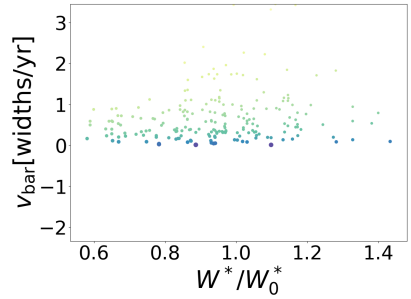

(d) Bar migration rate against local dimensionless channel width.

Figure 6.32: Scatter plots for scales and dynamics of sediment bars in the Rio das Araguaia (Brazil, 1984-2012).

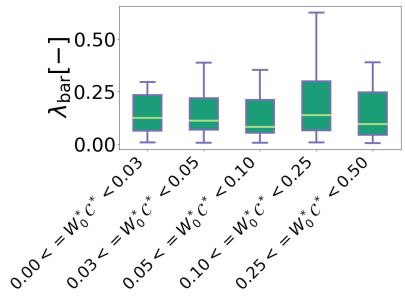

(a) Bar wavenumber against local dimensionless channel curvature.

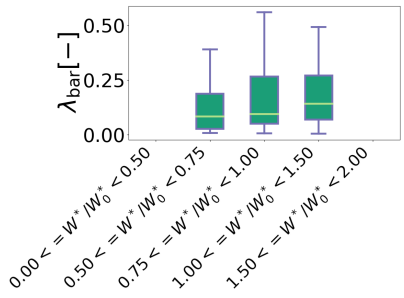

(b) Bar wavenumber against local dimensionless channel width.

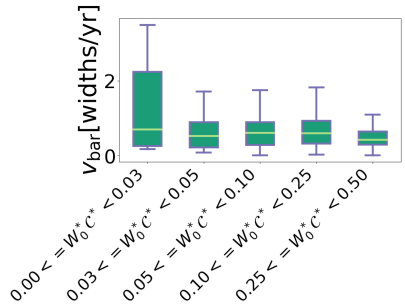

(c) Bar migration rate against local dimensionless channel curvature.

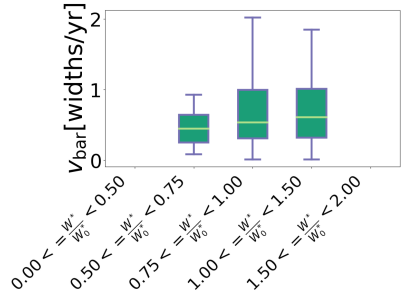

(d) Bar migration rate against local dimensionless channel width.

Figure 6.33: Boxplots for scales and dynamics of sediment bars in the Rio Araguaia (Brazil, 1984-2012).

6.5 DISCUSSION AND CONCLUSIONS

In this chapter I presented results and data that can be obtained by literature and gauging stations for Amazonian and African rivers and through remote sensing analysis. Firstly, I characterized a number of pristine meandering and transitional rivers from the point of view of the channel hydraulics and planform. The rivers analyzed are more or less homogeneous in terms of floodplain cover, planform restrictions, sediment sizes. The literature research combined with the remote sensing analysis through the software PyRIS allowed me to create a database of some South American and African rivers for which a characterization of the reference bankfull hydraulic geometry and planform structure was built. The limitations of such an approach are evident: data sources are sometimes contradictory, numbers from the gauging stations are not always reliable, resolution of remote sensing data is low, sediment supply estimates are interpolated through

total load formulas on reduced data, backwater effects are neglected, just to name a few. Moreover, during the observation period the Rio Araguaia encountered significant deforestation that forced a significant increase in the rates of sediment transport. However, in a number of rivers where redundant data were available, the results were found to be surprisingly consistent when comparing the relations 60 with the available values.

The characteristic values of the bankfull hydraulic geometry exhibit significant trends against the TSS per unit width. Specifically, while the dimensional quantities such as the channel width, depth and discharge show scattering trends, the dimensionless indicators of the bankfull hydraulic geometry (β, τ_*, d_s) display consistent trends (a more quantitative assesment of such consistency is reported in chapter 10). Hence, it seems that the sediment supply can be considered as a key driver for the bankfull hydraulic geometry of large pristine meandering rivers.

On the other hand, reference values for the planform descriptors (meander wavenumber and curvature ratio) display much weaker trends with the TSS; the median curvature is invariably similar for the analyzed reaches (the implications are discussed in chapter 10), while meander wavenumber splits into two classes: higher wavenumbers are related to meandering rivers with migrating bars, while lower wavenumbers are displayed by meanderng rivers with steady bars only. Moreover,

In sections 6.2 and 6.3 the temporal dynamics of bankfull channel width and planform descriptors is analyzed for several river reaches.

In section 6.2 I reconstructed the evolutionary bend-scale trends of the bankfull channel width in developing meander bends. By utilizing the individual bend sinuosity as a proxy of time, I defined a univocal quantity able to denote the evolutionary age of a meander bend; observations for tens or hundreds of bends over a 30 years period gave rise to an intense point cloud that reproduced, finally, boxplots showing the evolutionary dynamics of the bend-scale bankfull channel width. This is of particular importance since analytical morphodynamic models make rough assumptions on the evolutionary dynamics of bankfull channel geometry, such as the constancy of the channel width. The boxplots presented show an remarkably consistent result in a slightly decreasing channel width with increasing bend sinuosity. They never increase, but they do not to remain constant; this finding has implications also on the evolution of the streamwise bed slope, according to the model proposed in section 5.1 and to the results presented in chapter 7. The drop in channel width has different magnitudes in different rivers.

In section 6.3, evolutionary dynamics of bend-scale planform perturbations, including channel curvature, bend wavenumber and channel width oscillations, were computed in a similar manner. Such dynamics highlighted in particular the peak behavior of channel curvature and the complex behavior of width oscillations (this particular behaviors and their interactions will be explained in the next chapters). The statistics computed are consistent with the values known from the theories and with literature values for field-surveyed river reaches (see e.g. Lagasse et al. 2004; Zolezzi et al. 2012b; Eke et al. 2014a), despite obvious limitations arising especially a consequence of the low resolution of the satellite data employed. The most significant results arising from this kind of analysis are that:

- meander wavenumber reduces during the planform development in accordance with morphodynamic models;
- channel curvature has $\mathcal{O}(10^{-1})$ values and exhibit a peak at sinuosities ranges of $1.6 - -1.8$;
- the amplitude of width oscillation also displays $\mathcal{O}(10^{-1})$ values and peaks earlier than the curvature;
- width oscillations have maxima that shift far away from the bend apexes during the planform development.

Finally, in section 6.4 a dynamic characterization of bars in that particular class of meandering rivers that I herein consider as transitional was proposed. A remote sensing perspective offers a unique glimpse on the spatial structure and scales and of their evolutionary dynamics as a function of the channel planform. The results highlight the strong effect of channel curvature in inhibiting the migration rate and in promoting longer bars: when the channel curvature attains relatively high values, the steady bars (longer and not migrating) form in place of migrating bars. On the other hand, an increasing channel width promotes faster and shorter migrating bars, while steady bars tend to form when the channel width reduces significantly; however, in one case, when the channel width becomes significantly larger than the reference one, the bar migration rate reduces and the wavenumber drops.

7 THE HYDRAULIC GEOMETRY OF EVOLVING GRAVEL-BED MEANDERING RIVERS

This chapter reports the results of the system describing the evolution of bankfull hydraulic geometry in evolving gravel bed meandering rivers. Section 7.1 reports the results of the model applied to a sine-generated sequence of meandering bends and the effect of the ratio $\mathcal{R}_T$ between the planform development and the riverbed timescales is investigated. I discuss the outcomes of the model in section 7.2, where I also provide an estimate of $\mathcal{R}_T$ for a number of rivers of the Amazon basin and I illustrate qualitatively its relation with the migration coefficient and with the ratio between sediment and water discharges. A further discussion on the implications of the proposed model on the evolution of the morphodynamic regime is also reported.

7.1 RESULTS

In the present section I illustrate and discuss the outcomes of the model presented in section 5.1. Specifically, I investigate and discuss the role of the fundamental parameter arising from the formulation illustrated in section 5.1

$$\mathcal{R}_T = \frac{\sqrt{g^* \Delta D_s^{*3}}\Phi(\tau_{*0})}{2M(1-p_b)D_0^* U_0^*}, \tag{64}$$

which represents the ratio between temporal scales of planform development and riverbed change. The solution is mostly affected by $\mathcal{R}_T$, while the other parameters play a much more limited role in the evolution of the bankfull hydraulic geometry. The evolutionary model for the bankfull hydraulic geometry is coupled with the model defining the evolution of meander wavenumber $\lambda(t)$ presented in section 5.3.

Figure 7.1 reports the modeling outcomes from incipient meander formation to cutoff. The temporal evolution is plotted against the normalized meander sinuosity $(\sigma-1)/(\sigma_{cutoff}-1)$, which spans between 0 and 1 and allows to compare evolutionary scenarios with different cutoff times. The riverbed porosity p_b is assumed to be constant and equal to the commonly used value of 0.4 (although this is not crucial

to the aim of the present work). The floodplain material fraction p_f is set equal to that of the riverbed ($p_f = p_b$). The variables are plotted against meander sinuosity, consistently with the remote sensing analysis reported in the preceding section. Panel 7.1a shows the evolution river planform centerline in the normalized $(x^*, y^*)/W_0^*$ coordinate reference system. The channel axis consists of a sequence of identical, sine-generated meanders with one harmonic (i.e., no skewing and fattening occur). Panels 7.1b, c and d report the temporal evolution of the bankfull hydraulic geometry, namely the channel depth, width and slope, with respect to the initial values. Note that under the assumption of a single-harmonic, sine-generated periodic sequence of meanders, the cutoff occurs at the same value of sinuosity regardless the value of the timescale ratio R_T.

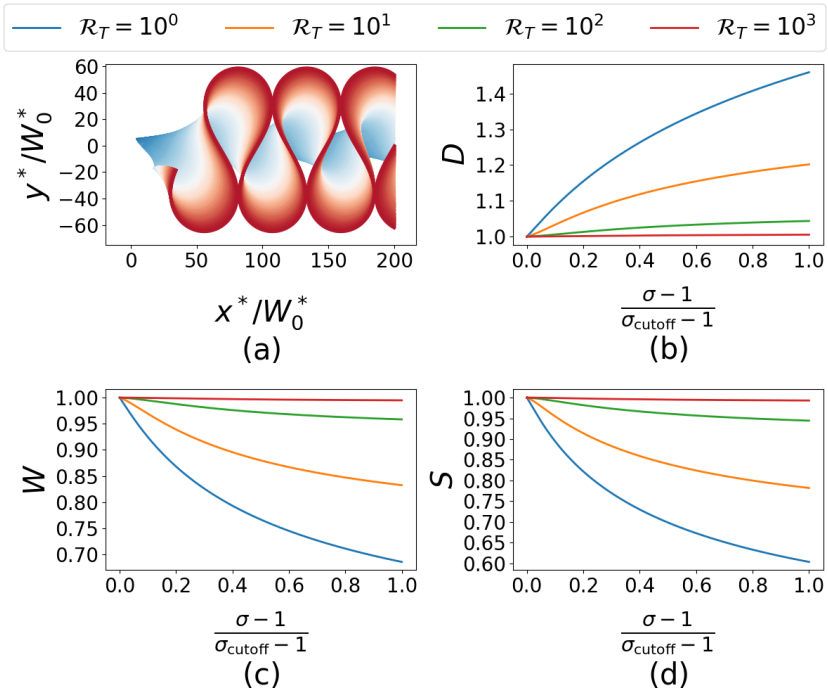

Figure 7.1: Evolution of the bankfull hydraulic geometry of a sequence of sine-generated meanders as a function of the timescale ratio $\mathcal{R}_T$. Initial conditions are $\beta_0 = 10$, $\tau_{*0} = 0.1$, $d_{s0} = 0.01$, $\lambda_0 = 0.1$. All the variables are plotted against meander sinuosity, which is used as a proxy of time. The floodplain porosity p_f is equal to the riverbed porosity $p_b = 0.4$. (*a*) Evolution of the river planform at intermediate timesteps for $\mathcal{R}_T = 10^1$. (*b*) Evolution of the normalized bankfull flow depth. (*c*) Evolution of the normalized bankfull channel width. (*d*) Evolution of the normalized channel slope.

Channel slope and width decrease uniformly during the development of the river planform. The magnitude of the drop of the channel width and slope is regulated by the value of the ratio $\mathcal{R}_T$ between the timescale of the riverbank shift and of the riverbed change: low values of $\mathcal{R}_T$ imply that the timescale of the planform development is comparable with that of the riverbed change and therefore the riverbed is not able to reshape towards the equilibrium channel slope and the bankfull channel width decreases accordingly. Conversely, when the ratio $\mathcal{R}_T$ is high, the planform development occurs slowly compared to the riverbed change: in this case, the riverbed is able to maintain the channel slope according to the incoming sediment supply. For values of $\mathcal{R}_T$ of 10^3 the bankfull hydraulic geometry keeps almost constant.

Figure 7.2 illustrates the role of the exchange of bed material between the river and the floodplain. The floodplain porosity p_f accounts for the percentage of eroded riverbank effectively contributing to the bed material load. I investigate three significant values of the floodplain porosity p_f, namely $p_f = 0$ (the floodplain is entirely composed by bed material which contributes to the sediment transport), $p_f = 0.4$ (the floodplain has the same bed material percentage as the riverbed), $p_f = 1$ (bed material incoming from the riverbanks is neglected).

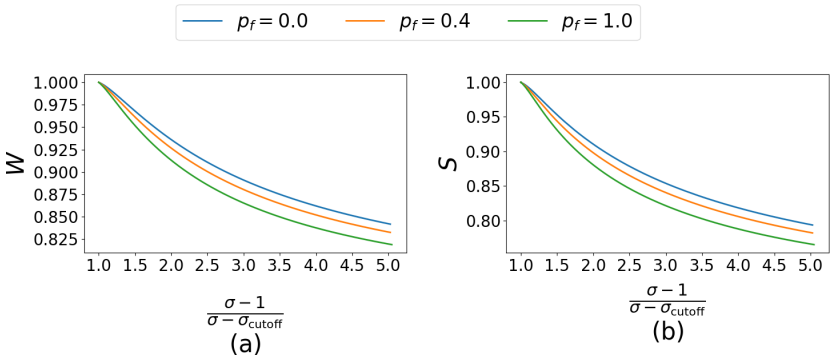

Figure 7.2: Evolution of the bankfull hydraulic geometry under changing floodplain porosity p_f. Initial conditions are $\beta_0 = 10$, $\tau_{*0} = 0.1$, $d_{s0} = 0.01$, $\lambda_0 = 0.1$, while $\mathcal{R}_T$ was set to 10. (*a*) Evolution of the normalized bankfull channel width. (*b*) Evolution of the normalized channel slope.

Figure 7.2 shows that exchange of sediment load between the riverbed and the floodplain does not play a crucial role in the overall evolution of bankfull hydraulic geometry. However, increasing the percentage of bed material load incoming from the floodplain reduces the change in bankfull hydraulic geometry. This suggests a net income from the

river banks to the channel, which pushes the river towards the sediment supply-driven channel slope.

7.2 DISCUSSION AND CONCLUSIONS

In the section 6.2 I first presented a statistical analysis of evolutionary remotely sensed data taken from the Landsat imagery. The previous section reports the result of the model for the evolution of bankfull hydraulic geometry; the key controlling parameter for the evolution of the bankfull hydraulic geometry is the ratio between floodplain and riverbed timescales $\mathcal{R}_T$. In the present section I discuss the results of the model with respect to the outcomes off the statistical analysis; specifically, I investigate the reference hydraulic characteristics of the natural meandering rivers presented in section 6.1 and seek the value of $\mathcal{R}_T$ for these rivers.

The statistical analysis reported in section 6.2, although referred to sand-bed rivers, can be regarded as a dynamic bend-scale analysis of the planform evolution of bankfull channel widths along four large meandering rivers from the Amazon basin. All four rivers display a slight decrease of the channel width during average bend growth, which means that, from a statistical point of view, the planform development of individual meander bends leads to a weak decrease in their average bankfull width. Results can be considered significant for sinuosities smaller than 3; the most populated classes are the ones related to the smallest sinuosities. The Huallaga river (figure 6.10c) shows a stronger decrease in bend-scale bankfull width with respect to the other three rivers, the Rio Beni (Figure 6.10a), Rio Mamorè (Figure 6.10b) and Rio Ucayali (Figure 6.10d). These results seem to discredit, on one hand, the commonly employed constancy of the bankfull channel width Zolezzi et al., 2009, e.g., on the other hand they enforce the inconsistency of those models predicting dramatic drops of the bankfull channel width during planform development.

A spontaneous question would be what values does the controlling parameter $\mathcal{R}_T$ attain in natural rivers.

Being the numerator of equation 17 equal to Q_s^*/W^* and the denominator roughly equal to $\mathcal{M}\,Q^*/W^*$ (note that $2(1-p_b) \simeq 1$) I can rewrite equation (17) in the following form

$$\mathcal{R}_T \simeq \frac{Q_s^*/Q^*}{\mathcal{M}}, \tag{65}$$

where Q^* is the water discharge. Equation (65) represents the ratio between sediment concentration and the migration rate, the latter given by

$$\mathcal{M} \sim \frac{\zeta^*}{\nu u_0^*}, \tag{66}$$

where ν is some representative curvature ratio of the channel planform (herein the median is used).

Figure 7.3 shows the dependence of $\mathcal{R}_T$ on the discharge ratio Q_s^*/Q^* (panel 7.3a) and on the migration coefficient $\mathcal{M}$ (panel 7.3b) for several of natural meandering rivers from the Amazon basin presented in section 6.1. Curvature values were computed through PyRIS by extracting the river planforms for the identified reaches. Visually, $\mathcal{R}_T$ correlates

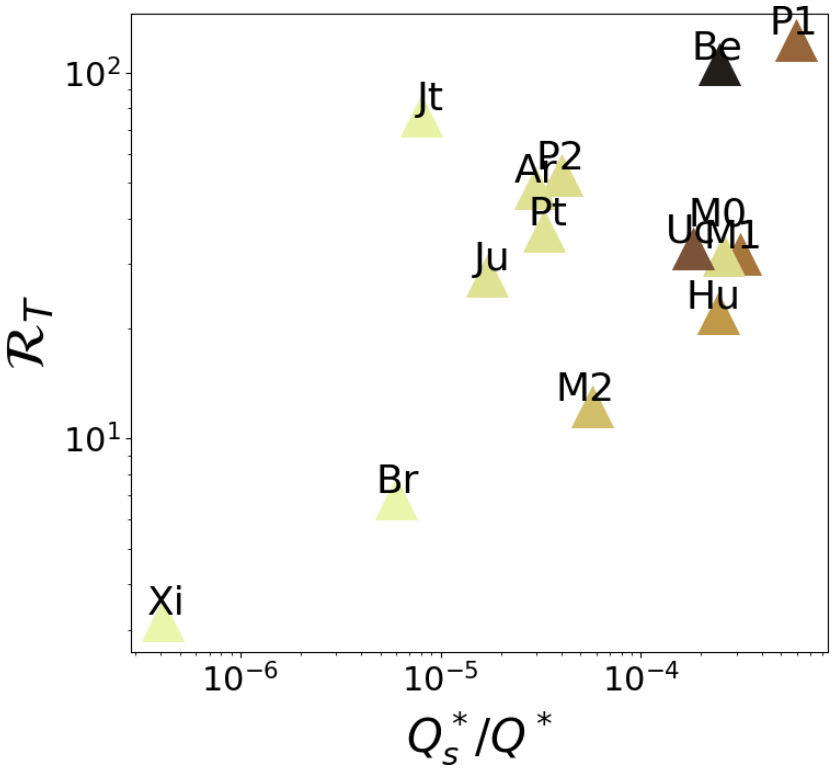

Figure 7.3: Values of $\mathcal{R}_T$ against the discharge ratio Q_s^*/Q^* for natural meandering rivers of the Amazon basin: Ar (Araguaia), Be (Beni), Br (Branco), Hu (Huallaga), Ju (Juruà), Jt (Jutai), Mo (Mamorèo), M1 (Mamorè1), M2 (Mamorè2), Ma (Madre dei Diòs), P1 (Purus1), P2 (Purus2), Uc (Ucayali), Pt (Putumayo), Xi (Xingu). The color of the markers represents the value of the TSS per unit width.

well with the sediment concentration and its values span within the range $10^0 \div 10^3$ and are mostly concentrated in the range $10^1 \div 10^2$.

Now I look how the results of the model proposed, for the values of $\mathcal{R}_T$ that occur in natural rivers, compare against the outcomes of traditional morphodynamic models. Figure 7.4 compares the results obtained with the present model with those predicted by the widely used, constant width model summarized in Zolezzi et al., 2009, which is employed in many other morphodynamic computations and assumes a constant channel width and a channel slope decreasing proportionally to meander elongation, and that proposed by Eke et al., 2014a, which introduces a bank erosion/deposition model to vary the channel width. The latter predicts a nonphysical drop in bankfull channel width. The authors overcame this problem by assuming the threshold Shields stress for bank erosion to change with bed slope. The corrected model is indicated in figure 7.4 as "Eke et al., 2014a *mod*". Panel 7.4a shows the evolution of the sediment transport capacity. Panels 7.4b, c and d report the evolution of bankfull channel geometry.

The three models (constant width, Eke et al. 2014a and Eke et al., 2014a mod.) do not treat explicitly the conservation of sediment transport (i.e., they do not employ the Exner equation). Indeed the sediment transport capacity reduces of about 90% or more. This means that 90% of the sediment transport carried throughout the channel during planform development is deposited, despite the assumption of a constant floodplain slope. The present model introduces the concept of sediment mass conservation in the context of bankfull channel geometry; the extended Exner equation employed herein generates a mechanism of compensation of the channel slope the mitigates the reduction in channel slope, resulting in a higher sediment transport capacity. The larger the ratio $\mathcal{R}_T$, the slowest the planform development compared to the riverbed adaptation rate, hence the bankfull channel geometry tends to keep constant leading to an almost constant sediment transport capacity. Finally, the evolution of bankfull channel width predicted by the novel modeling framework is supported by the field data reported in Figure 6.10 for relatively high values of $\mathcal{R}_T$, where the statistical planform development of individual meander bends highlights a slight decrease of bankfull channel width with bend sinuosity. A dramatic drop such as the one predicted by the original model of Eke et al., 2014a was not observed within the study cases reported in section 6.2. The modified model of Eke et al., 2014a predicts a variation of the channel width which is similar to the one obtained by our model; however, the sediment transport capacity is not conserved.

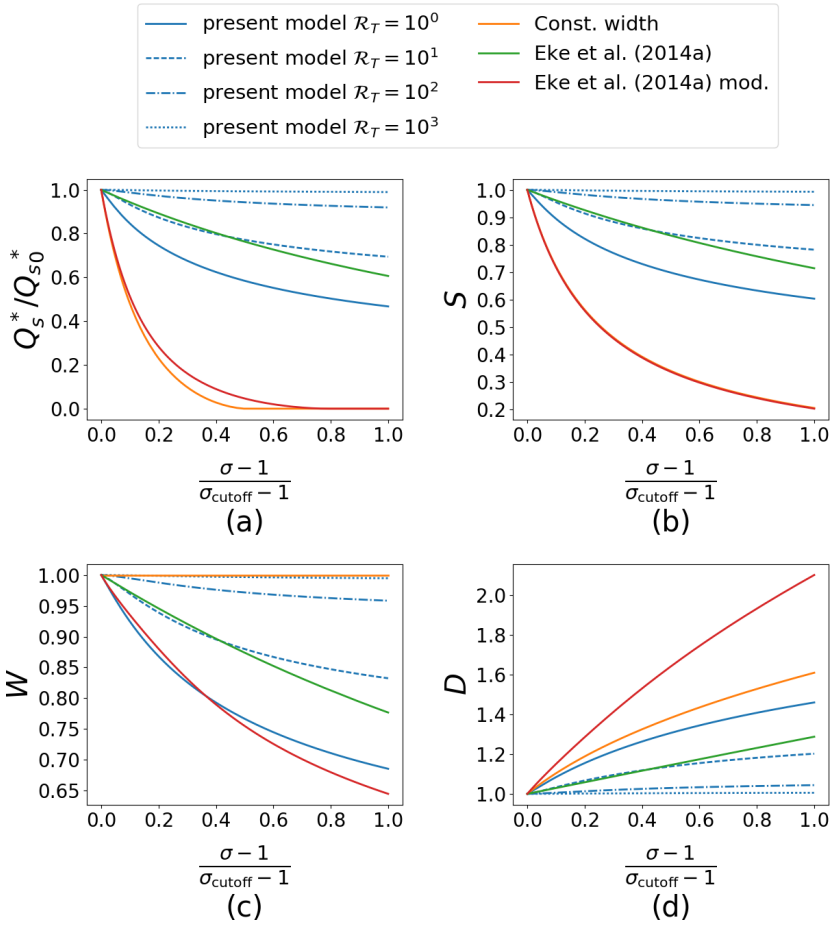

Figure 7.4: Evolution of the bankfull hydraulic geometry according to three different models: present model (blue lines), standard model detailed in Zolezzi et al., 2009 (orange line), physically-based bank erosion/deposition model proposed by Eke et al., 2014a without (green line) and with (red line) the modification to overcome dramatic width changes. (*a*) Evolution of the sediment transport capacity. (*b*) Evolution of the channel slope. (*c*) Evolution of the channel width. (*d*) Evolution of the channel depth.

The proposed model for the evolution of channel width is a threshold-based model: it predicts that the bankfull channel width undergoes widening (narrowing) when the bankfull flow velocity is higher than the equilibrium one. The channel slope, on the other hand, varies as a consequence of three different processes, (i) meander elongation, (ii) channel widening/narrowing, and (iii) the variation of transport capacity. The latter effect arises due to the implementation of the Exner

equation in the model and allows to decrease the effect of slope decrease associated with meander elongation. Its magnitude is ruled by the parameter $\mathcal{R}_T$, which accounts for the intensity of sediment transport processes with respect to bank erosion/accretion processes, and in the natural meandering rivers analyzed in the present section takes values that mostly plot in the range $10 \div 100$. Low values of $\mathcal{R}_T$ denote fastly evolving meanders, leading to a decrease in channel slope proportional to meander elongation due to the lack of time for the sediment transport to re-adapt to the sediment supply. On the contrary, high values of $\mathcal{R}_T$ are associated to slowly evolving meanders, whose riverbed has the time to adapt its morphology to the incoming sediment supply before the river keeps evolving.

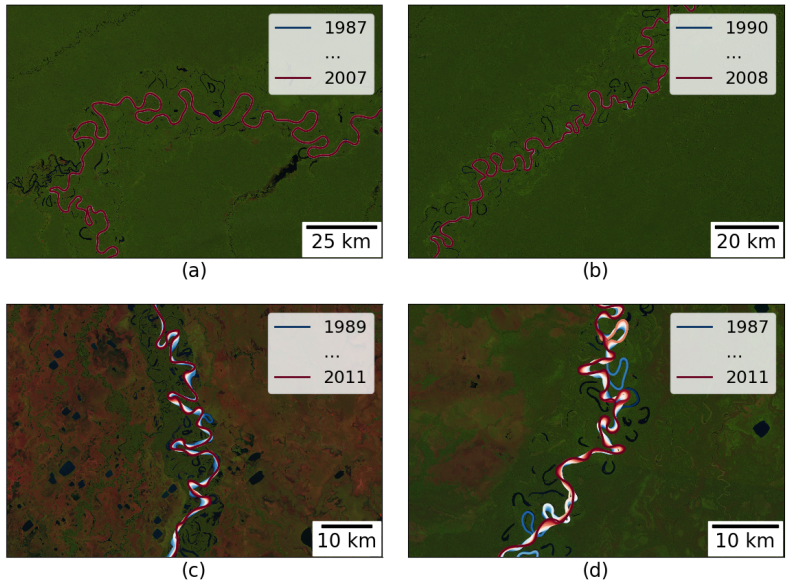

Figure 7.5: Planform structure of four large rivers from the Amazon basin. Flow enters from the bottom in all the pictures. (*a*) Rio Purus (Brazil). (*b*) Rio Jurua (Brazil). (*c*) Rio Mamorè (Bolivia). (*d*) Rio Beni (Bolivia).

Finally I discuss the possible implications of the present evolutionary model for the bankfull hydraulic geometry in the broader context of meander morphodynamic models. Zolezzi et al., 2009 investigated the transition between subresonant and superresonant regime in evolving meander bends. Subresonant meanders are generally associated with an upstream-skewed meander shape, while superresonant meanders are downstream-skewed. The most commonly occurring

scenario observed by Zolezzi et al., 2009 in the natural rivers provided by the dataset of Parker et al., 2007 was the transition from initially superresonant meanders to subresonant meanders. In some cases the reverse behavior was found. Their model predicted a significant variation of the aspect ratio and of its resonant value β_R during the planform development.

However, the model employed in the present chapter suggests that natural rivers should be more prone to such transitions when the planform development is fast ($\mathcal{R}_T$), whereas they should be inhibited in slowly evolving meandering rivers. Figure 7.5 provides a few examples of natural meandering rivers in the Amazon basin.

In panels 7.5a,b the Rio Purus and Rio Jurua are shown; these two rivers do not modify significantly their planform during the period of observation. Panels 7.5c, d illustrate two dynamic rivers, namely the Rio Mamorè and the Rio Beni. The Rio Purus and the Rio Jurua display a typically subresonant shape for all the meander bends illustrated, while the Rio Mamorè and the Rio Beni show a composition of upstream and downstream skewed meander bends, suggesting that rivers that evolve faster are more transition-prone.

More implications can be referred to the choice of the bankfull hydraulic geometry evolution model and, eventually, to the choice of $\mathcal{R}_T$. The complexity of meander loops is generally due to the rise of higher harmonics, whose amplitude depends directly on the bankfull hydraulic geometry. A rather constant bankfull hydraulic geometry may lead to completely different planforms with respect to a strongly changing bankfull geometry. Higher complexity means, eventually, lower sinuosities and smaller lateral planform space occupied by the river.

8 AUTOGENIC WIDTH CHANGE AND CURVATURE IN EVOLVING MEANDER BENDS

In this chapter I study the morphodynamics of channel width oscillations in space and time associated with the planform development of river meander bends. I focus the attention on "autogenic" width variations, which are forced by flow nonlinearities driven by the dynamics of channel curvature and also occur in the limiting case of equal rates of advance/retreat of the opposite river banks (i.e., the $\mathcal{K}$ parameter is set to 0). The proposed approach allows insight into the interaction between autogenic width variations and curvature in meander development and between forcing and damping effects in the formation of width variations. Model outcomes suggest that autogenic width oscillations mainly determine wider-at-inflection meandering river patterns, and affect their planform development particularly at superresonant aspect ratios, where the width oscillation reaches its maximum and reduces meander sinuosity and lateral floodplain size. The coevolution of autogenic width oscillation and curvature occurs through temporal hysteresis cycles, whereby the peak in channel curvature lags behind that of width oscillation. The values of width oscillation predicted by the model are consistent with those extracted from remotely sensed field data. For the sake of simplicity, the reference channel width is assumed to be constant and the role of sediment supply driven bed change described in the previous chapter is neglected.

8.1 RESULTS

I first investigate the coevolution of curvature and width oscillations as the meander develops in time.

In the absence of width variations the evolutionary dynamics of channel curvature consists of an initial stage characterized by the growth of the fundamental harmonic (e_1), while channel sinuosity keeps relatively small, followed by a second stage in which meander length, and therefore sinuosity, increases quite rapidly and higher or-

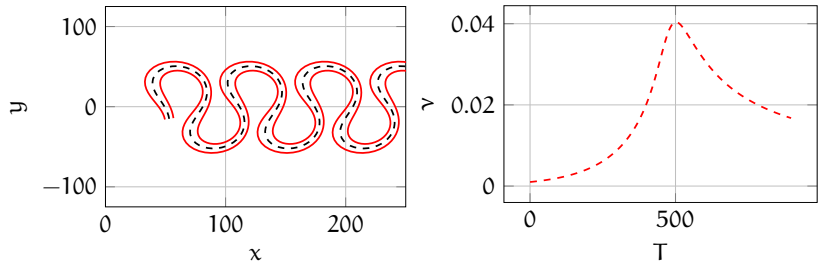

(a) Planform shape with centerline and banklines at $T = 790$.

(b) Temporal evolution of the curvature ratio ν.

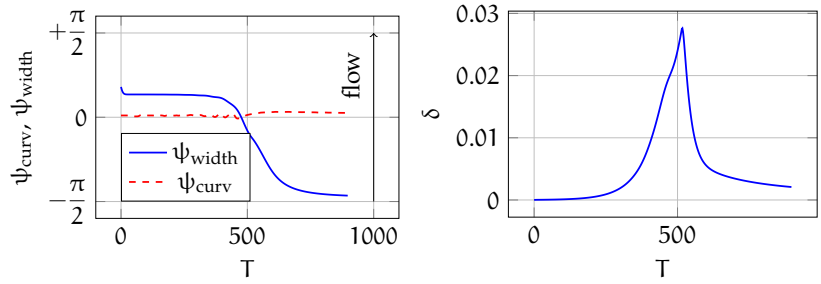

(c) Phase lag of the bend apex, ψ_{curv}, and of the widest section, ψ_{width}, with respect to the half-bend longitudinal position. Lag values of $-\pi/2$ ($+\pi/2$) correspond to the upstream (downstream) meander inflection.

(d) Temporal evolution of the dimensionless amplitude of width variations δ.

Figure 8.1: Evolutionary dynamics of a sub-resonant meander with autogenic width oscillations. Initial values of parameters: $\beta = 10$, $d_s = 0.01$, $\tau_* = 0.1$, $\lambda_0 = 0.1$, $|\theta_1| = 0.01$.

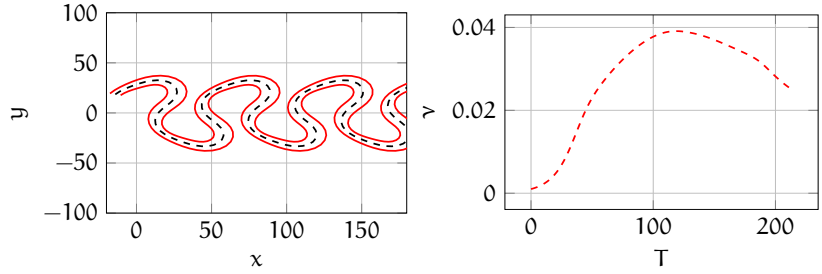

(a) Planform shape with centerline and banklines at $T = 193$.

(b) Temporal evolution of the curvature ratio ν.

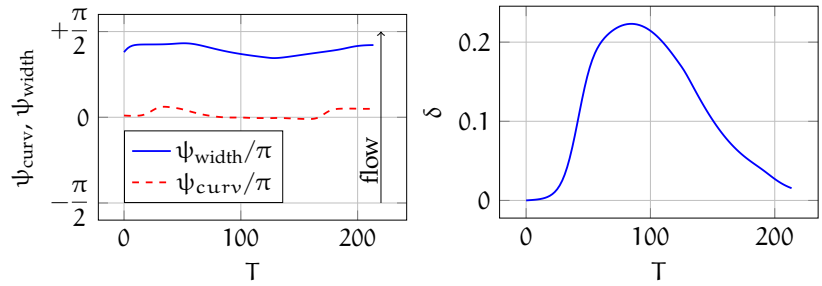

(c) Phase lag of the bend apex, ψ_{curv}, and of the widest section, ψ_{width}, with respect to the half-bend longitudinal position. Lag values of $-\pi/2$ ($+\pi/2$) correspond to the upstream (downstream) meander inflection.

(d) Temporal evolution of the dimensionless amplitude of width variations δ.

Figure 8.2: Evolutionary dynamics of a super-resonant meander with autogenic width oscillations. Initial values of parameters: $\beta = 20$, $d_s = 0.01$, $\tau_* = 0.1$, $\lambda_0 = 0.1$, $|\theta_1| = 0.01$.

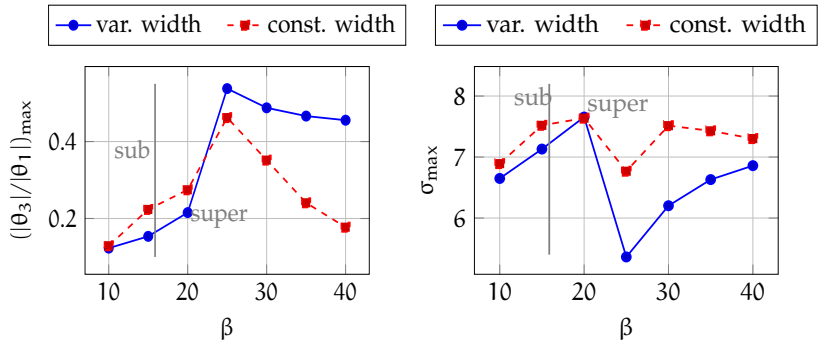

(a) The ratio between the maximum amplitude of the third and the first harmonic of the centerline inflection angle θ.

(b) Channel sinuosity evaluated at cut-off.

Figure 8.3: Effect of the autogenic width variations on meander's shape parameters: comparison between variable width (solid lines) and constant width simulations (dashed lines) as a function of the width ratio β. Initial values of parameters: $d_s = 0.01$, $\tau_* = 0.1$, $\lambda_0 = 0.1$.

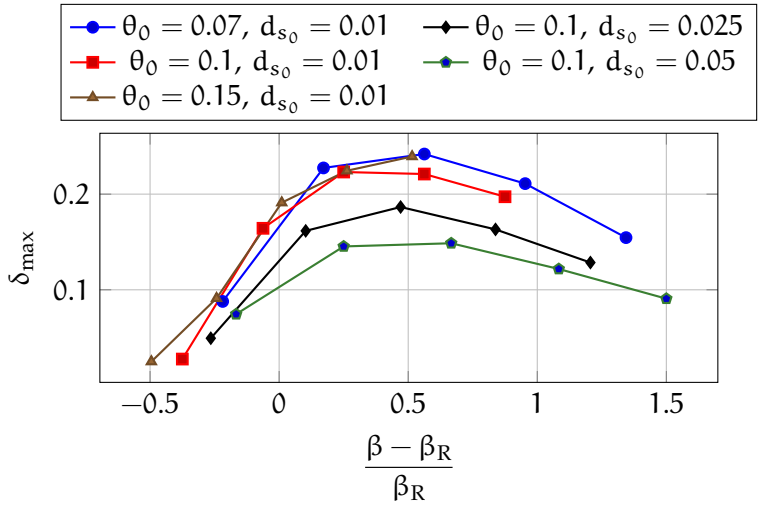

Figure 8.4: The peak amplitude δ_{max} of width variations as a function of the aspect ratio, measured with respect to its resonant value β_R, for different sets of flow conditions (τ_*, d_s) and initial meander wavenumber $\lambda_0 = 0.1$.

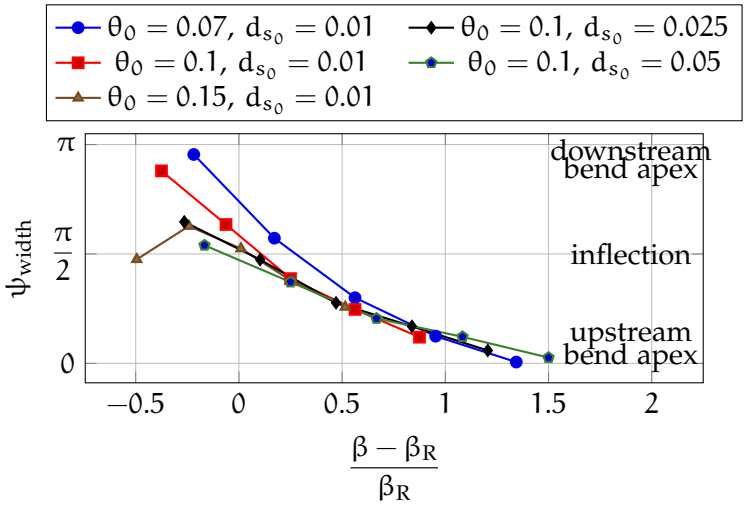

Figure 8.5: The position of the widest section ψ_{width} along half a meander wavelength between two consecutive apexes as a function of the width ratio, measured with respect to its resonant value β_R, for different sets of flow conditions (τ_*, d_s) and initial meander wavenumber $\lambda_0 = 0.1$. The values of ψ_{width} are computed when the width oscillation amplitude reaches its peak.

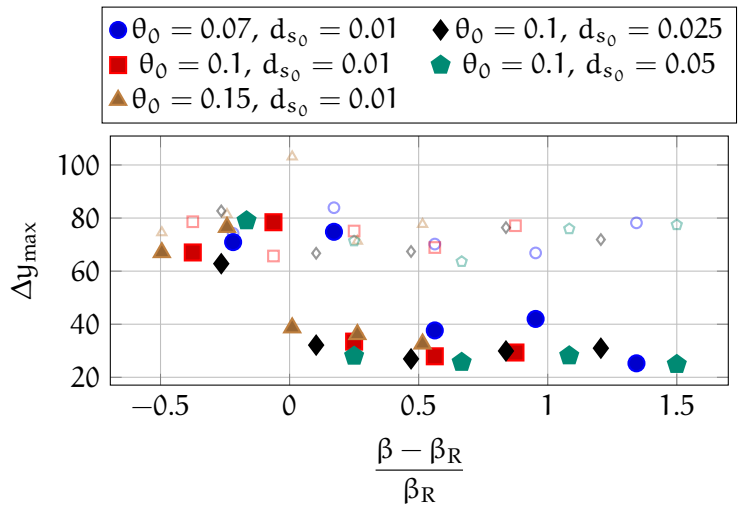

Figure 8.6: The maximum floodplain width Δy_{max}, scaled with the reference channel width, as a function of the width ratio, measured with respect to its resonant value β_R, for different sets of flow conditions (τ_*, d_s) and initial meander wavenumber $\lambda_0 = 0.1$ (full markers). Empty markers refer to the results of the equiwidth model ($\delta = 0$).

der components develop through nonlinear effects (see Seminara et al. 2001, figures 5-7). Such two-stage process is reflected by the temporal evolution of the curvature ratio ν, which initially grows up to a maximum value and then declines in a second stage due to the increase of the intrinsic meander length.

The model of Seminara et al., 2001 also suggests that the planform shape strongly depends on the width ratio β falling below or above the resonant value β_R. Sub-resonant meanders are typically downstream skewed, while super-resonant meanders exhibit upstream skewed loops and are prone to evolving much faster, as cutoff occurs at lower values of the rescaled time T. It is useful to remind that the term "resonant" refers to the unbounded response of the linear $\mathcal{O}(\nu)$ solution which occurs, for given values of τ_* and d_s, as β exactly matches β_R (Blondeaux and Seminara, 1985). The dependence of the resonant aspect ratio β_R on Shields stress and grain roughness can be found in Seminara and Tubino, 1992 (figure 4).

The above distinction between sub- and super-resonant meanders turns out to be relevant also in the present case in which width variations are taken into account, as their role on planform development is markedly different in the two regimes.

Figures 8.1 and 8.2 show the evolution of sub- and super-resonant meanders. The initial parameters value is the same in the two cases, but for the width ratio β, which falls below (figure 8.1) or above (figure 8.2) the resonant value ($\beta_R \simeq 15.8$). Figures 8.1a and 8.2a show the meander planform, at $T = 790$ and $T = 193$ respectively, which reflects the assumption of channel width oscillating at a double spatial frequency compared to centerline curvature and displays downstream ($\beta < \beta_R$) and upstream ($\beta > \beta_R$) skewed loops. The evolution in time of the curvature ratio ν and of the dimensionless amplitude of width oscillations δ are reported in figures 8.1b and 8.2b and in figures 8.1d and 8.2d, respectively. The behavior of the parameter ν is rather similar to that observed in constant width channels and is governed (see equation 39) by the opposing effects of the growth of θ_1, which characterizes the first phase, and the decrease of meander wavenumber that dominates the second phase, when channel sinuosity mainly develops.

The effect of width variations on the curvature ratio ν is negligible in sub-resonant regime, as shown in figure 8.1b, while it becomes relevant for $\beta > \beta_R$, leading to a time delay of the peak curvature and slowing down the decline of curvature in the final stage of planform development (figure 8.2b). On the other hand, the behavior of the amplitude of width oscillations is closely related to that of curvature, as its growth is driven by the $\mathcal{O}(\nu^2)$ autogenic term appearing in (54d), which results in a sharp increase of δ until a peak is reached

(figures 8.1c and 8.2c). Such an effect is counterbalanced by the linear $\mathcal{O}(\delta)$ term of equation (54d) that always produces a suppressing contribution, which increases with δ. The amplitude of width oscillations keeps relatively small in the sub-resonant case, while it becomes large for a longer time in the super-resonant case, being more persistently close to the peak value of nearly 0.2.

Figures 8.1c and 8.2c show the locations of the bend apex and of the widest section with respect to the inflection points. They are expressed in terms of the phase lags, ψ_{curv} and ψ_{width}, respectively, measured with reference to the half-bend section (therefore $-\pi/2$ and $\pi/2$ denote the positions of two consecutive inflection points). In both sub- and super-resonant cases the bend apex keeps nearly in phase with the half-bend section during meander evolution and deviates from this location only slightly due to nonlinear effects. On the other hand, the behavior of ψ_{width} is markedly different in the two cases. In the sub-resonant case (figure 8.1d) the phase lag ψ_{width} undergoes a strong variation in time, such that the widest section is initially located downstream the bend apex, and progressively slides back to the upstream inflection. On the contrary, in the super-resonant case (figure 8.2d) the position of the widest section is fairly stable in time and keeps closer to the inflection point.

A summary of the effect of autogenic width variations on the centerline evolution is given in figure 8.3, where the maximum amplitude of the third harmonic θ_3 of the inflection angle, scaled with that of the fundamental θ_1 (figure 8.3a), and channel sinuosity, ($\sigma = \lambda_0/\lambda$; figure 8.3b), evaluated at cut-off are reported for different values of the width ratio β. Results of the present theory are compared with those of equiwidth simulations, for the same set of parameters. At low values of β width variations tend to suppress the geometrical nonlinearities and produce more regular meander shapes with limited relevance of the third harmonic. However, as β crosses the resonant range such effect is reversed and becomes stronger, thus promoting the fattening and skewing of the meander shape in the final stage of evolution. Furthermore, when width variations are taken into account, the elongation of super-resonant meanders is strongly inhibited and therefore channel sinuosity attains smaller values, as shown in figure 8.3b, falling to a minimum for values of β above the resonant range.

Such behavior highlights the suppressing attitude of autogenic width variations on the activity of super-resonant meanders. A clear explanation can be given in the dependence of δ on flow parameters. Computing the peak value δ_{max} for different values of the reference parameters (β, τ_* and d_s) and measuring the width ratio β with respect to β_R, which depends on τ_* and d_s, a fairly coherent scenario is obtained,

as shown in figure 8.4. The value of δ_{max} exhibits a sharp increase as I move from sub-resonant to super-resonant meanders, reaches a maximum for β nearly equal to $1.5\,\beta_R$ and then declines for larger β. Figure 8.4 also shows that the amplitude of width oscillations is almost unaffected by τ_*, while it drops as the sediment gets coarser.

The position of the widest section when δ reaches its peak also exhibits a similar coherent behavior, as the different curves overlap, at least in the super-resonant regime, once they are represented in terms of the relative distance from the resonant state. Figure 8.5 suggests that the widest section is approximately located at the meander inflection at resonance; furthermore, it slides back from downstream to upstream the inflection point as β crosses the resonant value, and eventually reaches the upstream bend apex for wide channels. Comparing figures 8.4 and 8.5 it can be noted that the widest section is located half-way between the apex and the inflection point ($\psi_{width} \simeq \pi/4$) in the range of β values corresponding to the maximum amplification of width oscillations ($\beta \simeq 1.5\,\beta_R$).

Further evidence of the different evolutionary dynamics of sub- and super-resonant meanders can be obtained through the analysis of the width of the floodplain which is needed to accommodate meander development from the initial stage until cut-off. In figure 8.6 I report (with full markers) the envelope of the river belt width, measured as the maximum transverse distance between two consecutive bend apexes, for the same set of parameters of figures 8.4 and 8.5. Results of the present model highlight the existence of a sharp transition as the width ratio crosses the resonant value: subresonant meanders seem to require more space to develop, nearly 60–80 times their width, while super-resonant meanders keep more confined and the belt width drops to 20–40 times the channel width. As shown in figure 8.6 results of equiwidth simulations (empty markers) do not display a similar dependence on β. Therefore, such distinct behavior seems inherently associated with the effect of autogenic width variations on meander development.

8.2 DISCUSSION AND CONCLUSIONS

8.2.1 Mutual interaction between width and curvature under sub- and super-resonant regimes

The results presented in the preceding section provide further support to the idea that the evolutionary trajectories of meanders are

markedly different depending upon the width ratio falling below or above the resonant value.

The main outcome is that super-resonant meanders are more likely to display width oscillations driven by the autogenic mechanism, with a maximum value of their amplitude occurring in the range $(\beta = \beta_R \div 2\beta_R)$ and a corresponding phase lag that forces local widening to occur far downstream the bend apex. In such conditions width variations are found to weaken the planimetric activity of meanders, mainly reducing meander length and floodplain width (figures 8.3b and 8.6).

I now attempt to provide a mechanistic explanation of the behavior described in Section 8.1. Solution of system (57), along with equations (54)a-c, provides us with an in-depth understanding of the adjustment of width oscillation and of the interaction between width and curvature in the planform development of meander bends.

Equations (54)a,b suggest that the evolution of the channel axis is mainly driven by the linear $\mathcal{O}(\nu)$ term. Therefore the lateral migration rate depends on the position along a meander wavelength of the maximum of the excess flow velocity, U_{10}, at the bank. A typical scenario is reproduced in Figure 8.7a, where the phase lag of the U_{10} solution with respect to curvature distribution is plotted in terms of the width ratio and meander wavenumber, for given values of the flow parameters. Because meanders grow when the phase lag falls in the range $(-\pi/2 \div \pi/2)$, the figure shows that planform development occurs provided meander wavenumber keeps relatively small, regardless the value of the width ratio. In the (λ, β) plane of Figure 8.7a the resonant value β_R corresponds to the intersection of the marginal stability curve with the curve discriminating upstream from downstream migration.

On the other hand, β controls the direction of propagation of the channel planform, such that lower values of β (mainly sub-resonant) imply downstream migrating meanders, while higher values (mainly super-resonant) correspond to upstream migrating meanders. This is the main cause of the different evolutionary trajectories of meanders reported in Figures 8.1a and 8.2a. As a meander develops in time its length increases and therefore λ decreases, which implies a change in the phase lag of U_{10}. As pointed out in section 8.1, the increase of channel length is also responsible, through equation (39), for the reduction of curvature ratio ν experienced in the second stage of meander development.

Meander dynamics is also affected by width variations through the non-linear $\mathcal{O}(\nu\delta)$ contribution, which can either promote or inhibit morphological activity depending on the phase lag ψ_{width}. According to the stability analysis of Luchi et al., 2011, when width oscil-

lations are nearly in phase with curvature (wider-at-bends meander, $\psi_{width} = 0, \pi$) meander evolution is promoted, while their effect becomes weaker (or even negative at large β) as their peak shifts towards the inflection points ($\psi_{width} = \pm\pi/2$). Figure 8.5 suggests that the former condition is met when β is far from the resonant range, while the latter condition characterizes near resonant and super-resonant meanders, which may be the cause of the observed reduction of channel sinuosity reported in Figure 8.3b.

Equation (54d) highlights how forcing and suppressing terms interact in the formation of width oscillations. In this case a forcing effect is required to promote width variations because the linear $\mathcal{O}(\delta)$ contribution invariably produces a stabilizing effect. As an initially equiwidth, quasi-straight river with a weak periodic perturbation of its centerline curvature starts developing, curvature self-forces its own growth but also forces the width distribution to vary longitudinally due to nonlinear autogenic $\mathcal{O}(\nu^2)$ effect. Therefore, the amplitude of width variations experiences a relatively fast growth in the initial stage of development due to the increase of the curvature ratio. However, increasing values of δ imply an increasing role of the $\mathcal{O}(\delta)$ contribution. When these two contributions balance with one another, a peak is reached, and then the magnitude of the linear δ term becomes dominant and a decreasing stage is observed, enforced by the decline of curvature.

The above discussion clarifies the role of the non-linear $\mathcal{O}(\nu^2)$ solution as the main agent able to produce autogenic width variations. As this solution attains its maximum value within the resonant range, one could expect a corresponding maximum response of width oscillations in the same range. A glance at Figure 8.4 suggests that this is not the case, because the maximum value of δ consistently occurs for larger values of β, say $\beta \simeq 1.5\,\beta_R$.

The reason for this unexpected behavior is related to the change of position of width maximum with respect to curvature distribution, the phase lag ψ_{width}, experienced as the length of meander develops in time. If ψ_{width} is relatively stable in time, the amplitude δ of width variations is enforced, because the $\mathcal{O}(\nu^2)$ contribution continuously acts at nearly the same position along the meander wavelength (e.g., figure 8.1c), while the growth of δ is weaker when the phase lag continuously shifts through the meander over time. Through equation (54d) the phase lag of width variations is driven by the phase of the U_{20} component, which is reported in Figure 8.7b in the (λ, β) plane, for given values of the flow parameters, reprojected on half-wavelength. In this plane meander trajectory in time corresponds to a shift of the intrinsic wavenumber λ from its initial value to smaller values as sinuosity increases. Therefore, the phase of the U_{20} component experi-

ences a strong variation as the meander develops in time except for a range of values of β ($\beta \simeq 22$–25 in Figure 8.7b) centered around $1.5\,\beta_R$, which corresponds to the range where the maximum amplitude of width oscillations is predicted by the model (figure 8.4). I note that also the flow parameters slowly vary in time as meander develops. However, their variation doesn't produce, at least qualitatively, any significant change with respect to the scenario reported in Figure 8.7b.

Coevolution and mutual interaction between autogenic width oscillations and curvature, as they emerge from the present model, can be further visualized through curves representing meander planform evolution in the (ν, δ) parameter space (Figure 8.8). In the first stage of meander development width oscillation amplitude is forced quadratically by curvature through the $\mathcal{O}(\nu^2)$ term. Furthermore, the peak of width variations often occurs earlier than the peak of curvature, leading to a temporal hysteresis whose amplitude is mainly controlled by the width ratio β. Hysteresis curves show that the peak of curvature ratio ν depends on the characteristics of the flow field only slightly, weakly decreasing with the aspect ratio, while the peak of δ changes with β as illustrated in Figure 8.4.

8.2.2 Theoretical predictions and field observations

Available field observations confirm the predicted tendency of variable width meanders to behave differently from their equiwidth counterparts and their specific attitude to display lower values of sinuosity (Luchi et al., 2011). Moreover, various investigations carried out at the reach scale (e.g., Knighton 1972; Richards 1976; Hooke 1986; Luchi et al. 2010a) provide field evidence of autogenic processes driving spatial variations of channel width associated with the formation of central bars (the non linear $\mathcal{O}(\nu^2)$ contribution in the present theory). It is beyond the scope of this thesis to pursue a detailed quantitative comparison of model predictions with field data, which would require the availability of a comprehensive data set on width variations dynamics in developing meanders. I therefore focus the attention on few examples that highlight the ability of the theoretical model to capture, at least qualitatively, some key features characterizing the style of variable width meanders.

Our co-evolutionary model suggests that width oscillations mainly develop under super-resonant conditions and attain peak values, expressed in terms of the dimensionless amplitude δ, falling in the range $0.15 \div 0.22$, for the sets of flow conditions examined. The above range of predicted δ-values is consistent with the results of field observa-

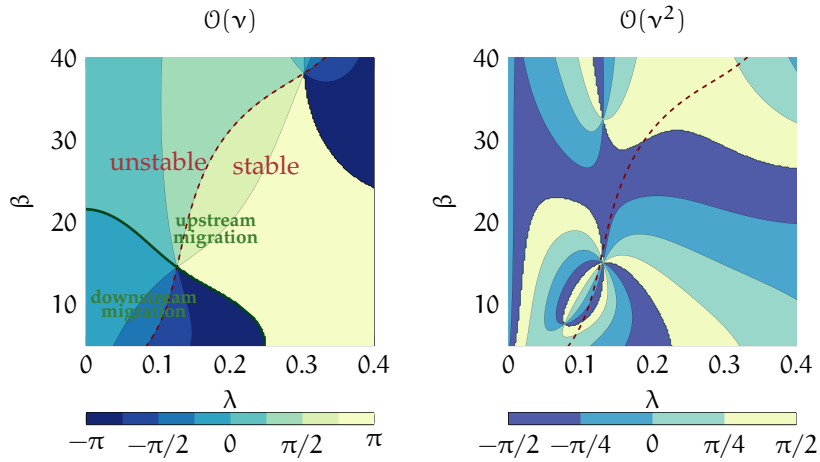

(a) The phase lag of U_{10}.

(b) The phase lag of U_{20}, reprojected on the half-wavelength.

Figure 8.7: The phase lag of the $\mathcal{O}(\nu)$ and $\mathcal{O}(\nu^2)$ perturbations of longitudinal velocity with respect to curvature distribution in the (λ, β) plane, with $\tau_* = 0.1$ and $d_s = 0.01$. The red dashed curve represents the marginal stability curve, separating unstable (meander formation) and stable conditions (meander suppression). The green continuous curve in panel *a* represents the separation between downstream migrating (mainly subresonant) and upstream migrating (mainly superresonant) meanders.

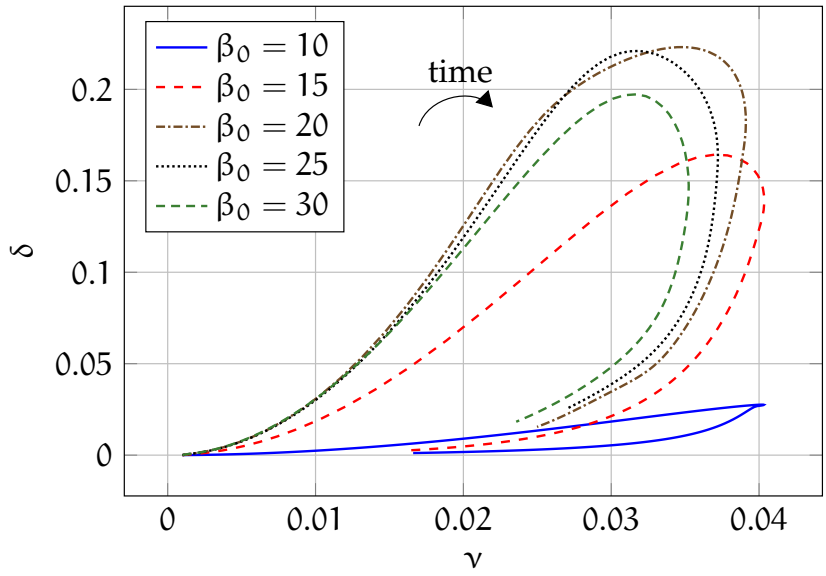

Figure 8.8: Temporal hysteresis curves in the coevolution of curvature and width variations in developing meanders, for different values of the aspect ratio β. Initial conditions: $d_s = 0.01, \tau_* = 0.1, \lambda_0 = 0.1$.

tions. In fact, Zolezzi et al., 2012b analyzed the dataset of Lagasse et al., 2004 and showed that width variation amplitudes of meandering rivers are generally of the order of $\mathcal{O}(10^{-1})$ and rarely attain values as large as 0.2.

Figure 8.9 illustrates the observed evolution of the centerline of two individual bends along Rio Beni and the resulting trajectories on the (ν, δ) plane, showing a hysteretic behavior similar to that predicted by the theoretical model, with the maximum curvature lagging behind the peak of δ. The figure also shows that sinuosity grows nearly monotonically as the meander bend develops in time.

In the following I use the information available in the large database compiled by Lagasse et al., 2004, where different styles of meanders were identified depending upon the intensity of spatial width oscillations, along with some data extracted from a preliminary analysis of evolutionary dynamics of width and curvature for some individual meander bends of two large highly dynamic, subtropical rivers, the Rio Beni (Bolivian Amazon) and the Rio Ucayali (Peruvian Amazon). The analysis was conducted through the remotely sensed image analysis software PyRIS (chapter 4). Each individual bend was isolated for each Landsat image frame (roughly one per year for thirty consecutive years between 1985 and 2015), and a bend scale analysis was performed to determine the local values of planform parameters (width,

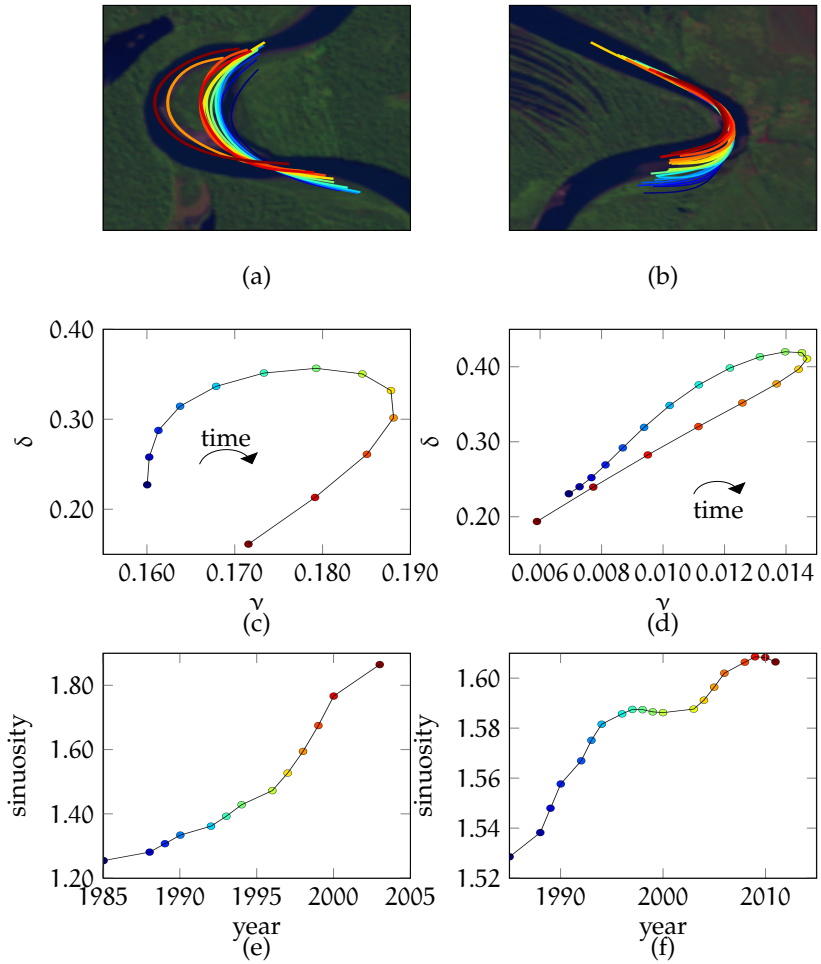

Figure 8.9: Evolutionary dynamics of width oscillation and curvature along two individual meander bends of the Rio Beni (Bolivian Amazon). (*a*, *b*) Multi-temporal positions of the channel centerline. Temporal spacing between subsequent centerlines is one-two years year. The underlying image is a 1996 Landsat (`landsat.usgs.gov`) false color. (*c*, *d*) Observed temporal relation between curvature ratio ν and amplitude of width oscillation δ. (*e*, *f*) Time growth of sinuosity. The colored marks represent the legend for panels (*a-d*).

curvature, Cartesian and intrinsic length). The examined reaches (400 km for the Rio Beni and 900 km for the Rio Ucayali) included nearly 240 and 270 meander bends respectively. Some of the bend could be monitored until cutoff.

The outcomes are reported in the box-plots of figure 8.10, in terms of the dimensionless parameters ν and δ. Being the age of individual bends not known a priori, here I use channel sinuosity as a proxy for bend age, allowing us to compare individual bends with a different evolutionary history and to build a statistical analysis over the entire reach and the whole three decades record of Landsat images. Therefore, figure 8.10 can be interpreted as a portrait of the overall temporal evolution of curvature and width oscillations along the examined reaches of Rio Beni and Rio Ucayali. The resulting average evolutionary trajectories of the parameters ν and δ are consistent with those predicted by the model (see figure 8.2b,d) and both exhibit a two-stage behavior characterized by a sharper growth in the initial stage. The peak value of curvature occurs when sinuosity is in the range $1.6 \div 1.8$. At larger values of sinuosity the curvature ratio ν follows a stage of slight decay, as predicted by the variable width model. On the other hand, after the peak δ-values keep nearly constant in the Rio Ucayali and slightly increases in the Rio Beni, while the model would predict a decreasing stage. Such discrepancy, might be related to the paucity of data with large sinuosity, and may also reflect the effect of missing ingredients in the present model. Among them: the allogenic role of the differences between of bank erosion and accretion rates at opposite banks, floodplain heterogeneity and the fine fraction of sediments of the investigated rivers.

Finally, hysteresis cycles of figure 8.8 highlight the weak dependence of the peak value of curvature on flow parameters even in the case of variable width. If I neglect the non-linear terms in system (57) I can readily derive an upper-bound value of curvature which is independent of hydrodynamics. By imposing

$$\frac{d}{dt}\nu = 0, \tag{67}$$

and keeping only the leading terms in (57)a,c I find that peak curvature is reached when the amplitude $|\theta_1|$ is equal to $1/\sqrt{2}$. Recalling (39) I then obtain:

$$\nu_{max} = \frac{1}{\sqrt{2}}\lambda_{max}, \tag{68}$$

where λ_{max} is the intrinsic wavenumber corresponding to the maximum curvature, whose relation with the initial value λ_0 can be obtained by interpolating the model results. I then find:

$$\nu_{max} \simeq 0.4\Lambda, \tag{69}$$

where Λ denotes the Cartesian wavenumber (which coincides with λ_0). I note that the above formula can be readily obtained from purely geometrical considerations. When tested on the whole dataset of Lagasse et al., 2004, for each river type of Brice, 1975's classification, equation (69) performs quite well, as most of the data fall below the predicted upper-bound, and correctly reproduces the dependence of curvature on the Cartesian length of meanders, as shown in figure 8.11. Furthermore, the predicted value of sinuosity at peak curvature, $\sigma|_{\nu_{max}} \simeq 1.77$, falls in the range where the largest values of ν are observed, according to the field data of figure 8.10a,c.

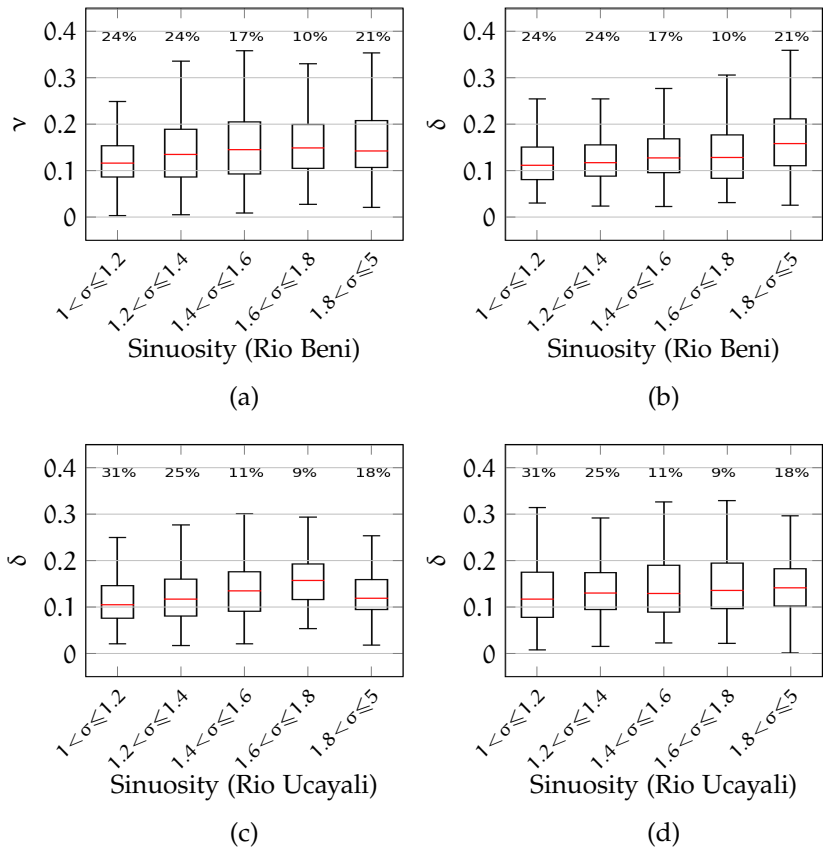

Figure 8.10: Reach-averaged evolution of meander bends of two large rivers from the Amazon basin extracted from three decades of Landsat images (1985-2015) of a 400 km reach (Rio Beni) and of a 900 km reach (Rio Ucayali). Box-plots of bend-scale values of: (*a*) curvature ratio ν, Rio Beni (Bolivian Amazon). (*b*) width oscillations δ, Rio Beni. (*c*) curvature ratio ν, Rio Ucayali (Peruvian Amazon). (*d*) width oscillations δ, Rio Ucayali. The upper and lower limits of boxes correspond to the 84th and 16th percentile, respectively, with vertical lines extending to the 95th and 5th percentile of the category. The percentage of bends, within the examined reach and the whole set of images, for each class of sinuosity σ is reported on top of each box.

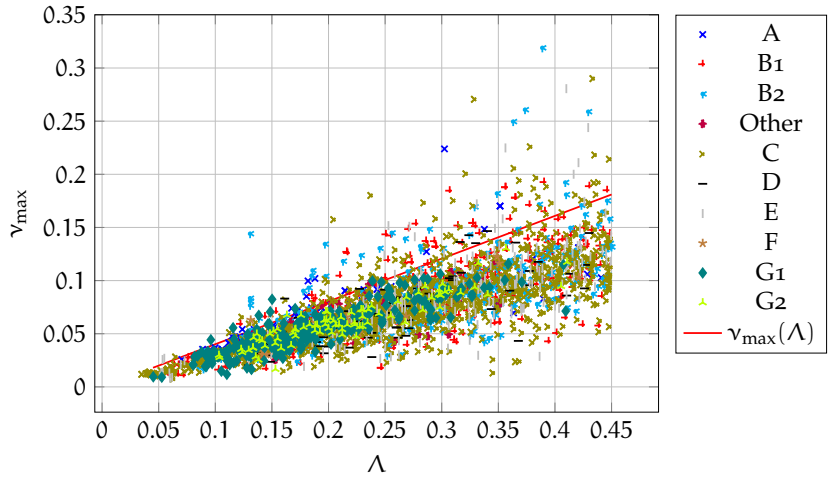

Figure 8.11: The predicted upper-bound value of peak curvature, ν_{max} is plotted as a function of the Cartesian wavenumber, Λ (red line), and is compared with observed values of curvature ratio, ν, from the whole dataset of Lagasse et al., 2004. River bends are classified according to Brice, 1975.

9 ALLOGENIC WIDTH CHANGE: THE ROLE OF BANK PULL AND BAR PUSH

The present chapter illustrates the results of the full nonlinear planform development model proposed at the end of section 5.3. The model couples autogenic and allogenic width oscillations and investigates the interaction between the two mechanisms, under the conditions of both bank pull-dominated ($\mathcal{K} > 0$) and bar push-dominated ($\mathcal{K} < 0$) planform development. The bankfull hydraulic geometry is computed through the model proposed in section 5.1 and extended in section 5.3 to account for nonlinear, curvature-driven contributions. The application of the full model is illustrated in section 9.1 and highlights the presence of two distinct hysteretic behaviors of amplitudes of curvature (ν) and width oscillation (δ)–one initially quadratic due to the autogenic mechanism, the other one initially linear due to the allogenic mechanism–that interact together giving rise to a more complex scenario for the total width oscillation. Whether the amplitude of the total width change is larger or smaller than that resulting from individual processes depends on the phase lags between the two; if they are out of phase, they produce a destructive interference which hampers the total width oscillation amplitude; on the contrary, they sum up in constructive interaction when they happen to be in phase. By exploring a range of parameters including the aspect ratio β and the timescales ratio $\mathcal{R}_T$, I find a minimum (in average) of width oscillation amplitude in purely autogenic conditions, while the largest width oscillation amplitudes are reached for higher absolute values of the bank shift ratio $\mathcal{K}$. In section 9.2 I discuss the results obtained through the model and I identify the range of parameters in the wavenumber-aspect ratio (λ, β) plane in which the interaction between autogenic and allogenic width oscillations is either constructive or destructive.

9.1 RESULTS

The present section reports the results of the planform development model presented in sections 5.2 and 5.3. The model requires initial conditions that were set as $\theta_{1_0} = 10^{-2}$, $\theta_{3_0} = 0$, $\lambda_0 = 0.1$, $\phi_{2_0} = 0$, $\tau_{*_0} =$

0.1, $d_{s_0} = 0.01$, while a range of values between 10 and 40 for the aspect ratio β_0 was investigated. Results presented herein refer to the following values of model parameters: (i) values for the ratio between planform and riverbed evolution timescales $\mathcal{R}_T = 10^0, 10^1, 10^2, 10^3$, (ii) $r_p = 0$ to neglect the percentage of bed material load in the floodplain sediment, (iii) 5 values of the normalized difference between erosion and accretion $\mathcal{K} = 0, \pm 0.1, \pm 0.2$, whereby a negative value represents a dominant bar push mechanism, a positive value a dominance of the bank pull mechanism, whereas $\mathcal{K} = 0$ suppresses the allogenic ratio and the width variation reduces to the autogenic one investigated in section 8.1. The role of the parameters $\mathcal{R}_T$ and r_p is investigated in section 7.1.

Figure 9.1 and 9.2 illustrate the planform evolution of a meandering river for two different values of the initial width-to-depth ratio β_0 and of the parameter $\mathcal{K}$. Panels 9.1a and 9.2a show the river centerline and banks when the centerline sinuosity σ is 80% of the sinuosity at cutoff σ_{cutoff}. Panels b and d show the amplitudes δ^{auto} and δ^{allo} and phase lags ω^{auto} and ω^{allo} of the autogenic and allogenic width oscillations, respectively, and their interaction. The autogenic width oscillation b^{auto} is defined as the one occurring when no allogenic contribution occurs and δ^{auto} is the amplitude of the autogenic oscillation. Conversely, the allogenic width oscillation b^{allo} is defined as the one occurring when no autogenic contribution occurs and δ^{allo} is the amplitude of the allogenic oscillation. The phase lags are defined as follows:

$$\omega^{auto} = -\frac{1}{2}\arg\left(b_2^{auto}\right), \quad \text{and} \quad \omega^{allo} = -\frac{1}{2}\arg\left(b_2^{allo}\right) \tag{70}$$

and they define the position of the widest cross section along an individual meander bend relatively to the bend apex of an equivalent sine-generated meander. Panels c report the three hysteresis curves for the channel curvature and the amplitudes of width variations.

Figure 9.1 shows an example of constructive interference between autogenic and allogenic width variations due to bar push-drive planform development ($\mathcal{K} < 0$); they both locate close to the inflection points ($\omega \simeq \pm\pi/2$) and their interference gives rise to a total width variation higher than that associated with individual autogenic and allogenic ones. The position is rather stable in time except some oscillations around incipient meander formation. The hysteresis curves show that the autogenic width variation is quadratically forced by the channel curvature ($\mathcal{O}(\nu^2)$), and the peak in autogenic width variation lags ahead the peak in channel curvature. On the other hand, the allogenic width variation is linearly forced by the channel curvature ($\mathcal{O}(\nu)$), therefore the allogenic behavior is linear. Its contribution sup-

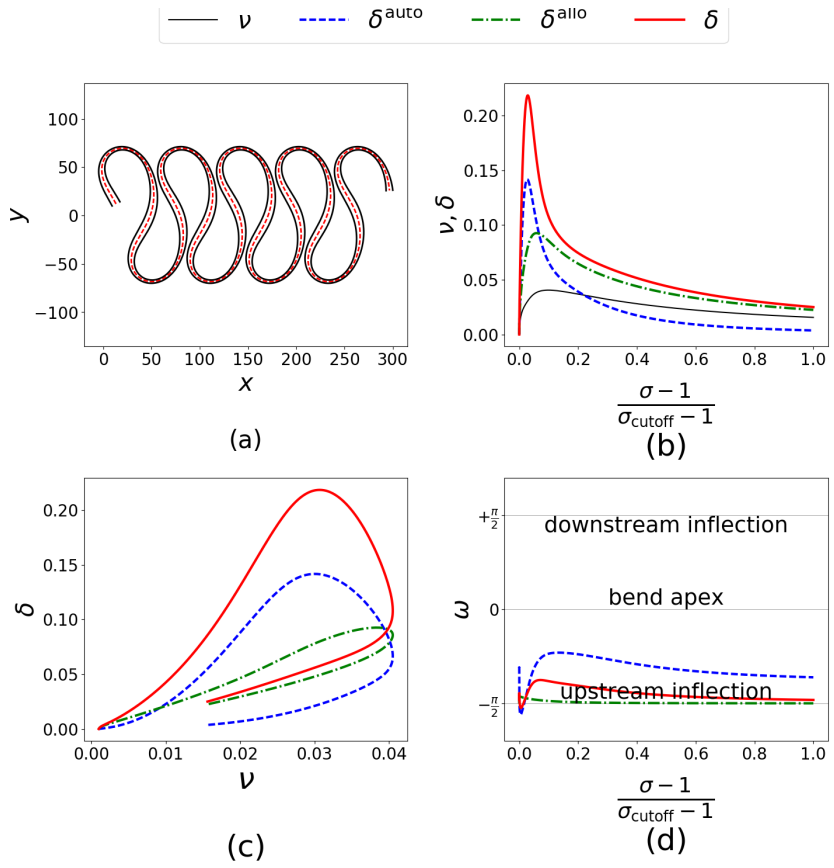

Figure 9.1: Planform evolution of a sequence of meander bends with self-evolving banks, $\mathcal{R}_T = 10$, $\mathcal{K} = -0.1$, initial conditions: $\beta = 35, \tau_* = 0.1, d_s = 0.01$ as a function of the norm alized sinuosity σ. Autogenic and allogenic width oscillations are in constructive interference. (*a*) River centerline (dashed red line) and banks (continuous black lines) during planform development (the channel width was rescaled for the sake of clarity). (*b*) Amplitudes of channel width oscillations. (*c*) Hysteresis curves of channel curvature and width variations. (*d*) Position of channel width oscillations.

ports the amplitude of width oscillation until cutoff, whereas the autogenic width oscillation decays rapidly after the peak holds up. Hence, in this case the bank pull process appears to be the process responsible for significant width oscillations in well developed meanders. The hysteresis of the total width oscillation amplitude δ is almost equal to the sum of the individual autogenic and allogenic hysteresis cycles.

Figure 9.2 reports the planform development of a meander with a positive $\mathcal{K}$, hence with a bank pull-driven planform development,

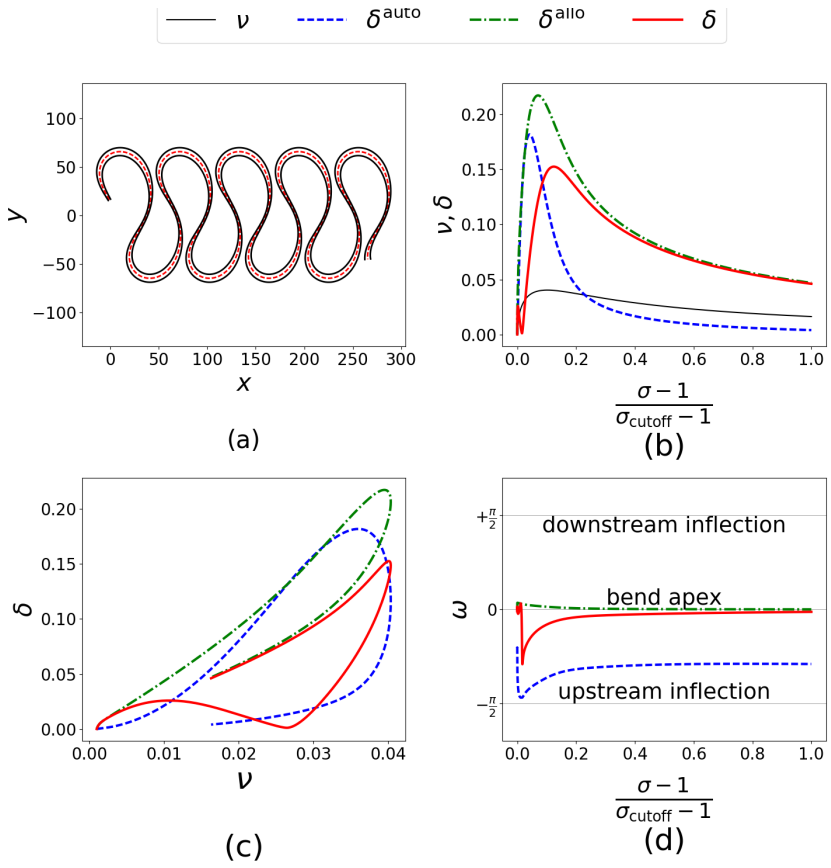

Figure 9.2: Planform evolution of a sequence of meander bends with self-evolving banks, $\mathcal{R}_T = 1$, $\mathcal{K} = +0.2$, initial conditions: $\beta = 30, \tau_* = 0.1, d_s = 0.01$ as a function of the norm alized sinuosity σ. Autogenic and allogenic width oscillations are in destructive interference. (*a*) River centerline (dashed red line) and banks (continuous black lines) during planform development (the channel width was rescaled for the sake of clarity). (*b*) Amplitudes of channel width oscillations. (*c*) Hysteresis curves of channel curvature and width variations. (*d*) Position of channel width oscillations.

leading to a *wider-at-bends* river pattern. However, the interference between autogenic and allogenic effects is destructive, due to the location of the autogenic width variation closer to meander inflections, while the latter shifts to the bend apex. The resulting amplitude of width variations δ is smaller than both the individual autogenic and allogenic ones and the resulting $\nu - \delta$ curve is rather complex. Except for oscillations in the beginning of the planform development, however, it recovers the shape of a hysteresis cycle with an intersection

before cutoff. The resulting width variation amplitude remains relevant until cutoff due to the presence of the allogenic width variation.

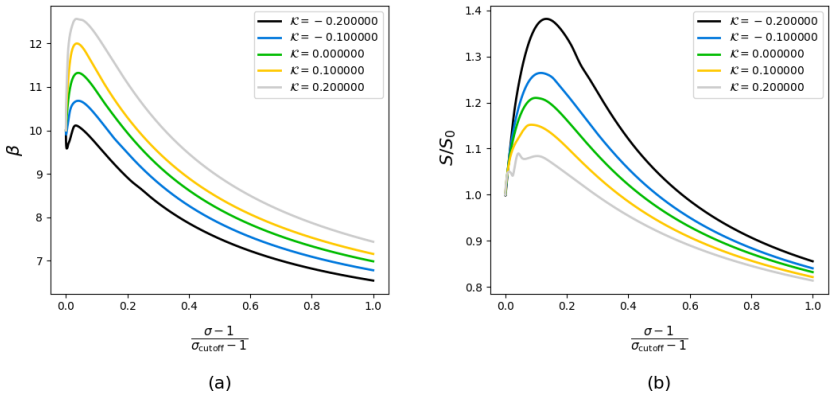

Figure 9.3: Evolution of the bankfull hydraulic geometry as a function of the bank shift ratio $\mathcal{K}$, with initial conditions $\beta = 10, \tau_* = 0.1, d_s = 0.01$. $\mathcal{R}_T$ was set to 10. (*a*) Aspect ratio. (*b*) Channel slope.

Figure 9.3 shows the evolution of the bankfull hydraulic geometry as a function of the parameter $\mathcal{K}$. The aspect ratio and the channel slope undergo a nonlinear increase in the initial stage of the planform development whose peak coincides with the peak in channel curvature, roughly around a sinuosity $\sigma \simeq 1.77$, see section 8.2, and lately to a decreasing stage. Section 7.1 shows that the magnitude of the drop in channel slope and aspect ratio depends on the parameter $\mathcal{R}_T$: larger values of magnitude of $\mathcal{R}_T$ would result in a rather stable bankfull hydraulic geometry, whereas values of $\mathcal{R}_T \sim \mathcal{O}(1)$ lead to a strong (sometimes nonphysical) decrease of channel slope and width. A bank pull-dominated planform development leads to a stronger initial bump and, in the late stage of the planform development, to larger channels with smaller bed slopes. On the contrary, bar push-dominated planform developments lead to slightly narrower channels with higher bed slope.

Figure 9.4 illustrates a more general picture of planform development of meandering rivers with freely variable width. The autogenic width variation (panel 9.4a) is mainly controlled by the initial aspect ratio of the channel; the curves appear to peak somewhere for values of $\beta > 30$, depending on the value of $\mathcal{K}$ which affects the peak amplitude δ_{max}^{auto} by changing the bankfull hydraulic geometry: an increasing value of $\mathcal{K}$ from -0.2 to +0.2 shifts the peak amplitude of the autogenic width oscillation towards lower values of aspect ratio β. The resonance aspect ratio is around $\beta_R \simeq 16$. On the contrary, the peak values of allogenic width variation amplitude δ_{max}^{allo} is almost equal to

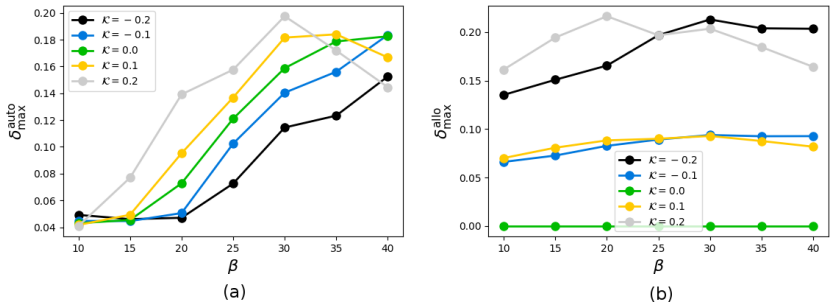

Figure 9.4: Width oscillation as a function of the aspect ratio for different values of $\mathcal{K}$, initial conditions $\tau_* = 0.1, d_s = 0.01$, timescale ratio $\mathcal{R}_\mathcal{T} = 10$. (*a*) Autogenic width oscillation amplitude. (*b*) Allogenic width oscillation amplitude.

the value of $\mathcal{K}$, regardless the value of the aspect ratio β (panel 9.4b), which has a very limited effect on it. The interaction between autogenic and allogenic width oscillation is reported in figure 9.5.

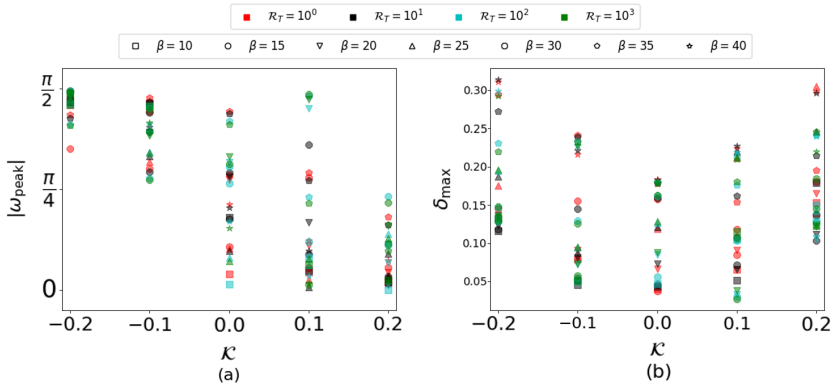

Figure 9.5: Influence of $\mathcal{K}$ on the channel width distribution. (*a*) Absolute distance between the widest section and the bend apex in radians at peak amplitude of width oscillation δ. $|\omega| = 0$ corresponds to the bend apex, $|\omega| = \pi/2$ to meander inflections. (*b*) Peak amplitude of width variations. The shape of the markers corresponds to the aspect ratio β, the color to the timescales ratio $\mathcal{R}_T$.

Figure 9.5 summarizes the results for the amplitude of width variations and the distance between the widest section and the bend apex for a range of parameters $\mathcal{R}_T$ spanning four orders of magnitude and β between 10 and 40. The location and magnitude of the autogenic contribution depends mainly on the change of phase of the nonlinear $\mathcal{O}(\nu^2)$ self-interaction of the channel curvature; although when $\mathcal{K} = 0$ width variations are distributed between the bend apex and meander

inflection, bank pull ($\mathcal{K} > 0$) shifts the widest section towards the bend apex, while bar push leads to a *wider-at-inflections* meandering pattern (figure 9.5a). The presence of bar push or bank pull enforces the magnitude of width variations (figure 9.5b), whereas a purely autogenic scenario ($\mathcal{K} = 0$) displays on the average a lower amplitude of width variations; when either one of the allogenic mechanisms occurs, leads to total width variation amplitudes δ up to 0.3, while the purely autogenic width variation is bounded to a maximum of 0.2.

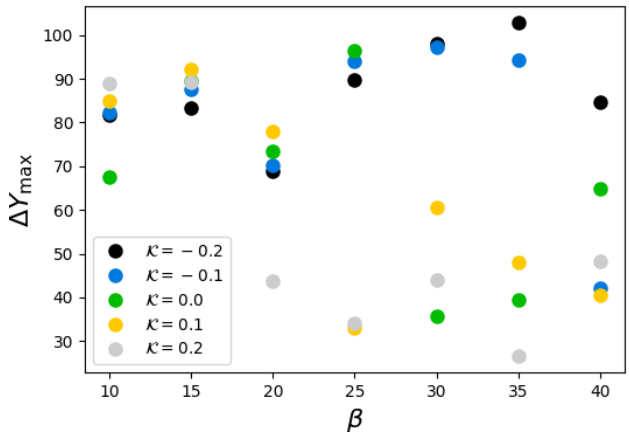

Figure 9.6: Dimensionless floodplain width as a function of the initial aspect ratio β and of the ratio between bank shift rates $\mathcal{K}$ for $\mathcal{R}_T = 100$.

Figure 9.6 shows the floodplain width (made dimensionless by dividing by the channel width) required by freely evolving periodic meandering rivers, as a function of the aspect ratio β and for different values of $\mathcal{K}$. The resonant value $\beta_R \simeq 16$, hence the floodplain width values start separating close to the resonance. This separation was observed also in section 8.1, where a different bankfull hydraulic geometry model is used and only autogenic width variations occur. The largest floodplain width occurs for small values of β and for negative values of $\mathcal{K}$ (bar push-dominated planforms). On the contrary, for large values of β with $\mathcal{K} \geqslant 0$ the floodplain width reduces considerably. However, such an effect is suppressed in bar push-dominated meanders, whereby a $\mathcal{K} < 0$ appears to inhibit the process of floodplain width reduction.

9.2 DISCUSSION AND CONCLUSIONS

This work provides a mathematical framework for meandering morphodynamic modeling that couples together several aspects of the planform development of river meanders. I restricted the attention to periodic meandering planform due to the complexity of the problem: an extension to arbitrary curvature and width distributions would involve a considerable amount of algebra. Significant step towards a generic planform descriptor were made by Zolezzi and Seminara, 2001a, who developed a linear analytical solution for the flow field and sediment transport in channels with arbitrary spatial curvature distributions, and by Frascati and Lanzoni, 2013, who extended such solution to include the effects of spatially varying channel width.

Nevertheless, the solution proposed herein allows to fully analyze the mutual interactions between curvature and width during the planform development of meanders, which requires a nonlinear analysis to include curvature self-interactions $\mathcal{O}(\nu^2)$ forcing autogenic width oscillations and mixed interactions $\mathcal{O}(\nu\delta)$ providing the feedback of width variations on curvature evolution. Furthermore, the analytical treatment of the allogenic process requires a periodic distribution of the channel curvature as well. The evolution of channel curvature and channel width variations is overimposed to a bankfull hydraulic geometry that changes in time according to the evolution of the channel planform. The model requires a large number of parameters whose effect on the planform development would require a deep insight and a quantification from field data. However, this is beyond the aim of the present chapter.

The present model allowed us to investigate the mutual interaction between autogenic and allogenic width variations during planform evolution. Such an interaction was shown to be either constructive or destructive, depending on the phase lags of the solutions for the channel curvature and the channel width. Figure 9.1 shows an example of constructive interaction, while a destructive interaction is reported in figure 9.2. Figure 9.7 shows the areas on the (λ, β) plane where the interaction occurs either as constructive or destructive inteference, depending on the difference between the phase lags of the $\mathcal{O}(\nu)$ and $\mathcal{O}(\nu^2)$ solutions.

The green line discriminates between unstable (left) and stable (right) meanders, hence I only consider the left hand side of the plane. The magenta line is the line discriminating between downstream (below the curve) and upstream (above the curve) meander migration, according to the linear theory; the intersection with the marginal stability curve represents the resonant aspect ratio (Blondeaux and Seminara, 1985; Seminara et al., 2001; Lanzoni and Seminara, 2006). Figure 9.7

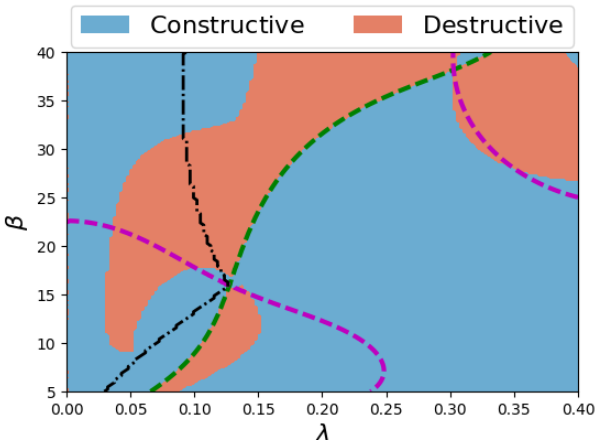

Figure 9.7: Areas of constructive and destructive interference between autogenic and allogenic width variations on the λ, β plane, for $\tau_* = 0.1, d_s = 0.01$ and $\mathcal{K} > 0$. For $\mathcal{K} < 0$ the scenario is reversed. The green line indicates meander stability, the black line represents maximum bend amplification.

tells an interesting story on the interaction between autogenic and allogenic width variations: subresonant meanders (area subtended to the magenta curve) experience a dominantly constructive interference and, specifically, the selection of meander wavelengths (maximum amplification curve) occurs in the constructive interference area. On the contrary, the selection of meander wavelengths in the superresonant regime (area above the magenta line lying on the maximum amplification line) occurs mainly in the destructive interference area (note that in bankfull conditions it is rare to find meandering rivers aspect ratios larger than 30).

The dynamics of mutual interaction between autogenic and allogenic width variations and curvature are affected by the evolution of the bankfull hydraulic geometry, which strongly depends on the ratio between floodplain and riverbed timescales $\mathcal{R}_T$. For low values of $\mathcal{R}_T$ the bankfull hydraulic geometry exhibits significant change during the planform development, leading to a reducing aspect β. In this scenario the constructive-destructive interference is subjected to change related to the variation of λ and β in the diagram in figure 9.7, but also in a change of the diagram itself due to the change in the bankfull flow conditions (τ_*, d_s). On the contrary, high values of $\mathcal{R}_T$ lead to a bankfull hydraulic geometry that keeps almost constant, hence β does not change when reducing λ during planform development; in the above scenario this may lead to an initially constructive and lately

destructive interference when $\beta > 10$, and to a constantly constructive interference when $\beta < 10$.

The coevolution of width variations and curvature during planform development was modeled by Eke et al., 2014a through a numerical model. The presence of the allogenic mechanism was ensured by the parameter $\gamma = E/A$. Although the bank erosion mechanism is described by a much more sophisticated model than the one implemented herein, the results they obtained are very similar to the ones provided by the present model. They showed a changing of position of width maxima when changing the parameter γ: high values of γ led to wider-at-bends configurations, whereas low values led to wider-at-inflections. However, although the mechanism of bar push/bank pull mechanism was analyzed in-depth in their work, the autogenic mechanism forcing width variations when $\gamma = 1$ was not clear. Particularly, a numerical model does not allow to separate the individual physical processes of autogenic and allogenic width change and to investigate their interaction.

10 ALTERNATE MIGRATING BARS AND MEANDERING

In this chapter I perform a strong, systematic integration between analytical nonlinear modeling and remote sensing in order to isolate the key factors governing the existence of migrating bars in large natural meandering rivers. I feed the theoretical model developed by Seminara and Tubino, 1989; Tubino and Seminara, 1990 with the hydraulic and planform data for the rivers presented in section 6.1 and show that the key control on the possibility of existence of migrating bars in meandering rivers in the sediment supply: meandering rivers with low sediment supply may form migrating bars, whereas meandering rivers with high sediment supply preferentially develop steady bars.

10.1 A BRIEF THEORETICAL BACKGROUND

The possibility of existence of alternate bars in meandering rivers was first investigated by Tubino and Seminara, 1990 through a nonlinear analytical perturbation model. The model structure is similar to the one presented in section 5.2 of this thesis, in the sense that two small parameters are identified and their interaction is expressed into an evolutionary equation. The two-dimensional flow field and sediment transport (corresponding to equations 30) is perturbed in the neighborhood of the reference normal flow conditions through two "small" parameters ν and ϵ, the latter defined as

$$\epsilon = \max\left(0, \frac{\beta - \beta_c}{\beta_c}\right), \tag{71}$$

where $\beta_c(\tau_*, d_s)$ is the critical aspect ratio: when the aspect ratio of the reference flow conditions is below the critical threshold alternate migrating bars cannot form, regardless the value of the curvature ratio ν. The square root of the value of ϵ represents the scale of the amplitude A_{bar} of alternate bars.

Under the assumption that $\mathcal{O}(\nu^2) \sim \mathcal{O}(\epsilon)$, the theory provides an evolutionary equation for the amplitude of alternate bars, which is valid at incipient bar formation, that reads:

$$\frac{dA_{bar}}{dt} = \left(a_1 + a_2 \frac{\nu^2}{\epsilon} \right) A_{bar}, \tag{72}$$

where a_1 and a_2 are coefficients depending on the reference flow conditions (β, τ_*, d_s) and on meander wavenumber λ. Equation (72) shows that alternate migrating bars may form in meandering rivers only when $\nu/\sqrt{\epsilon}$ is larger than a threshold depending on the reference flow conditions (provided $\beta > \beta_c$). Hence, one can defined a *critical curvature for alternate migrating bar suppression* $\nu_c(\beta, \tau_*, d_s, \lambda)$ such that alternate migrating bars may only form when $\nu < \nu_c$. The latter result had people for a couple of decades thinking that only rivers with low curvature ratios may form alternate migrating bars. However, the results reported in figure 6.5 of section 6.1 show that the reference (median) curvature ratio does not vary significantly between the selected river reaches, although some of them display alternate migrating bars whereas some do not.

10.2 RESULTS

The parameters involved in the analysis are four: three hydraulic parameters (β, τ_*, d_s) whose calculation relies on both literature data, gauging data and remote sensing analysis (channel widths and slopes), and two planform parameters (λ, ν) computed through statistical and spectral analysis of remotely sensed data. The methods employed are reported in section 6.1.

It is worth highlighting how the reference flow parameters depend strongly on the sediment supply (TSS) per unit width through exponential relationships of the type[1]

$$\text{parameter} = a \, (TSS^*/W^*)^b \, . \tag{73}$$

Figure 10.1 show the regression curves of the reference hydraulic and planform parameters, while table 10.1 reports the coefficients a, b and the regression correlation R^2 together with the p values for the t-test (p_t) and the Kruskal-Wallis test (p_{kw}) for the two groups (*observed steady* and *observed migrating*).

1 I deliberately correlate the TSS with the sediment supply, consistently with Constantine et al., 2014. It is a rather weak hypothesis though it has support in the fact that Amazon rivers did not experience the small glaciation that involved european rivers, hence Amazon rivers may be considered as close to equilibrium.

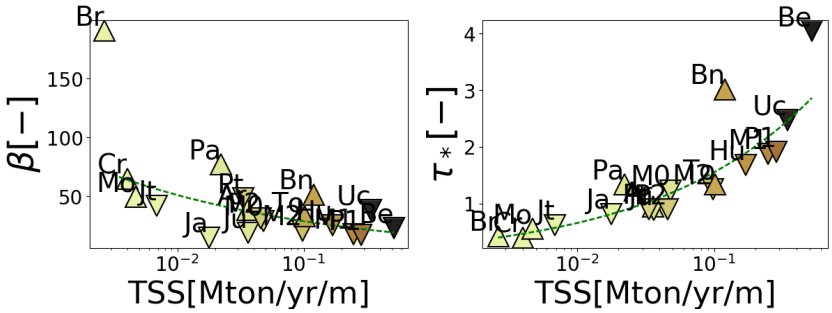

(a) Nonlinear regression of the aspect ratio.

(b) Nonlinear regression of the Shields stress.

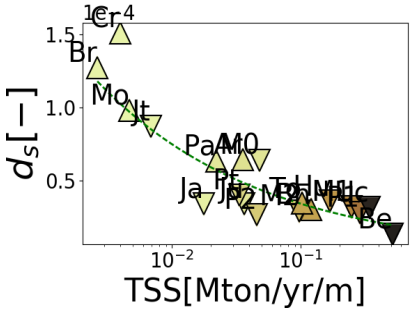

(c) Nonlinear regression of the relative roughness.

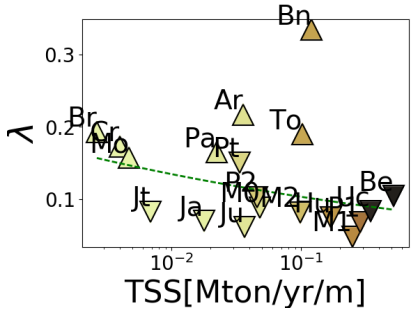

(d) Nonlinear regression of the reference meander wavnumber.

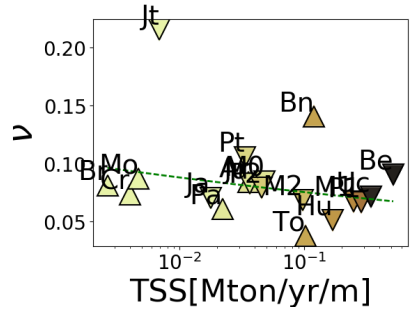

(e) Nonlinear regression of the reference curvature ratio.

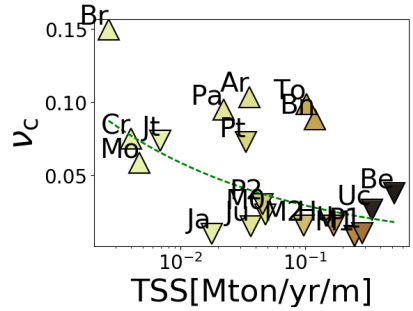

(f) Nonlinear regression of the critical curvature threshold.

Figure 10.1: Nonlinear regression for the reference hydraulic and planform parameters. Upward facing triangles are associated with migrating bars, downward facing triangles with steady bars.

variable	a	b	R^2	p_t	p_{kw}
β	17.189	−0.227	−0.642	0.00800	0.00091
τ_*	3.632	0.369	0.945	0.24654	0.16491
d_s	0.000	−0.311	−0.876	0.00418	0.01087
λ	0.078	−0.120	−0.411	0.00001	0.00021
ν	0.068	−0.045	−0.224	0.64360	1.00000
ν_c	0.016	−0.276	−0.531	0.00001	0.00039

Table 10.1: Regression data for the reference hydraulic and planform parameters.

The R^2 values indicate a good correlation between the reference hydraulic parameters and the sediment supply per unit width, although this is quite obvious for the Shields stress τ_*, which is directly computed from the TSS. On the other hand, meander wavenumber has a weak decreasing trend with the TSS per unit width, whereas the curvature ratio, as already shown in section 6.1, has no significant trend, which means that there is no significant difference between the reference curvature ratio of all the analyzed reaches. A more significant trend exists in the critical curvature threshold ν_c, which shows a decreasing trend with the TSS per unit width. It is also important to notice that ν_c has very low values of p_t and p_{kw}, meaning that there is a net distinction in the critical curvature threshold between meandering rivers with and without migrating bars. Such a distinction is inherited from the meander wavenumber, which also has an analogous distinction. Furthermore, according with the theoretical meander morphodynamic models (Blondeaux and Seminara, 1985; Seminara et al., 2001), the meander wavenumber is selected according to the most unstable modes, depending on the values of the reference hydraulic parameters β, τ_*, d_s, which in turn depend almost univocally on the sediment supply per unit width as shown above.[2] Hence, the sediment supply per unit width appears to be the key control on the existence of migrating bars in meandering rivers.

Figure 10.2 shows the comparison between the observed data and application of the nonlinear analytical model fed by remotely sensed and measured data.

2 The most unstable mode for given τ_*, d_s is shown in figure 9.7.

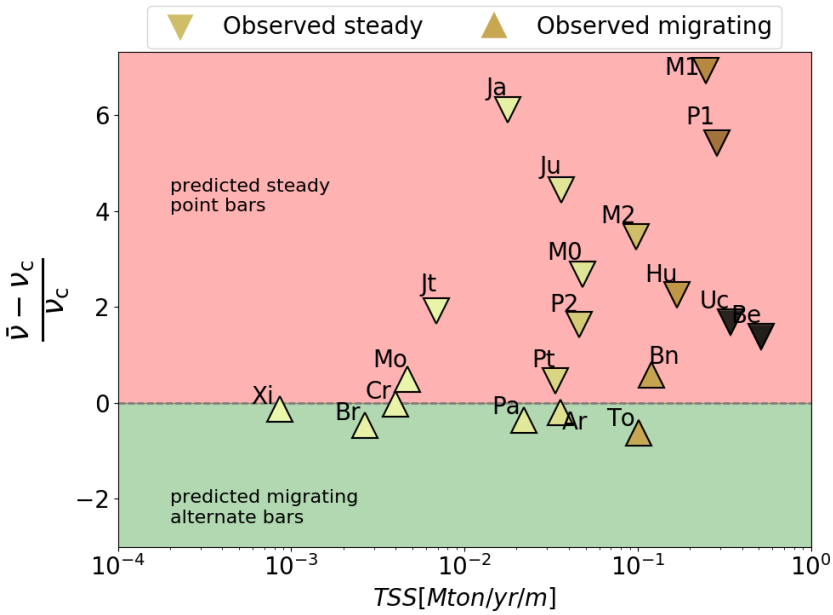

Figure 10.2: Observed vs predicted dominant bar style for the analyzed river reaches.

Except for the Rio das Mortes and the Rio Benue, that slightly exceed the threshold although they display migrating bars, the predicted results fit the observed ones. Moreover, despite the data scattering and the two rivers that have a wrong prediction, the trend in the normalized parameter $(\nu - \nu_c)/\nu_c$ shows quite clearly that the TSS per unit width plays a key role in controlling the bar style.

10.3 DISCUSSION AND CONCLUSIONS

The present chapters illustrates a fully integrated application of nonlinear modeling and remote sensing including data from gauging stations and literature. Despite the huge uncertainty in the retrieved data and the intrinsic spatial and temporal variability of natural meandering rivers that required to be simplified through statistics or spectral methods, the results are surprisingly consistent. Although a couple of test cases were wrong, the majority of the bar styles were correctly predicted.

The main outcome of this chapters is maybe that it is possible to integrate in-depth remotely sensed data into analytical models.

Moreover, I identified the key control on the bar style in natural meandering rivers. It is perhaps counter-intuitive that rivers with

lower sediment availability have higher bedform mobility, although they have the lowest planform mobility.

I here attempt to provide a brief mechanistic explanation on the reason why low supplied river reaches promote movable bedforms.

When there is high sediment supply, and enough (relative) curvature, the mechanism of sediment deposition is such that the bar accretion occurs laterally, and this persistently pushes the opposite bank to erode selectively and to continuously generate meandering at a rate that positively correlates with the TSS. This behavior was empirically observed by Constantine et al., 2014 for most of the rivers analyzed in the present thesis. Instead, in low sediment supplied river reaches the phase lag between the hydrodynamic shear and the bar morphology creates more favorable zones of sediment deposition immediately downstream the bar head and associated favorable zones of sediment entrainment at the bar tail, thus promoting the downstream migration of the bars.

Part IV

CONCLUSIONS

11 CONCLUSIONS AND FUTURE PERSPECTIVES

In this chapter I will briefly recall the main conclusions followed by some future perspectives. For a more in-depth overview of the discussion and conclusions the reader is referred to the related sections in the individual chapters of this thesis. Section 11.1 reports the brief summary of conclusions, with particular focus on the initial research questions. Section 11.2 introduces some ideas tackling with the question "where do we go from here?", either in terms of remote sensing analysis, of analytical modeling and their integration.

11.1 SUMMARY OF CONCLUSIONS

The core research objective of the present thesis is the integration of remote sensing and analytical modeling in the context of river morphodynamics for meandering and transitional patterns. The increasing availability of multitemporal datasets supports the idea that large scale, real world data is becoming more and more important in the study of the evolutionary dynamics of rivers, in terms of bedforms and planform. In this work I presented the software PyRIS, which allows to extract extensive morphodynamic information from multitemporal Landsat data. The choice of the Landsat data was mainly driven by the temporal span, starting in 1975 (1984 for good quality images) and hence allowing a 30+ years observation with two-three weeks of temporal resolution. The spatial resolution is quite low (30m) and hence the analysis is inevitably limited to large scale rivers (herein Amazonian rivers were considered).

On the other hand, a nonlinear analytical model for the evolutionary planform dynamics of meandering rivers incorporating bankfull hydraulic geometry, channel curvature and width oscillations was developed.

The submodel for the bankfull hydraulic geometry couples the effects of meander elongation with those of sediment supply conservation, leading to a more reliable formulation with respect to the one that is usually adopted in meander morphodynamic models. The

bankfull hydraulic geometry evolves in time through a reduction of the channel width and slope. The magnitude of the reduction is regulated by the parameter $\mathcal{R}_T$ representing the ratio between the planform timescale and the riverbed timescale. Estimates of $\mathcal{R}_T$ are computed for a number of pristine meandering rivers and the values mostly span within the range $10^1 \div 10^2$. According to the submodel, high values of $\mathcal{R}_T$ lead to a weak change of the bankfull hydraulic geometry, while low values lead to larger variations of the bankfull hydraulic geometry through time.

The model also accounts for "autogenic" (internally driven) and "allogenic" (bar push/bank pull driven) width oscillations and their feedbacks on the planform evolution of the channel curvature.

The data was analyzed in a systematic fashion and feedbacks for the theoretical predictions were found. Specifically, the multitemporal analysis of bend scale planform dynamics provided good support to model predictions:

A. the bankfull channel width slightly diminishes, on average, during the plan form development of meander bends;

B. meander wavenumber diminishes while the curvature ratio displays a growing phase followed by a decreasing phase;

C. width oscillations show a behaviour that is sometimes similar to that of the curvature (increasing and decreasing), while in other cases the display more complex trends;

D. the hysteresis between the amplitudes of curvature and width oscillations are observed in individual meander bends.

Moreover, the dynamics of migrating alternate bars along meander bends were analyzed: a strong dependence of the migration rate and wavenumber of migrating bars on the local planform structure was observed. On one hand, channel curvature reduces both the migration rate and wavenumber, leading to bars that are, in a sense, more similar to point bars. On the other hand, the channel width promotes shorter and faster bars, up to some limit where more complex processes come into play.

Finally, the existence of migrating alternate bars is analyzed by a full integration between analytical model and remote sensing: the model proposed by Tubino and Seminara, 1990 is fed with reference flow data retrieved from literature, gauging stations and information derived from postprocessing of remotely sensed data. The results are surprisingly consistent, despite the complexity and variability of the analyzed reaches, and highlight the key driver of the instream bar

regime: rivers with low sediment supply are migrating bars prone, while river with high sediment supply promote steady point bars.

The applications illustrated in the present thesis support to the idea that an integration between remote sensing and analytical models provides an extraordinary research tool: not only to get feedbacks from nature, but also to study and understand complex processes and to identify and isolate their drivers.

11.2 PERSPECTIVES

The work proposed in the present thesis open the way to a systematic integration between meander morphodynamic models and remote sensing. The increasing availability of remotely sensed datasets of higher and higher spatial and temporal resolution will build, in few years, a number of consistent datasets. The Sentinel databases from the ESA (European Space Agency) have a spatial resolution three times higher than that of Landsat images; however, the Sentinel mission is much more recent and therefore does not provide (yet) tens of years of earth surface scanning. However, the data sources are constantly increasing and it is inevitable to think about a constantly growing interaction between mathematical models and remotely sensed data. In this sense, an extension of PyRIS to a larger range of image sources would be the first challenge to address.

In the context of analytical modeling, on the other hand, the proposed model found good agreement, from both a qualitative and a quantitative point of view, with remotely sensed data. Its validity, especially in terms of bankfull hydraulic geometry, should be further investigated once elevation data become systematically available, in order to verify whether the assumptions made on the channel slope find agreement in the real world.

The entire analytical model should be further extended to the case of arbitrary curvature and width distributions; however, is should be kept in mind that several difficulties may arise in this case, since the analytical treatment of arbitrary curvature and width variations in a nonlinear context would increase exponentially the complexity of the mathematical formulation.

BIBLIOGRAPHY

Aalto, R., J. W. Lauer, and W. E. Dietrich

2008 "Spatial and temporal dynamics of sediment accumulation and exchange along Strickland River floodplains (Papua New Guinea) over decadal-to-centennial timescales", *Journal of Geophysical Research: Earth Surface*, 113, F1, F01S04, ISSN: 2156-2202, DOI: 10.1029/2006JF000627, http://dx.doi.org/10.1029/2006JF000627. (Cited on pp. 25, 65.)

Abad, J. D., G. C. Buscaglia, and M. H. Garcia

2008 "2D stream hydrodynamic, sediment transport and bed morphology model for engineering applications", *Hydrological processes*, 1459, August 2007, pp. 1443-1459, DOI: 10.1002/hyp. (Cited on p. 14.)

Abad, J. D., J. Vizcarra, J. Paredes, H. Montoro, C. Frias, and C. Holguin

2013 "Morphodynamics of the upper Peruvian Amazonian rivers, implications into fluvial transportation", in *International Conference IDS2013 -Amazonia*, Iquitos, Perú, pp. 1-10. (Cited on p. 14.)

Abizaid, C.

2010 "An anthropogenic meander cutoff along the Ucayali River, Peruvian Amazon", *Geographical Review*, 95, pp. 122-135, DOI: 10.1111/j.1931-0846.2005.tb00194.x. (Cited on pp. 7, 61, 65.)

Adami, L., W. Bertoldi, and G. Zolezzi

2016 "Multidecadal dynamics of alternate bars in the Alpine Rhine River", *Water Resources Research*, 52, 11, pp. 8938-8955, ISSN: 1944-7973, DOI: 10.1002/2015WR018228, http://dx.doi.org/10.1002/2015WR018228. (Cited on pp. 8, 10, 23, 65.)

Andersen, I. and K. G. Golitzen

2005 *The Niger river basin: A vision for sustainable management*, World Bank Publications. (Cited on p. 99.)

Armijos, E., A. Crave, P. Vauchel, P. Fraizy, W. Santini, J. S. Moquete, N. Arevalo, J. Carranza, and J. L. Guyot

2013 "Suspended sediment dynamics in the Amazon River of Peru", *Journal of South American Earth Sciences*, 44, pp. 75-84, DOI: http://dx.doi.org/10.1016/j.jsames.2012.09.002. (Cited on p. 99.)

Asahi, K., Y. Shimizu, J. Nelson, and G. Parker

2013 "Numerical simulation of river meandering with self-evolving banks", *Journal of Geophysical Research: Earth Surface*, 118, 4 (Dec. 2013), pp. 2208-2229, ISSN: 21699003, DOI: 10.1002/jgrf.20150, http://doi.wiley.com/10.1002/jgrf.20150. (Cited on pp. 14, 21, 37.)

Bai, X., L. J. Latecki, and W. Liu

2007 "Skeleton pruning by contour partitioning with discrete curve evolution", *IEEE transactions on pattern analysis and machine intelligence*, 29, 3, pp. 449-462. (Cited on p. 48.)

Begnudelli, L., A. Valiani, and B. F. Sanders

2010 "Advances in Water Resources A balanced treatment of secondary currents, turbulence and dispersion in a depth-integrated hydrodynamic and bed deformation model for channel bends", *Advances in Water Resources*, 33, 1, pp. 17-33, ISSN: 0309-1708, DOI: 10.1016/j.advwatres.2009.10.004, http://dx.doi.org/10.1016/j.advwatres.2009.10.004. (Cited on p. 14.)

Bisht, T., F. Monegaglia, S. Gramada, G. Zolezzi, and M. T. Pusch

in prep. "Morphometrics and morphodynamics of tight meander bends in a lowland European meandering river over one century", *Geomorphology*. (Cited on p. 52.)

Blondeaux, P. and G. Seminara

1985 "A unified bar–bend theory of river meanders", *Journal of Fluid Mechanics*, 157, 157, pp. 449-470, DOI: 10.1017/S0022112085002440. (Cited on pp. 4, 11, 22, 33, 70, 85, 112, 154, 174, 180.)

Bolla Pittaluga, M., R. Luchi, and G. Seminara

2014 "On the equilibrium profile of river beds", *Journal of Geophysical Research: Earth Surface*, 119, 2, pp. 317-332, ISSN: 21699011, DOI: 10.1002/2013JF002806. (Cited on p. 31.)

Brice, J. C.

1975 *Air Photo Interpretation of the Form and Behaviour of Alluvial Rivers*, tech. rep., U.S. Army Research Office, Washington University, 10p. (Cited on pp. 7, 33, 38, 82, 164, 166.)

1982 *Stream channel stability assessment*, tech. rep., Federal Highway Administration, US Department of Transportation, 42p. (Cited on pp. 6, 7, 12.)

Butler, H.

2004 "A guide to the Python Universe for ESRI users", in *Annual ESRI International Conference, San Diego, California, USA*. (Cited on p. 44.)

Callander, R. A.

1969 "Instability and river channels", *Journal of Fluid Mechanics*, 36, pp. 365-480. (Cited on pp. 8, 11.)

Camporeale, C., P. Perona, A. Porporato, and L. Ridolfi

2005 "On the long-term behavior of meandering rivers", *Water Resources Research*, 41, 12 (Dec. 2005), pp. 1-13, ISSN: 00431397, DOI: 10.1029/2005WR004109, http://doi.wiley.com/10.1029/2005WR004109. (Cited on pp. 37, 70.)

2007 "Hierarchy of models for meandering rivers and related morphodynamic", *Reviews of Geophysics*, 45, 2005, pp. 1-28. (Cited on pp. 31, 37, 70.)

Camporeale, C., E. Perucca, and L. Ridolfi

2008 "Significance of cutoff in meandering river dynamics", *Journal of Geophysical Research: Earth Surface*, 113, F1, F01001, n/a-n/a, ISSN: 2156-2202, DOI: 10.1029/2006JF000694, http://dx.doi.org/10.1029/2006JF000694. (Cited on pp. 23, 29.)

Carlson, T. N. and D. A. Riziley

1997 "On the relation between NDVI, Fractional Vegetation Cover, and Leaf Area Index", *Remote Sensing of Environment*, 62, pp. 241-252. (Cited on pp. 15, 24, 45.)

Chen, D. and J. G. Duan

2006 "Modeling width adjustment in meandering channels", *Journal of Hydrology*, 321, 1-4 (Apr. 2006), pp. 59-76, ISSN: 00221694, DOI: 10.1016/j.jhydrol.2005.07.034, http://linkinghub.elsevier.com/retrieve/pii/S002216940500377X. (Cited on pp. 31, 33, 83.)

Chinenyeze, M. A. J. and B. N. Ozibo

2017 "Geology of parts of Gboko and Makurdi Local Government Areas, Benue State, Nigeria", *International Journal Geology and Mining*, 3, 1, pp. 71-80. (Cited on p. 99.)

Choi, W., K. Lam, and W. Siu

2003 "Extraction of the Euclidean skeleton based on a connectivity criterion", *Pattern Recognition*, 36, 3, pp. 721-729. (Cited on p. 48.)

Colombini, M., G. Seminara, and M. Tubino

1987 "Finite-amplitude alternate bars", *Journal of Fluid Mechanics*, 181, pp. 213-232. (Cited on pp. 8, 9, 22, 130.)

Constantine, J. A.

2006 *Quantifying the Connections Between Flow, Bar Deposition, and Meander Migration in Large Gravel-Bed Rivers*, PhD thesis, University of California, Santa Barbara. (Cited on pp. 24, 65.)

Constantine, J. A., T. Dunne, J. Ahmed, C. Legleiter, and E. D. Lazarus

2014 "Sediment supply as a driver of river meandering and floodplain evolution in the Amazon Basin", *Nature Geoscience*, 7, 12, p. 899. (Cited on pp. 7, 12, 15, 24, 27, 29, 33, 43, 65, 99, 178, 182.)

Constantine, J. A., S. R. McLean, and T. Dunne

2009 "A mechanism of chute cutoff along large meandering rivers with uniform floodplain topography", *Geological Society of America Bulletin*, 122, 5-6 (Dec. 2009), pp. 855-869, ISSN: 0016-7606, DOI: 10.1130/B26560.1, http://gsabulletin.gsapubs.org/cgi/doi/10.1130/B26560.1. (Cited on pp. 14, 23.)

Coulthard, T. J. and M. J. Van De Wiel

2006 "A cellular model of river meandering", *Earth Surface Processes and Landforms*, 31, 1, pp. 123-132, ISSN: 1096-9837, DOI: 10.1002/esp.1315, http://dx.doi.org/10.1002/esp.1315. (Cited on p. 37.)

Crosato, A., F. B. Desta, J. Cornelisse, F. Schuurman, and W. S. J. Uijttewaal

2012 "Experimental and numerical findings on the long-term evolution of migrating alternate bars in alluvial channels", *Water Resources Research*, 48, 6, W06524, n/a-n/a, ISSN: 1944-7973, DOI: 10.1029/2011WR011320, http://dx.doi.org/10.1029/2011WR011320. (Cited on p. 8.)

Crosato, A. and E. Mosselman

2009 "Simple physics-based predictor for the number of river bars and the transition between meandering and braiding", *Water Resources Research*, 45, 3, W03424, n/a-n/a, ISSN: 1944-7973, DOI: 10.1029/2008WR007242, http://dx.doi.org/10.1029/2008WR007242. (Cited on p. 8.)

Darby, S. E.

1999 "Effect of riparian vegetation on flow resistance and flood potential", *Journal of Hydraulic Engineering*, 125, 5, pp. 443-454. (Cited on p. 71.)

Darby, S. E., A. M. Alabyan, and M. J. Van de Wiel

2002 "Numerical simulation of bank erosion and channel migration in meandering rivers", *Water Resources Research*, 38, 9 (Sept. 2002), pp. 2–1–2-21, ISSN: 00431397, DOI: 10.1029/2001WR000602, http://doi.wiley.com/10.1029/2001WR000602. (Cited on pp. 34, 37, 83.)

Darby, S. E., M. Rinaldi, and S. Dapporto

2007 "Coupled simulations of fluvial erosion and mass wasting for cohesive river banks", *Journal of Geophysical Research: Earth Surface*, 112, F3, F03022, n/a-n/a, ISSN: 2156-2202, DOI: 10.1029/2006JF000722, http://dx.doi.org/10.1029/2006JF000722. (Cited on pp. 37, 83.)

Darby, S. E. and C. R. Thorne

1996 "Development and testing of riverbank stability analysis", *J. Hydraul. Eng.*, 122, 8, pp. 443-45. (Cited on p. 37.)

De la Asunción, M., J. M. Mantas, M. J. Castro, and E. D. Fernández-Nieto

2012 "An MPI-CUDA implementation of an improved Roe method for two-layer shallow water systems", *J. Parallel Distrib. Comput.*, 72, 9, pp. 1065-1072, ISSN: 0743-7315, DOI: 10.1016/j.jpdc.2011.07.012, http://dx.doi.org/10.1016/j.jpdc.2011.07.012. (Cited on p. 14.)

De Vriend, H. J.

1977 "A mathematical model of steady flo w i n curved shallow channels", *J. Hydraul. Res.*, 15, 1. (Cited on p. 4.)

Dey, A. and R.K. Bhattacharya

2013 "Monitoring of river center line and width–a study on river Brahmaputra", *Journal of the Indian Society of Remote Sensing*, pp. 1-8. (Cited on p. 48.)

Dillenburg, S. R. and P. A. Hesp

2008 *Geology and geomorphology of Holocene coastal barriers of Brazil*, Springer, vol. 107. (Cited on p. 99.)

Duan, J. G. and P. Y. Julien

2005 "Numerical simulation of the inception of channel meandering", *Earth Surface Processes and Landforms*, 30, pp. 1093-1110, DOI: doi:10.1002/esp.1264. (Cited on p. 83.)

Duan, J. G. and Julien P. Y.

2010 "Numerical simulation of meandering evolution", *J. Hydrol.*, 391, pp. 34-46. (Cited on p. 37.)

Dunne, T., L. A. K. Mertes, R. H. Meade, J. E. Richey, and B. R. Forsberg

1998 "Exchanges of sediment between the flood plain and channel of the Amazon River in Brazil", *Geological Society of America Bulletin*, 110, pp. 450-467. (Cited on p. 99.)

Eaton, B. C., M. Church, and R. G. Millar

2004 "Rational regime model of alluvial channel morphology and response", *Earth Surface Processes and Landforms*, 29, 4, pp. 511-529, ISSN: 01979337, DOI: 10.1002/esp.1062. (Cited on p. 31.)

Eaton, B.C., R. G. Millar, and S. Davidson

2010 "Channel patterns: Braided, anabranching, and single-thread", *Geomorphology*, 120, 3, pp. 353-364, ISSN: 0169-555X, DOI: http://dx.doi.org/10.1016/j.geomorph.2010.04.010, http://www.sciencedirect.com/science/article/pii/S0169555X10001893. (Cited on p. 28.)

Edet, A. E. and O. E. Offiong

2002 "Evaluation of water quality pollution indices for heavy metal contamination monitoring. A study case from Akpabuyo-Odukpani area, Lower Cross River Basin (southeastern Nigeria)", *GeoJournal*, 57, 4, pp. 295-304. (Cited on p. 99.)

Edwards, B. F. and D. H. Smith

2002 "River meandering dynamics", *Phys. Rev. E*, 65 (4 Mar. 2002), p. 046303, DOI: 10.1103/PhysRevE.65.046303, http://link.aps.org/doi/10.1103/PhysRevE.65.046303. (Cited on p. 22.)

Einstein, A.

1926 "Die Ursache der Mäanderbildung der Flusslaeufe und des sogenannten Baerschen Gesetzes", *Die Naturwissenschaften*, 14, 11, pp. 223-224. (Cited on p. 4.)

Eke, E. C.

2013 *Numerical Modeling of River Migration incorporating erosional and depositional bank processes*, PhD thesis, University of Illinois at Urbana-Champaign, Urbana, Illinois. (Cited on p. 22.)

Eke, E. C., M. J. Czapiga, E. Viparelli, Y. Shimizu, J. Imran, T. Sun, and G. Parker

2014a "Coevolution of width and sinuosity in meandering rivers", *Journal of Fluid Mechanics*, 760 (Nov. 2014), pp. 127-174, ISSN: 0022-1120, DOI: 10.1017/jfm.2014.556. (Cited on pp. 12, 13, 21, 23, 28, 29, 31, 32, 34, 37, 39, 40, 70, 72, 82, 84, 89, 137, 144, 145, 176.)

Eke, E. C., G. Parker, and Y. Shimizu

2014b "Numerical modeling of erosional and depositional bank processes in migrating river bends with self-formed width: Morphodynamics of bar push and bank pull", *Journal of Geophysical Research*, 119, 2, pp. 1455-1483, DOI: 10.1002/2013JF003020.Received. (Cited on pp. 3, 13, 23, 27, 31, 34, 37, 39, 71.)

Engels, H.

1914 *Handbuch des Wasserbaues: fur das Studium und die Praxis*, tech. rep., Engelmann, Leipzig and Berlin, Germany. (Cited on p. 9.)

Engelund, F. and E. Hansen

1967 *A Monograph on Sediment Transport in Alluvial Streams*, Danish Technical Press, Copenhagen. (Cited on p. 97.)

Engelund, F. and o. Skovoaard

1973 "On the origin of meandering and braiding in alluvial streams", *J. Fluid Mech.*, 57, pp. 289-302. (Cited on p. 8.)

Ettmer, B. and C. A. Alvarado-Ancieta

2010 "Morphological development of the Ucayali River, Peru without human impacts", *Waldokologie Online*. (Cited on p. 7.)

Feyisa, G. L., Meilby H., Fensholt R., and S. R. Proud

2014 "Automated Water Extraction Index: A new technique for surface water mapping using Landsat imagery", *Remote Sensing of Environment*, 140, pp. 23-35. (Cited on pp. 15, 16, 24, 45.)

Filizola, N. and J. L. Guyot

n.d. "Suspended sediment yields in the Amazon basin: an assessment using the Brazilian national data set", *Hydrological Processes*, 23, p. 2009. (Cited on p. 99.)

Fisher, G. B., B. Bookhagen, and C. B. Amos

2013 "Channel planform geometry and slopes from freely available high-spatial resolution imagery and DEM fusion: implications for channel width scalings, erosion proxies, and fluvial signatures in tectonically active landscapes", *Geomorphology*, 194, pp. 46-56. (Cited on pp. 24, 47, 48, 64.)

Frascati, A. and S. Lanzoni

2009 "Morphodynamic regime and long-term evolution of meandering rivers", *Journal of Geophysical Research: Earth Surface*, 114, 2, pp. 1-12, ISSN: 21699011, DOI: 10.1029/2008JF001101. (Cited on p. 31.)

2013 "A mathematical model for meandering rivers with varying width", *Journal of Geophysical Research: Earth Surface*, 118, 3, pp. 1641-1657. (Cited on pp. 33, 174.)

Fredsøe, J.

1978 "Meandering and braiding of rivers", *Journal of Fluid Mechanics*, 84, 4, pp. 609-624. (Cited on pp. 8, 11.)

Gao, B.

1996 "NDWI — A normalized difference water index for remote sensing of vegetation liquid water from space", *Remote Sensing of Environment*, 58, pp. 257-266. (Cited on pp. 15, 16, 24.)

Gautier, E., D. Brunstein, P. Vauchel, J. M. Jouanneau, M. Roulet, and C. garcia

2010 "Channel and floodplain sediment dynamics in a reach of thee tropical meandering Rio Beni (Bolivian Amazonia)", *Earth Surf. Process. Landforms*, DOI: 10.1002/esp.2065. (Cited on pp. 7, 15.)

Gautier, E., D. Brunstein, P. Vauchel, M. Roulet, O. Fuertes, J. L. Guyot, J. Darozzes, and L. Bourrel

2007 "Temporal relations between meander deformation, water discharge and sediment fluxes in the floodplain of the Rio Beni (Bolivian Amazonia)", *Earth Surf. Process. Landforms*, 32, pp. 230-248, DOI: doi:10.1002/esp.1394. (Cited on p. 7.)

Graf, N. E.

2008 *50 years of channel change on a reach of the Big Blue River, northeast Kansas*, PhD thesis, Univ. of Wyoming, Manhattan, Kansas. (Cited on p. 4.)

Grenfell, M. C., R. Aalto, and A. P. Nicholas

2012 "Chute channel dynamics in large, sand-bed meandering rivers", *Earth Surface Processes and Landforms*, 331, December 2011, pp. 315-331, DOI: 10.1002/esp.2257. (Cited on p. 14.)

Grenfell, M. C., A. P. Nicholas, and R. Aalto

2014 "Mediative adjustment of river dynamics : The role of chute channels in tropical sand-bed meandering rivers", *Sedimentary Geology*, 301, pp. 93-106, ISSN: 0037-0738, DOI: 10.1016/j.sedgeo.2013.06.007, http://dx.doi.org/10.1016/j.sedgeo.2013.06.007. (Cited on p. 14.)

Güneralp, I., A. M. Filippi, and B. Hales

2014 "Influence of river channel morphology and bank characteristics on water surface boundary delineation using high-resolution passive remote sensing and template matching", *Earth Surface Processes and Landforms*, 39, 7, ESP-13-0265.R1, pp. 977-986, ISSN: 1096-9837, DOI: 10.1002/esp.3560, http://dx.doi.org/10.1002/esp.3560. (Cited on p. 24.)

Güneralp, I., A. M. Filippi, and B. U. Hales

2013 "River-flow boundary delineation from digital aerial photography and ancillary images using support vector machines", *GIScience & Remote Sensing*, 50, 1, pp. 1-25. (Cited on pp. 24, 64.)

Güneralp, I. and B. L. Rhoads

2007 "Continuous Characterization of the Planform Geometry and Curvature of Meandering Rivers", *Geographical Analysis*, 40, 1, pp. 1-25. (Cited on p. 50.)

2009 "Empirical analysis of the planform curvature-migration relation of meandering rivers", *Water Resources Research*, 45, 9. (Cited on p. 23.)

2011 "Influence of floodplain erosional heterogeneity on planform complexity of meandering rivers", *Geophysical Research Letters*, 38, 14, DOI: 10.1029/2011GL048134, http://doi.wiley.com/10.1029/2011GL048134. (Cited on p. 37.)

Gurnell, A., N. Surian, and L. Zanoni

2009 "Multi-thread river channels: A perspective on changing European alpine river systems", *Aquatic Sciences*, 71, 3 (Mar. 2009), pp. 253-265, ISSN: 1015-1621, DOI: 10.1007/s00027-009-9186-2, http://link.springer.com/10.1007/s00027-009-9186-2. (Cited on pp. 6, 14.)

Guyot, J. L. et al.

2007 "Water Quality and Sediment Behaviour of the Future: Predicitions for the 21st Century", in *Proceedings of Symposium HS2005 at IUGG2007*, Perugia. (Cited on p. 99.)

Guyot, J.L. and C. J. Bourges

1994 "Sediment transport in the Rio Grande, an Andean river of the Bolivian Amazon drainage basin", *IAHS*, 224, pp. 223-232. (Cited on p. 99.)

Guyot, J.L., N. Fillzola, J. Quintanilla, and J. Cortez

1996 "Dissolved solids and suspended sediment yields in the Rio Madeira basin, from the Bolivian Andes to the Amazon", *IAHS*, pp. 55-64. (Cited on p. 99.)

Hansen, E.

1967 *The formation of meanders as a stability problem*, Basic Res. Prog. Rep 13, Tech. Univ. of Denmark, Hydr. Lab. (Cited on pp. 8, 11.)

Haralick, R. M., S. R. Sternberg, and X. Zhuang

1987 "Image analysis using mathematical morphology", *IEEE transactions on pattern analysis and machine intelligence*, pp. 532-550. (Cited on p. 46.)

Harvey, J. W., B. J. Wagner, and K. E. Bencala

1996 "Evaluating the Reliability of the Stream Tracer Approach to Characterize Stream-Subsurface Water Exchange", *Water Resources Research*, 32, 8, pp. 2441-2451, ISSN: 1944-7973, DOI: 10.1029/96WR01268, http://dx.doi.org/10.1029/96WR01268. (Cited on p. 8.)

Hasegawa, K.

1977 "Computer simulation of the gradual migration of meandering channels." *In Proceedings of the Hokkaido Branch, Japan Society of Civil Engineering (in Japanese)*. (Cited on pp. 37, 70.)

Henriquez, A., K. Tyler, and A. Hurst

1990 "Characterization of fluvial sedimentology for reservoir simulation modeling", *SPE Formation Evaluation*. (Cited on p. 4.)

Henshaw, A. J., A. Gurnell, W. Bertoldi, and N. A. Drake

2013 "An assessment of the degree to which Landsat {TM} data can support the assessment of fluvial dynamics, as revealed by changes in vegetation extent and channel position, along a large river", *Geomorphology*, 202, Process geomorphology and ecosystems: Disturbance regimes and interactions, pp. 74-85, ISSN: 0169-555X, DOI: http://dx.doi.org/10.1016/j.geomorph.2013.01.011, http://www.sciencedirect.com/science/article/pii/S0169555X1300038X. (Cited on p. 43.)

Hodskinson, A. and R. I. Ferguson

1998 "Numerical modelling of separated flow in river bends: model testing and experimental investigation of geometric controls on the extent of flow separation at the concave bank", *Hydrological Processes*, 12, 8, pp. 1323-1338, ISSN: 1099-1085, DOI: 10.1002/(SICI)1099-1085(19980630)12:8<1323::AID-HYP617>3.0.CO;2-S, http://dx.doi.org/10.1002/(SICI)1099-1085(19980630)12:8%3C1323::AID-HYP617%3E3.0.CO;2-S. (Cited on p. 27.)

Hooke, J. M.

1979 "An analysis of the processes of river bank erosion", *Journal of Hydrology*, 42, 1-2 (June 1979), pp. 39-62, ISSN: 00221694, DOI: 10.1016/0022-1694(79)90005-2, http://linkinghub.elsevier.com/retrieve/pii/0022169479900052. (Cited on pp. 3, 27.)

1986 "The significance of mid-channel bars in meandering channels", *Sedimentology*, 33, pp. 839-850. (Cited on pp. 7, 159.)

2003 "River meander behaviour and instability", *Royal Geography Society*, pp. 238-253. (Cited on p. 22.)

2004 "Cutoff galore!: occurrence and causes of multiple cutoffs on a meandering river", *Geomorphology*, pp. 225-238, DOI: 10.1016/j.geomorph.2003.12.006. (Cited on pp. 23, 29.)

2007 "Spatial Variability, mechanisms and propagation of change in an active meandering river", *Geomorphology*, 84, 3, pp. 277-296. (Cited on pp. 7, 21.)

Hooke, J. M., E. Gautier, and G. Zolezzi

2011 "River meander dynamics: developments in modelling and empirical analyses", *Earth Surface Processes and Landforms*, 36, 11 (Sept. 2011), pp. 1550-1553, ISSN: 01979337, DOI: 10.1002/esp.2185, http://doi.wiley.com/10.1002/esp.2185. (Cited on p. 22.)

Hooke, J. M. and L. Yorke

2010 "Rates, distributions and mechanisms of change in meander morphology over decadal timescales, River Dane, UK", *Earth Surface Processes and Landforms*, 35, 13 (Oct. 2010), pp. 1601-1614, ISSN: 01979337, DOI: 10.1002/esp.2079, http://doi.wiley.com/10.1002/esp.2079. (Cited on pp. 3, 7.)

2011 "Channel bar dynamics on multi-decadal timescales in an active meandering river", *Earth Surface Processes and Landforms*, 36, 14, pp. 1910-1928. (Cited on pp. 7, 21, 23.)

Howard, A. D.

1992 "Modeling channel migration and floodplain sedimentation in meandering streams", *Lowland Floodplain Rivers: Geomorphological Perspectives*, pp. 1-41. (Cited on pp. 3, 21, 37.)

1996 "Modelling channel evolution and floodplain morphology", *Floodplain processes*, pp. 15-62. (Cited on p. 37.)

Ikeda, S., G. Parker, and K. Sawai

1981 "Bend theory of river meanders. Part 1. Linear development", *Journal of Fluid Mechanics*, 112, DOI: 10.1017/S0022112081000451. (Cited on pp. 12, 21, 28, 37, 69, 70, 83, 84.)

Jaeggi, M.

1984 "Formation and effects of alternate bars", *Journal of Hydraulic Engineering*, 110, pp. 142-156. (Cited on p. 8.)

Jang, C. L. and Y. Shimizu

2005 "Numerical simulation of relatively wide, shallow channels with erodible banks", *J. Hydraul. Eng.*, 31, 7, pp. 565-575, DOI: doi:10.1061/(ASCE)0733-9429(2005)131:7(565). (Cited on p. 83.)

Jansen, P., L. Van Bendegom, J. Van den Berg, M. De Vries, and A Zanen

1994 *Principles of River Engineering: The non-tidal alluvial river*, Delftse Uitgevers Maatschappij. (Cited on p. 10.)

Johannesson, H. and G. Parker

1989 "Linear theory of river meanders", *American Geophysical Union*, DOI: 10.1029/WM012p0181. (Cited on pp. 11, 21, 37, 70.)

Jones, E., T. Oliphant, P. Peterson, et al.

2001– *SciPy: Open source scientific tools for Python*, [Online; accessed <today>], http://www.scipy.org/. (Cited on p. 44.)

Kalkwijk, J. P. T. and H. J. de Vriend

1980 "Computation of the flow in shallow river bends", *Journal of Hydraulic Research*, 18, pp. 327-342. (Cited on p. 4.)

Kasvi, E., M. Vaaja, P. Alho, H. Hyyppä, J. Hyyppä, H. Kaartinen, and A. Kukko

2013 "Morphological changes on meander point bars associated with flow structure at different discharges", *Earth Surface Processes and Landforms*, 38, 6 (May 2013), pp. 577-590, ISSN: 01979337, DOI: 10.1002/esp.3303, http://doi.wiley.com/10.1002/esp.3303. (Cited on pp. 22, 23.)

Kinoshita, R.

1961 *Investigation of channel deformation in Ishikari River*, tech. rep. 36, Nat. Resour. Div., Minist. of Sci. and Technol. of Jpn, Tokyo, p. 139. (Cited on pp. 23, 82.)

Kinoshita, R. and H. Miwa

1974 "River channel formation which prevents downstream translation of transverse bars", *Shinsabo*, 12-17 (in japanese). (Cited on pp. 8, 10, 22.)

Kinzel, P. J., C. J. Legleiter, and J. M. Nelson

2013 "Mapping river bathymetry with a small footprint green lidar", *journal of the American Water Resources Association*, 49, 1. (Cited on p. 15.)

Kleinhans, M. G. and J. H. van den Berg

2011 "River channel and bar patterns explained and predicted by an empirical and a physics-based method", *Earth Surf. Processes Landforms*, 6, 36, pp. 721-738, DOI: 10.1002/esp.2090. (Cited on p. 23.)

Knighton, A. D.

1972 "Changes in a braided reach", *Geological Society of America Bulletin*, 83, pp. 3813-3822. (Cited on p. 159.)

Kondolf, G.

2006 "River restoration and meanders", *Ecol. Soc.*, 11, 2. (Cited on p. 4.)

Konsoer, K. M., B. L. Rhoads, E. J. Langendoen, J. L. Best, M. E. Ursic, J. D. Abad, and M. H. Garcia

2016 "Spatial variability in bank resistance to erosion on a large meandering, mixed bedrock-alluvial river", *Geomorphology*, 252, The Natural and Human Structuring of Rivers and other Geomorphic Systems: A Special Issue in Honor of William L. Graf, pp. 80-97, ISSN: 0169-555X, DOI: http://dx.doi.org/10.1016/j.geomorph.2015.08.002, http://www.sciencedirect.com/science/article/pii/S0169555X15301148. (Cited on p. 27.)

Kriegler, F.J., W. A. Malila, R.F. Nalepka, and W. Richardson

1969 "Preprocessing transformations and their effects on multispectral recognition", in *Proceedings of the Sixth International Symposium on Remote Sensing of Environment*, pp. 97-131. (Cited on p. 16.)

Lagasse, P. F., L. W. Zevenbergen, W. J. Spitz, C. R. Thorne, Ayres Associates, and Fort Collins

2004 *Handbook for Predicting Stream Meander Migration*, tech. rep., National cooperative highway research program. (Cited on pp. 7, 34, 38, 85, 113, 127, 128, 137, 161, 164, 166.)

Lamotte, S.

1990 "Fluvial dynamics and succession in the lower Ucayali River basin, Peruvian Amazonia", *Forest Ecology and Management*, 33–34, pp. 141-156. (Cited on p. 7.)

Lane, S. N.

1998 "Hydraulic modelling in hydrology and geomorphology: A review of high resolution approaches", *Hydrological processes*, 1150, February 1996, pp. 1131-1150. (Cited on pp. 4, 14.)

Langbein, W. B. and L. B. Leopold

1966 "River Meanders - Theory of Minimum Variance", *Geological Survey Professional Paper*, 422. (Cited on pp. 10, 11.)

Langendoen, E. J. and A. Simon

2008 "Modeling the evolution of incised streams. II: Streambank erosion", *J. Hydraul. Eng.*, 134, 7, pp. 905-915. (Cited on p. 37.)

Lanzoni, S., R. Luchi, and M. Bolla Pittaluga

2015 "Modeling the morphodynamic equilibrium of an intermediate reach of the Po River (Italy)", *Advances in Water Resources*, 81, pp. 95-102, ISSN: 03091708, DOI: 10.1016/j.advwatres.2014.11.004, http://dx.doi.org/10.1016/j.advwatres.2014.11.004. (Cited on p. 31.)

Lanzoni, S. and G. Seminara

2006 "On the nature of meander instability", *Journal of Geophysical Research: Earth Surface*, 111, 4 (Nov. 2006), F04006, ISSN: 21699011, DOI: 10.1029/2005JF000416, http://doi.wiley.com/10.1029/2005JF000416. (Cited on pp. 5, 28, 174.)

Lanzoni, S., A. Siviglia, A. Frascati, and G. Seminara

2006 "Long waves in erodible channels and morphodynamic influence", *Water Resources Research*, 42, 6, W06D17, n/a-n/a, ISSN: 1944-7973, DOI: 10.1029/2006WR004916, http://dx.doi.org/10.1029/2006WR004916. (Cited on p. 32.)

Latrubesse, E. M.

2008 "Patterns of anabranching channels: The ultimate end-member adjustment of mega rivers", *Geomorphology*, 101, 1 2, The 39th Annual Binghamton Geomorphology Symposium: Fluvial Deposits and Environmental History: Geoarchaeology, Paleohydrology, and Adjustment to Environmental Change, pp. 130-145, ISSN: 0169-555X, DOI: http://dx.doi.org/10.1016/j.geomorph.2008.05.035, http://www.sciencedirect.com/science/article/pii/S0169555X08002389. (Cited on p. 23.)

Latrubesse, E. M., M. L. Amsler, R. P. de Morais, and S. Aquino

2009 "The geomorphologic response of a large pristine alluvial river to tremendous deforestation in the South American tropics: The case of the Araguaia River", *Geomorphology*, 113, 3 4, Short and Long Term Processes, Landforms and Responses in Large Rivers, pp. 239-252, ISSN: 0169-555X, DOI: http://dx.doi.org/10.1016/j.geomorph.2009.03.014, http://www.sciencedirect.com/science/article/pii/S0169555X09001238. (Cited on pp. 22, 65.)

Latrubesse, E. M., J. C. Stevaux, and R. Sinha

2005 "Tropical rivers", *Geomorphology*, 70, 3–4, Tropical Rivers, pp. 187-206, ISSN: 0169-555X, DOI: https://doi.org/10.1016/j.geomorph.2005.02.005, http://www.sciencedirect.com/science/article/pii/S0169555X05000723. (Cited on pp. 14, 99.)

Lauer, J. W.

2006 *NCED Stream Restoration Toolbox - Channel Planform Statistics*, National Center for Earth-Surface Dynamics. (Cited on pp. 16, 25.)

Lauer, J. W. and G. Parker

2008 "Net local removal of floodplain sediment by river meander migration", *Geomorphology*, 96, 1-2, pp. 123-149. (Cited on pp. 13, 25, 34, 65, 73.)

Leeder, M. R. and P. H. Bridges

1975 "Flow separation in meander bends", *Nature*, 253, pp. 338-339, DOI: 10.1038/253338a0. (Cited on p. 27.)

Legleiter, C. J., L. R. Harrison, and T. Dunne

2011 "Effect of point bar development on the local force balance governing flow in a simple, meandering gravel bed river", *Journal of Geophysical Research*, 116, F1 (Feb. 2011), F01005, ISSN: 0148-0227, DOI: 10.1029/2010JF001838, http://doi.wiley.com/10.1029/2010JF001838. (Cited on p. 22.)

Legleiter, C. J. and P. C. Kyriakidis

2006 "Forward and Inverse Transformations between Cartesian and Channel-fitted Coordinate Systems for Meandering Rivers", *Mathematical Geology*, 38, 8, pp. 927-958, ISSN: 1573-8868, DOI: 10.1007/s11004-006-9056-6, http://dx.doi.org/10.1007/s11004-006-9056-6. (Cited on p. 53.)

Legleiter, C. J., A. Roberts D., W. A. Marcus, and M. A. Fonstad

2004 "Passive optical remote sensing of river channel morphology and in-stream habitat: Physical basis and feasibility", *Remote Sensing of Environment*, 93, pp. 493-510. (Cited on p. 15.)

Legleiter, C. J. and D. A. Roberts

2009 "A forward image model for passive optical remote sensing of river bathymetry", *Remote Sensing of Environment*, 113, 5 (May 2009), pp. 1025-1045, ISSN: 00344257, DOI: 10.1016/j.rse.2009.01.018, http://linkinghub.elsevier.com/retrieve/pii/S0034425709000297. (Cited on p. 15.)

Leopold, L. B. and T. Maddock

1953 *The hydraulic geometry of stream channels and some physiographic implications*, US Government Printing Office, vol. 252. (Cited on pp. 28, 31, 39, 83.)

Leopold, L. B., J. P. Miller, and G. M. Wolman

1964 "Fluvial processes in geomorphology", *Freeman, San Francisco*, p. 522. (Cited on p. 28.)

Leopold, L. B. and G. M. Wolman

1957 "River channel patterns: braided, meandering and straight", *Physiographic and hydraulic studies of rivers*. (Cited on pp. 6, 10.)

1960 "River Meanders", *Bulletin of Geological Society of America*, 71, pp. 769-794. (Cited on pp. 10, 21, 22.)

Lewin, J.

1972 "Late-stage meander growth", *Nature*, 240, 101, pp. 116-116. (Cited on p. 21.)

Li, C., M. J. Czapiga, E. C. Eke, E. Viparelli, and G. Parker

2014 "River bankfull geometry: shear velocity is viscosity-dependent but grain size-independent", DOI: doi:10.1080/00221686.2014.939113. (Cited on pp. 32, 72.)

Lima, J. E. F. W., P. M. C. dos Santos, and N. de Oliveira Carvalho

2001 *Diagnostico do fluxo de sedimentos em suspensao na Bacia–Araguaia-Tocantins*, tech. rep., Empresa Brasileira de Pesquisa Agropecuaria Embrapa Cerrados, Agencia Nacional de Energia Eletrica, Agencia Nacional de Aguas - ANA, Brazil. (Cited on pp. 96, 97.)

2004 *Diagnostico do fluxo de sedimentos em suspensao na Bacia–Araguaia-Tocantins*, tech. rep., Empresa Brasileira de Pesquisa Agropecuaria Embrapa Cerrados, Agencia Nacional de Energia Eletrica, Agencia Nacional de Aguas - ANA, Brazil. (Cited on pp. 96, 97, 99.)

Lima, J. E. F. W., W. T. A. Lopes, N. de Oliveira Carvalho, M. R. Vieira, and E. M. de Silva

2005 , in *International Symposium on Sediment Budgets*, 291, vol. IAHS, pp. 355-363. (Cited on pp. 96, 97, 99.)

Lu, S., B. Wu, N. Yan, and H. Wang

2011 "Water body mapping method with HJ-1A/B satellite imagery", *International Journal of Applied Earth Observation and Geoinformation*, 13, 3, pp. 428-434, ISSN: 0303-2434, DOI: http://dx.doi.org/10.1016/j.jag.2010.09.006, http://www.sciencedirect.com/science/article/pii/S0303243410001108. (Cited on p. 45.)

Luchi, R., W. Bertoldi, G. Zolezzi, and M. Tubino

2007 "Monitoring and predicting channel change in a free-evolving, small Alpine river: Ridanna Creek (North East Italy)", *Earth Surface Processes and Landforms*, 32, 14, pp. 2104-2119, ISSN: 1096-9837, DOI: 10.1002/esp.1511, http://dx.doi.org/10.1002/esp.1511. (Cited on pp. 12, 28.)

Luchi, R., M. Bolla Pittaluga, and G. Seminara

2012 "Spatial width oscillations in meandering rivers at equilibrium", *Water Resources Research*, 48, 5 (May 2012), n/a-n/a, ISSN: 00431397, DOI: 10.1029/2011WR011117, http://doi.wiley.com/10.1029/2011WR011117. (Cited on pp. 12, 32, 33.)

Luchi, R., J. M. Hooke, G. Zolezzi, and W. Bertoldi

2010a "Width variations and mid-channel bar inception in meanders: River Bollin (UK)", *Geomorphology*, 119, 1-2 (June 2010), pp. 1-8, ISSN: 0169555X, DOI: 10.1016/j.geomorph.2010.01.010, http://linkinghub.elsevier.com/retrieve/pii/S0169555X1000036X. (Cited on pp. 7, 12, 23, 32-34, 86, 159.)

Luchi, R., G. Zolezzi, and M. Tubino

2010b "Modelling mid-channel bars in meandering channels", *Earth Surface Processes and Landforms*, 35, 8 (Apr. 2010), pp. 902-917, ISSN: 01979337, DOI: 10.1002/esp.1947, http://doi.wiley.com/10.1002/esp.1947. (Cited on pp. 12, 13, 23, 33, 34, 36, 39.)

2011 "Bend theory of river meanders with spatial width variations", *Journal of Fluid Mechanics*, 681 (June 2011), pp. 311-339, ISSN: 0022-1120, DOI: 10.1017/jfm.2011.200, http://www.journals.cambridge.org/abstract%5C_S002211201100200X. (Cited on pp. 13, 32-34, 38, 53, 82, 86, 157, 159.)

Malard, F., K. Tockner, M. J. Dole-Olivier, and J. V. Ward

2002 "A landscape perspective of surface–subsurface hydrological exchanges in river corridors", *Freshwater Biology*, 47, 4, pp. 621-640, ISSN: 1365-2427, DOI: 10.1046/j.1365-2427.2002.00906.x, http://dx.doi.org/10.1046/j.1365-2427.2002.00906.x. (Cited on p. 8.)

Matsubara, Y., A. D. Howard, D. M. Burr, R. M.E. Williams, W. E. Dietrich, and J. M. Moore

2015 "River meandering on Earth and Mars: A comparative study of Aeolis Dorsa meanders, Mars and possible terrestrial analogs of the Usuktuk River, AK, and the Quinn River, NV", *Geomorphology*, 240, Planetary Geomorphology: Proceedings of the 45th Annual Binghamton Geomorphology Symposium, held 12-14 September 2014 in Knoxville, Tennessee, USA, pp. 102-120, ISSN: 0169-555X, DOI: http://dx.doi.org/10.1016/j.geomorph.2014.08.031, http://www.sciencedirect.com/science/article/pii/S0169555X14004589. (Cited on p. 4.)

Merwade, V. M.

2007 "An Automated GIS Procedure for Delineating River and Lake Boundaries", *Transactions in GIS*, 11, 2, pp. 213-231, ISSN: 1467-9671, DOI: 10.1111/j.1467-9671.2007.01042.x, http://dx.doi.org/10.1111/j.1467-9671.2007.01042.x. (Cited on pp. 24, 64.)

Merwade, V. M., D. R. Maidment, and B. R. Hodges

2005 "Geospatial Representation of River Channels", *Journal of Hydrologic Engineering*, 10, 3, pp. 243-251, DOI: 10.1061/(ASCE)1084-0699(2005)10:3(243). (Cited on p. 53.)

Meyer-Peter, E. and R. Müller

1948 "Formulas for bed-load transport", *Proc. 2nd Meeting IAHSR*, pp. 1-26. (Cited on p. 73.)

Moore, J. M., A. D. Howard, W. E. Dietrich, and P. M. Schenk

2003 "Martian Layered Fluvial Deposits: Implications for Noachian Climate Scenarios", *Geophysical Research Letters*, 30, 24, 2292, n/a-n/a, ISSN: 1944-8007, DOI: 10.1029/2003GL019002, http://dx.doi.org/10.1029/2003GL019002. (Cited on p. 4.)

Mosselman, E.

1992 *Mathematical modelling of morphological processes in rivers with erodible cohesive banks*, tech. rep., Delft Univ. of Technol., Delft, Netherlands. (Cited on pp. 3, 34, 83.)

1998 "Morphological modelling of rivers with erodible banks", *Hydrological processes*, 12, 8, pp. 1357-1370. (Cited on pp. 3, 22, 28, 34, 37.)

Mosselman, E. and A. Crosato

1991 "Universal bank erosion coefficient for meandering rivers", *J. Hydraul. Eng.*, 117, pp. 942-943. (Cited on p. 37.)

Motta, D., J. D. Abad, and M. H. Garcia

2012 "A simplified 2D model for meander migration with physically-based bank evolution", *Geomorphology*, 163-164, pp. 10-25. (Cited on pp. 23, 37, 83.)

Nanson, G. C. and E. J. Hickin

1983 "Channel Migration and Incision in the Beatton River", *J. Hydraul. Eng.*, 109, 3, pp. 327-337. (Cited on pp. 3, 22.)

Nanson, G. C. and A. D. Knighton

1996 "Anabranching rivers: their cause, character and classification", *Earth Surface Processes and Landforms*, 21, 3, pp. 217-239, ISSN: 1096-9837, DOI: 10.1002/(SICI)1096-9837(199603)21:3<217::AID-ESP611>3.0.CO;2-U, http://dx.doi.org/10.1002/(SICI)1096-9837(199603)21:3%3C217::AID-ESP611%3E3.0.CO;2-U. (Cited on p. 24.)

Nicholas, A. P.

2013a "Modelling the continuum of river channel patterns", *Earth Surface Processes and Landforms*, 38, 10 (Aug. 2013), pp. 1187-1196, ISSN: 01979337, DOI: 10.1002/esp.3431, http://doi.wiley.com/10.1002/esp.3431. (Cited on p. 14.)

2013b "Morphodynamic diversity of the world' s largest rivers", *Geology*, pp. 475-478, DOI: 10.1130/G34016.1. (Cited on p. 14.)

Nicholas, A. P., P. J. Ashworth, G. H. Sambrook Smith, and S. D. Sandbach

2013 "Numerical simulation of bar and island morphodynamics in anabranching megarivers", *journal of Geophysical Research*, 118, August, pp. 2019-2044, DOI: 10.1002/jgrf.20132. (Cited on p. 14.)

Ninomiya, Y.

2004 "Lithologic mapping with multispectral ASTER TIR and SWIR data", in *Proc. SPIE*, vol. 5234, pp. 180-190, DOI: 10.1117/12.511902, http://dx.doi.org/10.1117/12.511902. (Cited on p. 24.)

Odgaard, A. J.

1986 "Meander flow model. I: Development", *J. Hydraul. Eng.*, 112, 12, pp. 1117-1136. (Cited on p. 37.)

Oliphant, T. E.

2006 *A guide to NumPy*, Trelgol Publishing USA, vol. 1. (Cited on p. 44.)

Otsu, N.

1979 "A threshold selection method from gray-level histograms", *IEEE Trans. Sys., Man., Cyber.*, 9, pp. 62-66, DOI: doi:10.1109/TSMC.1979.4310076. (Cited on pp. 16, 45.)

Parker, G.

1976 "On the cause and characteristic scales of meandering and braiding in rivers", *Journal of fluid mechanics*, 76, 3, pp. 457-480. (Cited on p. 8.)

1979 "Hydraulic Geometry of Active Gravel Rivers", *Journal of the Hydraulics Division*, 105, 9, pp. 1185-1201. (Cited on pp. 31, 39.)

1990 "Surface-based bedload transport relation for gravel rivers", *Journal of Hydraulic Research*, 28, 4, pp. 417-436, DOI: 10.1080/00221689009499058, eprint: http://dx.doi.org/10.1080/00221689009499058, http://dx.doi.org/10.1080/00221689009499058. (Cited on p. 78.)

Parker, G. and E. D. Andrews

1986 "On the time development of meanders bends", *J. Fluid Mech.*, 162, pp. 139-156. (Cited on p. 37.)

Parker, G., P. Diplas, and J. Akiyama

1983 "Meander bends of high amplitude", *Journal of Hydraulic Engineering*, 09, pp. 1323-1337. (Cited on p. 37.)

Parker, G., Y. Shimizu, G. V. Wilkerson, E. C. Eke, J. D. Abad, J. W. Lauer, C. Paola, W. E. Dietrich, and V. R. Voller

2011 "A new framework for modeling the migration of meandering rivers", *Earth Surface Processes and Landforms*, 36, 1, pp. 70-86. (Cited on pp. 13, 27, 31, 34, 37, 39, 40, 71, 83.)

Parker, G., P. R. Wilcock, C. Paola, W. E. Dietrich, and J. Pitlick

2007 "Physical basis for quasi-universal relations describing bankfull hydraulic geometry of single-thread gravel bed rivers", *Journal of Geophysical Research: Earth Surface*, 112, F4. (Cited on pp. 28, 29, 31, 39, 72, 83, 147.)

Partheniades, E. and R. E. Paaswell

1970 "Erodibility of channels with cohesive boundary", *Journal of the Hydraulics Division*, 96, 3, pp. 755-771. (Cited on pp. 11, 37, 71, 83.)

Pavelsky, T. M. and L. C. Smith

2008 "RivWidth: A Software Tool for the Calculation of River Widths From Remotely Sensed Imagery", *IEEE Geoscience and Remote Sensing Letters*, 5, 1 (Jan. 2008), pp. 70-73, ISSN: 1545-598X, DOI: 10.1109/LGRS.2007.908305. (Cited on pp. 24, 47, 48, 64.)

Peakall, J., P. J. Ashworth, and J. L. Best

2007 "Meander-bend evolution, alluvial architecture, and the role of cohesion in sinuous river channels: a flume study", *Journal of Sedimentary Research*, 77, 3, pp. 197-212. (Cited on p. 37.)

Peixoto, J.M.A., B.W. Nelson, and F. Wittmann

2009 "Spatial and temporal dynamics of river channel migration and vegetation in central Amazonian white-water floodplains by remote-sensing techniques", *Remote Sens. Environ.*, 113, 10, pp. 2258-2266. (Cited on pp. 24, 65.)

Perucca, E., C. Camporeale, and L. Ridolfi

2007 "Significance of the riparian vegetation dynamics on meandering river morphodynamics", *Water Resources Research*, 43, 3, W03430, n/a-n/a, ISSN: 1944-7973, DOI: 10.1029/2006WR005234, http://dx.doi.org/10.1029/2006WR005234. (Cited on p. 28.)

Pizzuto, J. E. and T. S. Meckelnburg

1989 "Evaluation of a Linear Bank Erosion Equation", *Water Resources Research*, 25, 5, pp. 1005-1013. (Cited on pp. 12, 28, 37.)

Puhakka, M., R. Kalliola, M. Rajasilta, and J. Salo

1992 "River types, site evolution and successional vegetation patterns in Peruvian Amazonia", *Journal of Biogeography*, 19, 6, pp. 651-665. (Cited on p. 7.)

Repetto, R., M. Tubino, and C. Paola

2002 "Planimetric instability of channels with variable width", *Journal of Fluid Mechanics*, 457 (Apr. 2002), pp. 79-109, ISSN: 0022-1120, DOI: 10.1017/S0022112001007595, http://www.journals.cambridge.org/abstract%5C_S0022112001007595. (Cited on pp. 13, 33, 36, 39, 85, 90.)

Richards, K.

1976 "Channel width and the riffle-pool sequence", *Geological Society of America Bulletin*, 87, pp. 883-890. (Cited on p. 159.)

Rowland, J. C., E. Shelef, P. A. Pope, J. Muss, C. Gangodagamage, S. P. Brumby, and C. J. Wilson

2016 "A morphology independent methodology for quantifying planview river change and characteristics from remotely sensed imagery", *Remote Sensing of Environment*, 184, pp. 212-228, ISSN: 0034-4257, DOI: http://dx.doi.org/10.1016/j.rse.2016.07.005, http://www.sciencedirect.com/science/article/pii/S0034425716302620. (Cited on pp. 24, 47, 48, 64, 65.)

Rozowski, I. L.

1957 *Flow of water i n bends of open channels*, tech. rep., Academy of Sciences of the Uprainian SSR. Inst . Hydrol . and Hydraul. Engng., Jerusalem. (Cited on p. 4.)

Rüther, N. and N. R. B. Olsen

2007 "Modeling free-forming meander evolution in a laboratory channel using three-dimensional computational fluid dynamics", *Geomorphology*, 89, 3–4, pp. 308-319, DOI: doi:10.1016/j.geomorph.2006.12.009.. (Cited on p. 83.)

Schielen, R., A. Doelman, and H. E. De Swart

1993 "On the nonlinear dynamics of free bars in straight channels", *Journal of Fluid Mechanics*, 252, pp. 325-356. (Cited on pp. 8, 9.)

Schuurman, F., Y. Shimizu, T. Iwasaki, and M. G. Kleinhans

2016 "Dynamic meandering in response to upstream perturbations and floodplain formation", *Geomorphology*, 253, pp. 94-109, ISSN: 0169-555X, DOI: http://dx.doi.org/10.1016/j.geomorph.2015.05.039, http://www.sciencedirect.com/science/article/pii/S0169555X15003815. (Cited on p. 22.)

Schwendel, A. C., A. P. Nicholas, R. E. Aalto, Sambrook Smith G. H., and S. Buckley

2015 "Interaction between meander dynamics and floodplain heterogeneity in a large tropical sand-bed river: the Rio Beni, Bolivian Amazon", *Earth Surf. Process. Landforms*, DOI: 10.1002/esp.3777. (Cited on pp. 5, 7, 24, 29, 43.)

Schwenk, J. and E. Foufoula-Georgiou

2015 "Accelerated migration rates downstream of a human-induced cutoff in the Ucayali River, Peru", in *9th Symposium of River, Coastal and Estuarine Morphodynamics*. (Cited on pp. 5, 7, 24, 29, 61, 64, 65.)

Schwenk, J., A. Khandelwal, M. Fratkin, V. Kumar, and E. Foufoula-Georgiou

2016 "High spatio-temporal resolution of river planform dynamics from Landsat: the RivMAP toolbox and results from the Ucayali River", *Earth and Space Science*, 2016EA000196, n/a-n/a, ISSN: 2333-5084, DOI: 10.1002/2016EA000196, http://dx.doi.org/10.1002/2016EA000196. (Cited on pp. 7, 24, 43, 47, 61, 64, 65.)

Schwenk, J., S. Lanzoni, and E. Foufoula-Georgiou

2015 "The life of a meander bend: Connecting shape and dynamics via analysis of a numerical model", *J. Geophys.Res. Earth Surf.*, 120, 4, pp. 690-710, DOI: 10.1002/2014JF003252. (Cited on p. 23.)

Seminara, G.

2006 "Meanders", *Journal of fluid mechanics*, 554, pp. 271-297, ISSN: 0022-1120, DOI: 10.1017/S0022112006008925. (Cited on pp. 12, 22, 31, 37, 70, 82.)

Seminara, G. and M. Tubino

1989 "Alternate Bars and Meandering", in *River Meandering*, American Geophysical Union, pp. 267-320, ISBN: 9781118665602, DOI: 10.1029/WM012p0267, http://dx.doi.org/10.1029/WM012p0267. (Cited on pp. 8, 18, 177.)

1992 "Weakly nonlinear theory of regular meanders", *Journal of Fluid Mechanics*, 244, pp. 257-288, DOI: 10.1017/S0022112092003069. (Cited on pp. 112, 154.)

Seminara, G., G. Zolezzi, M. Tubino, and D. Zardi

2001 "Downstream and upstream influence in river meandering. Part 2. Planimetric development", *Journal of Fluid Mechanics*, 438, pp. 213-230. (Cited on pp. 5, 11, 14, 21, 23, 28, 31-33, 36, 37, 58, 60, 69, 70, 75, 79, 81, 83, 85, 91, 154, 174, 180.)

Serra, J.

1982 *Image analysis and mathematical morphology, v. 1*, Academic press. (Cited on p. 46.)

1986 "Introduction to mathematical morphology", *Computer vision, graphics, and image processing*, 35, 3, pp. 283-305. (Cited on p. 46.)

Siviglia, A., G. Stecca, D. Vanzo, G. Zolezzi, E. F. Toro, and M. Tubino

2013 "Advances in Water Resources Numerical modelling of two-dimensional morphodynamics with applications to river bars and bifurcations", *Advances in Water Resources*, 52, pp. 243-260, ISSN: 0309-1708, DOI: 10.1016/j.advwatres.2012.11.010, http://dx.doi.org/10.1016/j.advwatres.2012.11.010. (Cited on p. 8.)

Smith, J. D. and S. R. Mclean

1984 "A Model for Flow in Meandering Streams", *Water Resources Research*, 20, 9, pp. 1301-1315, ISSN: 1944-7973, DOI: 10.1029/WR020i009p01301, http://dx.doi.org/10.1029/WR020i009p01301. (Cited on p. 53.)

Solari, L. and G. Seminara

2005 "On width variations in meandering rivers", in *Proc. 4th IAHR Symp. on River, Coastal and Estuarine Morphodynamics, RCEM 2005*, Urbana, Illinois, USA, vol. 2, pp. 745-751. (Cited on p. 12.)

Song, C., C. E. Woodcock, K. C. Seto, M. P. Lenney, and S. A. Macomber

2001 "Classification and change detection using Landsat TM data: when and how to correct atmospheric effects?", *Remote sensing of Environment*, 2, 75, pp. 230-244. (Cited on pp. 44, 64.)

Spiegelberg, G.

2010 "Um modelo morfodinâmico: Desenvolvimento e aplicação no reservatório da usina hidroelétrica de estreito no Rio Tocantins", *Rio de Janeiro: UFRJ/COPPE*. (Cited on p. 99.)

Stuart, J. T.

1971 "Nonlinear stability theory", *Ann. Rev. Fluid Mech.*, 3, pp. 347-370. (Cited on p. 4.)

Subramaniam, S., A. V. Suresh Babu, and Roy P. S.

2011 "Automated Water Spread Mapping Using ResourceSat-1 AWiFS Data for Water Bodies Information System", *IEEE Journal of Selected Topics in Applied Earth Observations and Remote Sensing*, 4, 1 (Mar. 2011), pp. 205-215, ISSN: 1939-1404, DOI: 10.1109/JSTARS.2010.2085032. (Cited on p. 45.)

Sun, T., P. Meakin, T. Jossang, and K. Schwarz

1996 "A Simulation Model for Meandering Rivers", *Water Resources Research*, 32, 9, pp. 2937-2954, ISSN: 1944-7973, DOI: 10.1029/96WR00998, http://dx.doi.org/10.1029/96WR00998. (Cited on pp. 4, 21, 37.)

Swanson, D. C.

1993 "The importance of fluvial processes and related reservoir deposits", *J. Pet. Technol.*, pp. 368-377. (Cited on p. 4.)

Talmon, A. M., N. Struiksma, and M. C. L. M. Van Mierlo

1995 "Laboratory measurements of the direction of sediment transport on transverse alluvial-bed slopes", *Journal of Hydraulic Research*, 33, 4, pp. 495-517, DOI: 10.1080/00221689509498657, eprint: http://dx.doi.org/10.1080/00221689509498657, http://dx.doi.org/10.1080/00221689509498657. (Cited on p. 78.)

Torrence, C. and G. P Compo

1995 *A Practical Guide to Wavelet Analysis*, Report, Bulletin of the American Meteorological Society. (Cited on p. 106.)

Trigg, M. A., P. D. Bates, W. D. Wilson, G. Schumann, and C. Baugh

2012 "Floodplain channel morphology and networks of the middle Amazon River", *Water Resources Research*, 48. (Cited on p. 15.)

Tubino, M.

1991 "Growth of alternate bars in unsteady flow", *Water Resources Research*, 27, 1, pp. 37-52, ISSN: 1944-7973, DOI: 10.1029/90WR01699, http://dx.doi.org/10.1029/90WR01699. (Cited on p. 22.)

Tubino, M. and G. Seminara

1990 "Free–forced interactions in developing meanders and suppression of free bars", *Journal of Fluid Mechanics*, 214, pp. 131-159, ISSN: 1469-7645, DOI: 10.1017/S0022112090000088, http://journals.cambridge.org/article%5C_S0022112090000088. (Cited on pp. 8, 18, 22, 70, 129, 177, 186.)

Udo, E. and C. Uko

2014 "Characterization of Stabilized Mbo Residual Soils, Akwa Ibom State-Nigeria", *EJGE*, pp. 2875-2898. (Cited on p. 99.)

Van de Lageweg, W. I., W. M. van Dijk, A. W. Baar, J. Rutten, and M. G. Kleinhans

2014 "Bank pull or bar push: What drives scroll-bar formation in meandering rivers?", *Geology*, 42, 4, pp. 319-322. (Cited on pp. 23, 39, 71.)

Van der Walt, S., J. L. Schönberger, J. Nunez-Iglesias, F. Boulogne, J. D. Warner, N. Yager, E. Gouillart, and T. Yu

2014 "scikit-image: image processing in Python", *PeerJ*, 2, e453. (Cited on p. 44.)

Vermeulen, B., A. J. F. Hoitink, G. Zolezzi, J. D. Abad, and R. Aalto

2016 "Multiscale structure of meanders", *Geophysical Research Letters*, 43, 7, 2016GL068238, pp. 3288-3297, ISSN: 1944-8007, DOI: 10.1002/2016GL068238, http://dx.doi.org/10.1002/2016GL068238. (Cited on p. 106.)

Werth, K.

2014 *Geschichte der Etsch zwischen Meran und San Michele Flussregulierung, Trockenlegung der Mser*, tech. rep., Hochwasserschutz. (Cited on p. 9.)

Whiting, P. J. and W. E. Dietrich

1993 "Experimental constraints on bar migration through bends: Implications for meander wavelength selection", *Water Resources Research*, 29, 4, pp. 1091-1102, ISSN: 1944-7973, DOI: 10.1029/92WR02356, http://dx.doi.org/10.1029/92WR02356. (Cited on pp. 8, 10.)

Wilkerson, G. V. and G. Parker

2010 "Physical basis for quasi-universal relationships describing bankfull hydraulic geometry of sand-bed rivers", *Journal of Hydraulic Engineering*, 137, 7, pp. 739-753. (Cited on pp. 28, 29, 31, 39, 72, 83, 97.)

Williams, G. P.

1978 "Bank-full discharge of rivers", *Water Resources Research*, 14, 6, pp. 1141-1154, ISSN: 1944-7973, DOI: 10.1029/WR014i006p01141. (Cited on p. 28.)

Wittmann, H., F. von Blanckenburg, J. L. Guyot, L. Maurice, and P. W. Kubik

n.d. "From source to sink: Preserving the cosmogenic 10Be-derived denudation rate signal of the Bolivian Andes in sediment of the Beni and Mamoré foreland basins", *Earth and Planetary Science Letters*, 288. (Cited on p. 99.)

Xu, H.

2005 "A Study on Information Extraction of Water Body with the Modified Normalized Difference Water Index (MNDWI)", *Journal of Remote Sensing*, 5, pp. 589-595. (Cited on p. 45.)

2006 "Modification of normalised difference water index (NDWI) to enhance open water features in remotely sensed imagery", *International Journal of Remote Sensing*, 27, pp. 3025-3033. (Cited on pp. 15, 16, 24, 45.)

Zen, S., A. Gurnell, G. Zolezzi, and N. Surian

2017 "Exploring the role of trees in the evolution of meander bends: The Tagliamento River, Italy", *Water Resources Research*, 53, 7, pp. 5943-5962, ISSN: 1944-7973, DOI: 10.1002/2017WR020561, http://dx.doi.org/10.1002/2017WR020561. (Cited on p. 34.)

Zen, S., G. Zolezzi, M. Toffolon, and A. Gurnell

2016 "Biomorphodynamic modelling of inner bank advance in migrating meander bends", *Advances in Water Resources*, 93, pp. 166-181. (Cited on pp. 27, 34, 37, 83.)

Zhang, T. Y. and C. Y. Suen

1984 "A fast parallel algorithm for thinning digital patterns", *Communications of the ACM*, 27, 3, pp. 236-239. (Cited on p. 47.)

Zolezzi, G.

2014 "Continuous Wavelet characterization of the wavelengths and regularity of meandering rivers", *Geomorphology*, 252. (Cited on p. 106.)

Zolezzi, G., W. Bertoldi, and M. Tubino

2012a "Morphodynamics of Bars in Gravel-Bed Rivers: Bridging Analytical Models and Field Observations", *Gravel-Bed Rivers: Processes, Tools, Environments*, pp. 69-89. (Cited on p. 22.)

Zolezzi, G., R. Luchi, and M. Tubino

2009 "Morphodynamic regime of gravel bed, single-thread meandering rivers", *Journal of Geophysical Research*, 114, F1 (Jan. 2009), F01005, ISSN: 0148-0227, DOI: 10.1029/2007JF000968, http://doi.wiley.com/10.1029/2007JF000968. (Cited on pp. 28, 29, 31, 32, 142, 144-147.)

2012b "Modeling morphodynamic processes in meandering rivers with spatial width variations", *Reviews of Geophysics*, 50, 4. (Cited on pp. 12, 32-34, 70, 78, 83, 85, 87, 113, 127, 128, 137, 161.)

Zolezzi, G. and G. Seminara

2001a "Downstream and upstream influence in river meandering. Part 1. General theory and application to overdeepening", *Journal of Fluid Mechanics*, 438, pp. 183-211, ISSN: 1469-7645, DOI: 10.1017/S002211200100427X, http://journals.cambridge.org/article%5C_S002211200100427X. (Cited on pp. 4, 5, 11, 32, 33, 58, 70, 78, 174.)

2001b "Upstream influence in erodible beds", *Physics and Chemistry of the Earth, Part B: Hydrology, Oceans and Atmosphere*, 26, 1, pp. 65-70. (Cited on p. 32.)